Kirkwood, Robert A. (2017) *Superconducting single photon detectors for quantum information processing.* PhD thesis.

# Superconducting single photon detectors for quantum information processing

**Robert A. Kirkwood**

School of Engineering

University of Glasgow

This thesis is submitted for the degree of

*Doctor of Philosophy*

April 2017

# Abstract

Single photon detectors are a vital part of many emerging technologies which harness the quantum properties of light to benefit the fields of communication, computation and sensing. Superconducting nanowire single photon detectors (SNSPDs) offer high detection efficiency, low dark count rates, low timing jitter, and infrared sensitivity that are required by the most demanding single photon counting applications. This thesis presents SNSPDs fabricated and tested at the University of Glasgow that are integrated with optical structures which enable enhanced detection efficiency and integration with waveguide circuit technology.

The monolithic integration of waveguide circuit components presents a route towards realisation of an optical quantum information processor that has the stability and scalability to perform the demanding tasks of quantum computation. A novel process is introduced for incorporating superconducting detectors with single mode gallium arsenide waveguides and quantum dot single photon sources. Together these elements would enable the generation of quantum states of light which could be manipulated and detected on a single chip. Detectors are patterned in NbTiN thin superconducting films on to suspended nanobeam waveguides with better than 50 nm alignment accuracy. Low temperature electrical and optical testing confirms the detectors' single photon sensitivity under direct illumination as well as to waveguide coupled light. Measured detectors were found to have internal registering efficiencies of $6.8 \pm 2.4\%$.

Enhancing absorption of photons into thin superconducting films is vital to the creation of high efficiency superconducting single photon detectors. Fabricating an SNSPD on a dielectric mirror creates a partial cavity that can be tailored to enhance detection of light at specific wavelengths. Devices have been fabricated and tested in this thesis with enhanced detection efficiency at infrared and visible wavelengths for quantum cryptography, remote sensing and life science applications. Detectors fabricated in NbTiN on GaAs/AlGaAs Bragg mirrors exhibited a system detection efficiency of 1.5% at 1500 nm

wavelength for the best device measured. SNSPDs were also fabricated in NbN on aperiodic dielectric mirrors with a range of different bandwidths. A peak system detection efficiency of 82.7% at 808 nm wavelength was recorded.

# Acknowledgements

welcome. Whilst in Glasgow the support staff in the School of Engineering are always there to provide help when asked: Bill Ward, Tom O'Reilly, Elaine McNamara particularly so. Also academics in Glasgow Tim Drysdale, Tony Kelly, Charlie Ironside, and Doug Paul have been generous with support and insight.

Finally I'm grateful for the immeasurable support I've received from friends and family. To my parents Hilda and Adrian and my sister Claire for their boundless encouragement. To Ellie I owe a huge amount. Our game of international cat-and-mouse has been worth every minute. Also to my friends, Matus Krajnak at home in Glasgow, and to the others in Scotland and further afield who have put up with me and helped me to maintain my sanity.

# Table of contents

# List of figures

# List of tables

# Definitions & Abbreviations

**Acronyms**

| | |
|---|---|
| **AFM** | atomic force microscopy |
| **BCS** | Bardeen, Cooper, and Schrieffer |
| **BNC** | bayonet Neill-Concelman |
| **CCD** | charge coupled device |
| **CMOS** | complimentary metal-oxide-semiconductor |
| **CPD** | critical point drying |
| **cps** | counts per second |
| **CW** | continuous wave |
| **DBR** | distributed Bragg reflector |
| **DCR** | dark count rate |
| **DML** | dielectric multi-layer |
| **EBL** | electron beam lithography |
| **FDTD** | finite difference time domain |
| **FWHM** | full-width at half-maximum |
| **GM** | Gifford-McMahon |
| **HBT** | Hanbury-Brown Twiss |
| **HOM** | Hong–Ou–Mandel |
| **HSQ** | hydrogen silsesquioxane |
| **IPA** | isopropyl alcohol |
| **ITO** | indium tin oxide |
| **JTL** | Josephson transmission line |
| **JWNC** | James Watt Nanofabrication Centre |
| **KF** | Klein flange |
| **LHe** | liquid helium |
| **LIDAR** | light detection and ranging |
| **LOQC** | linear optical quantum computing |
| **MBE** | molecular beam epitaxy |
| **MMI** | multi mode interference |
| **MZI** | Mach–Zehnder interferometer |

| | |
|---|---|
| **NA** | numerical aperture |
| **NICT** | National Institute of Information and Communication Technology, Japan |
| **NIR** | near infrared |
| **nMP** | n-methyl-2-pyrrolidone |
| **NMR** | nuclear magnetic resonance |
| **OCT** | optical coherence tomography |
| **OFHC** | oxygen-free high thermal conductivity |
| **PCB** | printed circuit board |
| **PEC** | proximity effect correction |
| **PhC** | photonic crystal |
| **PL** | photo-luminescence |
| **PMMA** | Poly(methyl methacrylate) |
| **PNR** | photon number resolution |
| **PT** | pulse tube |
| **QD** | quantum dot |
| **QIP** | quantum information processing |
| **QKD** | quantum key distribution |
| **QPIC** | quantum photonic integrated circuit |
| **RIE** | reactive ion etch |
| **RSFQ** | rapid single flux quantum |
| **SDE** | system detection efficiency |
| **SEM** | scanning electron microscope |
| **SMA** | SubMiniature A |
| **SMF** | single-mode fibre |
| **SMP** | SubMiniature push-on |
| **SNB** | suspended nanobeam |
| **SNR** | signal-to-noise ratio |
| **SNSPD** | superconducting nanowire single photon detector |
| **SPAD** | single photon avalanche diode |
| **SPD** | single photon detector |
| **SPDC** | spontaneous parametric down-conversion |
| **SPS** | single photon source |
| **SQUID** | superconducting quantum interference device |
| **TCSPC** | time-correlated single photon counting |
| **TES** | transition-edge sensor |
| **UV** | ultraviolet |
| **VNA** | vector network analyser |

|        |           |
|--------|-----------|
| **ZEP** | ZEP-520A |

## Greek symbols

| | |
|---|---|
| $\epsilon_r$ | relative permittivity (dielectric constant) |
| $\eta$ | efficiency |
| $\eta_{absorption}$ | absorption efficiency |
| $\eta_{absorption}^{wg}$ | absorption efficiency of waveguide photons |
| $\eta_{coupling}$ | coupling efficiency |
| $\eta_{registering}$ | registering efficiency |
| $\eta_{waveguide}$ | waveguide transmission efficiency |
| $\kappa$ | absorption coefficient |
| $\lambda$ | wavelength |
| $\lambda_L$ | London magnetic penetration depth |
| $\mu_r$ | relative permeability |
| $\omega$ | angular frequency |
| $\Phi$ | photon flux |
| $\phi$ | phase |
| $\Phi_0$ | magnetic flux quantum |
| $\varphi$ | photon wavefunction |
| $\psi$ | superconducting charge carrier wavefunction |
| $\tau$ | time difference |
| $\tau_1$ | pulse rise time |
| $\tau_2$ | pulse fall time |
| $\theta_C$ | critical angle |
| $\triangle$ | Cooper pair condensation energy |
| $\xi$ | coherence length |

## Roman symbols

| | |
|---|---|
| $2m^*$ | Cooper pair mass |
| III–V | semiconductors comprised of compounds of elements in groups III and V of the periodic table |
| $A$ | cross sectional area |
| AC | alternating current |
| $B$ | magnetic field (flux density) |
| $C$ | kinetic inductance fitting parameter |
| $c$ | speed of light |
| $\boldsymbol{D}$ | electric displacement |
| $d$ | thickness |
| DC | direct current |

| | |
|---|---|
| $\mathcal{E}$ | electric field |
| $E$ | energy |
| $f$ | frequency |
| $g^{(1)}$ | first order correlation function |
| $g^{(2)}$ | second order correlation function |
| GSamples | billion samples |
| $h$ | Planck's constant |
| $\hbar$ | reduced Planck's constant, $h/2\pi$ |
| $H_C$ | critical magnetic field density |
| $I$ | intensity |
| $I_B$ | bias current |
| $I_C$ | critical current |
| $I_{delay}$ | current supplied to delay line on RSFQ chip |
| $J_C$ | critical current density |
| $J_{local}$ | local current density |
| $k$ | wavenumber |
| $\mathcal{L}$ | mean free path |
| $l$ | length |
| $L_K$ | kinetic inductance |
| $\bar{n}$ | mean number of photons per unit time |
| $\triangle n$ | standard deviation in photon number |
| $n$ | refractive index, photon number |
| $n_{eff}$ | effective refractive index |
| $n_s$ | Cooper pair density |
| $\boldsymbol{P}$ | electric polarisation |
| $\mathbf{P}$ | optical power |
| $P$ | polarisation |
| $\mathbb{P}_{out}$ | probability of an output pulse being generated by the RSFQ flip-flop logic circuit |
| $R$ | resistance |
| $\boldsymbol{R}$ | reflectance |
| $\mathcal{R}$ | detector count rate |
| RF | radio frequency |
| rpm | revolutions per minute |
| sccm | standard cubic centimetre per minute |
| $T$ | temperature |
| $\boldsymbol{T}$ | transmittance |
| $t$ | time |

| | |
|---|---|
| $T_C$ | superconducting transition temperature |
| $\triangle t$ | timing jitter |
| $\overline{\triangle t}$ | average timing jitter |
| $V$ | voltage |
| $v$ | velocity |
| $w$ | width |
| $x, y, z$ | position coordinates |
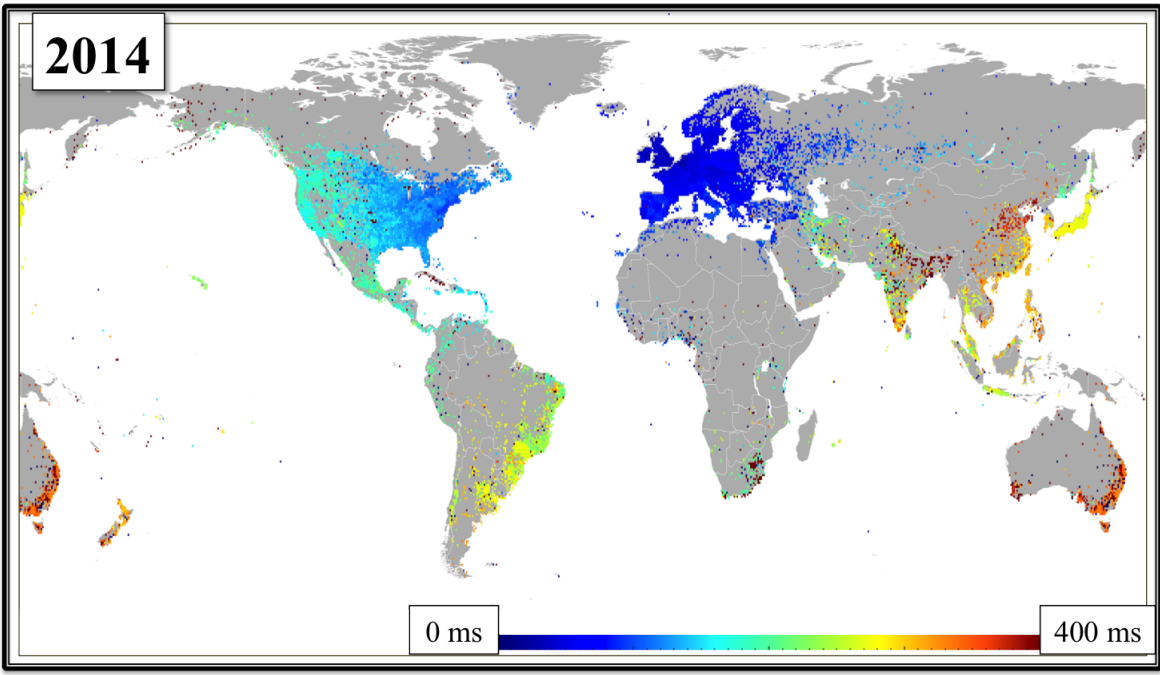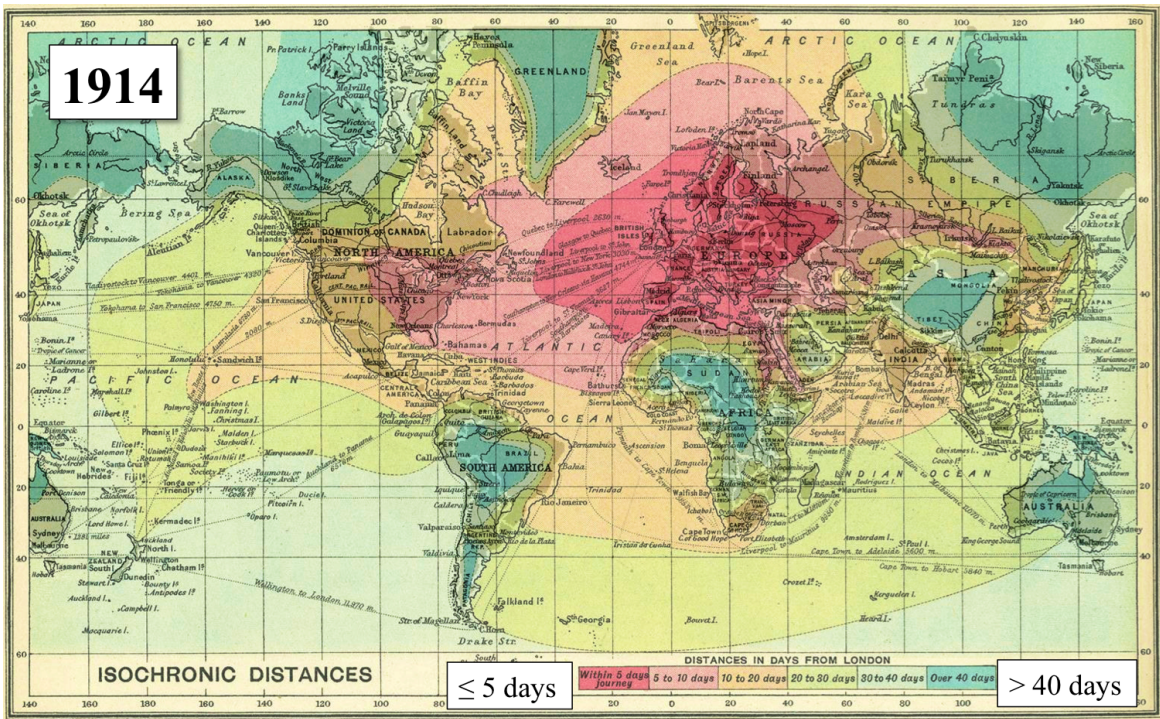
Maps showing the transmission times for messages sent from south east England in 1914 and 2014. A century ago messages carried by hand would take over 40 days to reach the most remote locations. Today messages sent over the internet reach the other side of the globe in a fraction of a second. Even including processing and routing times these messages travel on average around one third the speed of light. Images adapted from references 1 and 2.

# Chapter 1

# Introduction

The maps on the page opposite show how long it would take to send a message across the world in 1914 and in 2014. The monumental improvement seen over the course of a century illustrates the impact of advances in computation and communication technologies. Light has played no small part in the historical developments of these technologies with one example being the fibre optic network carrying messages between continents today at speeds very close to their physical limit. Attention is turning to the quantum mechanical properties exhibited by light on the smallest scales and particularly to the advanced capabilities that quantum technologies can bring to the fields of communication and computation.

Modern day computers are machines that process information by encoding data as high and low voltages (representing 0s and 1s) within an electronic circuit. Data are processed through logic gates which compare one or more input states to produce a determined output state. By combining large numbers of similar logic gates and feeding output states to successive logic gate inputs in the correct order algorithms and calculations can be applied to the initial input data. A modern computer can be programmed to perform a vast range of different algorithms although some functions are still extremely hard to compute and would require impossibly large amounts of processing power or time to complete.

Quantum computers promise to deliver exponential improvements over existing information processors that operate under the laws of classical physics. By encoding data bits on objects which are subject to the laws of quantum mechanics such as individual particles certain tasks can be performed that are intractable on modern classical computers. Factoring large numbers and

efficiently searching large datasets are two examples of these tasks which happen to be of great importance in the digital economy for instance in facilitating the secure transfer of private messages over the public internet. By manipulating light at the single photon level it may be possible to create a programmable quantum computer but the requirement for numerous components to operate together with high precision and minimal losses presents a formidable challenge.

The creation of a practical quantum information processor requires the co-operative development of multiple technologies each of which have become research fields in their own right. Research into optical and quantum computing is currently conducted by numerous scientific institutions as well as in Silicon Valley and the auxiliary quantum photonic technologies being developed along the way are already promising to deliver improvements in sensing and communications.

This thesis describes the author's work to create and characterise components for optical quantum information processing, particularly single photon detectors. Chapter 2 begins with a detailed background review of the current state of the art and a description of the relevant scientific theory. The methods used to fabricate and characterise devices are described in Chapter 3. A novel superconducting nanowire single photon detector integrated with gallium arsenide suspended nanobeam waveguides of single mode dimensions is presented. Low temperature electrical and optical characterisation of the detectors and waveguides is described in Chapter 4.

Chapter 5 describes efforts to include waveguide integrated detectors in so called quantum photonic integrated circuits. These integrated waveguide circuits aim to advance the state of the art for generating, routing, and detecting single infrared photons on a single chip. Consideration is also given to fast superconducting logic circuits which implement digital logic at low temperatures with minimal power consumption by transferring magnetic flux quanta between superconducting loops. These circuits are well suited to multiplexing single photon detectors and performing fast information transfer of the kind needed for linear optical quantum computing.

Chapter 6 presents work to enhance the performance of superconducting single photon detectors coupled to optical fibre. Stand-alone detectors are required with high efficiency at specific wavelengths corresponding to low loss transmission in silica fibres. Such detectors are highly desirable for the implementation of quantum secure communication over fibre optic networks. The same techniques used for wavelength-specific enhancement of detection
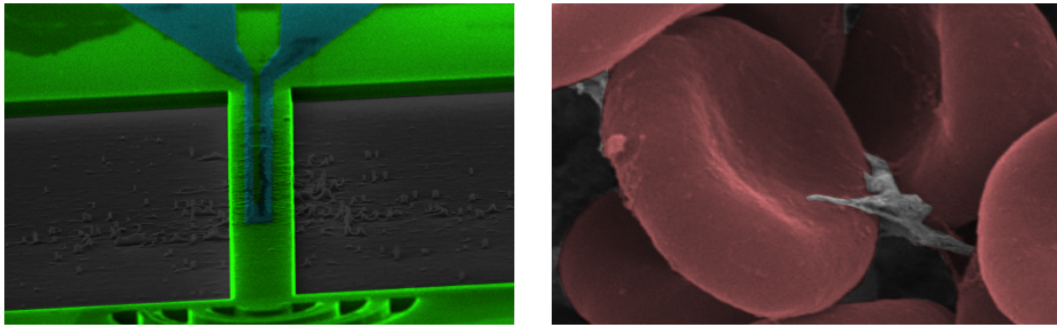
The picture on the left is a false coloured electron microscope image of a waveguide integrated superconducting single photon detector fabricated by the author. Rather than provide a scale bar an image of human red blood cells at the same magnification is included for comparison. Image adapted from reference 3.

efficiency are also adapted for wavelengths of interest in remote sensing and life science applications.

# Chapter 2

# Background and literature review

*This chapter aims to provide an overview of the relevant scientific theory covered in this thesis and a review of the current state-of-the-art in the field. The first section introduces photons and the history and theory surrounding light as a classical wave and quantum wavefunction. Methods for generating and detecting quantum states of light (i.e. single photons) are described in terms of basic characteristics and figures of merit. Existing photon counting technologies are described. Superconducting nanowire single photon detectors (SNSPDs) are introduced in terms of the interactions of single photons with thin superconducting films followed by a description of techniques responsible for the advance of SNSPD technology through electrical and optical optimisation. Next quantum information processing is introduced, with relation to computing and secure communications. Linear optical quantum computing is introduced as a candidate for creating a programmable universal quantum computer with qubits encoded on photons. Waveguide circuits are the strongest candidate for a practical scale optical quantum computer, therefore the concept is introduced of an optical quantum computer made with all components integrated on the surface of a single chip. The specific requirements for the integration of these components are discussed, including the details of optical waveguides, integrated single photon sources, and integrated single photon detectors. Consideration is also given to RSFQ superconducting logic circuits, a suitable candidate for fast read-out and feed-forward of information for an optical processor.*

## 2.1   Quantum photonic technology - history and background

### 2.1.1   Light: classical and quantum

Today photons are understood to be the elementary particles which constitute light. A laser beam for example is a stream of individual photons, each one a microscopic irreducible object whose behaviour is governed by the laws of quantum mechanics that can cause both wave-like properties and particle-like phenomena to be observed in laser beams under certain conditions. Historically the nature of light remained controversial for centuries as natural philosophers struggled to reconcile different observed optical effects with a consistent theory of light. Christiaan Huygens used phenomena such as diffraction and interference to argue that light was a wave [4] propagating in an invisible medium, known to pre-twentieth century scientists as the Luminiferous Ether. Conversely Isaac Newton postulated that light was a stream of particles, so called corpuscles, as evidenced by his famous demonstration of straight beams of light refracting through a pair of prisms [5] whereas James Clarke Maxwell's unification of electromagnetic forces in 1881 provided a succinct set of equations which describe how sympathetic oscillations in electric and magnetic fields can propagate as waves [6]. The experiments of Michelson and Morley in 1887 helped to disprove the existence of the Ether [7] and Einstein's theory of special relativity [8] published shortly afterwards incorporates light travelling through vacuum at a universally constant speed, unchanging for any observer moving in any direction at a constant speed. By 1905 the theories of Maxwell and Einstein could be used to accurately predict a vast number of optical phenomena including the interaction of light and matter on the atomic scale. In each case light can be described as a continuous classical wave and atoms as nuclei with electrons orbiting in quantised energy levels.

Maxwell's equations, considered a triumph of classical physics, are a staple of the modern undergraduate physics syllabus with many quality resources available to the interested reader including textbooks [9], lecture courses [10], and other media [11]. The following paragraphs introduce the mathematics of this framework as it is used to describe light waves and their interaction with matter. Describing relations between the electric field $\mathcal{E}$ and magnetic field $B$ Maxwell's equations allow wave-like solutions for coupled excitations in the $\mathcal{E}$

and $\boldsymbol{B}$ fields that propagate in free space with speed

$$c = \frac{1}{\sqrt{\mu_0 \epsilon_0}} = 2.998 \times 10^8 \text{m s}^{-1} \tag{2.1}$$

where $\epsilon_0$ and $\mu_0$ are the permittivity and permeability of free space respectively. The simple solution of an infinite plane wave travelling in the $z$ direction through free space has the electric field component

$$\boldsymbol{\mathcal{E}}(z,t) = \boldsymbol{\mathcal{E}_0} \sin(kz - \omega t + \phi) \tag{2.2}$$

where $\boldsymbol{\mathcal{E}_0}$ and $\phi$ are the amplitude and phase of a sinusoidal wave respectively. The angular frequency $\omega$ and wavenumber $k$ relate to the peak to peak wavelength $\lambda$ of the light as $k = 2\pi/\lambda = \omega/c$. The intensity $I$ is a measure of the energy flow per unit area carried by an electromagnetic wave. Over time-scales much longer than $\omega^{-1}$ the energy averaged over a large number of cycles becomes proportional to $\mathcal{E}_0^2$. What we know as the visible spectrum is a particular range of wavelengths forming a narrow window in the much wider electromagnetic spectrum. The visible range ($\lambda = 400 - 750$ nm) which can be detected by the rod and cone cells on human retinas coincides with the transparency of Earth's atmosphere and, by no accident, with a vast array of natural features and processes upon which our survival depends.

Light propagating within a dielectric medium is influenced by the properties of that material. The oscillating electric field is combined with the electric displacement $\boldsymbol{D}$ and the material specific electric polarisation $\boldsymbol{P}$,

$$\boldsymbol{D} = \epsilon_0 \boldsymbol{\mathcal{E}} + \boldsymbol{P}. \tag{2.3}$$

For isotropic media we can also introduce a constant $\epsilon_r$ which is the relative permittivity (or dielectric constant) of the medium. The speed $v$ at which light travels inside a dielectric medium is now given by

$$v = \frac{1}{\sqrt{\epsilon_r \epsilon_0 \mu_0}} = \frac{c}{n} \tag{2.4}$$

which gives us the refractive index $n = \sqrt{\epsilon_r}$ a quantity which relates the speed of light inside a medium to the dielectric properties of that medium. Expressing the refractive index as a complex number

$$n^* = n + i\kappa \tag{2.5}$$

introduces another important quantity. The real part $n$ of the refractive index describes the speed of light in a medium whilst the imaginary part $\kappa$, also known as the absorption coefficient, is a wavelength dependent quantity describing the amount of energy lost from the propagating light wave by absorption into the medium.

At the lowest intensities the energy carried by a light wave does not vary continuously to zero but is instead granular or quantised. This concept was first introduced by Max Planck at the turn of the 20th century [12, 13] and helped to explain why the spectrum of radiation from a black-body does not become infinitely intense at shorter wavelengths. In 1905 Einstein again used quantised light to explain the photoelectric effect [14]. These small packets of energy, which were soon after called photons [15], are characterised by their wavelength (or frequency) and Planck's constant $h$.

$$E = \frac{hc}{\lambda} = \hbar\omega \tag{2.6}$$

where $\hbar = h/2\pi$ is known as the reduced Planck constant.

The photoelectric effect concerns the absorption of a photon matching the energy gap between orbital levels of an atomic electron. The reverse also occurs when an electron in an excited state $E_1$ will relax to a lower energy state $E_0$ by emitting a photon with the exact gap energy $E_{photon} = E_1 - E_0$. This explains the narrow lines seen in emission spectra of gas lamps such as Na, Hg, and Ne. The bright lines appear at specific wavelengths in the visible spectrum corresponding to photon energies that match the electron energy levels unique to atoms of each element.

Mathematician Paul Dirac produced the first complete theory of a quantised electromagnetic field in 1927 [16]. The set of observable phenomena whose explanation demands a fully quantum theory form the field of quantum optics or quantum photonics. The early development of quantum optics owes a huge amount to Willis Lamb and Roy Glauber for the introduction of coherent light and the Laser during the 1960s [17–19]. As well as being used to study fundamental physical effects such as entanglement over long distances [20, 21] the quantum properties of photons can be exploited for secure communication and for encoding qubits in a quantum computer. These novel applications, collectively known as quantum information processing (QIP), hold much promise for future advancements in technology and require development of high quality single photon detectors (SPDs) and single photon source (SPS).

Humans, and a large number of other animals, are naturally capable of sensing extremely low levels of light. Rod cells similar to those found on the retina of a human eye are sensitive to faint light signals comprising just a few photons [22], although as reliable detectors for single photon counting experiments human eyes are perhaps not ideal [23]. The development of photonic technologies with sensitivity reaching the single photon level, such as sensitive detectors [24] and spectrometers, have helped to increase our understanding of areas as diverse as cosmology and molecular biology. In the modern era we have also harnessed the power of coherent light for fast global communications (see picture on page 2).

## 2.1.2   Single photon detectors

The ideal SPD as depicted in Figure 2.1 is a light sensitive box which emits a tick or a pulse when a photon hits it. The output pulse would ideally be infinitely narrow, immediate and should happen exactly once for every photon that arrives at the detector. It would not pulse when there are no photons present (a *dark count*) and it would not fail to pulse when any photon arrives (100% *efficiency*). The ideal detector would be continuously sensitive to photons, with zero time spent unresponsive (*dead time*) whilst resetting after registering the previous event. It is also beneficial for a photon detector to be able to register photons with a wide range of energies. Single optical photons of interest have energies in the range of 3 eV (visible) to 0.1 eV (mid infrared). Wavelengths 1550 nm and 1310 nm, corresponding to single photon energies of 0.8 eV and 0.95 eV respectively, have the lowest transmission losses in silica optical fibre and are referred to as telecoms wavelengths. These regions of the electromagnetic spectrum are the main focus of this thesis and provide rich ground for applications across imaging, communications, sensing, information processing, and beyond.

**Single photon detector figures of merit**

Any SPD can be characterised by a number of figures of merit [25]. Terms used throughout this thesis are described below.

– **Efficiency ($\eta$)**
A detector's efficiency is the probability that it will produce a 'click' given the
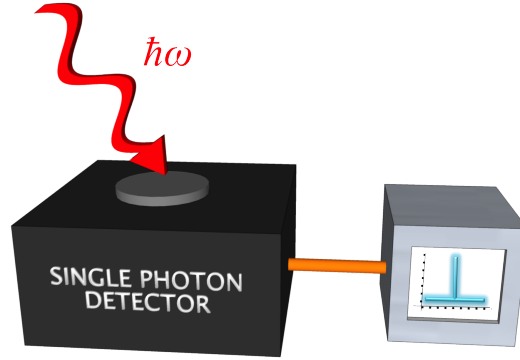
Fig. 2.1 The ideal single photon detector generates a fast, well defined electrical pulse for every photon that is incident upon it.

arrival of a photon. Efficiency can be calculated by illuminating a detector with a known optical power and comparing the input photon flux to the count rate from the detector.

$$\eta = \frac{\mathcal{R}}{\Phi} = \frac{\mathcal{R}hc}{P\lambda} \tag{2.7}$$

where $\mathcal{R}$ is the count rate from the detector in counts per second and $\Phi$ is the incoming photon flux. The number of photons per second is calculated by dividing the optical power P by the energy of one photon $E_{photon} = hc/\lambda$. For a detector operating in the single photon counting regime the count rate should scale linearly with input photon flux $\frac{d}{d\Phi}(\eta) \propto \Phi$. If the detector is operated outside of this regime it may become sensitive only to 2 or more photons arriving simultaneously. For a detector sensitive only to $n$-photon events $\frac{d}{d\Phi}(\eta) \propto \Phi^n$.

Efficiency is a compound quantity comprised of several constituent elements. The overall system detection efficiency (SDE) is a measured probability of an input photon making it all the way through the experimental system and resulting as a 'click' on the counting apparatus. There are distinct probabilities associated with coupling light onto the active area of the detector $\eta_{coupling}$, photons being absorbed in the active material $\eta_{absorption}$, and of absorbed photons triggering a voltage pulse which is faithfully recorded by the read-out electronics $\eta_{registering}$.

$$SDE = \eta_{coupling} \times \eta_{aborption} \times \eta_{registering} \tag{2.8}$$

Although the coupling efficiency is used in this work to specifically describe the geometric overlap of a light beam with a detector's active area the end user of a detector system may wish to consider the so-called insertion loss. For a

fibre-coupled detector system with an FC/PC fibre input port the insertion loss can be considered as the proportion of photons introduced to the input port that are lost before reaching the detector's active area. This would then be a combination of geometric coupling losses and any losses from the fibre inside the detector system, through tight bends, splices, or optical components such as lenses etc.

– **Dark count rate (DCR)**

Dark counts are strictly defined as counts generated by a detector in the absence of light. Noise intrinsic to the detector material and bias configuration can lead to spurious events being registered at the read-out circuit. There can also be sources of systematic unwanted counts. After-pulsing is the phenomenon by which there is a significant probability of 1 or more additional counts being registered after, and as a result of, registration of an incoming photon. Semiconductor detectors in particular exhibit strong afterpulsing effects. With devices for which this effect becomes problematic a gated bias circuit can be employed to reduce the number of dark counts and after-pulses, at the expense of losing signal photons that arrive at the detector whilst the gate is low (off). All experiments are also likely to have some level of background photon noise caused by light leaking into the system or more likely by emission of blackbody radiation particularly from surfaces of room temperature components (see further discussion in Section 2.2.3). Measurements of detector efficiency should take into account the background dark count rate (DCR),

$$\mathcal{R} = \mathcal{R}_{measured} - \text{DCR} \tag{2.9}$$

where $\mathcal{R}_{measured}$ is the recorded count rate.

– **Dead time/reset time**

Upon registering the arrival of a photon the state of a detector changes to the read-out state (e.g. the localised resistive state of an SNSPD) in which it is momentarily unresponsive to the arrival of further photons. The device reset time is the $1/e$ decay time for the device returning to a state with mean detection efficiency. Devices operated with gated bias will also remain unresponsive to photons when the gate is off. The dead time sets the maximum possible count rate for a device. The GHz data transmission rates demanded

for telecoms applications are orders of magnitude too fast for detectors that rely on slow thermal relaxation to reset (e.g. transition edge sensors).

– **Timing jitter**

The uncertainty in a detector's output pulse registration time is known as timing jitter. The time delay between absorption of a photon and registration at the read-out electronics will vary based on the material properties of the detector itself as well as the propagation of an electrical signal to the counter. Timing jitter is also referred to as the instrument response function.

– **Noise equivalent power (NEP) & specific detectivity (D*)**

The figure of noise equivalent power (NEP) gives an indication of the minimum detection signal from a photon detector that will be visible above noise on the detection channel. For single photon detectors this is calculated by the equation

$$NEP = \frac{h\nu}{\eta}\sqrt{2 \cdot DCR} \tag{2.10}$$

where the efficiency $\eta$ is the ratio of registered counts to incident photons (of energy $h\nu$) and DCR is the dark count rate. SNSPDs are capable of achieving NEP figures as low as $10^{-20}$ W.Hz$^{-1/2}$ [26] thanks mostly to the fact that for a good quality SNSPD (with detection efficiency that saturates at a moderate bias current) it is possible to balance a near-optimal detection efficiency with a vanishingly low dark count rate. Extending the concept of NEP to account for a detector's active area $A$ and the bandwidth of the incident signal $f$ Robert Clark Jones [27] suggested the figure of specific detectivity $D^\star$ (pronounced D-star), defined as

$$D^\star = \frac{\sqrt{Af}}{NEP}. \tag{2.11}$$

Originally intended for IR detectors for which noise power would scale linearly with device area this figure is less suitable for the assessment of fibre-coupled and waveguide integrated devices. For multi-pixel or large area SNSPDs however the effects of scaling do play an important role in device uniformity and reset time as well as presenting new challenges for biasing and readout circuitry.

– **Photon number resolution (PNR)**

Bolometric detectors produce a response proportional to the energy of an absorbed photon. Technologies such as superconducting transition-edge sensor (TES) utilise this ability to provide additional information about incident

radiation. When detecting photons of a known wavelength the output of a TES can be used to calculate the number of photons simultaneously absorbed at the detector. Conversely if the photon number is known prior to detection such a device can be used to calculate the wavelength of incoming light. Any single photon detector that has a binary response to absorbed radiation can only register the information that 'at least one' photon has been absorbed. Simultaneously illuminating several such detectors can allow multiple detection events to be registered from separate detectors at the same time, this is known as pseudo photon number resolution.

**Photon counting technologies**

**– Photomultiplier tube (PMT)**
PMTs are the original single photon counting technology. Originally constructed from vacuum tubes with a large collection surface housing a phosphorescent coated photocathode. The absorption of a photon triggers the release of a photo-electron which is accelerated through a series of dynodes, each successively amplifying the photocurrent. Older PMT devices were large, heavy and hand-assembled as shown in Figure 2.2 (a), although the large collection area was an advantage. Modern PMTs utilise micro-channels in semiconductor photocathodes to massively parallelise the charge transport and fit sensitive detectors into centimetre scale packaging. PMTs are still used in many particle counting experiments in high energy and astrophysics.

**– Single photon avalanche diode (SPAD)**
SPADs are presently the most easily available 'off the shelf' single photon counter for optical wavelengths [28]. A semiconductor junction reverse biased close to the breakdown voltage will respond to the absorption of an optical photon with energy greater than or equal to the band gap energy by accelerating the excited electron-hole pair and causing the fast creation of more electrons and holes which multiply in an avalanche. This allows the excited charge carriers to be amplified with near infinite gain creating a measurable photocurrent and requiring the bias to be reset to allow the device to return to its original state. Silicon SPADs have been developed with high detection efficiency and low timing jitter at visible wavelengths. At wavelengths beyond 900 nm the energy of a single photon is lower than the band gap energy of Si [29] leaving Si-SPADs transparent and with negligible detection efficiency. Frequency up-conversion of signal photons is possible [30, 31] or lower band gap materials such as

InGaAs and Ge can be used to detect infrared photons, particularly for the large number of applications at telecom wavelengths [32, 33]. Smaller band-gap SPADs unfortunately suffer from very high DCRs and generally require gated operation [34]. Recently InGaAs SPADs have been operated with sinusoidal bias to enable a high count rate [35, 36] and free-running InGaAs SPADs have been demonstrated with low dark counts [37].

(a)                                              (b)
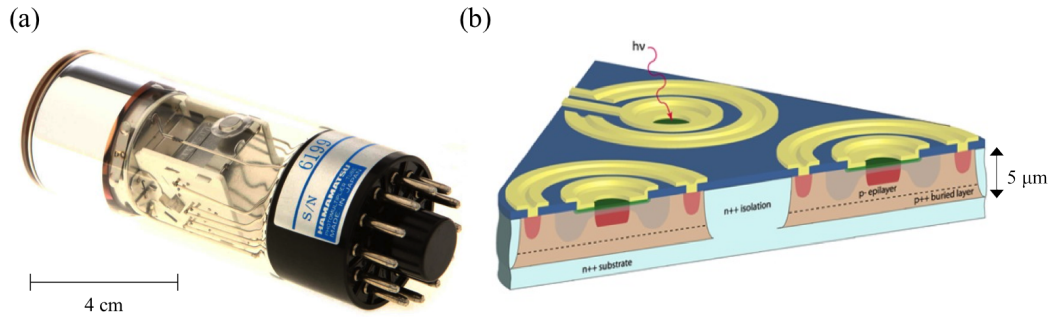


Fig. 2.2 Established single photon detector technologies. **(a)** A photomultiplier tube sold by Hamamatsu Photonics[38]. **(b)** Schematic of a CMOS compatible Si-SPAD array. [39]

Several types of photon counting technologies exploit the effects of superconducting materials to create sensitive detectors. Section 2.2.1 provides some background to the physics of superconductivity and the means by which the absorption of photons with vanishingly small energy can generate observable effects in superconducting materials.

– **Transition edge sensor (TES)**
The TES utilises the steep change in resistance of a material as it undergoes the superconducting to normal-resistance transition. Biasing a superconductor in the middle of the transition means that a tiny change in temperature (caused by the absorbed energy of a photon) causes a large and measurable change in device resistance. TESs can achieve near unity detection efficiency at telecoms wavelengths [40] and can also be adapted for sensitivity to a broad range of the electromagnetic spectrum by selection of superconducting material and absorbing medium. These bolometric detectors are also capable of photon number resolution but are limited by their slow thermal recovery time.

– **Superconducting nanowire single photon detector (SNSPD)**
SNSPDs employ superconducting material (originally NbN) deposited in a thin film and patterned to sub-micron dimensions ideally uniform in width

and free from constrictions. When current biased the absorption of a single photon at the nanowire perturbs the superconducting state increasing the local resistance. The thin film is quickly cooled by the substrate causing the device to reset in a few nanoseconds and allowing SNSPDs to be operated continuously without bias switching or gating [41]. Whereas SPADs require the absorption of a photon with at least the semiconductor band-gap energy to excite charge carriers in the material superconducting detectors generally exploit a much smaller energy gap making them sensitive to longer wavelength single photons [42, 43]. The pairing energy of superconducting charge carriers (see Section 2.2.1) is generally on the scale of a few meV, several hundred times smaller than the energy of a single optical photon.

– **Other superconducting detectors**

Superconducting materials have found several other applications in SPDs [25]. SPDs created from superconducting tunnel junctions have a detection mechanism analogous to that of semiconductor detectors [44]. These energy resolving detectors have found applications in astronomy and life sciences [45]. Microwave quantum optics at milliKelvin temperatures is an ideal low noise test environment for quantum optical phenomena relevant to on-chip quantum information processing [46]. Single microwave photon detection lies beyond the upper bounds of wavelength sensitivity for most of the aforementioned technologies however a novel system proposes a superconducting qubit coupled to a microwave resonator for use as a single microwave photon detector [47].

**Integrating detectors with optical waveguide circuits**

A major focus of this thesis is the integration of photon counting technology with planar lightwave circuits at near infrared (NIR) wavelengths compatible with quantum dot (QD) single photon emitters. Although the applications of single photon avalanche diodes (SPADs) are widespread and the technology relatively mature, the complex heterostructure required for semiconductor detectors would considerably complicate any efforts at integration with existing optical waveguide technology. Superconducting detectors offer a conceptually simple means of integration with optical waveguides via placement of the detector's active element in direct contact with the dielectric within which light is guided. For larger scale integration niobium based superconductors could be directly substituted with materials such as MoSi to enable compatibility with CMOS foundry processes.

## 2.1.3   Single photon sources

A source of photons is a prerequisite for performing quantum optics experiments. Lasers and thermal sources such as filament emission lamps provide light generated through non-deterministic processes comparable to the way that particles of radiation are emitted randomly by atoms in a sample of radioactive material. The number of photons $n$ emitted by a source in a certain time frame will follow a statistical distribution related to the Poisson distribution which describes the expected frequency of discrete random events. A Poissonian photon source emitting an average of $\bar{n} = 1$ photons per unit time will have a statistical variance of $(\triangle n)^2 = 1$ and standard deviation of $\triangle n = 1$ meaning at many times the source will emit 0 or 2, 3, etc. photons simultaneously with the average over a long time tending towards $\bar{n} = 1$ (see Figure 2.3). Measurements of the emission from sources such as lasers confirms the Poissonian distribution of photons whereas thermal light sources tend to fluctuate over longer time scales creating broader so called super-Poissonian distributions for $n$.

Linear optical quantum computing (LOQC) as described in Section 2.3.2 can involve encoding a qubit on a single photon with the choice of two optical modes (e.g. two waveguide paths). To reliably prepare qubit states for an optical quantum logic gate it must be possible to determine when such a single photon state has been created [48], however measurement of a quit state necessarily involves loss of information [49, 50]. The reliable outcomes of quantum logic gates are dependent on receiving the correct incoming photon state, therefore variance in photon number from the source will directly increase the error rate further downstream in a quantum information processor. This creates a requirement for SPSs capable of reliably generating $n = 1$ photon states with minimal occurrences of $n \neq 1$ states [51, 52].

Correlated photon pairs can be generated through the process of spontaneous parametric down-conversion (SPDC) which converts 1 pump photon with energy $E_P$ and momentum $\boldsymbol{k}_P$ into two photons with conserved energy and momentum such that

$$E_P = E_s + E_i \text{ and}$$
$$\boldsymbol{k}_P = \boldsymbol{k}_s + \boldsymbol{k}_i \tag{2.12}$$

where indices $s, i$ represent the created photons referred to as signal and idler. The idler photon from a correlated pair source can be routed to an SPD to herald the generation of a pair leaving the signal photon free for use in the photonic logic gate. Down-converted photon pairs are generated at

| Photon statistics | St. dev. and mean | Classification | Second order correlation | Example source |
|---|---|---|---|---|
| Super-Poissonian | $\triangle n > \sqrt{\bar{n}}$ | Bunched | $g^{(2)}(0) > 1$ | Thermal |
| Poissonian | $\triangle n = \sqrt{\bar{n}}$ | Coherent (random) | $g^{(2)}(0) = 1$ | Laser |
| Sub-Poissonian | $\triangle n < \sqrt{\bar{n}}$ | Anti-bunched | $g^{(2)}(0) < 1$ | Quantum dot |

Table 2.1 Classification of photon emission by variance and correlation

random time intervals and the photon number follows a Poissonian distribution, therefore increasing the pump power necessarily casues the generation of more undesirable multi-photon states. SPDC sources must therefore be run at a very low pair generation rate and massive multiplexing is required to generate the large number of single photon states required for high data rate QIP [53]. An appealing feature of semiconductor QDs as SPSs is that they are able to reliably emit $n = 1$ photon states at high repetition rates without producing multi-photon states.
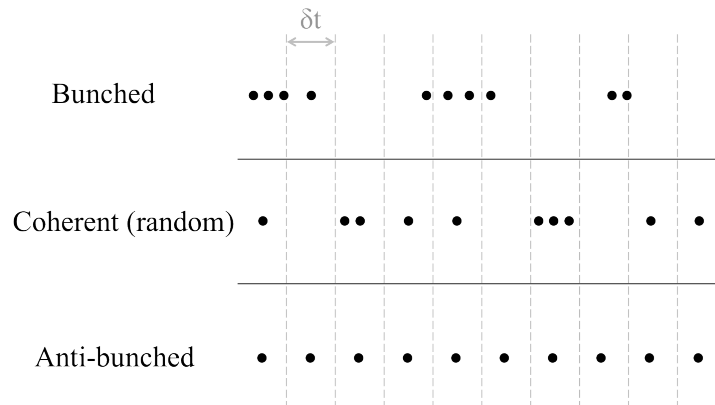


Fig. 2.3 Photon streams from various light sources. Dividing the streams into equal time bins ($\delta t$) illustrates that mean photon number $\bar{n}$ can be the same for each source whereas variance $(\triangle n)^2$ can vary based on the emission pattern. [54]

SPSs are typically characterised by the first and second order correlation functions $g^{(1)}(\tau)$ and $g^{(2)}(\tau)$. First order correlation can be measured from the self-interference pattern of a photon in a Michelson interferometer. The coherence time (or length) of a SPS describes how long the light emitted has a predictable phase. Constant phase allows for the visibility of interference fringes in a Michelson interferometer. Any shift in frequency or discontinuity in phase will cause the visibility of those fringes to wash out. The $1/e$ decay time

of the visibility of interference fringes is known as the first order correlation function (or the coherence time) of a light source.

A Hanbury-Brown Twiss (HBT) interferometer can be used to measure the second order correlation of a photon source. In this case $g^{(2)}(\tau)$ indicates the statistical distribution of photons emitted from the source (see table 2.1) [55–57]. For an ideal SPS $g^{(2)}(0) = 0$ implying that no multi-photon states are ever emitted. Light emitted with these characteristics at steady time intervals is known as anti-bunched. By routing the stream of photons from an SPS through a 50:50 beam-splitter to two similar SPDs so called coincidence counts can be recorded when both SPDs trigger simultaneously. A variable time delay is introduced to the optical path leading to one detector and the number of coincidence counts measured as a function of the time difference $\tau$ between the two paths. The absence of multi-photon states means that at $\tau = 0$ the number of coincidence counts will drop to zero as shown in Figure 2.4. Recorded data from correlation measurements on SPSs are shown in Figure 2.4. In both cases semiconductor QDs are used as a source of single photons and Photo-luminescence (PL) is stimulated by pumping the QD with laser light. For pulsed pump light QDs ideally emit 1 photon per cycle and therefore the correlation data consists of a comb of peaks spaced by $1/f$ where $f$ is the pump frequency. The peak at $\tau = 0$ is missing or at least suppressed to $< 0.5$ times the average peak height dependent on DCR and non-zero multi-photon emission probability. QDs pumped by a continuous wave (CW) laser will display a dip in the otherwise continuous coincidence rate at $\tau = 0$.

The indistinguishability of two photons can also be tested with a 50:50 beam-splitter and two SPDs. For two photons $\varphi_{1,2}$ arriving simultaneously at the two input ports of the beam-splitter the four possible outcomes are shown in Figure 2.5. If the two photons are identical the probability amplitudes of outcomes (i) and (ii) sum to zero meaning that photons will always appear as pairs at one or other output ports of the beam splitter. A Hong–Ou–Mandel (HOM) measurement involves recording coincidence counts with SPDs placed at the outputs of the beam-splitter. By varying the arrival time of photons introduced to one input port of the beam-splitter the distinguishability of the photons will be tuned. If both photons are otherwise indistinguishable in terms of wavelength and phase the measurement will reveal a coincidence rate of zero for $\tau = 0$, a so called HOM dip as shown in Figure 2.5 (a) and (b).

Although the development of SPSs and SPDs are closely linked it can be necessary to benchmark one against the other. The current state of the art
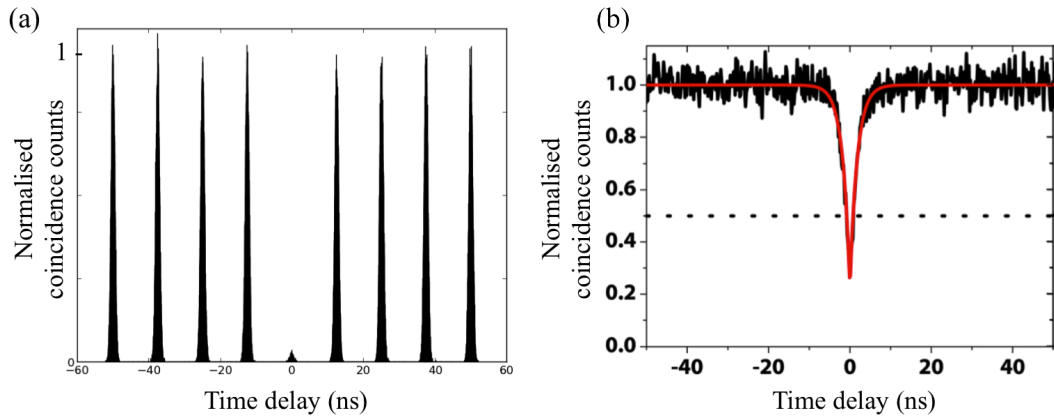
Fig. 2.4 **(a)** An HBT measurement of a semiconductor QD under pulsed excitation will display a comb of coincidence peaks at the frequency of the pump laser. At time difference $\tau = 0$ there are zero coincidence counts if the QD emits only 1 photon per pulse. Detector dark counts or non-ideal QDs can create finite coincidences at $\tau = 0$. **(b)** Performing the same measurement with a CW pump laser creates a continuous coincidence rate with a characteristic dip at $\tau = 0$. Data measured at the University of Sheffield by Dr. Nicola Prtljaga, adapted from reference 58.

in photonic technology makes it often easier to obtain a robust single photon detector than an efficient source of anti-bunched indistinguishable photons.
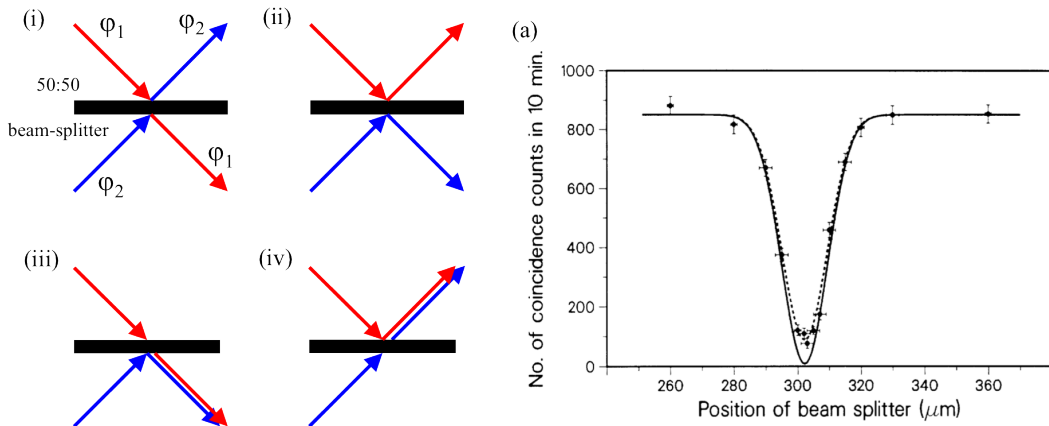


Fig. 2.5 **(i–iv)** Two photons incident simultaneously at a 50:50 beam-splitter can leave in one of four configurations. For indistinguishable photons the probabilities of configurations (i) and (ii) cancel out meaning the photons will always leave the beam-splitter as a pair on the same side. **(a)** A HOM measurement shows a dip in coincidence counts measured from the beam-splitter outputs as the incident photons are tuned into and out of distinguishability by moving the beam-splitter position. The solid line represents the ideal case whereas the experimental data are fitted to the dashed line which has a dip 0.9 times the depth. Data adapted from reference 59.

## 2.2 Superconducting nanowire single photon detectors

The first demonstrations of an SNSPD came in 2001 from Gregory Gol'tsman and co-workers who investigated how the current is disturbed in a thin film of superconducting NbN after the absorption of an optical photon [60]. Patterning the thin film into a sub-micron width constriction effectively confines this effect creating a sensor that will give a fast voltage pulse on absorption of a photon and reset on a picosecond timescale [61]. Since 2001 the concept has been developed widely with worldwide research improving and optimising the technology [44, 62, 63]. The following sections describe the optimisation of SNSPD design from the perspective of optical effects (2.2.2 coupling and absorption) and of electrical properties (2.2.3 registering, dark counts, and timing jitter). This is followed by a brief description of the recent introduction of new superconducting materials and efforts to multiplex read-out electronics to pave the way for larger arrays of detectors operating simultaneously. First an introduction is offered to the relevant phenomena in superconductivity.

### 2.2.1 Superconductivity in thin films and nanowires

Superconductivity is a low temperature state of matter first observed by Heike Kammerlingh Onnes in 1911 [64]. Through the 20th century the phenomena associated with superconductivity have been studied and increasingly sophisticated theoretical descriptions of the macroscopic effects and microscopic physics [65–67] have been adopted.

The sudden onset of zero-resistance is one of the hallmark macroscopic effects observed at small range of temperature below a critical level $T_C$, originally observed in bulk samples of Hg, Pb and Ti, the effect was observed to be material dependent.

The second hallmark of superconductivity is the complete and active expulsion of magnetic field from inside a piece of superconducting material, known as the Meissner effect [68]. This effect suggests the existence of a critical magnetic field density $H_C$ within a material above which the superconducting state is unable to form. Below $H_C$ the magnetic field expulsion is analogous to the skin depth effect of the electric field in metals. The magnetic field intensity outside a superconducting material drops off exponentially at the materials edge with a characteristic length, or penetration depth, $\lambda_L$ first described by
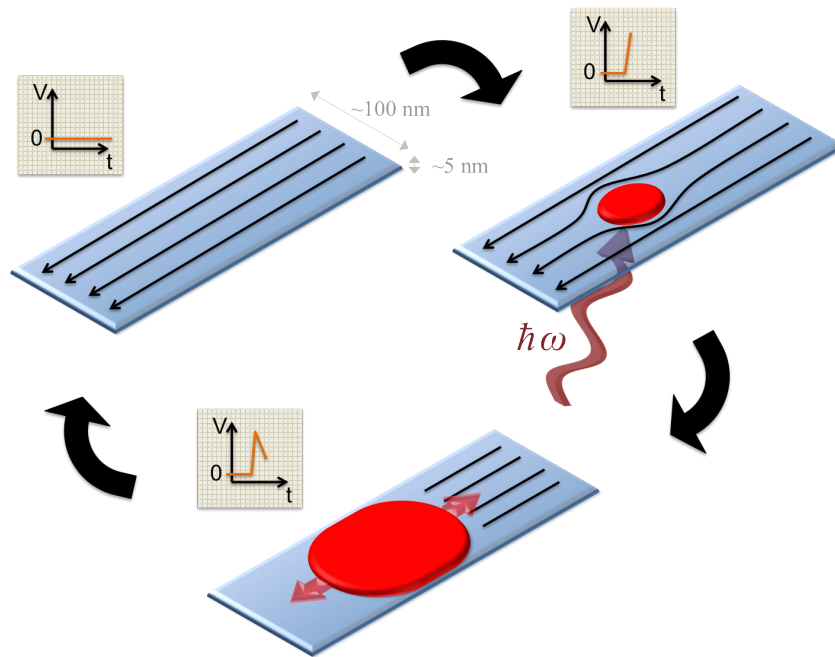
Fig. 2.6 Photon detection in a superconducting nanowire. A thin strip of super-conducting material (shown in blue) is patterned to sub-micron dimensions (width 100 nm, thickness 7 nm) and current biased at low temperature. Absorption of an optical or infrared photon causes a perturbation of the superconducting charge carriers (shown in red). Being confined by the wire edges this quickly spreads to create a resistive hotspot that covers the width of the nanowire. Current is diverted into a load resistor creating a measureable voltage pulse. The superconductor cools as heat is lost into the substrate causing the nanowire to reset to its initial state.

F. and H. London [69]. The later discovery of superconductivity in another class of materials, known as Type II superconductors, found that magnetic flux was in fact able to penetrate these superconductors but it does so only in quantised amounts. Magnetic field penetrating a Type II superconductor creates a vortex of supercurrent the centre of which contains a single quantum of magnetic flux $\Phi_0$, and with the absence of supercurrent carriers this core has finite resistance. The presence of a persistent supercurrent generates a Lorentz force on the vortex moving it laterally to the current. Material defects will tend to pin vortices in place until an increase in current generates a large enough force to move them on.

The first full microscopic theory of superconductivity came in 1965 from Bardeen, Cooper, and Schrieffer [65]. They described the effect where at low temperatures sympathetic phonon modes allow the resistance free movement of pairs of charge carriers with opposite momenta through the material lattice. So called Cooper pairs were bosons with charge 2e, condensation energy of

$2\triangle$, and an effectively infinite mean free path $\mathcal{L}$. Each half of the Cooper pair requires an excitation of $\triangle$ to become an electron-like quasi particle that will travel with finite $\mathcal{L}$ obeying Ohmic behaviour. Later Ginzburg and Landau published a more comprehensive theory [66, 70] that describes time-dependent and spatially varying superconducting states in terms of a quantum mechanical wavefunction $\psi$ with coherence over the length scale $\xi$.

Thin films of superconducting material below $T_C$ and $H_C$ will support the flow of superconducting current up to a critical density $J_C$ which is determined by the material and geometry of the film. Although $T_C$ is a material dependent parameter for bulk superconductors a thin film will see a sharp reduction in $T_C$ for films with thickness $d$ close to $d \simeq \xi$ the coherence length [71]. The lateral magnetic penetration depth is described by $\lambda_L$. For NbN nanowires of width $w \simeq 100$ nm the length scale of $\lambda_L \gg w$ leaving the magnetic field fairly uniform across the narrow nanowire. Under normal conditions, the Earth's magnetic field is expelled from NbN nanowires however magnetic penetration effects can be observed in wider strip lines [72], or wires of different superconducting materials.

In 2001 thin films of NbN ($2\triangle \simeq 6$ meV) were under investigation [60]. When patterned to sub-micron dimensions and current biased slightly below the critical level $J_C$ the absorption of optical photons (energy $\sim 1$ eV) were observed to cause a transient normal resistive spot which diverts the supercurrent causing nearby current density to exceed $J_C$ thus making the resistive hotspot grow in size [61]. With the hotspot being confined to the nano-patterned region it grows in a number of picoseconds to create a resistive barrier with a measurable voltage drop. Although Joule heating causes the superconductor's temperature to increase and the resistive region to grow the device current can be diverted to a load resistor $R_L$ allowing the hot quasi particles to relax back to the superconducting state dissipating energy into the substrate. This basic description of the detection mechanism is illustrated in Figure 2.6.

The development from basic principles followed a technology driven path with device specifications being ever improved and new avenues for application opened by progress. A firm theoretical understanding of the microscopic physics occurring within a triggered device on the picosecond timescale has tended to follow behind [73–78].

Current biased nanowires of superconducting material have a current distribution dependent on the geometry of the nanowire [79]. Straight sections of wire have slightly higher $J_C$ in the centre compared to the edges. This

is inferred from measurements of superconducting detectors using polarised light, which also has a lateral variation in absorption probability for different polarisations [80]. Arguably the greater effect on current distribution comes from bent or curved nanowires. Current crowds around the inside of a curve raising $J_C$ locally and ultimately reducing the limit of $I_C$ in the connected straight sections of wire [81]. This can cause increased dark count rates in detectors as well as a reduction in local $\eta_{registering}$ on the outside of the bend, a particular problem for waveguide integrated nanowires [82].

Naturally the applicability of SNSPDs has been boosted greatly by advances in supporting technology. Primarily the cooling technology required to operate detectors at $< 5$ K has come a long way in the past 20 years [83]. Refrigeration is no longer limited to low temperature physics labs and innovative designs for practical cooling systems are commercially available [84, 85]. Bench top systems capable of continuous closed-cycle operation at 2 K are now commonly used for SNSPD detector systems [86] and paired with "turn-key" electronics to make systems accessible to non-expert users. Cutting edge cooling technology will continue to allow SNSPDs to be operated in more flexible environments [87].

The SNSPD offers highly desirable performance in terms of most SPD figures of merit (see Section 2.1.2). Since its inception in 2001 the technology has matured and in doing so is finding ever-increasing applications. Several review articles cover the development of the field in considerable detail [88, 89, 41]. The following is a broad selection of noteworthy applications of SNSPDs: remote sensing [90–93], life sciences [94, 95], SPS characterisation [96–100], fundamental physics and metrology [101–108], quantum key distribution [109–112], arrayed detectors for imaging [113–117], ground-to-space communications [118], and pseudo photon number resolution [119–121]. For a comprehensive review of SNSPDs integrated with quantum photonic circuits see Section 2.3.2.

## 2.2.2 Optical optimisation

### Coupling

Modifications to the initial nano-bridge design were necessary to make SNSPDs viable devices for photon counting applications. The coupling efficiency $\eta_{coupling}$ of a detector is the probability of incoming light to impinge upon the active area of the detector. The superconducting wire must be scaled up to cover

even the minimum area of a focussed optical beam. By uniformly extending and meandering the wire in a boustrophedon pattern (visible in Figure 2.7) a suitable area can be covered, usually with approximately 50% fill factor [122, 123].

Although free-space optics offer the broadest range of techniques for focussing light onto a detector the low temperature operation of the superconducting film is less compatible with such an open system. Addressing a detector with optical fibre allows for greater radiation shielding around the detector whilst still delivering light into an area of just a few square microns. The core of single mode telecoms fibre (SMF-28) is 9 μm in diameter. The divergence from a fibre placed immediately over a detector at a separation of $\sim 20$ μm is small enough that a 10 μm $\times$ 10 μm meander will couple light with high efficiency. A number of methods have been developed for packaging detectors with precisely aligned optical fibre [124–126], both single mode and multi-mode [127].

Extending the total nanowire length to increase optical coupling comes with several corollaries. The effects of nanowire uniformity and increased kinetic inductance are discussed elsewhere in this work. When coupling light to an extended thin wire it is very important to consider the polarisation of the light as it arrives at the detector. Unsurprisingly a polarisation (electric field vector) parallel to the long axis of the nanowire will be preferentially absorbed in comparison to perpendicular polarisation. For a basic meander detector the variation in detection rate between perpendicular and parallel polarised photons can be close to 50%. Modified designs can be used to enhance or suppress polarisation sensitivity of an SNSPD [128–131]. The practicality of fabricating such designs often precludes their implementation when other means of polarisation control are readily available. Antennas have been shown to improve coupling in to photodetectors [132]. Plasmonic dipole antennas were shown to enhance detection efficiency of NIR photons in SNSPDs [133].

**Absorption**

Improved geometric coupling aside there is still considerably less than unity probability for the absorption of a photon impinging on a thin film at normal incidence. Index contrast between the superconducting material and the medium through which photons reach the detector are responsible for reflection and subsequent loss of light. Yet more light is likely to be transmitted through
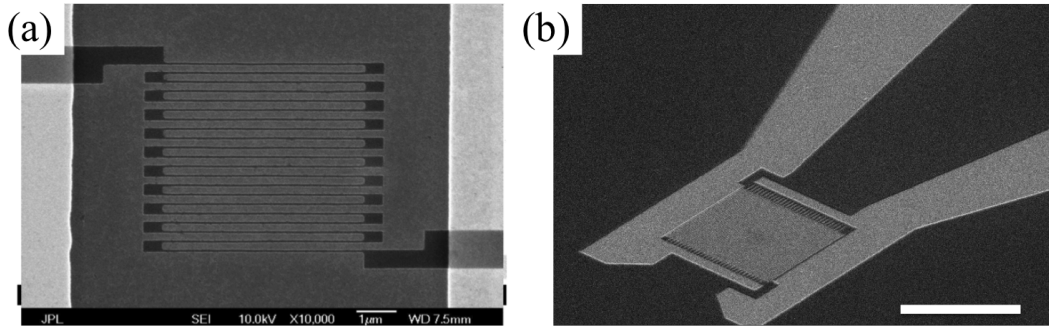
Fig. 2.7 **(a)** An SEM image of a superconducting nanowire meander. Figure adapted from reference 63, IEEE 2007. **(b)** Nanowire detector with an active area of 10 µm × 10 µm. The coplanar waveguide RF transmission line is visible in the top right of the image. Scale bar 10 µm

the thin active layer of the detector and be lost into the substrate. The absorption probability $\eta_{absorption}$ for 5 nm NbN sputtered on an MgO substrate is close to 15%. Inclusion of an optical cavity in device design can dramatically enhance absorption into the detector by tailoring reflection of light to create a maximum of the electric field inside the superconducting material. A number of cavity designs have been successfully demonstrated for enhancing performance of SNSPDs (see table 2.2 and Figure 2.8).

Initially cavity structures were realised by depositing a layer of $SiO_2$ above the detector with carefully controlled thickness (using hydrogen silsesquioxane (HSQ) electron sensitive resist) [134, 135]. A metallic (Ti/Au) mirror deposited on top of the dielectric completes the cavity offering a broadband and modest enhancement to $\eta_{absorption}$ for light coupled through the backside of the chip. Generally an increase in the number of dielectric boundaries included in the cavity design will create higher reflectivity with a corresponding trade-off in spectral width. Tailoring a cavity to a more precise range of wavelengths enables higher peak absorption to be reached with the advantage of then being able to reduce the fill factor of the nanowire meander without suffering losses [136, 137].

Coupling light through the substrate also brings some challenges to efficient alignment and packaging of detectors not to mention the limitation of the substrate material's transparency window. Light exiting the bare facet of a single mode optical fibre will diverge following the equation for a Gaussian beam,

$$w(z) = w_0\sqrt{1 + \left(\frac{z\lambda}{\pi w_0^2}\right)^2} \qquad (2.13)$$

| Cavity type | Coupling | $\eta_{absorption}$ | SDE | Ref. |
|---|---|---|---|---|
| No cavity | Front side | 37% | 20% | [61] |
| Metallic mirror (front side) | Back side | *unknown* | 67% | [134] |
| Metallic mirror with 2-layer cavity | Back side | 98% | 82% | [136] |
| SiO$_2$ half-wavelength layer | Front side | 40% | 15% | [138] |
| Metallic mirror with 2-layer cavity | Front side | 99.5% | 93% | [139] |
| Distributed Bragg reflector (TaO$_5$) | Front side | 95% | 92% | [140] |
| Aperiodic DMLs (TiO$_2$/SiO$_2$) | Front side | 98% | 80% | [141] |

Table 2.2 A variety of optical cavity structures have been employed to enhance SNSPD detection efficiency. Absorption efficiency into the nanowire detector and SDE are quoted where available from the stated references. All devices were characterised with NIR light. Schematics of these cavities are shown in Figure 2.8.

where $w_0$ is equal to the fibre core diameter and $w(z)$ is the width of the beam after propagating over optical length $z$. For propagation through the substrate medium the refractive index $n$ is taken into account by substituting $z = z_0/n$ and $\lambda = \lambda_0/n$. Coupling light in this manner through the back side of a substrate requires either focussing optics, substrate thinning, or the fabrication of a large area detector (which is more likely to suffer from non-uniformity and high kinetic inductance).

Tanner *et al.* [138] first proposed a front-side coupled optical cavity with an SiO$_2$ layer of half-wavelength optical thickness for $\lambda = 1310$ nm. Front-side coupling was also employed by Marsili *et al.* in a detector design that achieved a record 93% SDE at $\lambda = 1550$ nm [139]. The device was patterned in a WSi superconducting film deposited on top of a metallic Au mirror and a layer of SiO$_2$. Above the device layers of SiO$_2$ and TiO$_2$ complete the optical stack.

The deposition of a metallic mirror above or below the detector can preclude later attempts to precisely align a focussed optical spot with the nanowire meander. This problem is circumvented by the use of dielectric reflectors which allow for devices to be carefully aligned using illumination at a wavelength outside the cavity stop-band. A narrower reflection band with stronger field enhancement at the detector can be achieved with an increased number of dielectric layers forming a distributed Bragg reflector (DBR) [140].

A DBR utilises a stack of alternating dielectric layers with different refractive indices $n_i$ to greatly enhance interference effects caused by the overlapping reflections coming from each interface [142, 143]. Growth of each layer is carefully controlled to ensure the thickness equates to $\frac{1}{4}n_i\lambda_0$ where $\lambda_0$ is the central wavelength to be reflected by the mirror. The stack of $\lambda_0/4$ pairs with one final $\lambda_0/2$ layer on top cause maximal constructive interference directly above the DBR mirror. An absorbing medium such as a superconducting film placed in the few nanometres above the DBR benefit from hugely enhanced absorption. Although peak reflection approaches 100% as the total number of layers tends to infinity at optical wavelengths >99% reflectivity can be achieved with only 10 or 20 pairs.

Effective simulations of DBR design parameters are found in reference 144. Treatment of the DBR-detector system as a one dimensional optical stack enables fast calculation of the electric field at superconducting layer. Conversion into $\eta_{absorption}$ is trivial with a known absorption coefficient. Several superconducting sample films were grown at the University of Glasgow and characterised using ellipsometry in order to collect reliable data for the refractive index and absorption spectra.

Further improvements can be made by tailoring the absorption profile of the detector-cavity system. Aperiodic dielectric multi-layers can be designed by optimisation algorithm to generate reflectivity spectra inaccessible to periodic DBR structures [141]. An in-depth theoretical treatment of absorption engineering can be found in reference 145. Waveguide coupled detectors offer very high $\eta_{absorption}$ by coupling light into the detector directly from a travelling waveguide mode allowing for tens of microns of interaction length [146]. The design and simulation of waveguide integrated nanowire detectors is discussed in detail in Section 3.2.5 and in Chapter 4.

### 2.2.3 Electrical optimisation

**Registering**

The registering process covers everything from the immediate result of photon absorption through to the appearance of a 'click' or increment of 1 count at a digital counter. The biasing and read-out electronics clearly have a role to play as well as signal transmission across the surface of the chip and out to room temperature. A DC bias is established across the detector most commonly
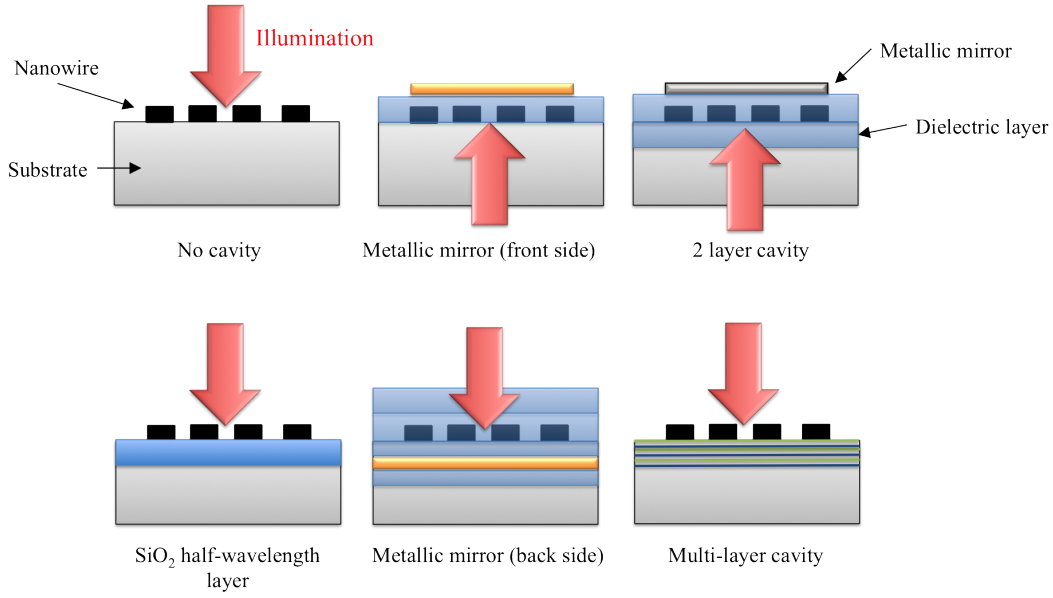
Fig. 2.8 SNSPD designs incorporating optical cavities. Optimising absorption of incident photons is a key factor in enhancing detection efficiency. Partial cavities are formed around a superconducting nanowire by reflective surfaces such as metallic mirrors or the interfaces between dielectric layers with differnet refractive indices. Each configuration pictured corresponds to an item described in the rows of table 2.2.

with a stable battery powered voltage source and series resistor connected to the DC arm of a bias tee which acts to separate voltage pulses generated at the device onto the AC arm (see diagram 3.20). Figure 4.6 (a) in Chapter 4 shows a typical pulse shape generated by an SNSPD after $\sim$55 dB amplification (with 2 room temperature low noise amplifiers (see Section 3.2.3). The pulse shape is asymmetrical with the fast rise time $\tau_1$ dependent on the combined hotspot and load resistances $R_{hotspot} + R_L$ where as fall time $\tau_2$ is dependent only on $R_L$, typically $R_L \ll R_{hotspot}$. The return of the bias current to the nanowire after the wire switches is dictated not by the cooling of the wire (this happens very quickly [147, 148]) but by the kinetic inductance $L_K$ of the nanowire [149].

$$
\begin{aligned}
\tau_1 &= \frac{L_K}{R_L + R_{hotspot}} \\
\tau_2 &= \frac{L_K}{R_L}
\end{aligned}
\tag{2.14}
$$

Although the geometry of the nanowire itself is largely dictated by the need to couple light to the detector and for narrow wires to provide high registering probability the transmission lines through which fast voltage pulses are read out can have a large effect on pulse shaping and timing jitter [150]. Coplanar

waveguides patterned on the chip's surface are designed to transmit RF signals up to several GHz frequency with $50\Omega$ impedance [151–153]. Although chips are usually wire-bonded the sample mount design and connected coaxial cabling can be impedance matched to improve signal transmission.

Amplifiers are selected to increase the signal parameters above threshold values necessary to trigger a digital counter. Low noise amplifiers are often used with bandwidth suitable to resolve the fast leading edge of the detection pulse with sub-nanosecond resolution.

The inclusion of a shunt resistor in parallel with the nanowire causes the diversion of bias current upon the creation of a resistive region in the nanowire ($R_{hotspot} > R_{shunt}$). Balancing the inductance, resistance, and device cooling allow for an SNSPD to be operated at maximum count rate without latching [154, 73, 155] or going into relaxation oscillations [156]. Although the dynamics of the detector reset process can be straightforwardly explained through circuit simulations the physics occurring in the leading edge of the detector response, within the first picoseconds after photon absorption, have received active debate and warrant closer investigation [157].

Pre-detector system losses notwithstanding a comprehensive study of SNSPD detectors in 2008 [158] showed clearly that of the photons absorbed into a nanowire less than 100% cause counts to be registered. It also showed a slight decrease in $\eta_{registering}$ for parallel polarised photons in comparison to perpendicular polarisation.

The registration of a photon absorbed into a nanowire detector is largely dependent on the bias current $I_B$ in the nanowire, or more specifically the local current density $J_{local}$ in the region of absorption. The original hotspot model suggests that the photon absorption causes the almost immediate breaking of a large number of Cooper pairs and a volume of energetic quasi-particles to form within the wire. The supercurrent is thus diverted into the region between the resistive hotspot and the wire edges, increasing $J_{local}$ and quickly surpassing the critical level $J_{local} > J_C$. With the entire cross section of the wire now resistive the current is diverted into the load resistor $R_L$ and an increase in voltage can be read-out. Newer theories of the detection mechanism also introduce the role of vortices and vortex-antivortex pairs to the registering process [80]. The crossing of a vortex across the nanowire brings a quantum of magnetic flux and creates a fast voltage pulse in the read-out circuit. There is a potential energy barrier to the crossing of these vortices which can be exceeded either by

random fluctuations (a dark count) or by the absorption of a photon (a photon count).

Either way in most realisations of an SNSPD there will be areas of the detector in which $\eta_{registering}$ is reduced due to $J_{local}$ being lower than the threshold value for count registration. Naturally when biasing a nanowire detector it is necessary to raise the bias current as high as possible to maximise $\eta_{registering}$. The detector switches to the normal state for $I_B > I_C$ however this will occur as soon as $J_C$ is reached in one section of the nanowire, not necessarily all. For a number of reasons the current density in parts of the wire may remain below the optimal level for efficient detection even when the detector is biased optimally. Edge effects of the nanowire can themselves reduce $J_{local}$. Artefacts of film deposition and of lithography can introduce surface oxides and deformations to the wire edges or inhomogeneities to the superconductor itself. The most serious instances of these cause constrictions in the nanowire. As $J_{local}$ will be increased in a constricted section of nanowire every un-constricted part of the detector is rendered less sensitive [159].

Nanowire geometry is also of great importance since current crowding around tight bends can cause highly increased $J_{local}$ with the same damaging effect on $\eta_{registering}$ for the rest of the detector [81]. Occurring on a length scale far below the optical wavelength it is challenging to probe this effect optically. An increase of bend radius can be implemented to help mitigate the negative effects of current crowding [146, 129].

The minimum energy resolution of an SNSPD is proportional to the nanowire width with the ultra-thin NbN nanowires proving to be sensitive into the mid-infrared [160, 42, 43]. However a direct result of reducing the nanowire width is an increase in kinetic inductance and corresponding extension of the detector reset time. Excessive kinetic inductance can be a limiting factor for detectors requiring a large active area or a high maximum count rate. A novel solution is the superconducting nanowire avalanche detector (SNAP) [161]. Bias current will be distributed evenly amongst several identical nanowires when connected in parallel. The formation of a hotspot in one wire causes the fast redistribution of current into the other nanowires forcing them beyond their critical current and causing the device to switch. This fast avalanche effect preserves the desirable operation of SNSPDs whilst reducing the kinetic inductance, thus enabling the development of detectors with very large active area and fast reset time [162].

**Dark counts**

Dark counts are spurious events registered by the counting electronics without a signal photon being absorbed at the detector. The DCR scales exponentially with bias current $I_B$ at currents close to $I_C$. In a practical detector there will be extrinsic dark counts (caused by leaked light and blackbody radiation) and intrinsic dark counts (a property of the superconducting nanowire itself [26]). According to Planck's law peak emission of radiation from a black-body at $T = 300$ K is at $\lambda = 9.7$ μm increasing to $\lambda = 1450$ μm at $T = 2$ K. The Stefan-Boltzmann law describes how the total energy $E_{SA}$ emitted per unit surface area scales as $E_{SA} \propto T^4$. At cryogenic temperatures the blackbody emission has moved from the mid-infrared into the microwave spectrum and the intensity has sharply dropped off. Nonetheless the coupling of blackbody photons into an experiment from room-temperature materials can be a significant effect if not mitigated by filtering [163, 164]. The mechanisms by which the ultimate lower limit of intrinsic DCR are limited bear some consideration and are likely linked to the microscopic details of the photon detection mechanism [80]. Imperfect nanowires will also suffer a contribution to the DCR from the geometric effect of constrictions and tight bends [82] and also possibly thermal fluctuations [165].

**Timing jitter**

Timing jitter is a measure of the uncertainty in the time taken for a count to be registered following absorption of a photon. Time correlated single photon counting (TCSPC) is often used to characterise detector jitter (see Chapter 3). A typical detector response function is near-Gaussian with full width at half maximum (FWHM) around 150 ps or less, the lowest reaching $< 20$ ps. The histogram recorded by TCSPC represents a sum of timing jitter contributed by the bias circuit and read-out electronics, including any jitter in the laser trigger signal, superimposed on to the intrinsic jitter of the SNSPD. It has become apparent that measuring the lowest possible jitter is limited by the read-out electronics more so than the detector itself. Low temperature amplification can be employed to reduce electronic noise and improve recorded jitter. Alternative methods for isolating the intrinsic jitter of an SNSPD are also being investigated (see Chapter 6). Despite the limitations of read-out technology studies of jitter in SNSPDs have unanimously shown it to be inversely proportional to the bias current within the nanowire [166, 41].

Generally an increase in the cross-sectional area of a nanowire will increase the maximum bias current it can support but at the cost of reduced detection efficiency. Probing the microscopic processes that truly limit detector jitter remains challenging with existing technology however several studies have found a contribution from the geometry of the meandered nanowire [167, 150]. Propagation of successive pulses from different areas of the nanowire result in different arrival times at the counter, accounting somewhat for the intrinsic jitter of a large area device.

### 2.2.4 Novel materials for improved performance

For thin crystalline films such as NbN it cannot be understated just how much nanowire device performance is limited by the choice of substrate and subsequent effect on film quality, uniformity and the presence of constrictions. The first SNSPDs were fabricated only on MgO and $Al_2O_3$ substrates to minimise lattice mismatch with NbN. For a large variety of reasons it has been desirable to translate SNSPD technology to other material platforms. Intensive optimisation of NbN film growth, particularly at high substrate temperatures, has lead to the production of device quality films on Si, $SiO_2$, GaAs, diamond [168] and $MgF_2$ [169]. Each choice of substrate is tailored to specific applications ranging from DBR mirrors to optical waveguide circuits and broadband through-substrate transmission. Improvements in film growth techniques have not only improved the quality of NbN grown on lattice mis-matched substrates, but introduced a number of other superconducting materials such as NbTiN [170], WSi [139], MoSi [171–173], and MoGe [174] which can be grown on a broader range of surfaces and maintain the superconducting properties necessary for efficient single photon detection. Not only deposition conditions but surface polishing and chemical treatments must be thoroughly optimised to attain the highest detector performance [140]. Research and application of 2-dimensional materials has seen an explosion over the past decade. One material in that class is $NbSe_2$ which can be prepared using exfoliation techniques and will exhibit superconductivity at low temperatures in samples just a few atomic layers thick. The suitability of $NbSe_2$ as a superconducting photon detector is currently under investigation, some initial results are shown in Figure 2.9.

High temperature superconductors such as $MgB_2$ and $YBa_2Cu_3O_{7\text{-}x}$ (YBCO) present the opportunity to realise a superconducting SPD operating at higher temperatures with ultra-fast reset time and reduced costs for cooling. However
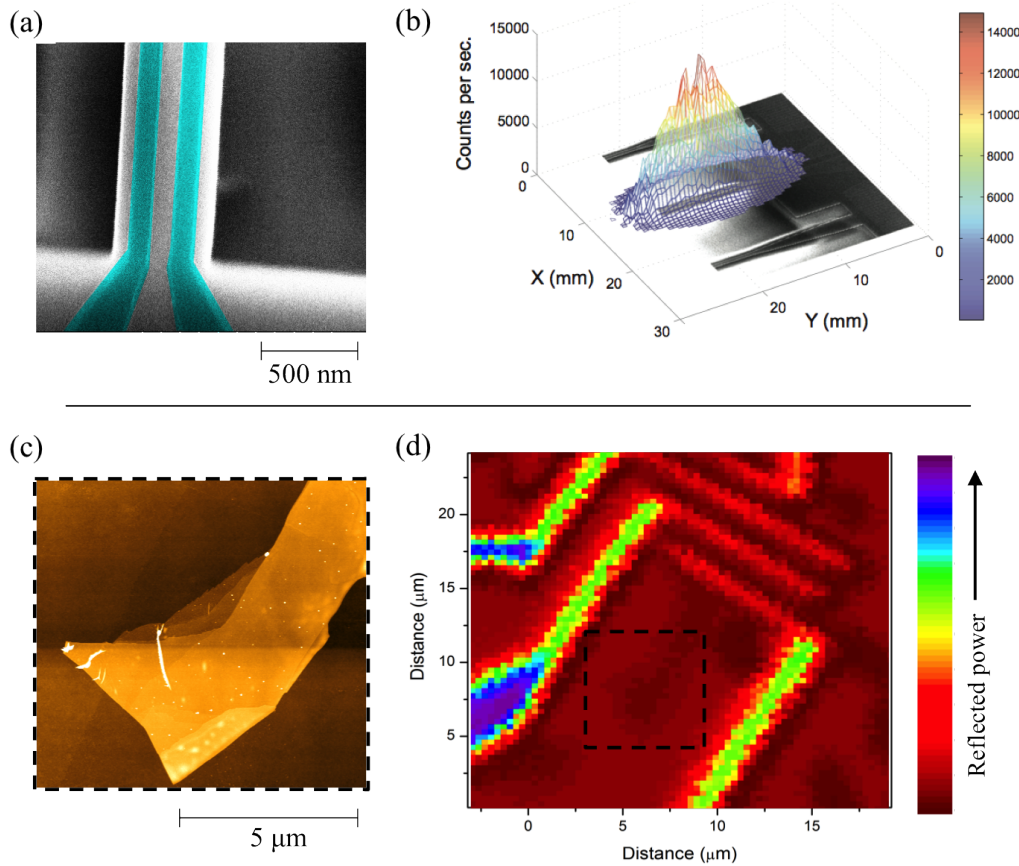
Fig. 2.9 Novel materials for single photon detection. **(a)** MoSi is an amorphous superconductor that has been deposited in thin films and patterned into nanowires integrated with Si optical waveguides. **(b)** At 350 mK MoSi nanowires show high sensitvity to single photons at $\lambda = 1550$ nm. Data measured by Dr. Jian Li adapted from reference 173. **(c)** NbSe$_2$ forms a layered structure with atomically thin flakes that can be exfoliated in a similar way to graphene. Samples were fabricated at the Cambridge Graphene Centre by Dr. Antonio Lombardo and the author. The possibility of observing superconductivity in samples just a few atomic layers thick makes this material a candidate for single photon detection. **(d)** Exfoliated samples have gold contacts added by electron beam lithography (EBL). The reflectivity of devices at $\lambda = 1550$ nm was mapped at the University of Glasgow using a nano-optical set up at 3.7 K (see Section 3.2.4).

development of SPDs in these materials presents a serious challenge in comparison to low temperature superconductors due to the different microscopic physics of the superconducting state and the fact that the superconducting properties can so easily be degraded through nano-patterning and thermal cycling. Nonetheless single optical photon detection has been demonstrated in MgB$_2$ nanowires [175, 176]. Fabrication techniques have been developed to create nanowires in YBCO [177] and more recently the photo-response has been measured [178]. Although the prospect of operating superconducting SPDs

above liquid nitrogen temperature is appealing the development of superconducting materials has been extremely challenging. Meanwhile improvements in closed-cycle refrigeration technology have made it cheaper and easier to make compact detector systems using existing low temperature superconductors.

### 2.2.5 Schemes for multiplexed detector read-out

Read-out electronics for SNSPDs are described in Section 3.2.3 utilising amplifiers operated at room temperature. Cryogenic amplification is significantly more costly than room temperature equivalents, a compromise that is satisfactory for many given applications. Where existing read-out schemes fall short is in scaling up to multi-pixel detectors and arrays. The traditional bias and read-out scheme requires 1 coaxial cable per detector to run from the detector at low temperature out to the room temperature electronics. Metallic coaxial cables carry a heat load to the cold-head and consequently limit the number of detector pixels that can be individually biased and read out given the available cooling power. An imaging array or information processor might contain thousands of individual SNSPD elements that require simultaneous operation. Clearly the existing bias and read-out scheme will never scale to meet these demands hence new multiplexing strategies are being developed. Pseudo photon number resolving detectors have been demonstrated employing series resistors to modify pulse height [179, 180]. Although it is conceivable to extend this scheme to address a multi-pixel array the range of resistance values necessary to resolve even a dozen separate detectors will quickly exceed the limits of fabrication and the resolution of the technique.

At the US National Institute for Standards and Technology a row-column read-out scheme has been developed that requires just $2N$ read-out lines for an array of $N \times N$ pixels [181], biased via $N$ separate bias lines. This strategy has enabled the realisation of a 64-pixel detector array for NIR imaging or communications [115].

Rapid single flux quantum (RSFQ) circuits offer another possibility for multiplexing SNSPDs. These superconducting logic circuits operate at the same temperature as the detectors and a single chip can be used to bias and read-out multiple detectors with a single read-out line and minimal cold-head to room temperature wiring [182, 183]. Although existing demonstrations only show 4-pixel operation the technology of RSFQ circuits is highly promising for

reading out much larger arrays as well as performing other logical operations at high speed in close proximity to detectors (see Chapter 5).

## 2.3   Quantum information processing

### 2.3.1   A short introduction to quantum information

Information can be encoded in physical systems and transferred or processed [184]. High and low voltages in an electrical circuit represent **1**s and **0**s, the classical *bits* of information. Silicon-based CMOS integrated circuits are the most abundant form of information processors today. Although they are comprised of millions of components and can be programmed to perform a vast array of functions the basic building blocks of the information processor are mostly simple logic gates. A logic gate is a small sub-section of a circuit which produces one or more output bits by comparing one or more input bits and applying some logical rule [185]. By combining logic gates, feeding one set of outputs to the next set of inputs, circuits can be made to perform calculations and other functions on input data. A functionally complete set of logic gates (such as NOT and AND also known as NAND) is one which can be used to produce all possible combinations and input and output bit values. A processor with access to a large enough number of NAND gates and a large enough memory can then effectively compute any calculable function [186, 187].

It follows that if the system on which information is encoded is subject to the laws of quantum mechanics then the information itself will undergo the same quantum mechanical effects [188]. By isolating physical objects such as single particles it is possible to encode a quantum bit (qubit) of information. Quantum logic gates perform logical operations with qubits as inputs and outputs and can be combined in functionally complete sets in a similar way to their classical counterparts. Where quantum logic gates differ is that the quantum mechanical wavefunction of the output qubit remains intact and effects of entanglement and superposition are preserved. Due to this effect a qubit register can exist at one time in a superposition of many possible states. Exploiting this parallelism allows a quantum information processor to perform certain tasks with exponentially greater efficiency than a classical computer.

With the computing power and communication bandwidth that is widely available today processes such as encrypting information and sorting large

datasets are commonplace and serve an important role in the digital economy. Shor's algorithm for factorizing large integers [189, 190] and Grover's algorithm for efficiently searching a list [191] are two outstanding examples of quantum algorithms whose exponentially superior efficiency is likely to have enormous impact when implemented on a reasonable sized quantum computer. Reference 51 is a detailed resource describing the principles of encoding and processing quantum information with examples of algorithms and error correction schemes for quantum computers.

Candidate systems for encoding qubits include trapped ions, nuclear magnetic resonance (NMR) of nuclear spins, superconducting quantum interference devices (SQUIDs), and photons [192]. Each medium comes with its own proposed schemes for information processing and read-out. The practical operating details of each system vary greatly and each constitutes its own distinct field of scientific and technological endeavour.

Two physical parameters that do offer some level of comparison between different candidates are timescales for qubit coherence and read-out. The read-out timescale is set by how long it takes to interrogate the system and recover information about its state. This is in some ways linked to the coherence time, which is defined by the length of time a set quantum state of the system remains intact without being altered (or the wavefunction collapsed) by unwanted interactions with the outside world. Clearly a system with very high coherence time will be very hard to read out. Equally a system that interacts strongly and quickly with the read-out mechanism is likely to also interact with its surroundings and lose coherence before the intended computation takes place.

Photons can be used as flying qubits, capable of long coherence times and speed of light routing of information. Qubits can be encoded on polarization states, or the paths and time bins of photons moving through an optical network [193].

The advent of universal quantum computation at practical scales is much lauded as a revolutionary and disruptive technology. The literature is rich with detail of the theoretical foundation for quantum information processing as well as speculation as to the breadth of its applications and imminence of its arrival. It is clear that there are phenomena unique to quantum mechanics that if harnessed can enable advanced techniques of computation and secure communication. In terms of quantum information processing, short of a full scale programmable quantum computer, it is likely that quantum technologies

will be applied first to simulations of complex systems and the generation of random number strings. Quantum entanglement can also be exploited to ensure true security of cryptographic communication, an application which is of immediate and widespread interest in society [194].

**Quantum key distribution**

Quantum cryptography exploits quantum effects to facilitate secure communication on a channel sensitive to eavesdroppers. This enables the verification of securely shared data and for any compromised sections of bit stream to be discarded. Quantum key distribution (QKD) is a method of exchanging an encryption key for a coded message between two separate parties (Alice and Bob). The archetypal example of a quantum cryptographic protocol is known as BB84, after its invention by Bennett and Brassard in 1984 [195]. A simple version is outlined below. Today QKD has been demonstrated on inter-city fibre optic networks [109, 110] as well as through free space between islands in the Atlantic Ocean. In August 2016 the Chinese Micius satellite was launched hoping to demonstrate the first ground to space exchange of quantum cryptographic keys. Commercial QKD systems are available from manufacturers such as ID Quantique [196]. It has been shown that for a variety technologies used in commercial QKD systems there are technological loop-holes that render systems vulnerable to eavesdropper attacks [197, 111]. The security of any practical communication channel should be considered holistically as it extends beyond the message carrying medium right to the actual persons receiving and sending information.

– **BB84.**
Figure 2.10 describes the process for exchanging a cryptographic key with the BB84 protocol. Alice decides to securely send the key to an encrypted message to Bob by encoding 0s and 1s in the polarization states of photons. Two non-orthogonal sets of basis states are chosen for encoding the bits. In the first basis horizontal and vertical polarization code for 0 and 1 respectively. In the second basis $+45°$ and $-45°$ diagonal polarizations code for 0 and 1 respectively. Alice sends a string of photons to Bob, each containing a 0 or 1 encoded in a basis that Alice has randomly chosen. Bob measures these photons by making his own random selection of bases. Where Alice's and Bob's choices of basis agree Bob will measure the same value that Alice intended. Where Bob chooses the other basis to Alice there is a 50% chance of him measuring a 0 or

a 1. Alice and Bob then communicate over a classical channel and compare the basis states they each chose for every photon. Bob now discards all bits that he measured in the incorrect basis. The bits that are left make up the secure 'sifted' key. They intrinsic security of this system is contained in the fact that any eavesdropper (Eve) who measures the photons in between Alice and Bob will collapse the photon wavefunction without gaining full knowledge of the basis in which it was prepared. Eve can re-send photons on to Bob but Bob will be aware of an increased error rate in his recorded bits. It has been shown that an error rate of less than 11% between Bob and Eve's bit values is indicative of a secure communication channel.



| Alice's bit | 0 | 1 | 1 | 0 | 1 | 0 | 0 | 1 |
|---|---|---|---|---|---|---|---|---|
| Alice's basis | + | + | × | + | × | × | × | + |
| Alice's polarisation | ↑ | → | ↖ | ↑ | ↖ | ↗ | ↗ | → |
| Bob's basis | + | × | × | × | + | × | + | + |
| Bob's measurement | ↑ | ↗ | ↖ | ↗ | → | ↗ | → | → |
| Shared secret key | 0 | | 1 | | | 0 | | 1 |
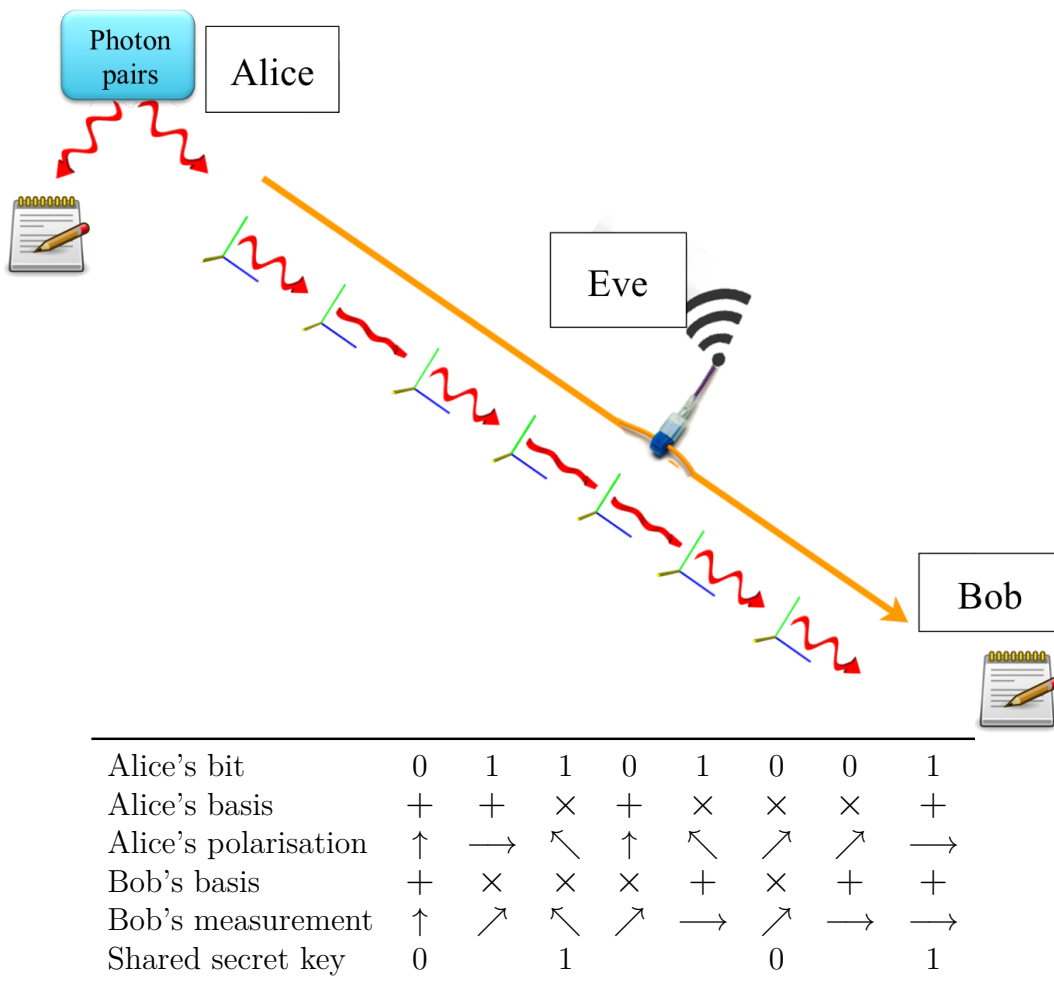
Fig. 2.10 BB84 protocol for quantum key distribution. A secure key is transmitted across a public channel from Alice to Bob using polarized photons. Alice and Bob compare encoding and measurement bases for each bit, rejecting mismatches to leave the so called sifted key which will be used for encryption. If the channel is intercepted by Eve the error rate within the sifted key will exceed 11%.

## 2.3.2   Quantum photonic integrated circuits

This section deals with QIP in optical waveguide circuits. Optical QIP encodes a qubit onto two optical modes occupied by one photon. It is possible to perform universal quantum logic operations on optical qubits using networks capable of only linear optical transformations without the need for challenging non-linear photon-photon interactions. Waveguide circuits present the most realistic platform for creating such optical networks since they can provide large scale integration of the many necessary components that will require very high stability and low losses to operate correctly. There is therefore great interest in developing quantum photonic integrated circuits (QPICs) towards the goal of realising a universal programmable quantum computer.

**Linear optical quantum computing**

Photonic quantum computation can be achieved with a qubit being encoded on a single photon superimposed on two optical modes [198]. Initially this system had a major flaw, namely that optical switching could only be achieved through strong non-linear interactions between multi-photon states [199] which are not easily achieved at the single photon level. In 2001 Knill, Laflamme and Milburn published a crucial theoretical description of a universally programmable quantum computer that utilised only linear optical elements [48]. Linear optical quantum computation (LOQC) requires SPSs and SPDs, beam-splitters and phase shifters, and a means of feeding-back the results of photon detection to reconfigure parts of the circuit. Table 2.3 provides a brief explanation of what each component is required for and of how each component can be realised in an optical waveguide circuit. Using these design principles there have been efforts to realise optical quantum logic gates with a variety of photonic technologies [200–202] promoting both commercial applications and fundamental physics along the way [203–208]. After demonstrating all-optical CNOT gates [209] using bench-top free-space optics it soon becomes apparent that this strategy is not scalable nor inherently stable. Effective quantum computation requires a system that can faithfully process and feed forward information with incredibly high fidelity. Waveguide losses, beam splitter imbalances, phase shifter uncertainties and detector inefficiencies all degrade the chances of ever seeing a meaningful result from a complex quantum computer. Monolithic integration therefore offers the only platform that might be stable and uniform enough to

get there [210]. Even then reducing the loss from every single component is still a huge challenge facing the field [192].

| Components required for LOQC | Purpose | QPIC implementation |
| --- | --- | --- |
| Single photon source | Generate photons on demand | Heralded photon-pair source, semiconductor quantum dot, nitrogen vacancy centre in diamond, SWCNT |
| Propagation medium | Transmission of photons, path encoding qubits | Waveguides |
| Beam-splitters | Routing and interacting photons | Directional coupler |
| Phase shifters | Changing photon or qubit phase | Heaters, electro-optics, electro-mechanical actuators |
| Single photon detectors | Registering presence and location of photons | Superconducting nanowire single photon detectors (SNSPD), transition edge sensors (TES) |
| Information feed-forward | Reconfiguring the circuit to allow the outcome of one computation to influence the next | Rapid single flux quantum (RSFQ) logic, field programmable gate array (FPGA) [211] |

Table 2.3 The components necessary for LOQC [48] and the purpose fulfilled by each. The final column contains examples of how each component could be implemented in a quantum photonic integrated circuit (QPIC).

Passive waveguide circuits comprised of the parts mentioned so far have been proven very useful with a combination of off-chip sources and detectors for making working quantum circuits. At the University of Bristol significant efforts have proceeded with silicon and silica waveguides [212]. Operated at $\lambda = 840$ nm initially due to the constraints of using Si-SPAD detectors, it was intended to move out to longer wavelengths to take full advantage of low loss

transmission in waveguides as well as the host of telecoms components that make experiments considerably more practical at $\lambda = 1310$ nm or $1550$ nm. Switching to SNSPDs as off-chip detectors enabled the demonstration of on-chip entanglement and fast switching in waveguide circuits at $\lambda = 1550$ nm without the need for post-processing of data to remove noise or to stitch together data from protracted experiments [213–215].

Integration of an on-chip parametric down-conversion source with silicon waveguide circuits was achieved by Silverstone *et al.* [216] in 2014. The device was able to operate as a Mach–Zehnder interferometer (MZI) and perform fast switching between waveguides verified with off-chip SNSPDs. This represents a large step towards the kind of integration necessary to implement on-chip optical quantum logic gates, although parametric down-conversion sources can be severely limiting for quantum optical circuits for reasons detailed below.

**Waveguide integrated single photon sources**

Reliable single photon sources are essential components of quantum photonic integrated circuits. For the purpose of quantum optics experiments and LOQC an ideal SPS would supply single photons on demand that are sharply defined in emission time, spatial mode, frequency, polarisation, and phase to such an extent that successive photons are indistinguishable and can be interfered with high visibility (see HOM experiment). The first established SPSs for waveguide circuits are semiconductor QDs, nitrogen vacancies (NV centres) in diamond, and parametric down-conversion sources (which produce correlated pairs of single photons) [217].

One fundamental limitation of silicon/silica waveguide circuits at present is the lack of a deterministic SPS. SPDC is a probabilistic process that creates photon number states with a Poissonian probability distribution (see Section 2.1.3). This means that for an average generation rate of 1 pair of correlated photons per unit time there is a finite probability of higher number states being generated. This amount increases as the source is pumped harder releasing multiple pairs into the optical network simultaneously and increasing the processor error rate. To employ these as sources of single photons a sufficiently low generation rate must be used so that an acceptably small number of multi-photon states are present in the system. The resulting slow rate of data processing would be unlikely to confer any advantage over existing computing technologies. An alternative solution being worked on currently is

to run massive numbers of correlated pair sources in parallel using half of the generated photon pair as a herald marking which particular source has fired and somehow feeding this information forwards quickly enough to enable the signal photon to be used in the waveguide network.

Semiconductor QDs are often grown in III-V materials such as GaAs, InAs, GaN etc. and are easily integrated with waveguide circuits [218]. In a QD single photon emission ideally comes from a true two level system i.e. an exciton decays via radiative recombination of the electron and hole. Real QD systems however can exhibit a larger number of available decay channels (including non-radiative decay) as well as splitting of the available energy levels. Embedding a QD in a waveguide with limited permissible transmission modes will suppress unwanted transitions within the QD improving the observed linewidth of emitted photons. Inclusion of photonic crystal (PhC) cavities enables so called Purcell enhancement of QD emission [219, 220]. Static electric fields can be used to finely tune separate QDs inducing indistinguishability of separately emitted photons either by applying a Stark shift to the band gap [221] or by electro-mechanically adjusting a cavity around the QD [222].

Possible excitation schemes for quantum dots include above-band pumping and resonant pumping (both with either CW or pulsed laser light) and electrical pumping. Resonant pumping with a short pulsed laser allows for the narrowest linewidth photons to be produced and is the most likely to provide a deterministic source of indistinguishable photons suitable for interference and quantum computation. Unfortunately the introduction of pump light into waveguide modes creates the greatest problem for on-chip filtering. Coupling of pump photons into travelling waveguide modes should be very poor, however once in a waveguide mode pump photons and PL photons of the same wavelength can be extremely difficult to separate before both reach a detector. Orthogonal polarisations are often used off-chip to separate pump and PL in this situation and there is the possibility of introducing polarisation selection on-chip, although it remains to be seen if the strong selectivity/extinction needed can really by achieved in waveguide components.

Novel SPSs that have found limited application in QPICs are colour centres in diamond [223] (nitrogen and silicon vacancies) and single walled carbon nanotubes, which can be doped to emit light at optical wavelengths when electrically pumped [224]. Correlated pairs of photons can also be generated within optical waveguides by exploiting non-linear material properties to achieve spontaneous four wave mixing. Waveguide integrated photon pair sources have

been demonstrated in GaAs/AlGaAs [225, 226], periodically poled LiNbO$_3$ [227, 228] and Si [229] waveguides. Table 2.4 aims to compare some of the advantages and disadvantages of waveguide compatible single photon sources.

| | Quantum dots | Down conversion | NV centres in diamond | Carbon nanotubes |
|---|---|---|---|---|
| **Monolithic integration** | ***** | ***** | ***** | * |
| **Compatibility with waveguide media** | *** | *** | *** | *** |
| **Deterministic placement** | **** | ***** | ***** | ** |
| **Tunable** | ***** | ***** | * | * |
| **Optical pumping** | ***** | **** | ***** | * |
| **Electrical pumping** | *** | * | ***** | ***** |
| **Infrared/telecom wavelength** | **** | ***** | ** | **** |
| **Operating temperature** | ** | ***** | **** | **** |
| **Sub-Poissonian** | ***** | *** | ***** | ***** |
| **Indistinguishable** | ***** | ***** | ***** | * |
| **Repetition rate** | ***** | * | **** | * |
| **Reproducibility** | *** | ***** | ***** | *** |

Table 2.4 Comparison of the merits of waveguide compatible single photon sources. A 5 star rating system is use to indicate the relative performance or compatibility of sources in each category.

**Planar optical waveguide components**

As well as SPSs and SPDs LOQC requires phase shifters and beam splitters to perform operations on photons traversing the network as well as electronics to feed forward information from triggered detectors to influence other switches or sources. As mentioned above the obvious way to realise a stable and scalable optical quantum computer is to integrate all the required parts in a monolithic platform. There are a number of systems capable of guiding and transforming light some of which are detailed below.

**– Optical waveguides**
Waveguides are structures which confine light of certain wavelengths to propagate is a determined direction. Combining advances in both optics and materials science it is now possible to confine light on a scale comparable to its wavelength and to faithfully transmit single photons over a useful distance without loss.

Planar light-wave circuits confine light either within PhCs or along tracks [230, 231] with a high index contrast with the surroundings akin to an optical fibre.

Single mode waveguides confine light in an area close to the optical wavelength whereas multi-mode waveguides are generally larger structures which can support a number of different configurations of the electromagnetic field, this is illustrated in Figure 2.12. Importantly two photons occupying different waveguide modes will not be entirely indistinguishable and interference effects will be suppressed. Waveguides suitable for single photon experiments are ridge waveguides, suspended nanobeams (SNBs) [232] and PhC waveguides.
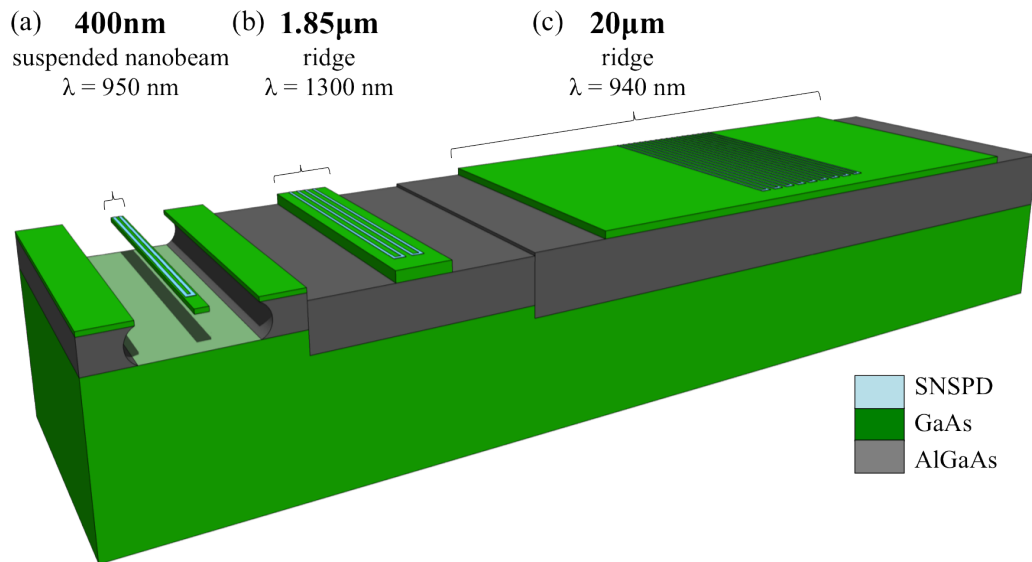


Fig. 2.11 3-D scale schematic comparing the dimensions of GaAs waveguide integrated detectors from the literature with devices realised in this thesis. The width of each waveguide is marked in bold font. **(a)** Suspended nanobeam waveguides presented in this thesis are of single mode dimensions at $\lambda = 950$ nm and house a single hairpin of superconducting nanowire on top. **(b)** GaAs/AlGaAs ridge waveguides in reference 233 house two electrically independent nanowire detectors. **(c)** Devices demonstrtead in reference 234 demonstrate a NbN SNSPD integrated with a ridge waveguide and embedded InGaAs QDs. The large area meandered SNSPD placed on top of a much wider waveguide alleviates the demand for precise alignment during fabrication. The effects of waveguide width on the supported optical modes is visible in Figure 2.12.

Theoretical treatment of certain dielectrics and semiconductors showed that a photonic band-gap could be created in a material by patterning it on a scale comparable to the wavelength at which you wish it to be transparent [235–240]. Artificial photonic band-gap materials rely not on simple index contrast but on the creation of a PhC structure in order to engineer a specific transparency

band. PhC waveguides can be patterned to create strongly confined optical modes with the additional benefit of careful mode selection to enable low loss beam propagation around tight corners [241] (a major problem for ridge and nanobeam type waveguides). The flexibility of PhC design allows for structures with tailored bandwidth, mode confinement and even variable group velocity to be created using existing lithographic techniques.
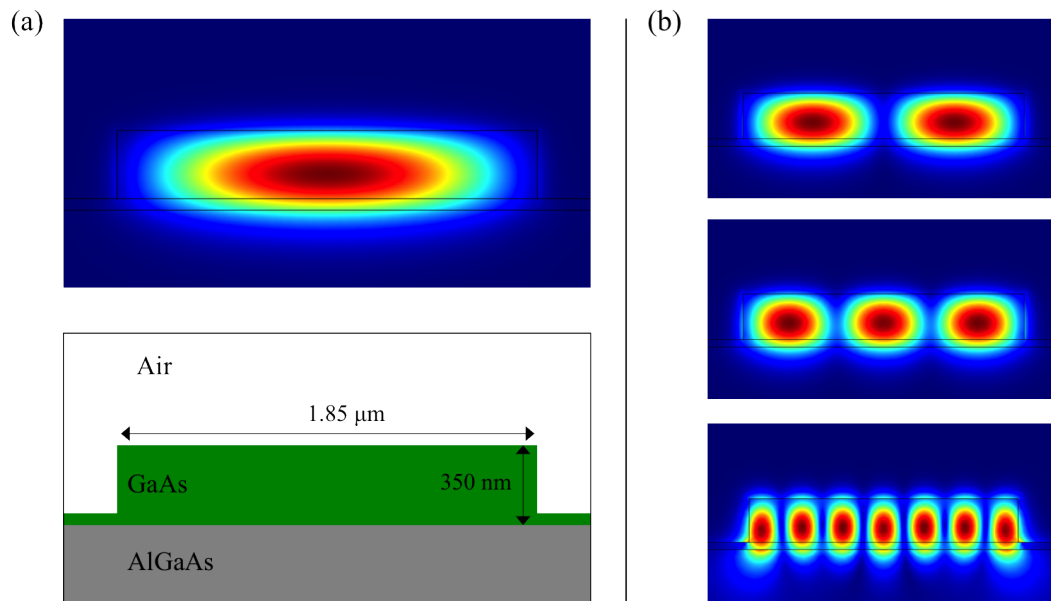


Fig. 2.12 **(a)** A simulation of the fundamental mode at $\lambda = 950$ nm in a GaAs/AlGaAs ridge waveguide (width 1.85 µm). **(b)** The waveguide supports multiple higher order modes. Pictured are the 2nd, 3rd and 7th modes from a COMSOL simulation.

**Waveguide integrated detectors**

Development of SNSPDs integrated with waveguide circuits has progressed consistently since 2012 with a number of devices demonstrated on different material platforms. Table 2.5 summarises the range of devices demonstrated to date giving details of waveguide and detector materials as well as additional functionality including integration of SPSs.

– **Beam-splitters and phase shifts**
Beam splitters are a passive element in waveguide circuits that can be implemented by way of directional couplers. Two waveguides are brought within close proximity such that the optical mode of one overlaps with the other. After a certain propagation distance in this configuration light entering the coupler via one 'input' waveguide will be split between the two and appear at

| Waveguide Material | Detector Material | On-chip photon source | Additional features | In figure | Reference |
|---|---|---|---|---|---|
| $Si_3N_4$ | NbN | × | | | 146, 242 |
| $Si_3N_4$ | NbN | × | Arrayed waveguide gratings for FLIM[1] | | 116 |
| $Si_3N_4$ | NbN | SWCNT[5] | | 2.13(b) | 243 |
| $Si_3N_4$ | NbTiN | × | | | 244, 245 |
| Si | NbN | × | | | 246 |
| Si | NbN | × | Multi-pixel device | | 247 |
| Si | NbN | × | $SiN_x$ membrane transfer of detectors | 2.13(d) | 248, 249 |
| Si | NbN | × | Cavity enhanced absorption | 2.13(c) | 250 |
| Si | NbTiN | × | Cavity enhanced absorption | | 251 |
| Si | MoSi | × | | | 173 |
| Diamond | NbN | × | Potential for NV centre[2] single photon emitters | | 252 |
| GaAs | NbN | × | | | 253, 254 |
| GaAs | NbN | × | Auto-correlator | | 233 |
| GaAs | NbN | × | Pseudo photon number resolution | | 180 |
| GaAs | NbN | QD[3] | | | 255 |
| GaAs | NbN | QD[4] | Detection of PL on-chip | 2.13(a) | 234, 256, 257 |
| $SiO_2$ | W/Au | × | Photon number resolution | | 258 |

Table 2.5 Waveguide integrated SPDs. [1] Fluorescence-lifetime imaging microscopy. [2] Nitrogen vacancy. [3] InAs quantum dots embedded in waveguides but no on-chip detection of PL. [4] InGaAs quantum dots. [5] Single walled carbon nanotubes.

two 'output' waveguides with an intensity/probability split determined by the interaction length $l$. A 50:50 beam splitter has $l$ tuned such that light incident at one input port is split evenly between both output ports. For quantum light this equates to a 50% probability of a photon appearing in either output path.

Another variation on the beam-splitter is the multi mode interference (MMI) coupler [259, 260]. These designs place output waveguides at the anti-nodes of a wide box-shaped region placed after a single-mode waveguide [261]. Numerical optimisation of MMI designs can achieve polarisation splitters [262] or beam-splitters with an incredibly small foot-print [263].
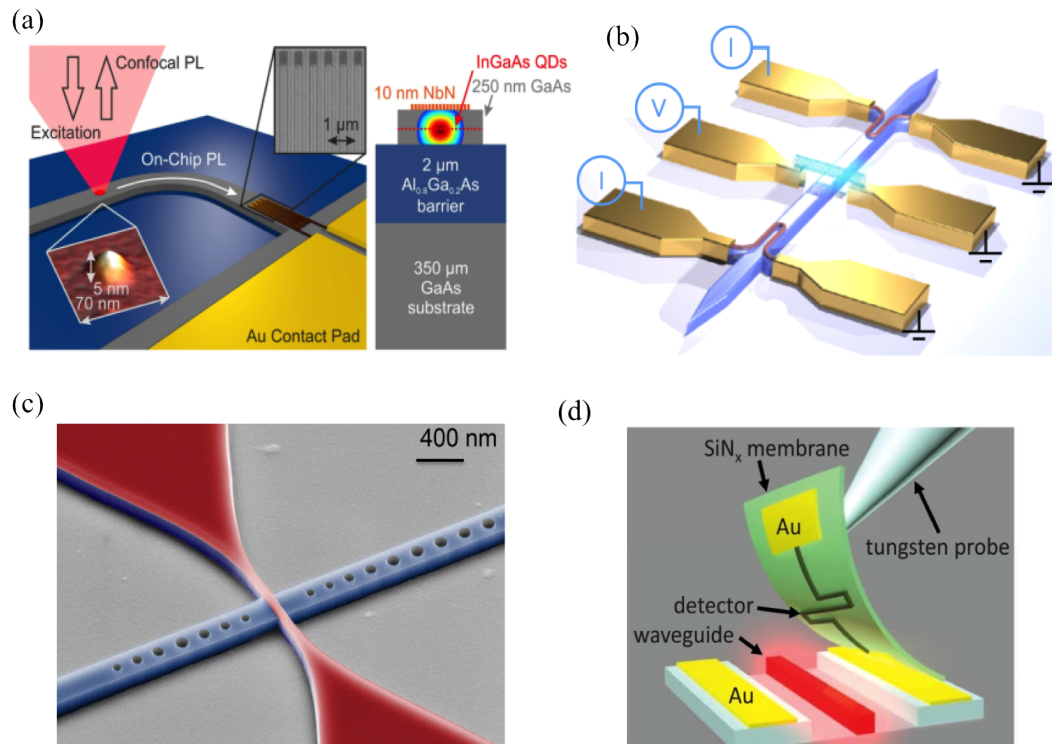
Fig. 2.13 **(a)** Devices demonstrated by G. Reithmaier *et al.* at the Technical University of Munich, adapted from reference 234. SNSPDs were fabricated from NbN thin films on 20 μm wide GaAs/AlGaAs ridge waveguides with embedded InGaAs QDs. **(b)** A device conceived between the Universities of Darmstadt and Münster, Germany incorporates a novel non-classical light source with integrated SNSPDs on Si waveguides. A single walled carbon nanotube is deposited in the centre of a $Si_3N_4$ waveguide with NbN detectors at either end making a device capable of performing correlation measurements. Adapted by permission from Macmillan Publishers Ltd: *Nature Photonics* [243], copyright 2016. **(c)** By incorporating a 1D PhC into the waveguide design a very short section of superconducting nanowire (pictured in red) can be engineered to exhibit near unity $\eta_{absorption}$ decreasing the likelihood of defects in the superconducting film limiting the detection efficiency. Image adapted with permission from reference 250. Copyright 2016 American Chemical Society. **(d)** A novel innovation in QPIC fabrication is to deposit superconducting films on thin $SiN_x$ membranes allowing SNSPDs to be screened and selected for high performance before being transplanted onto waveguide circuits. Image adapted from reference 248.

Switching of photons between paths can be achieved by MZIs (shown in Figure 2.14) or by other active switching mechanisms [213]. Phase shifts can be implemented via mechanical strain [264], heating, or electro-optic modulation [265, 266]. GaAs waveguides are able to implement path switching by the activation of micro electromechanical actuators and by voltage biasing PhC waveguides [267] or interfacing with QD spin states at a path intersection [268].
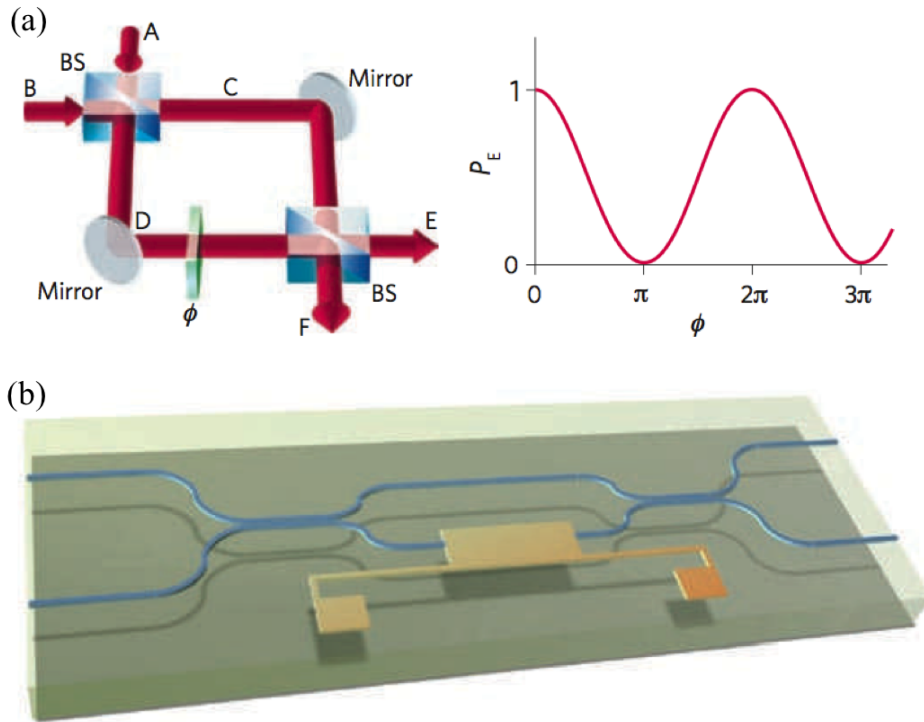
Fig. 2.14 **(a)** An MZI can be used to switch the output path of a photon by tuning the phase shift $\phi$ on one arm of the interferometer. The graph shows the probability of a photon exiting the MZI via port E as a function of the applied phase shift $\phi$. **(b)** Schematic of an MZI implemented in silica-on-silicon waveguides. Adapted by permission from Macmillan Publishers Ltd: *Nature Photonics* [201], copyright 2009.

– **Filters**

Filtering can be achieved in waveguide circuits by a number of means. Of relevance to this thesis are narrow band-pass type filters. These select a specific wavelength of light that can be passed through to the downstream waveguide circuit whilst other wavelengths are rejected and effectively removed from the signal path. 1 dimensional PhC cavities will act as a filter when placed in a waveguide path. The cavity is designed to support an optical mode with narrow spectral width. Wavelengths not in tune with the cavity mode will be strongly reflected by the cavity region, effectively removing the unwanted signal from the circuit downstream. Another type of filter is a coupled ring resonator. Again the ring forms a cavity with a sharply defined optical mode. A ring placed next to a waveguide track will couple in photons from the waveguide track that are of resonant frequency. A second coupled waveguide track on the opposite side of the ring resonator can be used to drop photons out of the cavity routing them in the desired direction for further processing, or for rejection.

– **Coupling light in and out of waveguide circuits**

Although the vision of a fully integrated QPIC handles all generation, routing, and detection of light within surface guided modes it is advantageous to address the various components of a waveguide circuit by coupling light on or off the chip for external characterisation. Similarly for quantum photonic circuits with a lower degree of integration it is necessary to interface the waveguide components with off-chip processing such as detection, filtering, or single photon generation. Coupling of light into or out of waveguide propagating modes can be achieved via a number of means, largely with geometric modifications to waveguides that efficiently scatter light from a certain point in the waveguide circuit into a mode that can be collected via off-chip focussing optics or optical fibre. Transformations of light at the coupling region are largely reciprocal (in the absence of any absorbing medium) meaning that although a significant component of the optical power may be effectively lost into the substrate or into other uncollected modes the in-coupling or out-coupling behaviour of the same coupler will be identical in all respects other than time direction.

To avoid the need for long extended waveguides and with clean cleaved facets diffraction gratings can be built into waveguides at arbitrary positions around a chip surface and create preferential scattering from the waveguide mode to a perpendicular travelling wave that can be collected by an optical fibre or focussing optics [269, 270]. Figure 2.15 shows full-depth grating couplers in Si and in GaAs. Such diffraction gratings can be etched into the waveguide material, defined at full depth [271] (in the same etch step as the waveguides themselves) although shallower features (requiring additional EBL and etching steps) can be simpler in design and create fewer back reflections. The upwards scattered mode can have strong wavelength and angular dependence, as well a large lateral divergence [272, 273]. The lateral divergence is related to the effective numerical aperture of the coupler and can therefore be mitigated by widening the waveguide laterally. Being located on the chip surface grating couplers can be extended two-dimensionally making more efficient use of surface area than end-facet coupling methods.

– **Information feed-forward**

To achieve a complex processor network on-chip it is necessary for the outcome of one quantum logic gate to be fed forward and to effect the configuration of other parts of the circuit. With photons travelling through the circuit at $v = c/n$ the electrical feed-forward must be completed extremely fast in order
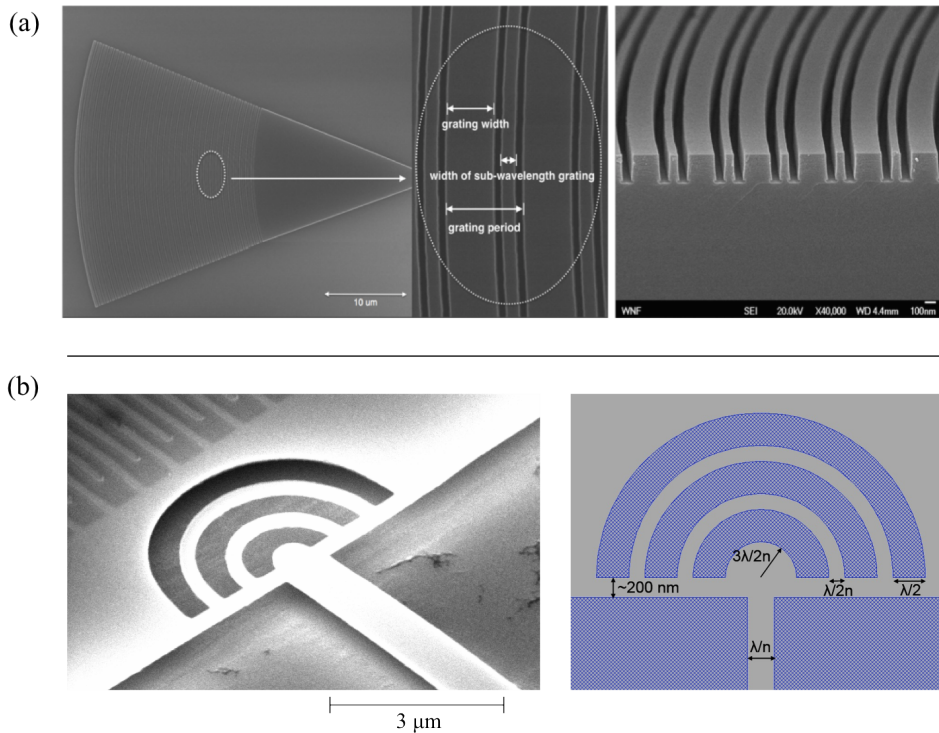
Fig. 2.15 Waveguide grating couplers. **(a)** A grating coupler design for coupling SOI waveguides to optical fibre [271]. Note the lateral taper to cover tens of microns of area. Sub-wavelength features in the grating reduce back reflections from the waveguide allowing the design to be patterned and etched to full depth in a single process step with the waveguide. **(b)** SEM of a grating coupler for GaAs suspended nanobeam waveguides fabricated by the author. The design parameters were optimised at the University of Sheffield.

to be effective. Optical delay lines can be implemented to put a photon on 'hold' for a certain amount of time. The maximum hold time is unlikely to be limited by the photon's coherence time and more so the amount of real estate available to house the delay lines on-chip. Even with a densely packed delay line using low-loss tight bends 1 mm$^2$ of space is still required to buy just a few nanoseconds of hold time [274]. Quantum memories are useful for this exact purpose [275], faithfully storing photons full quantum state on a solid-state object with sufficient coherence time allowing it to be translated back to a flying qubit when the circuit is reconfigured [276].

### 2.3.3 Rapid single flux quantum logic

One candidate technology for electronic feed-forward in a QPIC are RSFQ logic circuits. Operating at clock rates up to 100 GHz without significant errors this

digital superconducting technology has the high speed and low timing jitter required by QPICs as well as extremely low power consumption.

RSFQ was originally developed as a contending technology for computer processors based on integrated circuits. With the continued rapid advance of semiconductor circuit technology, RSFQ has only found a handful of niche applications. The 1991 review by Likharev and Semenov describes in clear detail the operating principle of basic RSFQ circuits and describes a number of designs for the implementation of digital logic [277].

The basic elements of RSFQ circuits are superconducting loops which are able to store or pass single quanta of magnetic flux each of which represents a digital bit in a logic circuit. The transfer of magnetic flux is associated with a voltage pulse:

$$V(t)dt = \Phi_0 = h/2e = 2.07 \text{ mV·ps}$$

A clock pulse similar to the data bit is distributed to the circuit and logic gates can be built up in a modular fashion to create a digital information processors that can comprise $> 10,000$ Josephson junctions operating at GHz rates in a low temperature environment.

RSFQ logic has been demonstrated as a means of electrically multiplexing and reading out SNSPDs [278, 279, 182] as well as performing logical operations [280] with SNSPD signals [183] such as digital flip-flops (see Chapter 5). Development is also under way of single layer fabrication methods for RSFQ circuits. These single layer thin NbTiN films could lead to monolithically integrated nanowire detectors with nearby nano-bridge junctions for RSFQ logic circuits.

# Chapter 3

# Fabrication and experimental methods

*This chapter is comprised of two sections, the first detailing fabrication methods for the realisation of superconducting nanowire single photon detectors (SNSPDs) and integrated waveguide circuits. The techniques detailed here were developed and used by the author to create devices characterised in later chapters. The second section describes testing of detectors and optical waveguides at low temperature using a number of electrical and nano-optical techniques.*

## 3.1   Fabrication Methods

Fabrication of SNSPDs and waveguide circuits was carried out in the James Watt Nanofabrication Centre (JWNC) at University of Glasgow which ranks amongst the best nanofabrication facilities in Europe. It contains the workspace, tools, technical support staff, and user community in which cutting edge fabrication techniques can be developed, optimised, and shared. This Chapter begins with explanations of the tools and processes used to fabricate SNSPDs and waveguide circuits. Figures 3.12 to 3.14 contain schematics of an SNSPD integrated with a gallium arsenide suspended nanobeam (SNB) waveguide as it progresses through the stages of fabrication. The layered GaAs/AlGaAs substrates pictured were grown by molecular beam epitaxy (MBE) at the University of Sheffield (Figure 3.12 step i.) and passed to a commercial foundry (Star Cryoelectronics, USA) for the deposition of thin superconducting NbTiN films. Following film growth wafers are diced and the samples sent to the University of Glasgow for further processing. All successive steps detailed in

figures 3.12 to 3.14 (steps iii. – xiv.) were optimised and performed in the JWNC by the author.

### 3.1.1  Electron beam lithography

Lithography in general is a process in which a pattern is selectively removed from a radiation sensitive polymer called a resist to create a mask. The pattern can then be transferred onto a substrate either by etching downwards removing material or by depositing material to build up new layers. Resists are polymers whose solubility in a certain solvent changes after exposure to radiation (either electrons or photons). Photolithography involves flood illumination of an entire sample underneath a mask plate which casts a shadow of the pattern onto the resist. Using a bright light source an entire wafer can be uniformly exposed in less than one minute. However the minimum feature size within a pattern is restricted by the diffraction limit of the illuminating light (usually approx. 200 nm). Electron beam lithography (EBL) is a versatile tool better applied for patterning fine features. Surpassing the diffraction limit of light an electron accelerated by 100 kV has a wavelength of just 3.88 pm (which is actually smaller than the inter-atomic spacing of the resist molecules). A focussed beam of electrons scanned across the surface of a resist-coated sample can pattern incredibly fine features with arbitrary geometry. However the serial nature of the writing process makes the time cost of EBL scale up sharply with overall pattern size.

**Vistec VB6 EBL tool**

The main electron beam lithography tool in the JWNC is the Vistec VB6 EHR UWF which contains a column in which electrons are accelerated and focussed onto samples as well as a moveable sample stage and robotic loading that coordinates with control electronics and a pattern generator. A basic schematic of the tool is shown in Figure 3.1. The source is a Schottky emission gun consisting of a tungsten filament with an extremely sharp tip and a reservoir of $ZrO_2$ which heats up when current biased to temperatures $\sim 1000$ K. Electrons are accelerated away from the tip by a 100 kV potential and into the column which focusses a beam through apertures and magnetic lenses. The beam passes between a pair of metallic plates which allow for a static voltage to be activated quickly diverting electrons off axis away from the aperture and blanking the beam. Position control coils divert the focussed spot to locations on the sample

(a)

Source at 100kV

Blanking

Pattern generator

Fast position control

Control computer

Interferometer

Vid. amp.

Stage

Mech. drive

(b)

Polycrystalline tungsten heating filament

ZrO reservoir

<100> W crystal

(c)

200 nm
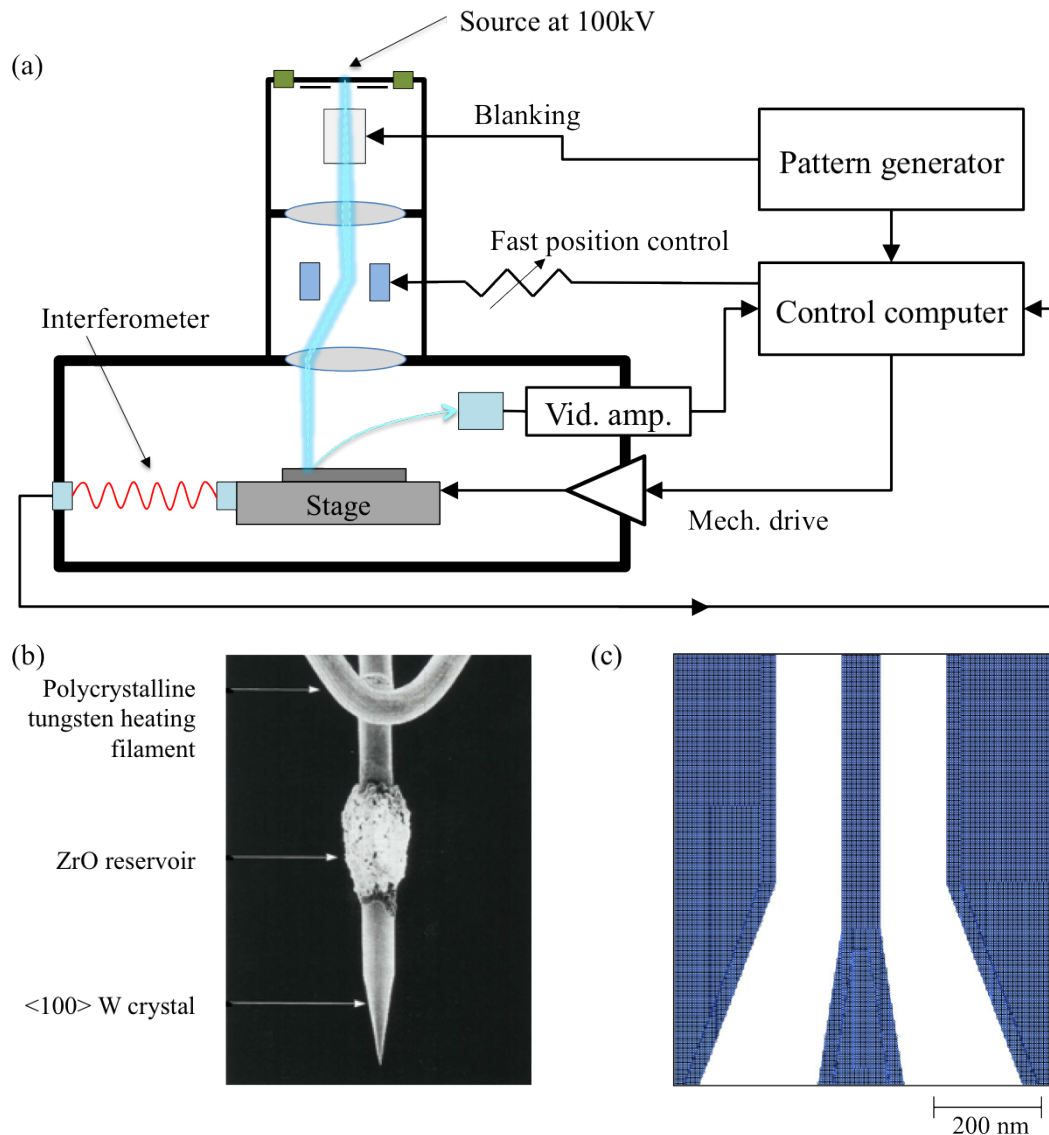
Fig. 3.1 **(a)** Schematic showing some of the key elements of the EBL tool. Electrons are accelerated from the source and focussed down the column onto the sample. A control computer coordinates the sample stage position and diversion of the beam over the sample surface. In combination with the beam blanker patterns are created by selectively exposing regions of the resist-coated sample. **(b)** A scanning electron microscope (SEM) image adapted from reference 281 showing a tungsten tip in a typical Schottky emission gun. The sharpest point is close to 1 µm diameter. **(c)** A section of the pattern file for a hairpin nanowire is represented graphically with areas in blue to be exposed by the e-beam. Individual beam shots are represented by small circles with diameter approximately that of the full width at half maximum of the focussed beam.

surface dictated by the pattern generator. The maximum lateral distance over which the beam is diverted is approximately 650 µm in any direction which constitutes a so called write field. The pattern generator assigns a grid of points over the area of the write field and creates patterns by selectively exposing the beam at the relevant points. To pattern larger areas the sample stage moves position allowing new write fields to be exposed. The stage position is monitored by an interferometer and feedback electronics enable write fields to be well aligned to each other (referred to as stitching). The beam current expressed in nA is a measure of how many electrons pass through the beam cross section in 1 second. Higher beam currents correspond to wider beam spot sizes with the VB6 adjustable between 1 nA (4 nm) and 131 nA (45 nm) beams sizes.

A pattern generator maps pattern files to a grid of up to 1,048,576 points. Separation of smallest grid points can be adjusted but 1.25 nm is most commonly used. All shapes in a pattern are made of polygons and all polygons are patterned by exposing successive dots (beam shots) to all locations making up that polygon. Therefore all shapes must have $x$ and $y$ dimensions in multiples of 1.25 nm. The variable resolution unit (VRU) parameter sets the separation of successive beam shots in terms of grid points. Wider spacing allows a large area to be covered with fewer shots. For larger features it may be possible to deliver the required dose by positioning a 45 nm beam at points on a grid much wider than 45 nm apart, allowing a high to dose to spread into the area between beam shots and expose the resist there to the necessary level.

**Resist**

The resist used for all EBL in this thesis is ZEP-520A (ZEP), a positive tone resist manufactured by ZEON chemicals. ZEP is a copolymer of methyl $\alpha$-chloroacrylate and $\alpha$-methylstyrene similar to Poly(methyl methacrylate) (PMMA) a more popular and much cheaper resist. The inclusion of chlorine atoms and phenyl groups to the polymer chain give ZEP a higher sensitivity and better etch resistance than PMMA [282]. During the development process the areas of a positive resist that were exposed will be washed away by the developer fluid whereas development of a negative resist causes all but the exposed areas to be washed away.

ZEP resist is spin coated onto samples in a solution with Anisole (methoxybenzene) mixed 1:1 by weight. A spin time of 60 seconds at a speed of 4000 rpm

is used creating a resist layer of 110 nm thickness confirmed by measurements with atomic force microscopy (AFM) and a Dektak profilometer. Resist thickness strongly influences the electron beam (e-beam) dose required to pattern a specific feature. Across the central part of a spun sample the resist thickness is likely to remain constant and highly uniform however surface tension at the edges creates ramping of the resist depth. For this reason the patterning of sensitive features is confined to regions > 1 mm from the substrate edge. Baking is performed on a metallic hotplate set at 180°C with samples placed directly on the surface for 4 minutes to evaporate excess solvent from the resist mixture. Backside smoothness plays a vital role in seating the sample absolutely flat under the e-beam to achieve the best possible alignment. It is possible for stray resist to accumulate on the substrate back-side during spinning which cannot be cleaned before baking has been completed. The substrate backside is cleaned in a watch-glass with a cotton swab and acetone. The procedure must be performed with great care to avoid any acetone coming into contact with the resist mask or any mechanical force breaking the chip (0.37 mm GaAs will split under a few grams of weight).

**Exposure**

The interaction of energetic electrons with resist molecules causes a change in their chemical structure. In the case of ZEP it undergoes main-chain scission, a process which splits the polymer chains which make up the resist leaving smaller monomers or oligomers with much higher solubility in o-xylene (developer fluid). A number of factors beyond the simple dose parameter interact to influence the dimensions of features on the final developed resist mask. For the smallest features critical to device performance it is vital to control all aspects of pattern design, exposure, and development. Dose is defined as the number of electrons incident per unit area per second conventionally expressed in $\mu C.cm^{-2}$. A fast moving electron can transfer energy via inelastic collisions with electrons and nuclei within the resist or substrate. The collision rate $\mathcal{R}_{collision}$ of accelerated electrons is

$$\mathcal{R}_{collision} \propto \frac{species\ scattering\ cross\ section \times species\ density}{electron\ acceleration\ energy}.$$

The electrons arrive with high enough energy at the sample surface that they penetrate through the resist layer and some distance into the substrate with minimal interactions. Some electrons collide and cause back-scattering of atomic
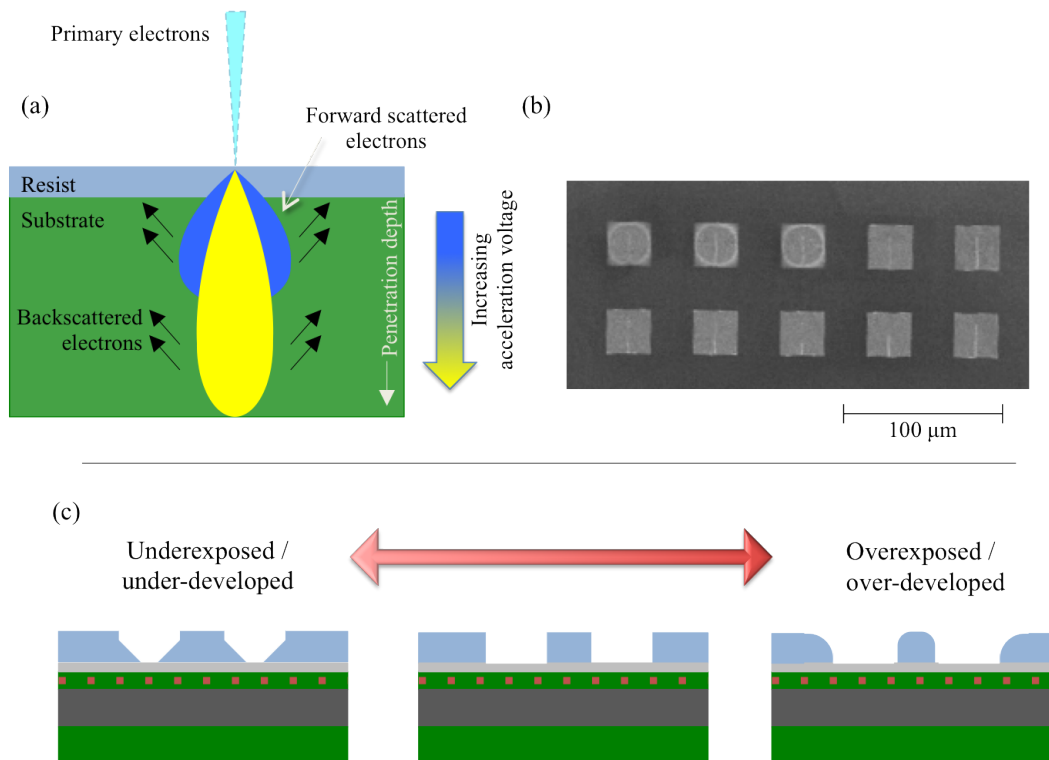
Fig. 3.2 **(a)** Diagram of the scattering profile of a beam of electrons accelerated at 100kV and focussed onto a resist-coated sample. Most electrons penetrate far into sample with small angular divergence caused by interactions with atoms in the substrate. Secondary electrons knocked out of atomic orbital by the high energy electron beam are back-scattered into the resist layer with a shorter mean free path, interacting with the (ZEP) resist molecules breaking down the long chain polymers. **(b)** A dose test is used to determine the clearing dose for features of a certain size. The same shape is patterned repeatedly with varying doses. Patterns in the top left of the grid are underexposed. **(c)** Cross section schematic of a substrate with EBL patterned resist mask. In the centre is the optimised pattern and to either side the distorting effects of over- and underexposure can be seen. The development process also has a strong influence in over or under-sizing of patterned features.
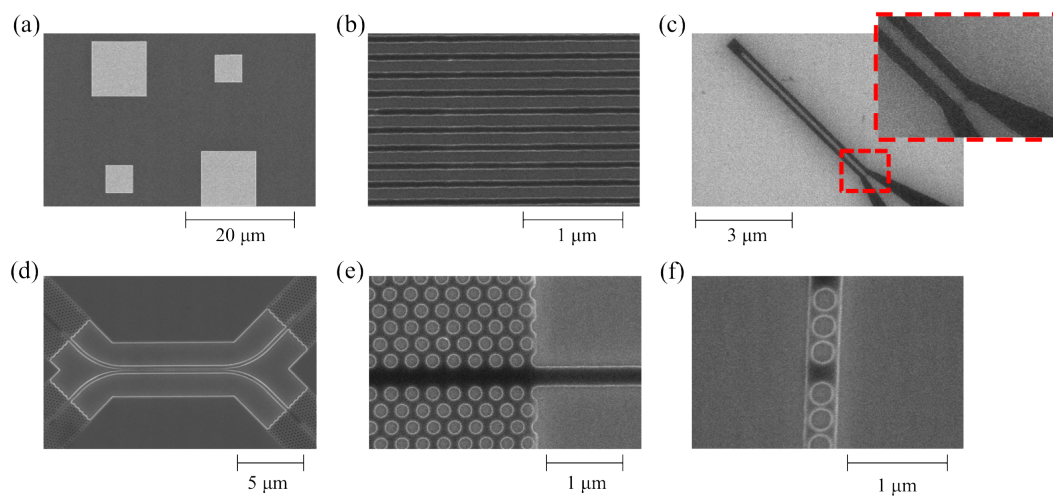
Fig. 3.3 SEM images show the critical features patterned in various stages of EBL. If these features are distorted or the wrong size in the resist mask the resulting devices are likely to be inoperable. The features are: **(a)** alignment markers, to be patterned in Au film, **(b)** nanowires to be etched into the superconducting material, **(c)** a hairpin nanowire to be aligned to an optical waveguide (the inset shows how poor exposure can cause a short circuit between wires), **(d)** a waveguide directional coupler to be etched into GaAs, the beam-splitting ratio is strongly dependent on the gap width between waveguides, **(e)** single mode waveguides in photonic crystal (PhC) and nanobeams, to be etched into GaAs, **(f)** a 1 dimensional PhC incorporated into a nanoebeam waveguide for wavelength–dependent filtering.

electrons from within the substrate or resist material. It is these secondary electrons which are the main source of the scission reactions that break polymer chain links and increase the solubility of separated ZEP monomers and oligomers in resist. So the substrate material, resist material, resist thickness, and beam dose all affect the number of electrons delivered to the sample as well as how far those electrons spread, and the spatial distribution of scission reactions that take place. The sum result of all of these factors is generally known as the exposure. Finally the development stage introduces more variability to the pattern outcome since the development reaction (i.e. the dissolving of ZEP monomers and oligomers) will progress at a rate dependent on the temperature, the concentration of development fluid (especially when failure to move away reaction products can effectively reduce the local concentration of developer slowing the reaction rate), and the exact exposure pattern received by the ZEP (see figure Figure 3.2 (c)).

Effective pattern design takes into consideration not only the intended geometry of the feature you wish to create but also the effects of additional exposure received from secondary electrons scattered from other beam shots in nearby areas. Proximity effect correction (PEC) software uses a point spread function to simulate the scattering of electrons through resist and substrate in order to estimate the effective exposure that will be received by all areas of the resist given a specific dose and pattern geometry. The pattern is then fractured into smaller subsections so that the delivered dose can be adjusted for each subsection resulting in a more even distribution of received exposure. This technique can also incorporate the over-dose/under-size principle which aims to create a resist mask shape of area A by patterning a smaller area B (centred at the same position as A) and using a dose higher than the clearing dose for B. Another technique used to improve the uniformity of exposure for nanowires is the inclusion of "dummy" wires around the edge of a detector's active area. These wires will not be electrically relevant to detector operation but during exposure they create a similar exposure environment for sections of wire at the edge of the active area to those sections in the centre (see Figure 3.4). When patterning meandered nanowires in ZEP the pattern file contains lines of 60 nm width separated by 120 nm. PEC provides multiplication factors to each small polygon within the larger detector geometry which are then applied to the base dose of 180 $\mu$C.cm$^{-2}$. After completing fabrication the nanowires are measured by SEM as 90 nm wide with 90 nm separation. Figure 3.3 shows

patterned resist for features such as nanowires and photonic crystals (PhCs), the dimensions of which are critical to device performance.
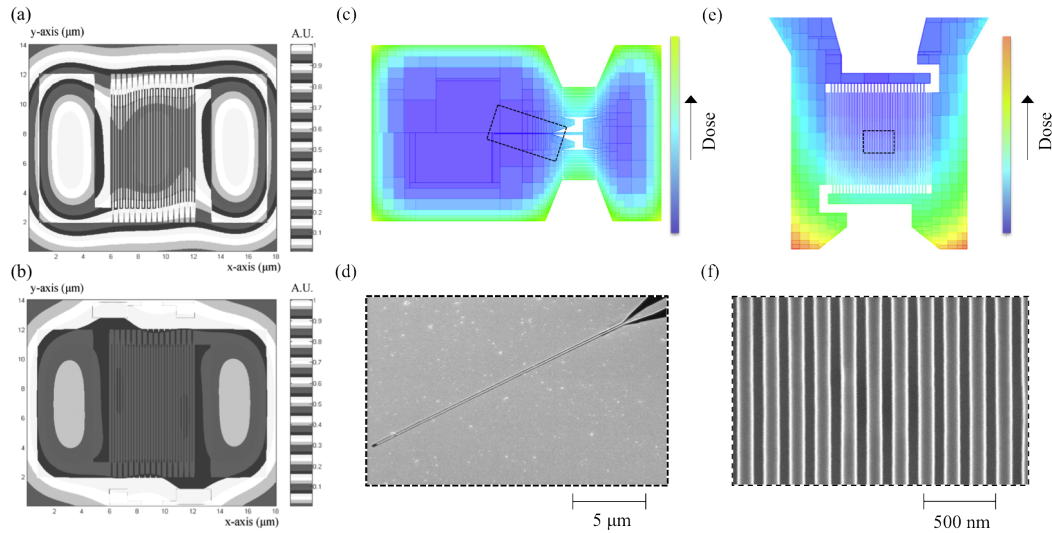


Fig. 3.4 **(a, b)** Simulations from reference 122 show the effective exposure received over the area of an SNSPD when a uniform dose is used **(a)** and when dose is adjusted to compensate for the local pattern geometry **(b)**, so called proximity effect correction (PEC). IEEE 2005. Examples are shown of devices patterned in the JWNC. Colour maps show the compensated dose profile for a hairpin nanowire **(c)** and a meandered SNSPD **(e)**. SEM images of the pattened resist show the uniformity achieved in the resist mask **(d, f)**.

**Developing and removing resist**

Following exposure resist is developed in pure o-xylene at 4°C for 3 minutes with gentle agitation. The low temperature development process reduces the otherwise high sensitivity to development duration and temperature and creates well defined sub–100 nm features. After development samples are rinsed thoroughly with IPA and dried with a nitrogen gun. After dry etching processes, samples are given 5 minutes $O_2$ plasma ashing to remove species from the mask surface that are the reaction product of ZEP and the RIE chemicals. The remainder of resist is removed in a glass beaker of n-methyl-2-pyrrolidone (nMP) at 80°C for 2 hours with gentle agitation followed by thorough rinsing with acetone and IPA. Samples are dried with a nitrogen gun. A subsequent short plasma ash can be used however oxidation of the exposed superconducting material will begin quickly with an observable increase in the nanowire resistance at room temperature occurring after just a few minutes of exposure to $O_2$ plasma (100 W).

**Layer to layer alignment**

To realise nanowire detectors integrated with single mode SNB waveguides in GaAs it was necessary to perform 3 stages of electron beam lithography with additional etch and deposition stages. The total alignment tolerance over the entire process is < 50 nm. Examples of good alignment and misalignment can be seen in Figure 3.6. A number of steps were taken to optimise the standard alignment process in the VB6 to achieve reliable alignment through all three e-beam stages. Alignment, or registration, of samples is carried out inside
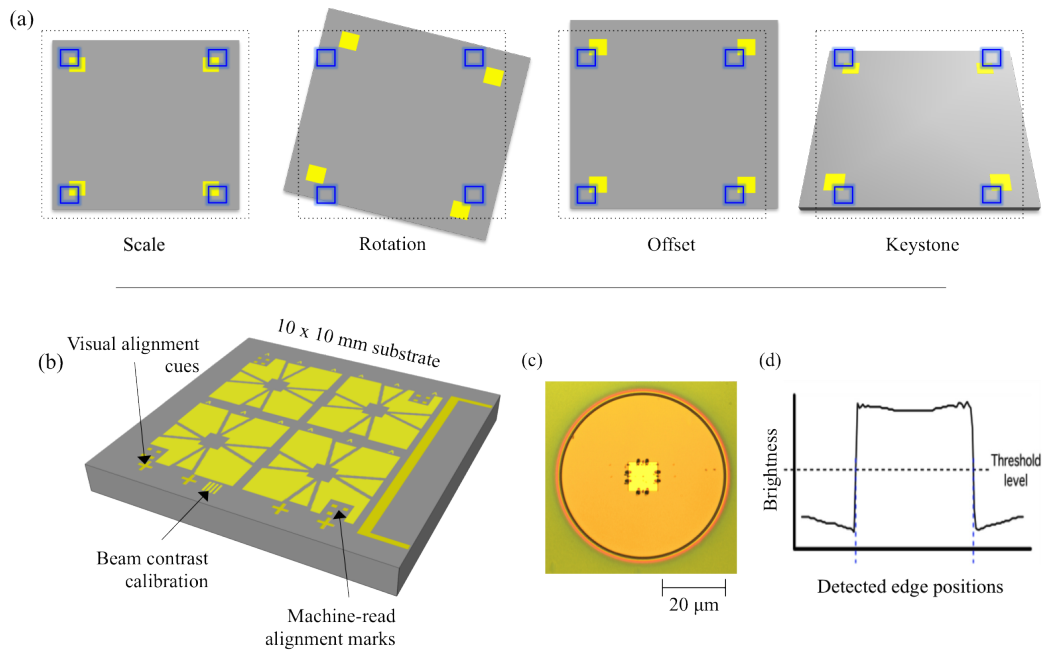


Fig. 3.5 **(a)** Alignment markers are used to adjust the orientation of an EBL pattern when the substrate (grey and gold) is found to be misaligned from the expected position (blue squares). Four degrees of freedom can be accounted for. **(b)** The Au pattern on a chip contains machine alignment markers as well as markers visible under an optical microscope by the EBL tool operator to establish the initial rough orientation of the sample. **(c)** Square alignment markers are read by scanning the e-beam over their location in SEM mode. **(d)** Line scans over the edges of a metallic marker allow the precise position to be detected by signal contrast.

the VB6 by a machine process directed by software created in-house. The electron beam is first used in SEM mode to locate and view regions of the surface containing precisely defined alignment marks. Using four alignment marks at the corners of a square the alignment can compensate for 4 degrees of substrate misalignment namely scale, rotation, offset and keystone (see Figure 3.5). The beam spot size is reduced and a series of line scans are carried out over each marker. Analysis of the backscattered electron signal is used to

identify edges by their contrast. The measured positions of marker edges are compared to the design file and the differences between the two are used to create transformation matrices that will adjust the positions which the beam is directed to during patterning. The e-beam patterning, metal deposition, and
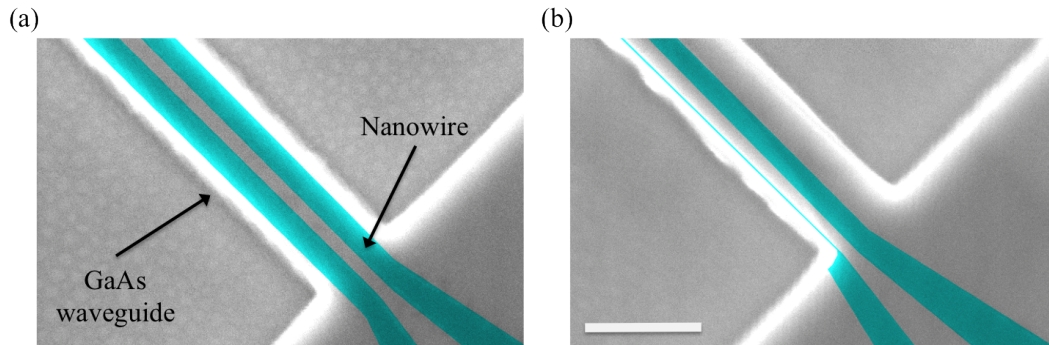


Fig. 3.6 Hairpin nanowire detectors are aligned to nanobeam waveguides over 3 stages EBL. Devices **(a)** and **(b)** are oriented perpendicular to each other on the same chip. A small linear misalignment of $\sim 100$ nm is enough to destroy device **(b)**. Scale bar is 500 nm for both images.

lift-off that creates the alignment marks must be optimised to reduce errors in maker reading that translate to errors in the written pattern. The first stage of e-beam lithography involves patterning 10 μm squares in the exact centre of a write field. This ensures that the position of the square is as accurate as possible and that no significant beam shape distortion occurs due to beam deflection. Using the narrowest beam size (4 nA) enables low edge roughness and precise dosing to be achieved. Good quality lift-off is ensured by the use of a sufficient adhesion layer, sonication during lift-off, and deposition of a deep metallic layer without exceeding the resist depth (shown in Figure 3.7). Deposited metallic films are 80 nm Au with an underlying 10 nm Ti for adhesion to the NbTiN surface, chosen so that markers can be fabricated together in the same step with coplanar waveguides and bond pads for detectors. This material choice also creates sufficient contrast with GaAs or Si substrates in order to be machine readable in the VB6.

Samples are typically processed as 10 mm square dies with 4 square markers located as close to the corners as possible after accommodating for resist edge beading and the clamp used to secure the sample see Figure 3.5 (b). This helps to minimise errors in the translation matrix due to the relationship

$$Total\ alignment\ error \propto \frac{Single\ marker\ position\ error}{Marker\ separation}.$$

### 3.1.2   Sputtering and deposition

**Superconducting thin film deposition**

SNSPDs are reliant on high quality ultrathin films for their high single photon sensitivity and fast energy relaxation. Typically NbN just 5 nm or 10 nm in thickness needs to be deposited uniformly over a substrate large enough to make a practical device. Such NbN films are a few tens of atoms thick and their crystalline structure depends strongly on the substrate-film interface. A mismatched crystal lattice in the substrate material will quickly induce enough strain in the deposited NbN to cause breaking of the single-crystal structure and consequent deterioration of the superconducting properties. DC magnetron sputtering is a favoured method for superconducting film deposition creating a plasma in a low pressure nitrogen/argon gas flow which bombards the surface of a metal alloy target. Material ejected from the target is deposited onto the substrate in a mixture dictated more by the local environment than by the stoichiometry of the atomic species involved. Gas pressures, plasma current, target ageing, substrate temperature, and deposition rate are some of the interrelated variables that all contribute to film quality and eventual device performance. Understandably optimisation of film growth is an arduous task. For the majority of devices fabricated by the author in this thesis thin films of NbTiN were used (courtesy of Star Cryoelectronics, USA). NbTiN has a fine crystalline structure and a lower lattice constant than NbN making it suitable for deposition on GaAs substrates. Having a lower superconducting transition temperature $T_C$ than NbN causes NbTiN nanowires to have greater sensitivity to low energy single photons whereas a faster count rate should be achievable with NbTiN detectors thanks to the kinetic inductance being lower than equivalent NbN detectors[283]. Patterned NbTiN films of $5-10$ nm thickness can have $T_C \simeq 10$ K which is high enough for detectors to perform well at temperatures achievable in Gifford-McMahon (GM) or L-He based cryostats. The highest $T_C$ for DC magnetron sputtered NbTiN is achieved by heating the substrate over $450°$C during deposition. Unfortunately at temperatures close to $500°$C the arsenic in GaAs substrates begins to evaporate causing serious degradation of the sample surface so the film deposition temperature must be carefully balanced to achieve the highest uniformity films with the best $T_C$ [284].

**Evaporation and lift-off of metallic films**

Alignment markers and bond pads are patterned by EBL and deposited by electron-beam evaporation. An initial layer of 10 nm Ti is deposited to provide adhesion before 80 nm Au is deposited. Longer sections of Au bond pads likely contribute to the heat-sinking of superconducting film via the Al bond wires. Figure 3.7 shows the effect of depositing excessively thick metallic layers in comparison to the resist depth and edge-profile i.e. unsuccessful lift-off results in the metallic film either removing intended features (c) or depositing metallic film over unintended areas (b). The resist depth used is 110 nm and is partially constrained by the need to keep a low aspect ratio for the smallest patterned features. Lift-off is performed by transferring the sample into a glass beaker of nMP (commercial name Shipley 1165) and heating to 80°C in a bath of ethylene glycol with gentle agitation. After 2 hours of heating and agitation the beaker is placed in a ultrasonic bath for $10-20$ seconds until all residual metal is removed. Finally the sample is cleaned with acetone and IPA and dried with a nitrogen gun.
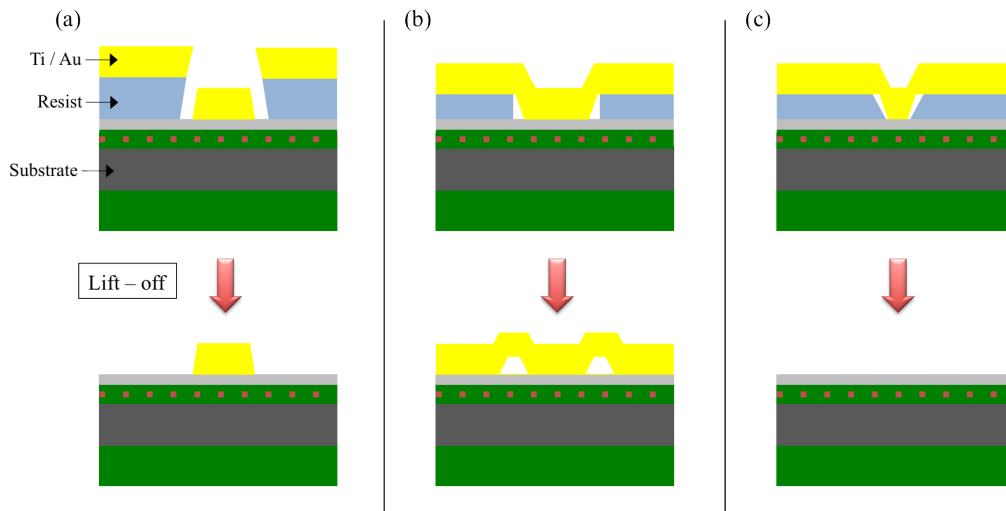


Fig. 3.7 **(a)** Metallic films are deposited by electron beam evaporation to create alignment markers and bond pads. **(b)** A film deposited too thickly may not detach during lift-off. **(c)** Underdevelopment of the resist mask can reduce adhesion of the metallic film causing features to be lost during lift-off.

### 3.1.3   Etching

**Reactive ion etching (RIE)**

Reactive ion etch (RIE) utilises physical and chemical processes for the controlled removal of materials from a sample surface. Figure 3.8 shows the layout of an etching machine and illustrates the processes that occur during an etch. Reactive ion species in plasma react at the sample surface at a higher rate than those aqueous solution and the acceleration of the charged species increases the energy with which material is oblated from the exposed substrate surface. A
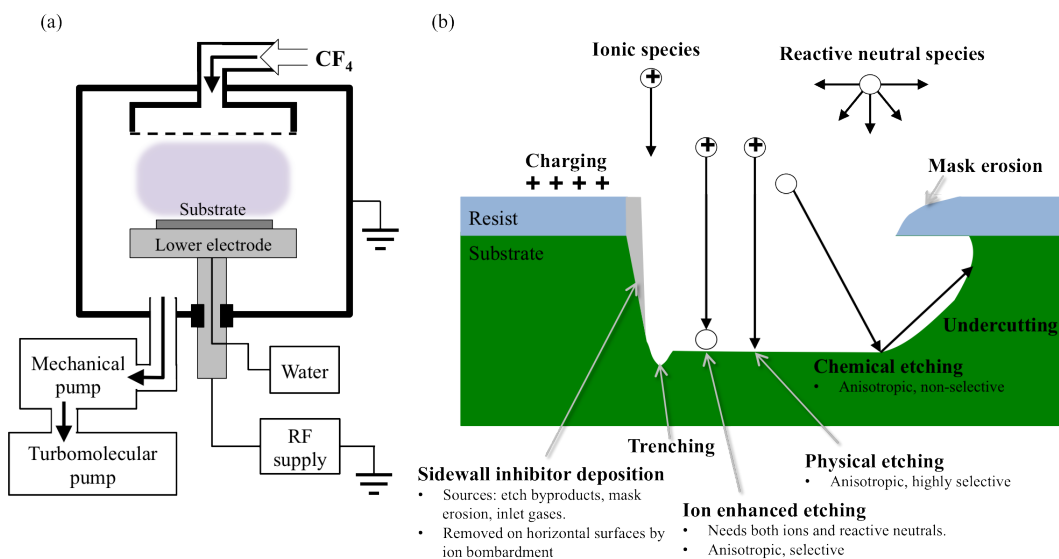


Fig. 3.8 **(a)** Schematic of the chamber and gas fow used for RIE with $CF_4$ adapted from reference [285]. **(b)** Diagram showing the chemical and physical processes occuring during RIE.

dry etching process is used to selectively remove areas of superconducting thin film underneath an e-beam resist mask. The reactive species $CF_4$ is pumped into a vacuum chamber at 50 sccm to a pressure of 30 mTorr at room temperature. High frequency power of 80 W is applied between two electrodes, one of which is the plate on which the sample is placed. The use of ultra-thin superconducting films ($\sim 7$ nm thick) and wire widths close to 100 nm means that the nanowires are approximately 2-dimensional and edge effects such as scalloping are negligible during the etch process. The duration of the etch is 55 seconds to ensure full clearance of a 7 nm NbTiN film from the narrowest sections of the pattern. An Oxford Plasmalab 80 Plus is used to run this RIE recipe with small adjustments being made to accommodate different film thickness or materials.

Waveguides are etched into GaAs to a depth of at least 140 nm using a recipe developed at the University of Sheffield mixing RIE with inductively coupled plasma (ICP) for improved waveguide edge smoothness. The recipe uses $SiCl_4$ at a flow rate of 18 sccm and a pressure of 9 mTorr with an RF power of 250 W in an Oxford Plasmalab System 100 RIE machine. The etch time is tailored to allow the deepest possible etching of waveguide features including the clearance of material from the centre of small holes in photonic crystal sections. An upper limit is placed on etching time by the selectivity of the ZEP etch mask. After $> 3$ minutes there is a significant chance the ZEP mask will be entirely etched through and the underlying NbTiN severely damaged.

**Wet etching**

The GaAs SNB waveguides require a wet etching process to be released from the underlying substrate. Submerged in aqueous HF (48%) the buried AlGaAs layer in the substrate etches quickly and isotropically causing a scalloping effect which removes material underneath thin nanobeams. GaAs does not interact strongly with the etching solution making the process highly selective. Interactions do occur with the deposited superconducting and metallic films. Perhaps surprisingly the superconducting nanowires are not significantly damaged during the short 20 s etch however the Ti adhesion layer between the NbTiN film and Au features was found to cause significant issues. The high etch rate of Ti in HF causes destructive damage at the edges of Ti/Au features serious enough to electrically isolate regions Au from the underlying NbTiN films[286]. To mitigate this effect Ge can be used as an alternative adhesion material or metallic bond pads can simply be excluded from the design making electrical contacts via the continuous NbTiN film instead. One of the most
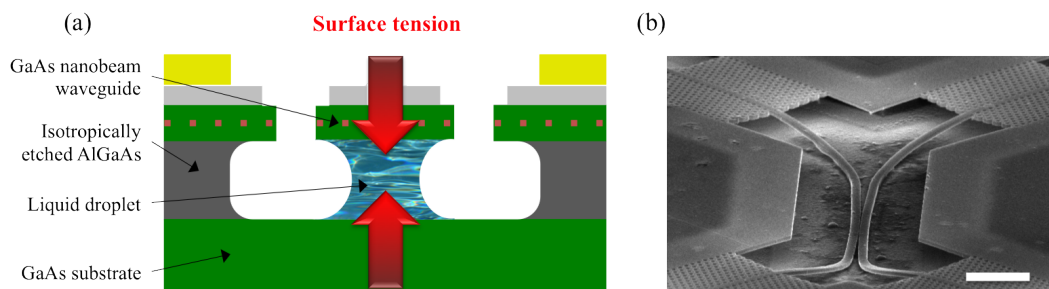


Fig. 3.9 **(a)** A cross-section schematic showing how residual liquid generates bending force on SNB waveguides whilst drying. **(b)** An SEM image of two long SNB waveguide which have collapsed following an aqueous HF etch. Scale bar is 2 μm.

challenging aspects of using an aqueous process to create suspended structures is the inevitable removal of the liquid to dry the devices before they can be tested freely in air and vacuum. When almost dry a small amount of liquid trapped in the newly created gap between the underside of the nanobeam and the substrate below will exert a force on the surfaces with which it is in contact. As the molecules evaporate from the droplet's surface its size shrinks and more tension is exerted on the nanobeam and substrate, slowly pulling the two closer together. Being long ($> 10$ μm) and thin (140 nm) the nanobeam is flexible and the surface tension of even acetone droplets (much lower than $H_2O$ or other solvents) is enough to bend a beam down into contact with the substrate 1 μm below. Once in contact van der Waals interactions between the waveguide and substrate render the collapse irreversible and reduce the waveguide transmission to near zero.

There are two approaches to avoiding waveguide collapse after wet etching. The first is to limit the length of sections of nanobeam. It was found empirically that waveguides of $\leq 15$ μm length largely survive the drying process after an HF etch probably due to the reduced flexibility of the GaAs top layer where SNBs are attached to the more rigid edges. Critical point drying (CPD) is the second method for releasing suspended structures. The HF etch solution is replaced with $H_2O$, acetone and then liquid $CO_2$ at high pressure. Raising the temperature it is possible to pass the critical point at which $CO_2$ becomes a supercritical fluid which can be pumped away from the sample without surface tension being exerted on delicate suspended features. At lower pressures the $CO_2$ returns to the gaseous state and the dry sample can be safely handled in air.

### 3.1.4   Metrology

Figures 3.10 and 3.11 show images captured from various metrology techniques. Microscopy and profilometry offer insights into the state of a sample at different stages in the fabrication process and results can be interpreted to aid trouble-shooting during process development.

**Optical microscopy**   is the fastest method to perform a general appraisal of a sample surface. Tools such as the Leica INM20 Optical Microscope have a large field of view and have objectives for up to $100\times$ magnification. This microscope can laterally resolve features down to the diffraction limit of light

(a) Scanning Electron Microscopy

(b) Optical Microscopy

(c) Energy dispersive X-ray spectroscopy
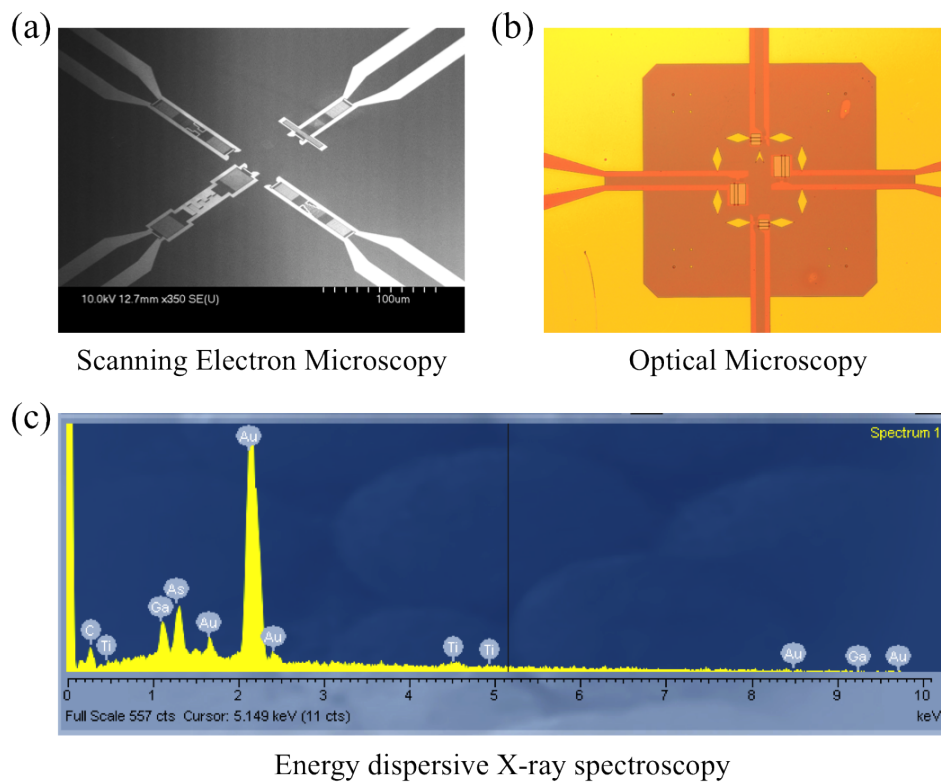
Fig. 3.10 Examples of metrology techniques used for sample characterisation in the JWNC. **(a)** An image is captured of 4 SNSPDs in the Hitachi S4700 SEM and similar scene viewed under an optical microscope is shown in **(b)**. **(c)** The measured spectrum of EDX spectroscopy taken over an Au bond pad. Peaks corresponding to Au and Ti are clearly defined alongside the Ga and As signal from the substrate. At low energy one peak signals the presence of C likely in residues of ZEP resist.

($\sim$ 200 nm). Using white light in an optical microscope also creates thickness-dependent colour and brightness contrast for resist layers and superconducting thin films. Because of this light microscopy can be used to quickly assess the outcomes of etch processes, resist spinning, development, and stripping. Using an objective lens with a relatively small depth of focus enables some qualitative assessment of the morphology of surface features. For instance once the sacrificial AlGaAs layer is removed from underneath GaAs waveguides the waveguide depth and underlying surface as separated by over 1 μm. Such separation in focal length makes it easily possible to identify which waveguides are suspended above the substrate and which have collapsed (see Figure 3.9).

**Scanning electron microscopy** is another powerful characterisation tool an SEM creates images with accelerated electrons which have a diffraction limit orders of magnitude smaller than photons in the visible spectrum. In the Hitachi S4700 SEM a beam of electrons is focussed and scanned over the substrate with two detectors collecting either back-scattered or secondary electrons. The angle and energy with which electrons are scattered is different in each case, each providing slightly different information dependent on the material and topology of the sample. Sample conductivity also has a strong influence on imaging[287]. Non-conductive substrates quickly accumulate charge at an exposed site causing beam deflection and distorting images. Build up of large static charges can also cause things to move around on the substrate if they are not securely stuck down. It should also be obvious that EBL resists are sensitive to exposure under electron beams and will likely undergo chemical and structural changes when imaged in an SEM, proportional to the dose received[288]. As many stages of fabrication require SEM imaging in the presence of EBL resist the potentially destructive effects of exposure must be considered.

**Energy dispersive X-ray spectroscopy (EDX)** is an additional feature within the Hitatchi S4700 SEM which exploits the phenomenon of emission of high energy photons from atomic electron orbitals stimulated by interactions with the electron beam. X-ray photons are emitted at wavelengths dependent on unique energy level structure of the atomic species. As such the EDX can be used to perform elemental analysis of samples directly under the SEM beam. The X-ray signal is generated in a volume totalling several cubic microns underneath the area where the electron beam strikes the surface. Therefore measurements

of surface features will include significant signal from the underlying substrate material.

(a)

(b)



Atomic force microscopy                    Profilometry
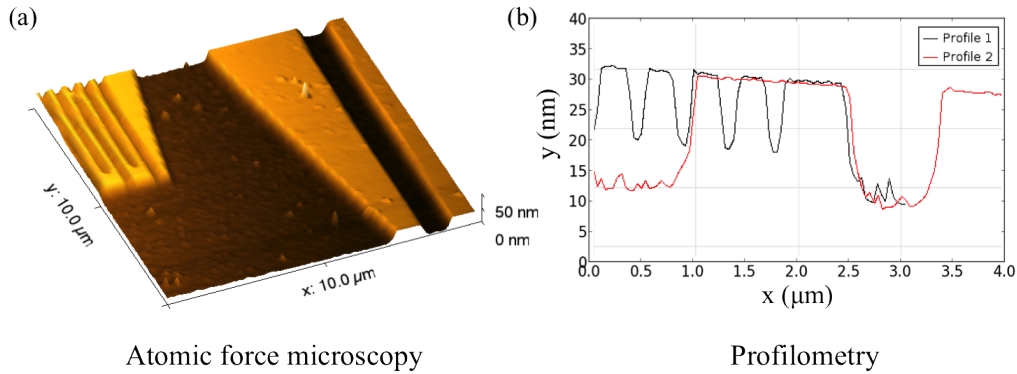
Fig. 3.11 Surface morphology is characterised by profilometry. Atomic force microscopy **(a)** can generate 2-dimensional maps or lower resoltuion linescans **(b)** can be performed quickly on a Dektak profilometer.

**Atomic force microscopy (AFM)** is used to measure surface topology with sub nanometre accuracy. A laser interferometer is used to precisely follow the vibrations of a miniature silicon cantilever with a nano-patterned needle-like tip. As the tip is brought close to contact with a surface it is forced to follow the morphology as it is moved laterally. The interferometer feeds back the tip height allowing a detailed map of the surface to be built by raster scanning the tip over an area and displaying the height data for each line scan. AFM is commonly used to verify layer depths after etching or deposition as well as checking surface roughness or uniformity.

**Profilometry.** A Dektak profilometer performs line-scans of a substrate measuring surface topology much like an AFM with a significantly larger tip. The Dektak typically resolves heights with an accuracy of around 5 nm and single line scans can cover a long distance very fast providing sample characterisation with lower resolution than an AFM but in much less time.
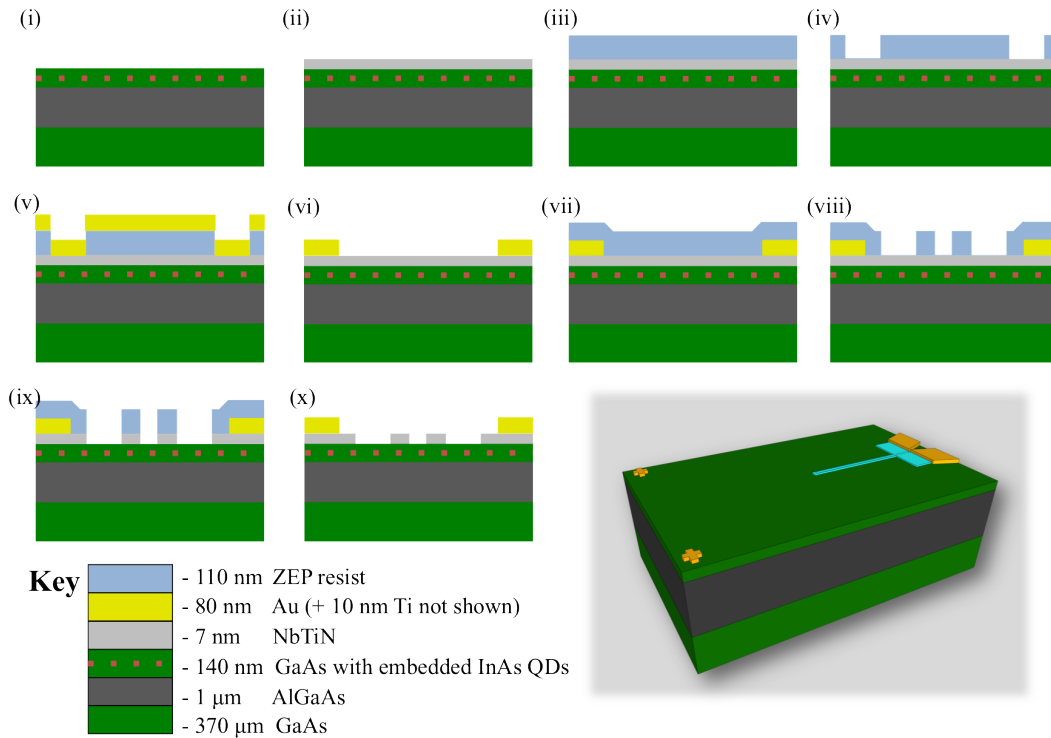
Fig. 3.12 Detector fabrication (thicknesses not to scale).

**(i)** – Substrates are grown by molecular beam epitaxy at the EPSRC national centre for III-V technologies. A GaAs wafer (green) is grown to a depth 370 μm and additional layers of AlGaAs (1 μm, dark grey) and GaAs (140 nm) are then grown on top. During growth of the top GaAs layer a small amount of InAs is introduced which self-assembles into quantum dots (QDs) (red).

**(ii)** – Thin films of superconducting NbTiN ($\sim$7 nm, light grey) are grown on top of the wafers at a commercial facility.

**(iii)** – Substrates are cleaned with acteone, isopropanol (IPA) and $N_2$ gas to prepare for EBL. ZEP-520A positive resist (110 nm, blue) is spun onto the sample and baked to remove the solvent.

**(iv)** – EBL of alignment markers and electrical contact pads is performed in a Vistec VB6 tool with 100 kV accelerating voltage and base dose 180 μC.cm$^{-2}$. The pattern is developed in o-xylene at 4°C.

**(v)** – Metallic features are deposited onto the chip by electron beam evaporation. An initial layer of Ti (10 nm, not shown) is used for adhesion followed by Au (80 nm, yellow).

**(vi)** – Excess metal and resist are removed in nMP solvent at 80°C and the sample placed briefly in an ultrasonic bath to complete lift-off.

**(vii)** – A second round of EBL is used to pattern the nanowires and coplanar transmission lines using the same resist.

**(viii)** – Exposure and development are similar to step iv.

**(ix)** – The pattern is transferred into the superconducting film by RIE in CF$_4$ gas.

**(x)** – The sample is cleaned of resist by $O_2$ plasma ashing and chemical stripping as in step vi.

**Inset** – A 3D schematic showing the hairpin shaped nanowire in light blue.
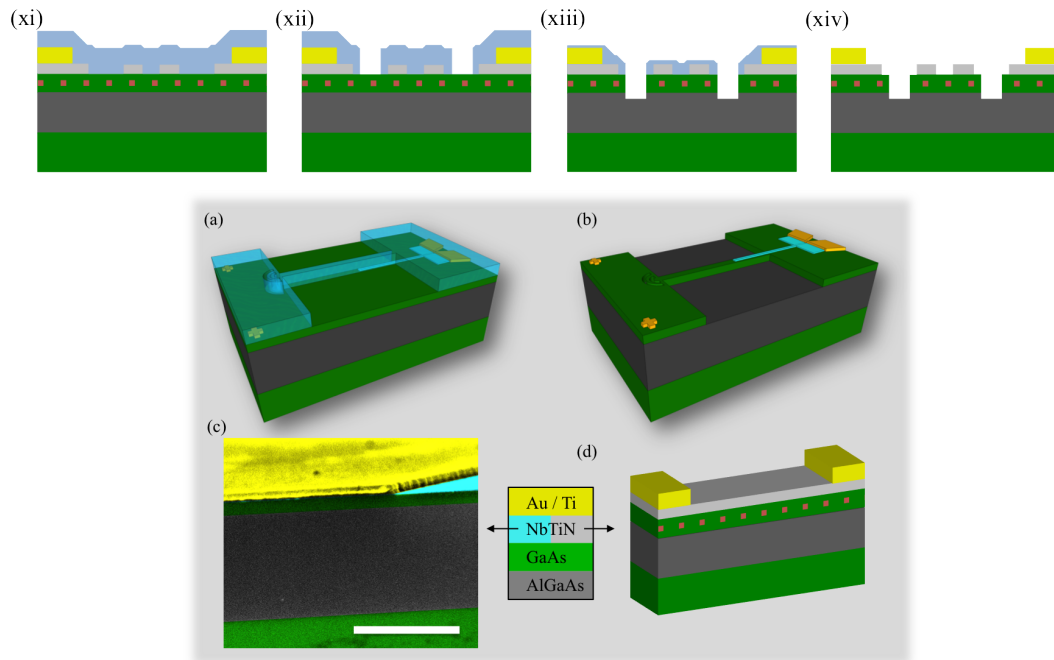
Fig. 3.13 Dry etching of waveguide circuits around hairpin nanowires, continued from Figure 3.12.

**(xi, xii)** – Similar resist, exposure and development processes are used in a 3rd stage of EBL. The final e-beam pattern defines the waveguide circuit geometry and must be aligned to the hairpin nanowires on the surface of the chip with nanometre precision.

**(xiii)** – A combined dry etch process uses RIE with $SiCl_4$ and inductively coupled plasma to transfer the waveguide design into the GaAs substrate top-layer to a depth $> 140$ nm.

**(xiv)** – Plasma and nMP cleaning are used to remove resist residues (see Figure 3.12 vi).

**Inset**– 3-D drawings show the waveguide circuit layout in resist **(a)** and transferred into the GaAs substrate top-layer **(b)**. **(c)** False coloured scanning electron micrograph showing a cross section of layered GaAs/AlGaAs substrate, scale bar is 1 µm. Green layers are GaAs and grey is the sacrificial AlGaAs layer. Visible on the chip surface are deposited metallic layers (Ti/Au, coloured yellow). **(d)** A schematic view shows the layers not to scale with red dots indicating the location of InAs QDs embedded in the waveguide layer. NbTiN is shown in grey (as opposed to light blue in **(c)**) for clarity.
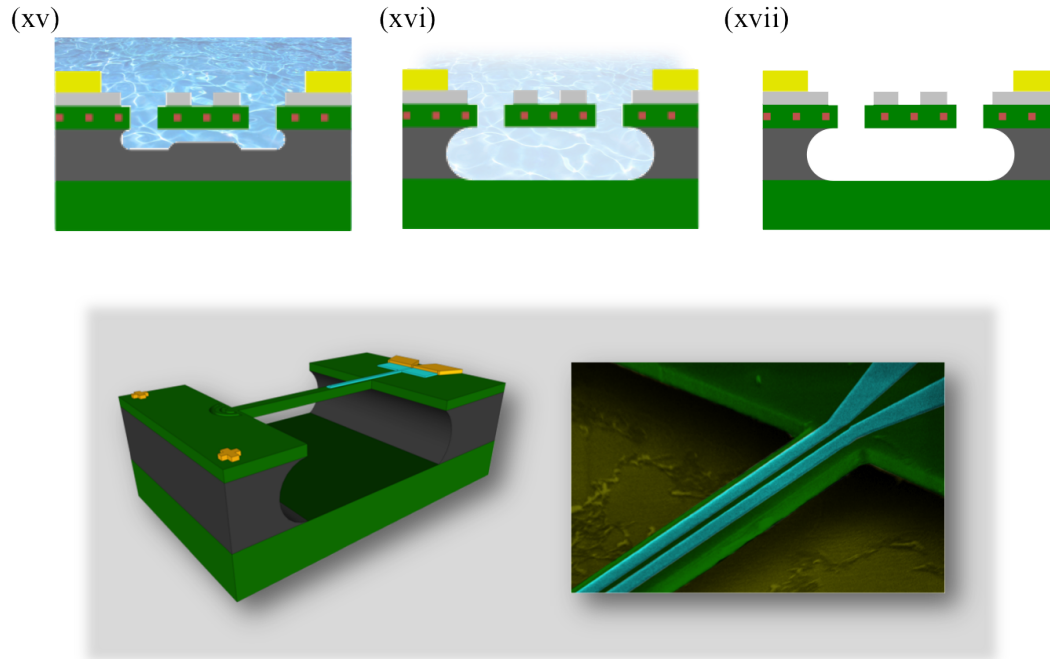
Fig. 3.14 Wet etching processes are used to release waveguides from the underlying substrate by removal of the AlGaAs sacrificial layer. Continued from Figure 3.13.
**(xv)** – Samples are submerged in concentrated aqueous hydrofluoric acid (HF, 48%). The eposed AlGaAs is dissolved isotropically by the HF.
**(xvi)** – Samples must be dried carefully to avoid structural collapse. CPD is used to replace the liquid $H_2O$ with $CO_2$ which can be held at its critical point by balancing temperature and pressure. The critical $CO_2$ exerts no surface tension on the waveguide structures whilst it is removed.
**(xvii)** – Completed devices are ready for characterisation. Although flexible the waveguides will only collapse if immersed in liquid and dried without CPD.
**Inset** – Drawing of the completed device (left) and a scanning electron microscope image of a working device (right) shown with false colour. The nanobeam waveguide is 400 nm wide.

## 3.2 Experimental Methods

This section aims to explain how some of the measurements presented in later Chapters were performed. Standard characterisation methods of SNSPDs and optical waveguides can be found in the literature although some of the apparatus described here are custom built to serve a specific purpose. Schematics of experimental apparatus are shown and methods described for measurement, calculation and interpretation of data. Cryostats were designed and assembled by Dr. Mike Tanner, Dr. Chandra Mouli Natarajan, Dr. Robert Heath and the author. Where measurements require automation the author used or adapted computer programmes written by Dr. Chandra Mouli Natarajan and Dr. Robert Heath.

### 3.2.1 Device screening and preparation

After fabrication devices are screened by measuring resistance at room temperature $R_{300K}$ with a 2-wire measurement on a digital multi-meter (DMM) operating in a low current (10 μA) range. A comparison is made between measured resistance and an estimate of device resistance based on nanowire geometry and the measured square resistance $R_{\square}$ of the superconducting film. Devices with too high or too low $R_{300K}$ are rejected. Excessive resistance suggests seriously constricted nanowires whereas too low $R_{300K}$ suggests a partially shorted circuit.

Samples are cleaved to size and the back side polished if required before mounting on a custom machined sample mount made from oxygen-free high thermal conductivity (OFHC) copper with 10 μm gold plating pictured in Figure 3.15. SubMiniature push-on (SMP) connections are fitted to the under side of the sample mount penetrating through to the top side. Custom cut printed circuit board (PCB) is soldered to the central conductor of the SMP connectors and provides a base to wire bond to the bond pads on chip. A coplanar waveguide transmission line is patterned on the chip for each device. A Kulicke & Soffa model 4123 wedge wire bonder is used to connect Al bond wires from the signal line to the PCB and from the ground plane to the sample mount. Samples are secured to the sample mount with a small amount of silver paint or nitrocellulose.

Devices can be aligned with high precision to the core of a single mode optical fibre and secured in a small package pictured in Figure 3.15 (c). Precision

(a)

(b)

Optical fibre

Steel shims

Zirconia ferrule

Au-plated
oxygen free
high thermal
conductivity
copper

(c)
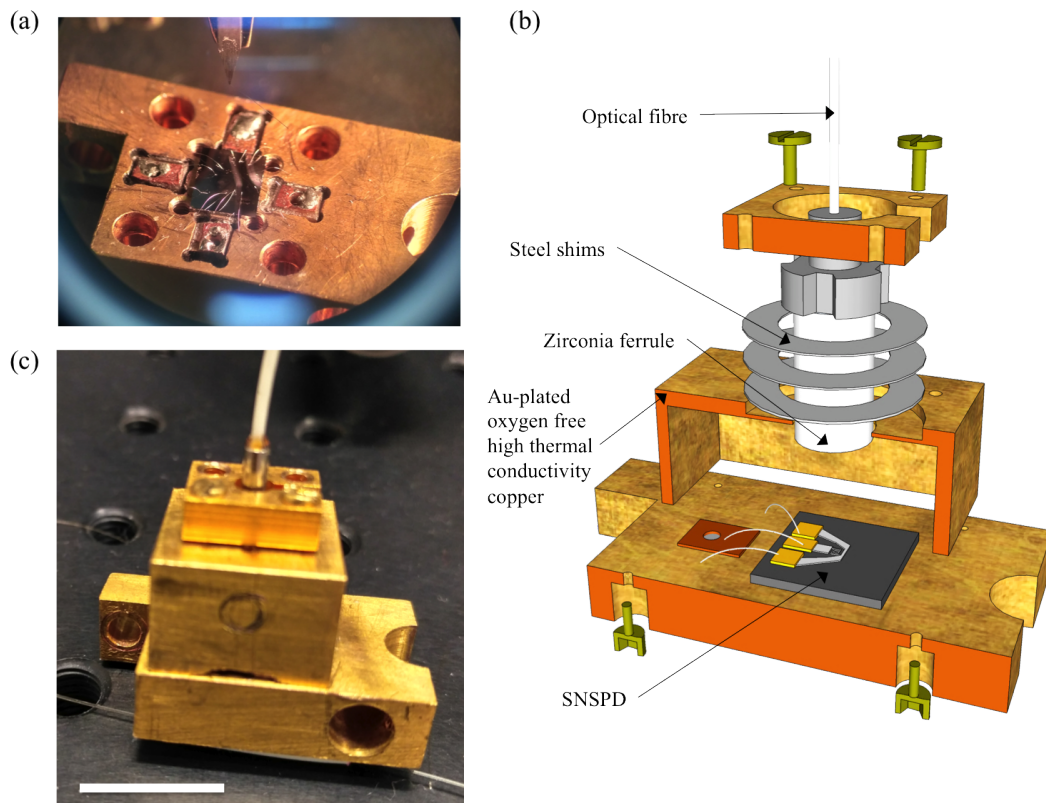
SNSPD

Fig. 3.15 **(a)** An SNSPD shown on a sample mount with Al wire bonds connecting coplanar waveguides on the surface of the chip with rectangular PCBs. **(b)** Exploded view of a packaged SNSPD aligned with optical fibre. Steel shims are used to set the fibre ferrule at fixed distance from the sample surface. The screws attaching the sample mount to the copper cap can be adjusted to allow precision of alignment of the optical fibre core over the detector's active area. A hole in the sample mount (not pictured) allows optical access to the polished back surface of the chip during alignment. **(c)** Photograph of a detector packaged for electrical and optical characterisation at low temperature. White scale bar is 1 cm.

alignment is performed by viewing the device through the substrate using a confocal microscope and infrared sensitive charge coupled device (CCD) pictured in Figure 3.16. Alignment of a single pixel detector is described in Chapter 5. All the elements of the detector package are shown in exploded view in Figure 3.15 (b). Thin steel shims are used to control the separation between the chip surface and the end of the zirconia ferrule. Optical coherence tomography is performed to verify the distance of separation (the process is described in reference 144). The effect of misalignment between an optical fibre and a square-shaped detector is described well in reference 289 with use of coupling simulations.
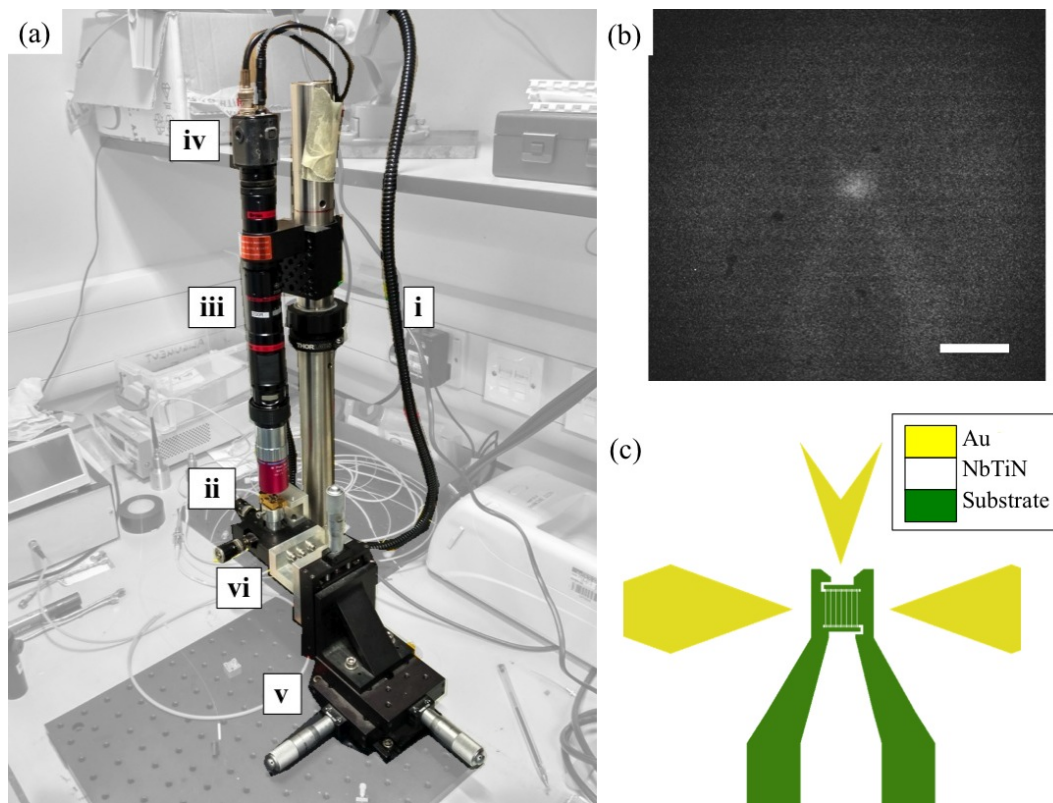
Fig. 3.16 Precision alignment of SNSPDs with single mode optical fibre is performed under a confocal microscope. **(a)** A source of visible and infrared illumination is fed into the microscope via a waveguide (i) and focussed onto the surface of a mounted sample (ii) through a Mitutoyo long working distance IR objective lens (iii). The microscope field of view is monitored by a phosphor coated near infrared (NIR) sensitive CCD camera (iv). The translation stage (v) allows movement of the whole device package to locate the device active area and the smaller positioners (vi) move the copper cap into a precise position holding the fibre core directly over the detector. **(b)** Image captured by an infrared sensitive CCD attached to a confocal microscope used to align SNSPDs with single mode optical fibre. The detector is viewed through the back of the substrate with laser light from the fibre core visible in the centre of the image. Scale bar is 20 μm. **(c)** The design layout of the same detector. The active area of the nanowire meander is the central green section.

## 3.2.2  Closed-cycle refrigeration

The majority of devices fabricated in this work will only operate below certain threshold temperatures as thermal noise will destroy the superconducting state and blur the energy levels of semiconductor QDs. Liquefied helium was the original cooling technology used by H. Kammerlingh Onnes to induce superconductivity and to this day probably the most direct way to cool a sample to 4.2 K is by submersion in a bath of liquid helium (LHe) [290, 64, 291]. This method is not ideal however since such cryogenic liquids require

skilled handling and are potentially dangerous. Over the past century more sophisticated cooling techniques have created closed-cycle and cryogen-free systems as well as reaching lower temperatures allowing new materials and phenomena to be studied. Moreover it is the development of more compact and easily operated cryocoolers that has brought low-temperature technologies to a broader audience, arguably more so than the development of high-temperature analogues. Two types of cryocoolers have been used at the University of Glasgow for low temperature electrical and optical characterisation of superconducting detectors and integrated optical waveguide circuits. The refrigerators are based around a GM cooler and a pulse tube (PT) cooler both of which contain high purity He within sealed transmission lines and use a separate compressor to pump expanded He away from the cold-head compressing and recycling it through the system in much the same way as a domestic refrigerator.

GM coolers contain a rotary valve motor at the base of the cold-head bolted to a room temperature mounting flange which receives much of the vibration of the motor. Around this flange a vacuum can is built to surround the cryostat. Separated from the mounting flange the first and second cooling stages extend some distance linearly with fixings to enable the anchoring of components. More vibrations are created by pistons inside the first and second stage cylinders as well a small amount of mechanical movement contributed by the expansion of compressed He gas. Overall GM coolers generally oscillate $\pm 20$ μm along the cold-head axis in sync with the rotary motor as well as a few microns perpendicularly.

PT coolers are usually more expensive for an equivalent amount of cooling power but contain no moving parts within the cold-head and therefore achieve much lower mechanical vibration during operation. The PT rotary motor is detached from the cold-head and can be mounted away from the cryostat to avoid transferring vibrations to the sample although expanding He gas inside the cold head creates a few microns of movement.

The cryostats built around GM and PT coolers are described in the following sections with detail of the optics and electronics included within the vacuum space as well as the measurements carried out by the author to characterise devices. Section 3.2.5 includes a schematic of an LHe bath cryostat and external optics used at the University of Sheffield to perform quantum optics experiments involving QD photo-luminescence (PL).

### 3.2.3 Low temperature electrical and optical measurements

A cryostat was assembled at the University of Glasgow utilising a Sumitomo RDK101D cold head with an air-cooled HC-4A Zephyr compressor shown in figures 3.17 and 3.18. The parts forming the body of the cryostat were custom designed and machined at the University of Glasgow including Au-plated radiation shielding, plates thermally anchored to the cooling stages for anchoring components and flange plates with electric and optical feed-throughs. From room temperature the cryostat reaches a base temperature of 2 K within a few hours and will operate continuously with 0.13 W of cooling power (at 4.2 K) for $\sim$10,000 hours until servicing is required to replace the absorbing medium or any worn mechanical parts. The cryostat and radiation shielding are housed within a steel vacuum can and the 34 litre volume is pumped down to a pressure $< 1 \times 10^{-4}$ mbar using a pump station consisting of an Adixen ATP80 turbo molecular pump backed by an ACP15 Roots roughing pump. Any gasses present inside the system while the compressor is operational will eventually condense onto the cold-head. This cryo-pumping effect reduces the pressure inside the vacuum can but can cause extra load on the system if there is a significant leak. Vacuum systems are leak-checked using He gas and a He leak detector system. A He flow rate $< 10^{-10}$ mbar.s$^{-1}$ is tolerable for system operation. An array of 16 bare optical fibres are fed through individually drilled holes in an Al flange plate. A recess in the plate allows liquid epoxy to be poured over the feed-through region after placement of the fibres creating a vacuum-tight seal when the epoxy dries. Hermetically sealed electrical connectors are fixed to more flange plates to enable RF signal transmission and thermometry read-out. SMA bulkheads which transmit frequencies up to 18 GHz with 50 $\Omega$ impedance are fitted into D-shaped drilled holes and tightened over rubber washers forming a vacuum seal. Thermometer cables are soldered to 12-pin Fischer connectors. Brass coaxial cable is used for biasing and readout of SNSPDs at the cold head. The thermal conductivity of this RF cabling causes the largest contribution to heat-load on the cold head under normal operation and places a limit on the number of devices that can be operated simultaneously. Sections of the white polymer sheath are removed from the coaxial cable to allow for thermal anchoring at the 40 K and 2 K stages and an excessive length ($\sim$1 m) of cable is contained within the cryostat and wound around the lower portion of the cold-head to maximise the thermal separation from the room temperature SMA connectors. Excessive lengths of optical fibres
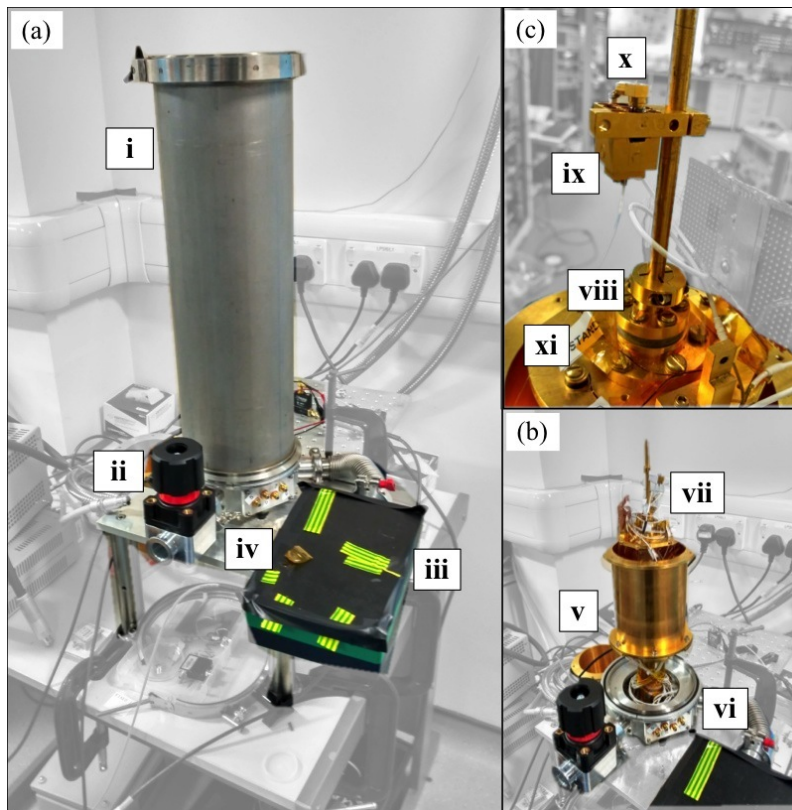
Fig. 3.17 A cryostat is built around a GM cryocooler with a base temperature of 2 K. **(a)** The operational cooler is housed within a vacuum can (i) with Klein flange (KF) connectors (ii) for pumping out the chamber. A fibre optic break-out box (iii) houses connections for several single mode optical fibres which run ot the cold-head. The main body and rotary motor of the cold-head lie underneath and bolted to the Al plate visible in the picture (iv). **(b)** Au plated radiation shields (v) are bolted to the 1st (40 K) cold-head stage. SubMiniature A (SMA) bulkheads allow connection of up to 8 RF electrical lines (vi). At the second (2 K) stage of the cold-head (vii) there is a post for mounting packaged devices. **(c)** A stand-off stage is created by separating the 2 K stage with a Pb puck (viii) to reduce thermal oscillations. A fibre coupled SNSPD (ix) is bolted to the stand-off stage with a spliced fibre connection. RF electrical connections are made by SMP connectors (x). Si diode thermometers (xi) are visible at the 2 K and stand-off stages.

are also wound around the base of the cold-head to allow for many devices to be repeatedly spliced into the refrigerator without the need to replace the fibre feed-through although silica optical fibres have extremely low thermal conductivity so can be included in large quantity within the cryostat without introducing significant heat load. The Zephyr compressor cycles at 0.7 Hz causing temperature oscillations with the same period. Although the magnitude of fluctuations is $< 0.5$ K this variation can cause significant fluctuations in device temperature of an SNSPD thermally anchored to the 2 K stage directly
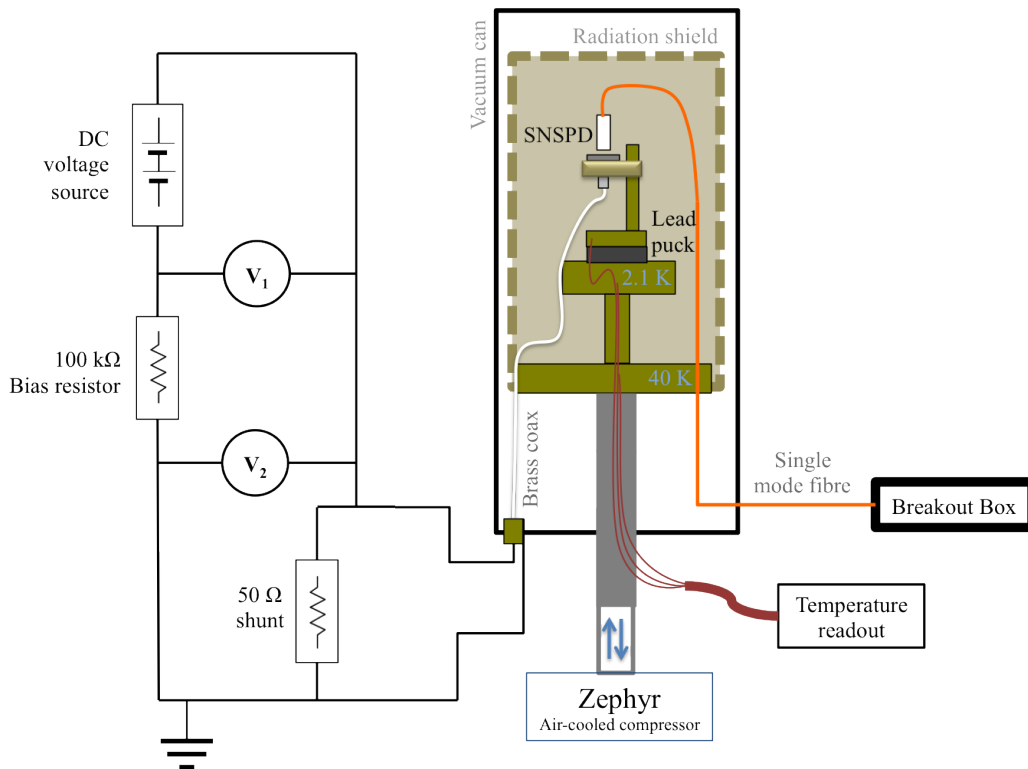
Fig. 3.18 Schematic of electrical and optical connections to the various cryostat stages. The electric circuit shown is used to perform DC measurements of superconducting critical current $I_C$ and critical temperature $T_C$ (with the 50 Ω shunt removed).

affecting the detector count rate which scales exponentially at bias currents close to the temperature dependent critical level $I_C(T)$. A stand-off stage is included above the cold-head separated from the 2 K stage by a Pb puck. The low thermal conductivity of Pb significantly dampens the thermal oscillations bringing the stand-off stage to 2.2 K ± 0.1 K. To further mitigate the effects of oscillating base temperature measurements of the detector can be synchronised to the compression frequency.

## Measuring the critical temperature

The critical temperature $T_C$ of superconducting films or devices can be measured whilst cooling down or warming up the cryocooler. The wire bonded sample is bolted to the stand-off stage and connected to brass coaxial cable with an SMP connector rated for signal transmission up to 40 GHz. Outside the refrigerator high frequency signal transmission lines utilise coaxial cables with SMA type connectors. For the DC and low frequency elements of the bias circuit coaxial components with bayonet Neill-Concelman (BNC) connectors are used (rated

up to 4 GHz with 50 $\Omega$ impedance). To perform a resistance measurement over the device a DC voltage source and bias resistor are connected as shown in Figure 3.18 with the 50 $\Omega$ shunt resistor removed. Housed within a Stanford Research Systems Simple Instrumentation Module (SIM-900) mainframe the bias voltage is provided by a SIM928 Isolated Voltage Source which uses multiple battery cells to deliver $\pm 20$ V with a resolution of 1 mV and noise as low as 10 $\mu V_{rms}$ (1 kHz bandwidth). The bias resistor is a 100 k$\Omega \pm 1\%$ carbon resistor housed in a conductive box with BNC connectors. A SIM970 Quad Digital Voltmeter is primarily used to read both voltages $V_1$ and $V_2$, corresponding to the bias voltage and the voltage drop across the device under test respectively. For devices with particularly low switching currents noise in the bias circuit can be reduced by swapping the SIM voltmeters for a Keithley 2000 multimeter and including in-line BNC low pass filters such as the Mini-circuits 50 $\Omega$ BLP-50+ which heavily attenuates noise from DC to 48 MHz. Temperatures are recorded from 3 Si diode thermometers situated at the 40 K, 2 K, and stand-off stages of the cold head. Thermometers are addressed by a 4-point resistance measurement with Constantan wires connected to a SIM922 Diode Temperature Monitor which compares measured resistance values to a stored 256 point calibration curve in order to give continuous temperature measurements with 4-digit accuracy between 1.4 K and 475 K. During warm-up or cool-down the thermometer temperatures and voltage across the device are measured simultaneously at short time intervals. During thermal cycling between base temperature and 15 K the system cools down faster than it heats up over the same range therefore the thermometer temperature is likely closer to equilibrium with the device during warm-up. Data are recorded during both cool-down and warm-up to give upper and lower bounds for $T_C$.

Several features of the measured resistance as a function of temperature are instructive about the properties of the superconductor. The position of the sharp transition to zero resistance is known as $T_C$. The distance between device operation temperature and the superconducting transition is proportional to the current a superconducting wire can support before switching to the resistive (or normal) state. The width of the transition gives some indication of the uniformity of the superconducting film since serious changes in material properties across a detector will manifest at a range of separate transitions for different sections of the nanowire. The presence of a residual resistance far below the transition is evidence of series resistance within the system. The measurement cabling should provide $\sim 1$ $\Omega$ of series resistance and additional

contact resistance between bond wires and the superconducting material can be introduced by surface oxides or residual e-beam resist. Additionally a section of nanowire that is significantly constricted may turn superconducting only at lower temperatures and currents than those provided.

**Measuring the critical current**

Voltage across a superconducting nanowire can be measured as a function of bias current $I_B$ using the arrangement shown in Figure 3.18. As well as measuring the voltage across the device voltage is measured before the bias resistor to provide an accurate indication of the applied bias. A shunt resistor can be included in parallel with the device under test which will effectively divert current when $R_{device} \gg R_{Bias}$ enabling fast cooling of the nanowire reducing the likelihood of hysteretic or latching effects. The measured current–voltage characteristic of a shunted nanowire will register a maximum resistance of $R_{max}^{-1} = R_{device}^{-1} + R_{shunt}^{-1}$. The presence of the shunt resistor causes the circuit to switch as soon as $R_{device} > R_{shunt}$ therefore it is not possible to measure the maximum possible value of $R_{device}$ in this configuration.

The onset of the normal resistive state is evidenced by a sharp change in the gradient of the current–voltage characteristic. The bias current associated with this transition is referred to as $I_C$ the critical current. In fact this switching current is likely lower than the intrinsic value of $J_C/A.l$ for the superconducting film, where the nanowire volume is the product of its cross sectional area $A$ and length $l$. For the practical purposes of operating the detector however this switching current is the more relevant figure.

**Measuring kinetic inductance**

Alternating current in superconducting wires is subject to kinetic inductance $L_K$ as a result of the inertia of superconducting charge carriers. The magnitude of $L_K$ is dependent on material properties as well as $l$ and $A$.

$$L_K = \frac{m^*}{2n_s e^2} \frac{l}{A} \tag{3.1}$$

where $n_s$ is the density of superconducting charge carriers, $2m^*$ the Cooper pair mass, and -e the electron charge. Meandered nanowire single photon detectors can use a film of $< 10$ nm thickness with $< 100$ nm width wires patterned up to a total length exceeding 0.5 mm. The extremely high aspect ratio of these

wires leads to correspondingly large $L_K$. As the bias current $I_B$ in a nanowire
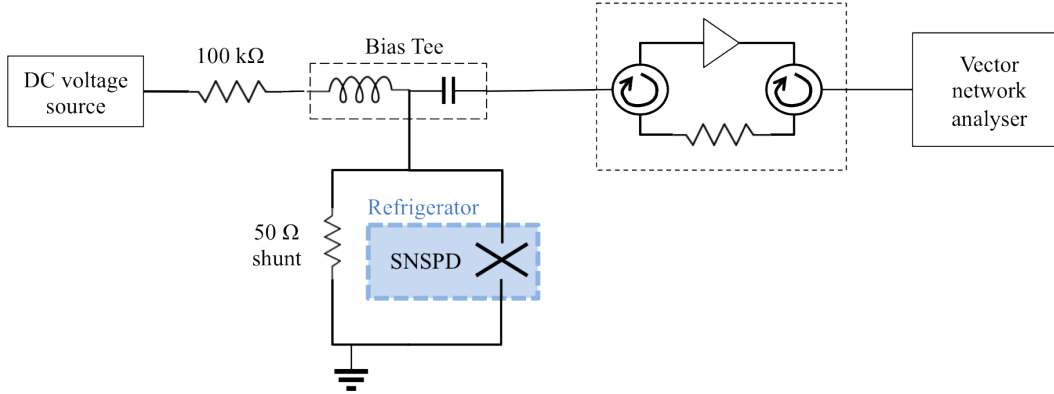


Fig. 3.19 Schematic of the electronic apparatus used to measure the kinetic inductance of an SNSPD. The vector network analyser (VNA) signal is attenuated to a level low enough to gently perturb rather than suppress the superconducting properties of the SNSPD. The return signal is amplified to a readable level for the VNA.

reaches critical level $I_C$ the maximum superconducting current density $J_C$ is exceeded and the material transitions to the normal resistive state. The change in $L_K$ as the nanowire approaches this transition is given by the relationship

$$\frac{L_K}{L_{K0}} = 1 + \frac{4}{9} C^2 \left(\frac{I_B}{I_C}\right)^2 \tag{3.2}$$

The free parameter $C$ is a value equal to 1 for a wire of perfectly uniform width along its entire length. The value of $C$ scales down towards 0 for non-uniform wires exhibiting progressively wider variations in $A$ along the wire length.

An AEA VIA Bravo 50 MHz VNA is connected as shown in Figure 3.19 on the AC arm of a Picosecond Pulse Labs 5575A-104 12 GHz bias tee. The circuitry shown in between the VNA and the SNSPD acts to attenuate the VNA output to a safe level for the superconducting nanowire. The returning signal is amplified to a suitable level for the VNA to register. The total inductance is measured as a function of bias current and data for $I_B \leq I_C$ are fitted to (3.2).

**Measuring detection efficiency**

System detection efficiency (SDE) is the ratio of counts registered by a detector $\mathcal{R}$ to the input photon flux $\Phi$. From Chapter 2:

$$SDE = \frac{\mathcal{R} - DCR}{\Phi} \tag{3.3}$$

where DCR is the dark count rate measured from the detector at a fixed bias current with $\Phi = 0$. The intrinsic properties of the superconducting nanowire at the operating temperature and extrinsic influence of unwanted light coupling into the system both contribute to the DCR. Light lost within the system due to imperfect transmission of components or poor coupling to the detector will influence SDE. By measuring the component losses it is possible to make adjustments to the SDE figure although quoting the system as a whole is more relevant from a user's perspective. Detection efficiency is measured using a
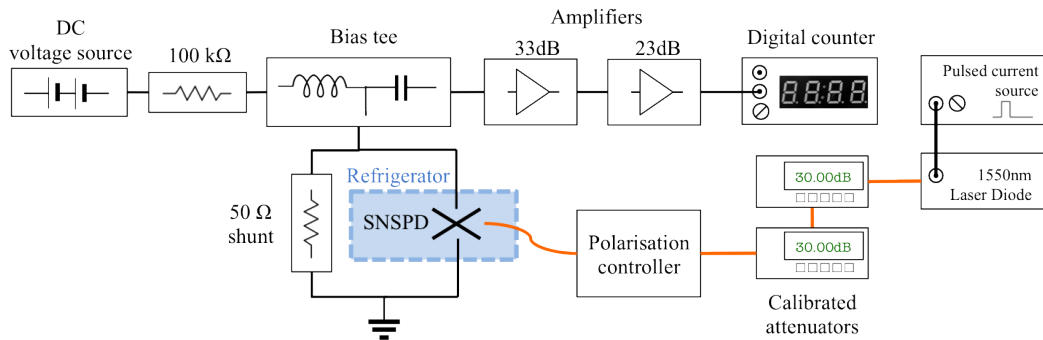


Fig. 3.20 Schematic of the apparatus used to measure SDE. An adjustable pulsed current source is used to gain switch a diode laser which emits light into single mode optical fibre (orange lines). Light is routed through programmable digital attenuators and a polarisation controller before being directed to a current biased SNSPD. Detector output pulses are split to the AC arm of a bias tee and amplified before being sent to a digital counter.

light source with a calibrated power meter and optical attenuators. Either pulsed or continuous wave laser light can be used to illuminate a detector with each requiring a slightly different calculation of efficiency $\eta$. Measurements of optical power by a standard power meter are most reliable for continuous wave (CW) illumination. Different power meter heads are used depending on laser wavelength. All light is routed through optical fibres and in-line components as far as the refrigerator. The core diameters of optical fibres are selected to ensure light of the target wavelength is confined in a single optical mode that propagates with low loss through the fibre core. Experiments conducted at $\lambda = 1550$ nm use SMF-28 standard telecoms single mode fibre with a core diameter of 9 μm. Experiments at shorter wavelengths utilise 780HP and SM980 fibres or similar, with a core diameter of 5 μm these fibres are single mode for light at 940 nm or 1064 nm.

A diode laser is used as a light source for efficiency measurements with an Agilent 81110A 165/330 MHz pulse pattern generator used to create CW output or short pulses with variable duration. For CW illumination the detector reset

time $\tau_2$ sets the fundamental time interval for measurements. Low photon flux can be defined as the mean photon number per time interval $\bar{n}$ being $\bar{n} \ll 1$. For a detector with $\tau_2 = 10$ ns and a 1550 nm diode laser with 1.5 mW CW output power the beam must be attenuated by 100 dB to reach the low photon number regime. Standard power meters are unable to measure such a wide dynamic range in order to calibrate the attenuation stage. Instead a pair of attenuators are used in series, each being calibrated within a range of at least 60 dB with the Thorlabs PM-300 power meter. As an example the detection efficiency measurement in Figure 6.5 is performed using two calibrated JDS uniphase HA9 attenuators and a Thorlabs diode laser LP940-SF30 ($\lambda = 940$ nm).

To perform an SDE measurement on an SNSPD the detector is current biased and the count rate recorded as a function of input photon flux over a range from $\bar{n} = 0$ (a blocked beam) to $\bar{n} \gg 1$. This measurement can be repeated at a number of bias levels to show the dependence of SDE on bias current. For $\bar{n} \simeq 0$ the count rate will remain at a finite level, this is the bias-dependant DCR. The highest count rate for the detector will also saturate at some point. For CW illumination the maximum possible count rate is largely dictated by the reset time of the detector whereas is the case of pulsed illumination the count rate of an SNSPD will saturate at the pulse repetition rate of the laser given that each pulse contains a high enough number of photons to account for imperfect detection efficiency (the observed count rate will also include any dark counts occurring in between laser pulses).

Detector counts are registered via the AC arm of the bias tee with output pulses routed through an amplifier chain which can be monitored on an oscilloscope to check pulse shape, amplitude, and duration. The amplifier chain consists of two RF Bay low noise amplifiers. The LNA–1000 has a $10 - 1000$ MHz frequency range, $30 - 33$ dB gain, and $1.8 - 2.3$ dB noise and the LNA–580 has a $10 - 580$ MHz frequency range, $21.5 - 23$ dB gain, and 0.7 dB noise. With the detector pulse visibility and amplitude confirmed the signal is routed to an Agilent 53131A 225 MHz universal digital counter. The counter is set to register pulses over a specified threshold voltage and programmed to record detector counts in intervals of 0.7 seconds to synchronise with the PT cooling cycle. The maximum count rate is limited by a 500 ps minimum interval and the need for incoming pulses to exceed the trigger threshold for at least 4.4 ns in order to be registered. The trigger level accuracy is $\pm 15$ mV $+ 1\%$ of the threshold value.

**Polarisation control**

Polarisation control is implemented by adding fixed amounts of strain and torsion to loops of optical fibre either with manually operated "bat ears" or a motorised digitally addressed polarisation controller. Using the detector count rate as feedback it is possible to set the rotations that lead to a maximum and a minimum count rate. For a standard nanowire meander detector these maximum and minimum count rates correspond to parallel and perpendicular orientation of the electric field vector with the nanowire direction respectively.

The Agilent 11896A electronic polarisation controller can be programmed to perform $10^4$ fixed polarisation transformations with good repeatability. Each programmed state represents a point of the surface of a Poincaré sphere although the degeneracy of addressed states is unknown as is the exact mapping of addresses in the controller to absolute points on the Poincaré sphere. Without polarisation control it is impractical to estimate the exact polarisation state at the detector because temperature variations and other haphazard changes in the environment will influence the polarisation in a standard optical fibre causing unknown variations between experiments. To probe the polarisation sensitivity of an SNSPD during efficiency measurements 256 states of the polarisation controller are selected and an efficiency measurement performed for each. The repeatability of polarisation states during these measurements is explored in reference 133.

**Measuring timing jitter**

Figure 3.21 shows the apparatus used to probe detector timing jitter. A mode-locked 55 mW 980 nm laser drives a Kphotonics CNT-1550-TK erbium-doped fibre laser ($\lambda = 1560$ nm, spectral bandwidth 8 nm) at a 50 MHz repetition rate producing narrow optical pulses which are split between an SNSPD under test and an InGaAs fast photodiode (Thorlabs DET10C/M, 700-1800 nm, 10 ns rise time). A PicoQuant HydraHarp 400 is used for time-correlated single photon counting (TCSPC) recording SNSPD pulse arrival time in 1 ps time-bins. An inverting amplifier is included in the SNSPD signal line and a passive inverter used for the fast photodiode signal to provide the negative polarity pulses necessary to trigger the HydraHarp. Device dark counts occur at random time intervals and create a background noise floor. Plotting TCSPC events in a histogram allows visualisation of the detector response function which is usually Gaussian for an SNSPD. Conventional jitter measurements will collect TCSPC

events until the peak height of the response function is at least an order of magnitude above the noise floor.



Fig. 3.21 Schematic of apparatus for measuring SNSPD timing jitter by TCSPC. Narrow laser pulses are generated by an erbium doped fibre laser at 50 MHz and routed through single mode fibre (orange lines) to a 50:50 beam-splitter. One output of the beam-splitter is connected to an InGaAs photodiode which triggers one input of the TCSPC electronics starting a clock. The other beam-splitter output is attenuated and routed to the SNSPD. Detector output pulses are amplified and used to trigger the other TCSPC channel, stopping the clock.

## 3.2.4   Nano-optical measurements

### Reflection mapping

A second cryostat system installed at the University of Glasgow is used for nano-optical testing. Adapted from a miniature confocal microscope system for focussing light from semiconductor QDs [292] a few adaptations create the capability for sub-micron scale optical characterisation of SNSPDs [293] and integrated waveguide circuits. A Cryomech PT403 pulse tube cooler is connected to a water-cooled CP830 compressor providing 0.25 W cooling power at 4.2 K and achieving a base temperature of 3.7 K. Within the cryostat a miniature confocal microscope is mounted on a stack of Attocube piezoelectric motors. Thermometers, control wiring for the piezoelectric motors, and single mode optical fibres are attached similarly to the cryostat described above based around a GM cooler. Extra black-body radiation shielding is provided by mylar foil surrounding the Au plated steel radiation shield. The PT cools to base temperature over several hours and can run continuously up to the recommended service interval of 12,000 hours. The confocal microscope consists of a lens tube with a collimating lens (Geltech 352280-C, NA = 0.15) and an

Fig. 3.22 A cryostat built around a pulse-tube crycooler containing a miniature confocal microscope mounted at the 3.7 K stage and driven by piezoelectric motors. **Red box** Optical components are connected to perform reflection mapping of a sample surface. Bright broadband light is routed to the microscope through single mode optical fibre (orange lines). Reflected light is collected by the microscope optics and focussed back through the fibre. An optical circulator separates the reflected signal and routes it to an InGaAs photodiode to measure its intensity. Piezoelectric motors adjust the height and focus of the microscope and move it laterally to build up scanned images. **Green boxes** Attaching a diode laser to the optical input with variable attenuators and a polarisation controller in between allows SNSPDs to be probed with single photons. A bias tee is used to separate the DC current bias from the fast output pulses from the detector. Pulses are amplified and sent to a digital counter.

objective lens (Geltech 352330-C, NA = 0.68) both of which have anti-reflection coatings which are designed for 1050 nm to 1620 nm wavelengths. Two sets of microscope lenses can be interchanged for use in the system, one for wavelengths close to 1550 nm and one for 950 nm (with a suitable anti-reflection coating). The microscope focus is adjusted by an Attocube ANPz101 piezoelectric motor and two ANPx101 motors provide $x$ and $y$ translation. Each of these motors

travels close to 5 mm. An Attocube ANSxy100 is included in the motor stack allowing for fast scans in the $xy$ plane with sub-nanometre step size. This scanning motor operates by applying a fixed DC voltage (0 – 120 V at 300 K) which covers a 40 μm × 40 μm area at room temperature with non-linear step size. At low temperature the maximum scan area is closer to 35 μm × 35 μm with uniform steps (see 144 for further detail). The ANP- motors use a ratcheting mechanism to drive the motors with a saw-tooth voltage being applied causing the titanium body to be pushed step-wise along a fixed railing. Fixings underneath the confocal microscope are adapted to fit the same sample mounts as shown in Figure 3.15.

With bright laser light the miniature microscope can be used to image a sample surface with the equipment configuration pictured in Figure 3.22 (red box). Fibre circulators for wavelength ranges 1525 nm $< \lambda < 1610$ nm and 1054 nm $< \lambda < 1074$ nm are used in conjunction with the corresponding light sources. Light reflected from the sample surface back through the optics is routed through the circulator towards an InGaAs photodiode which measures the reflected power. Scanning the microscope over the device area using the piezoelectric motors enables reflection data to be systematically collected for lines or grids of spatial coordinates. A grid of reflection data creates a map of the sample surface as seen in Figure 3.23. Performing a high resolution line scan over a sharp edge with high contrast enables the spot size to be calculated. The measured reflection as a function of distance will be a convolution of the Gaussian beam profile with the step-function of the high contrast edge. Assuming that the beam is a fundamental Gaussian shape and well focussed de-convolving the measured data returns a figure for the beam waist width. The optics are capable of focusing a spot with FWHM of 1.3 μm at $\lambda = 1550$ nm although vibrations make the practical resolution limit closer to 2 μm. The beam focus is found by varying the separation of the microscope from the sample with the $z$ axis motor and monitoring the intensity of reflected power when positioned over a flat and highly reflective surface. Away from focus light reflected from the surface will diverge beyond the acceptance angle of the objective lens and therefore the highest reflected power is observed when the spot is in optimal focus.

**Spatial mapping of single photon detector counts**

Replacing the bright light source and circulator with a laser and attenuators allows the miniature microscope to be used for probing spatial variations in the
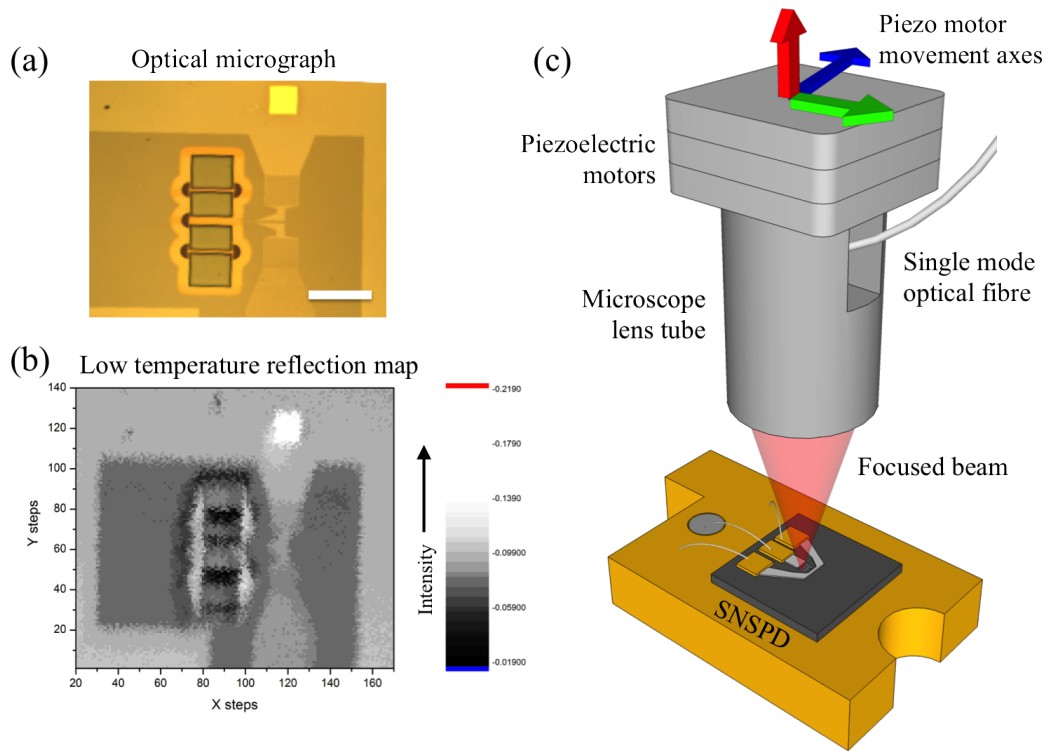
Fig. 3.23 Sub-micron sized features can be imaged at low temperature under a miniature confocal microscope. **(a)** A sample containing waveguides and a detector as seen under a optical microscope, scale bar 15 μm. **(b)** The same device cooled to 3.7 K. The miniature microscope is raster scanned over the device area and reflected light ($\lambda = 1050$ nm) is collected to build up an image. **(c)** The microscope consists of a lens tube containing high numerical aperture (NA) collimating and objective lenses bolted to a stack of piezoelectric positioning motors. Single mode fibre delivers laser light to the microscope which focuses an optical spot of $\sim 2$ μm onto the sample surface. The peizo motors focus and scan the spot over the area of interest.

single-photon response of a detector or waveguide circuit as shown in Figure 3.22 (green boxes). By recording the detector count rate at each position as the microscope is scanned over an area of interest it is possible to build up a count map as shown in Figure 3.24. Wavelength dependent measurements are performed with a similar set up by replacing the diode laser with a tunable wavelength source. Three tunable lasers are routed to an optical switch allowing for a wide range of wavelengths to be covered in a single experiment. The three laser sources are a Yenista OSICS ECL–1400 (1340 nm $< \lambda <$ 1440 nm), an Agilent HP 8168F (1440 nm $< \lambda <$ 1590 nm), and a Yenista OSICS T100–1620 (1560 nm $< \lambda <$ 1680 nm) all of which are routed through a Yenista OSICS SWT optical switch. Further details on tuned wavelength measurements with this set up can be found in Chapter 5 and references 144 and 294.

(a)

(b)
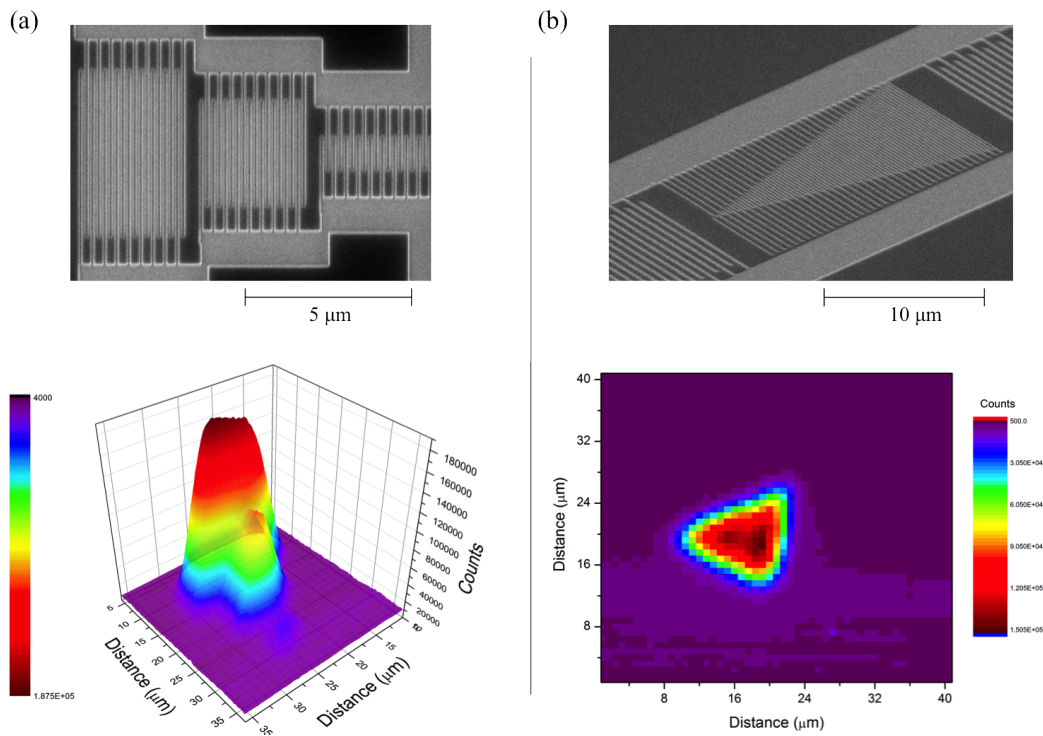


Fig. 3.24 The spatial variation in single photon response is mapped for irregularly shaped SNSPDs. SEM images show the active areas of stepped rectangular **(a)** and triangular **(b)** shaped detectors. The apparatus in Figure 3.22 were used to probe these devices with single photons at $\lambda = 1550$ nm. Count maps show a high count rate (red) when the nanowire is illuminated and the background count level (purple) when the microscope spot is focussed away from the device.

Given the 2 μm spot size at $\lambda = 1550$ nm and the nanometre step size of the Attocube scanning motors the system can resolve spatial variations in count-rate over distances much smaller than the area of a typical meandered SNSPD. When the pulse-tube cooler is operating however there are mechanical vibrations which cause oscillation of the microscope relative to the sample's position. Figure 3.25 (g) illustrates how an oscillating optical spot will create a highly distorted image making vibration damping essential for the collection of meaningful data. The entire refrigerator can be winched off the ground and re-seated at different angles onto rubber feet and vibration absorbing foam to minimise lateral oscillations of the microscope. A number of mechanical isolation features are also incorporated into the refrigerator design. The rotary motor is separated from the PT403 cold-head and mounted at some distance. The cold-head itself is separated from the mounting flange by sprung bellows and flexible copper braids are used to separate the 1st and 2nd cold stages

from the microscope mounting plate providing mechanical isolation with good thermal conductivity.
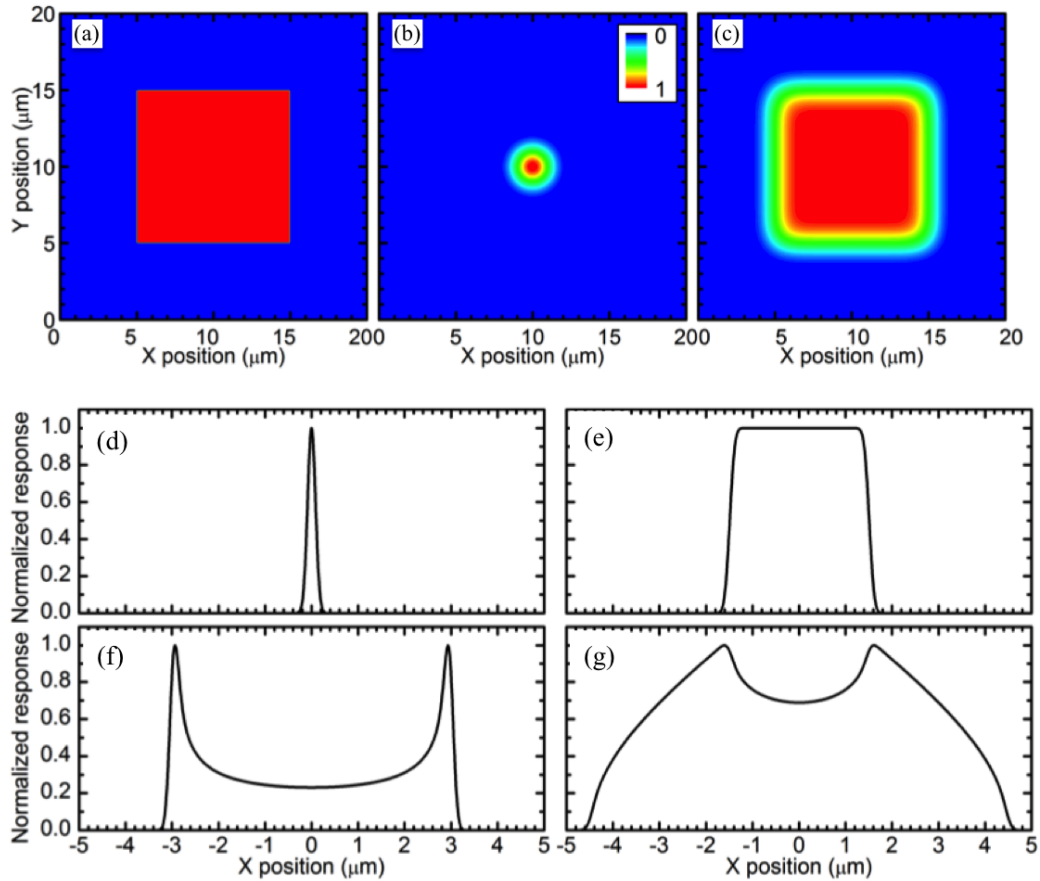


Fig. 3.25 Figure adapted from the PhD thesis of Dr. Robert Heath [144]. The miniature microscope builds up images by scanning an optical spot over features on the substrate. **(a)** represents a feature with clear outline to be imaged by the microscope spot **(b)** which has a Gaussian intensity profile. **(c)** The scanned image is equivalent to a convolution of the feature shape and the spot profile. **(d, e)** Cut-throughs are shown of the beam profile and convoluted image respectively. **(f)** The effective beam profile is now shown for the same microscope spot undergoing lateral oscillations with 3 μm amplitude. Convolving the oscillating beam with the same square feature would return the image in **(g)** which is clearly distorted to a great extent.

### 3.2.5    Waveguide and quantum dot optical characterisation

**Simulating waveguides with integrated detectors**

In the context of optical waveguides an optical mode is a certain oscillating configuration of the electric (and magnetic) field that is supported within a specified volume. Optical modes are wavelength dependent and propagate at speed $v = c/n_{\text{eff}}$. For waveguides comparable in size to the optical wavelength the field distribution associated with an optical mode is continuous over material boundaries and therefore an effective index $n_{\text{eff}}$ is used rather than the refractive index of the bulk material. The archetypal model for a waveguide uses ray optics

(a)

(b)

cross-section 1     cross-section 2     cross-section 3
"Bare waveguide"    "Headstock"         "Nanowire"

(c)

$n_{\text{eff}} = 2.800...$          $n_{\text{eff}} = 2.755...$          $n_{\text{eff}} = 2.777...$

$\kappa_{\text{eff}} = -1.06 \times 10^{-6}$      $\kappa_{\text{eff}} = 0.0499...$      $\kappa_{\text{eff}} = 0.0395...$
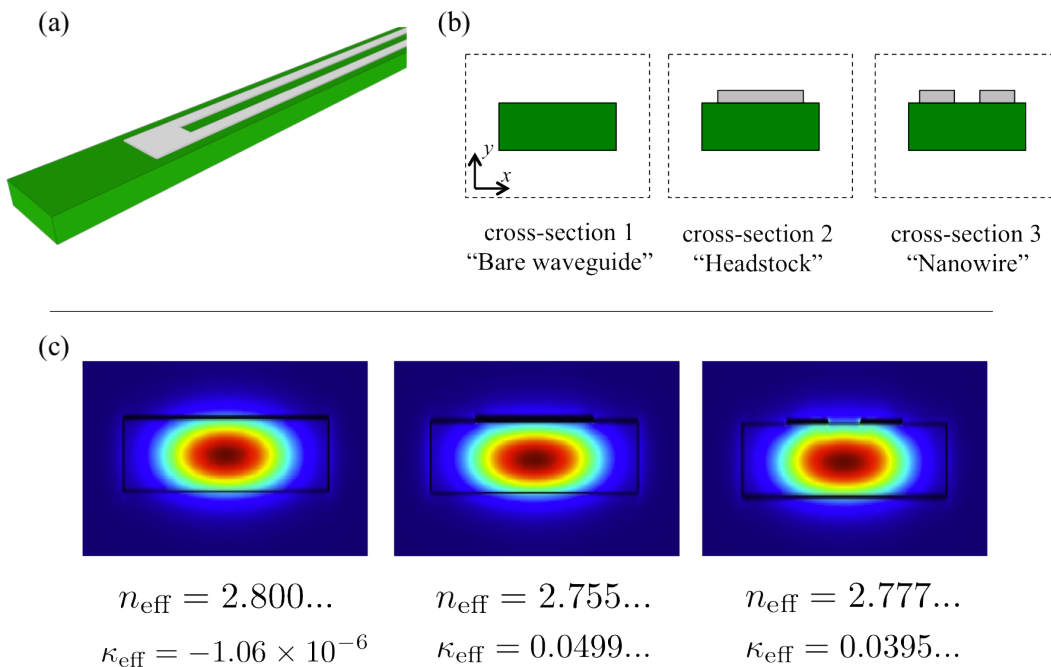
Fig. 3.26 Waveguide integrated detectors are modelled to simulate the absorption of waveguide photons into an NbTiN nanowire. **(a)** A hairpin shaped nanowire is patterned in 7 nm thick NbTiN along the top of an SNB waveguide. **(b)** Three different cross sections represent the material profile at all points along the modelled section of SNB waveguide and integrated detector. **(c)** Plots of the simulated electric field distribution in a cross sections of a GaAs SNB waveguide 140 nm high and 400 nm wide with an NbTiN nanowire on top. The Mode Solutions package within the Lumerical TCAD software[295] is used to calculate the effective index of the waveguide mode in each cross section and the calculated mode parameters $n_{\text{eff}}, \kappa_{\text{eff}}$ can be used to calculate reflections and absorption respectively.

to describe a glass optical fibre in which total internal reflection causes light to propagate uninterrupted inside a low index core by reflecting below some

critical angle $\theta_c$ from the interface with the higher index cladding. Losses from this perfect fibre model only occur through absorption, the presence of defects, or if the fibre is curved enough that certain ray vectors exceed $\theta_c$ and escape into the cladding. This waveguiding principle is similar for planar waveguide circuits although at dimensions approaching the optical wavelength Gaussian beam propagation provides a better model for designing and predicting waveguide behaviour. Calculating the electric field distribution in anything other than a circularly symmetric fibre requires numerical rather than analytical solution and there are a number of software packages designed to solve such problems by finite element analysis and other computational methods.

For the Gaussian approach we must consider light as a three dimensional time-varying electric field $\mathcal{E}(x, y, z, t)$. With the propagation axis $z$ being shared with the centre of the fibre core the case of a straight fibre of uniform diameter the expression simplifies to $\mathcal{E}(x, y)e^{-ikz}e^{i\omega t}$ for propagation in the positive $z$ direction with angular frequency $\omega$ and wavenumber $k = \omega(\mu_r\epsilon_r)^{0.5}/c$. The permittivity and permeability of the waveguide material are denoted by $\mu_r$ and $\epsilon_r$ respectively. Now any physical solution to $\mathcal{E}(x, y)$ will represent the electric field distribution of one optical mode. Without any changes in the waveguide geometry $\mathcal{E}(x, y)$ will remain constant as the beam propagates. Figure 3.26 shows how the absorption into waveguide integrated SNSPDs is calculated by simulating just 3 cross-sections of the system. The simulated values of $n_{\text{eff}}$ and $\kappa_{\text{eff}}$ are used to perform simple calculations of absorption and reflection of a beam propagating in discrete time steps. Changes in the waveguide geometry equate to changes in $n_{\text{eff}}$ and by Fresnel's equations some fraction $\boldsymbol{R}$ of the light is reflected with the rest coupling into the new optical mode $\boldsymbol{T} = 1 - \boldsymbol{R}$ (assuming no absorption into the waveguiding media). Using this fast method a vast range of waveguide and nanowire parameters can be explored such as detector dimensions, misalignment, and nanowire material. Full 3-dimensional finite difference time domain simulations of waveguide integrated detectors can be performed but require $\sim 1$ day of computation time (in Lumerical's FDTD software package[295]) for a single iteration. These simulations are used to confirm the accuracy of results obtained by the simpler method. The simple propagation model does not account for bends in the waveguide which exhibit losses inversely proportional to the bend radius in empirical observations.

**Photoluminescence measurements**

Figure 3.27 shows a LHe bath cryostat installed at the University of Sheffield and used for the testing of III-V semiconductor QD samples. Housed in a narrow vacuum tube devices are placed far down inside the helium dewar with a window at the top providing optical access for a host of photonic experiments. With this arrangement pump light can be focussed on a QD whilst emitted photons are collected from a separate part of the chip having travelled there through on-chip optical waveguides and been scattered upwards by a grating coupler as shown in Figure 3.28.

Absorption measurements on waveguide integrated SNSPDs were performed by John O'Hara at the University of Sheffield using similar optics to Figure 3.28 with the sample placed in a He flow cryostat. PL was stimulated by focussing $\lambda = 632$ nm laser light onto a region of a sample with embedded QDs. Using shorter wavelength pump light than the QD band gap ensures that a broad range of excitonic transitions in a number of nearby QDs are stimulated. PLs from the wetting layer and QDs is emitted in all directions but optical waveguide features patterned into the GaAs surface layer will guide light preferentially in the patterned channels. Grating couplers scatter light upwards out of the waveguide mode towards a large objective lens which focuses this light into collection optics for filtering and analysis. A long pass filter is first applied to remove light at the pump wavelength and the remaining PL is directed to a spectrometer. Within the spectrometer a diffraction grating spreads the PL spatially as a function of wavelength (similar to white light dispersing through a prism). A Si-SPAD is positioned to collect a narrow section of the dispersed PL spectrum effectively selecting and measuring the intensity of a thin band of wavelengths $\triangle\lambda$. A high resolution spectrometer will be able to resolve $\triangle\lambda \leq 1$ nm which is easily enough to reject PL signal from the wetting layer or even unwanted exciton transitions within a single QD or nearby QDs. Having selected the PL of a single excitonic line the stream of single photons can be fed through a 50:50 beam-splitter to perform a Hanbury-Brown Twiss measurement of the second order correlation function $g^{(2)}(\tau)$ of the source as shown in Figure 3.29. Sensitive single photon detectors placed at the beam-splitter outputs record a so-called coincidence count when both detectors fire simultaneously. A variable delay in the path to one detector allows the coincidence count rate to be measured as a function of $\tau$ the difference between the two optical path lengths (in units of time). In practice the output signals of the single photon detectors can be routed to the 'start' and 'stop' triggers of a TCSPC module
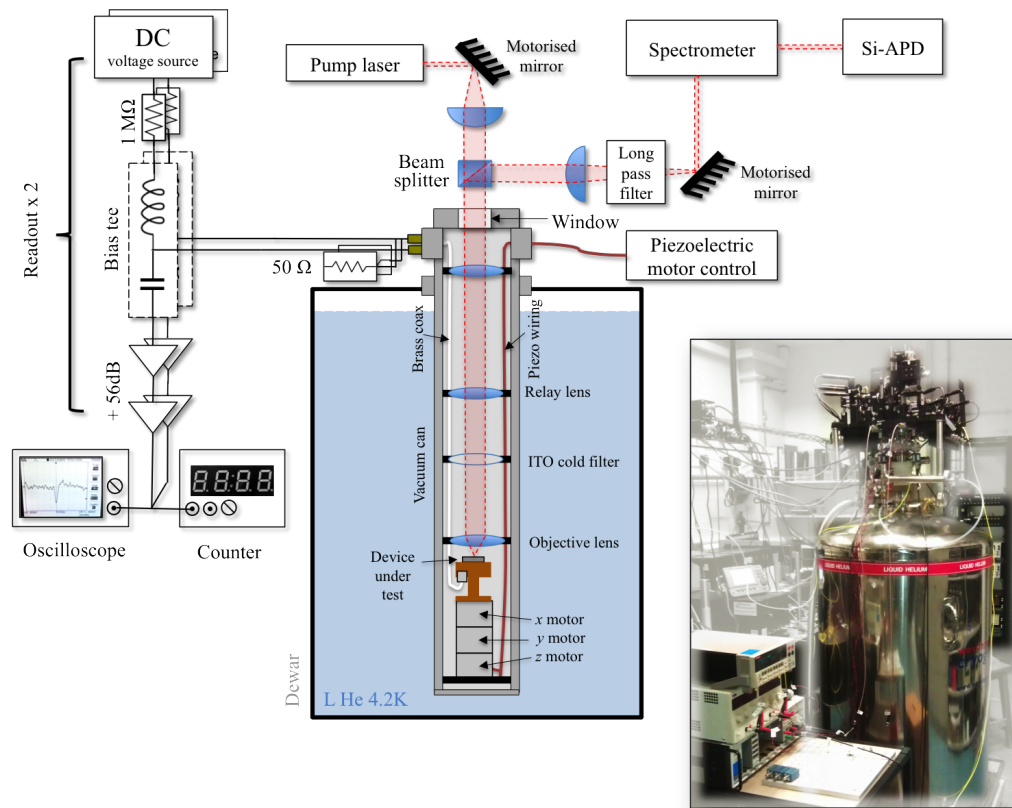
Fig. 3.27 A cryostat and optics assembled at the University of Sheffield for measuring QD PL and testing integrated waveguide circuits. Samples are cooled inside a vacuum can with a small amount of He exchange gas that is submerged in an LHe dewar. At the base of the vacuum can samples are mounted on top of 3 piezoelectric motors which allow different areas of the sample to be moved into focus. Optics address the sample by focussing light through free space down the axis of the vacuum can through a number of lenses and one vacuum sealed window. The room temperature optics include lasers for pumping QDs as well as filters and spectrometers for analysing PL. A sample mount is custom built with electrical connections for brass coaxial cables to handle biasing the detectors and transmitting voltage pulses to the room temperature amplification and digital counting electronics. **Inset** A photograph of the apparatus. Most of the free-space optics are mounted on a bread board on top of the large LHe dewar.

which will record the time difference between successive counts. This way $g^{(2)}(\tau)$ can be plotted with $\tau$ being varied in steps equal to the TCSPC time-bins.

(a)



(b)

(c)
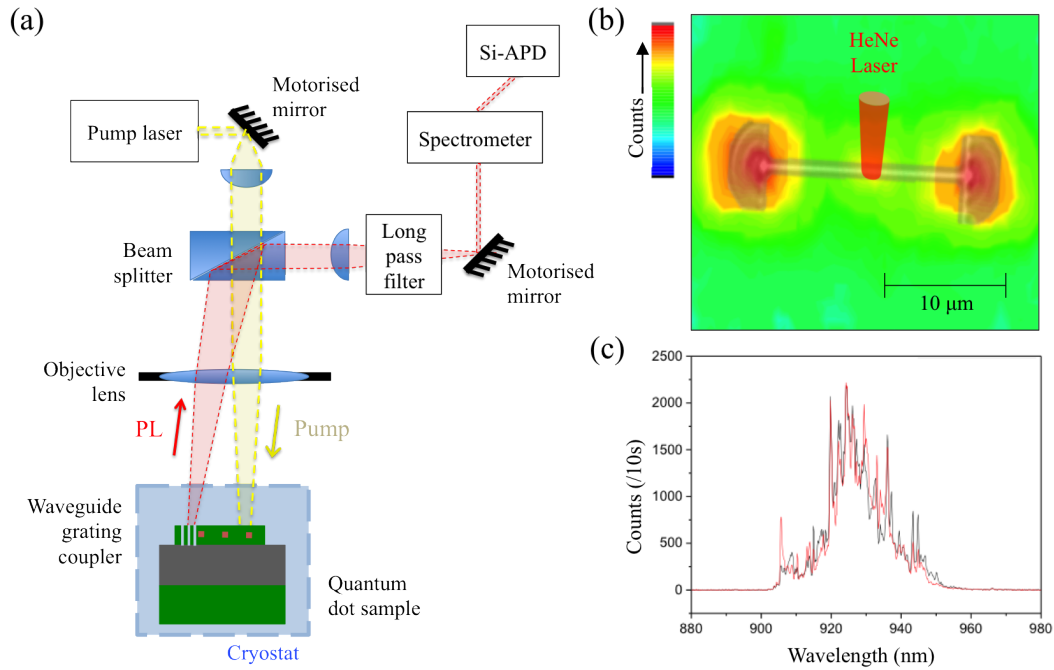
Fig. 3.28 Schematic of the optics used for photoluminescence measurements on samples mounted in a LHe or a He flow cryostat. **(a)** Independently adjustable optics allow for two optical spots to be focussed independently onto a sample surface through one objective lens. Pump light at $\lambda = 632$ nm is focussed on a fixed position at the centre of an SNB waveguide (outline overlaid on **(b)**). Motorised mirrors are used to scan the second optical spot over the whole are of the SNB waveguide and grating couplers. Collected light is long-pass filtered to remove the pump wavelength. The intensity of PL signal is recorded as a function of collection position with the strongest signal cleary visible above the grating couplers. **(c)** Spectral distribution of the collected PL. A broad range of wavelengths are generated by the InAs wetting layer and QDs embedded in the waveguide. The red and black line graphs show the spectra of PL collected from the left and right couplers respectively. Data collected by John O'Hara at the University of Sheffield.
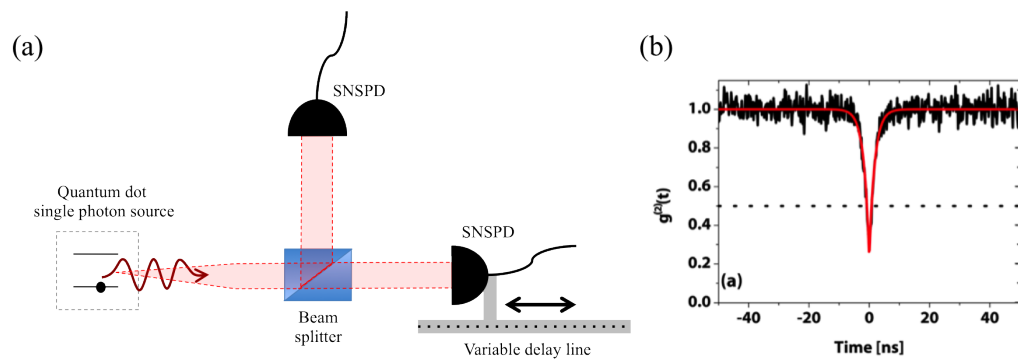
Fig. 3.29 **(a)** Schematic for a Hanbury-Brown Twiss measurement of the second order correlation function $g^{(2)}(\tau)$ of photons from an single photon source (SPS) under CW excitation. A variable delay line on one output of the beam-splitter introduces a time difference $\tau$ between the two paths. For an anti-bunched stream of photons from a quantum emitter the coincidence count rate will approach 0 as $\tau$ approaces 0. **(b)** An example of the measured $g^{(2)}(\tau)$ for an InAs/GaAs quantum dot sample. The recorded $g^{(2)}(0) = 0.23 \pm 0.02$ is typical of a QD single photon source. Adapted from reference 58.

# Chapter 4

# Superconducting detectors integrated with GaAs waveguide circuits

*This Chapter highlights the results of attempts to combine superconducting nanowire single photon detectors (SNSPDs) with GaAs waveguides. Single mode waveguides are a vital component needed to enable the observation of quantum effects with indistinguishable photons [59] in waveguide circuits. Existing demonstrations of SNSPDs integrated with GaAs/AlGaAs waveguides have used larger multi-mode waveguides [255, 234, 256, 257], perhaps due to the increase in fabrication challenges involved with pushing to single mode dimensions. A fabrication process was developed by the author at the University of Glasgow to integrate NbTiN SNSPDs with single mode suspended nanobeam (SNB) waveguides which is detailed at the end of Section 3.1. The waveguide design is discussed and characterisation of NbTiN thin films is presented. Fabricated detectors are characterised individually with low temperature electrical and optical techniques detailed in Section 3.2.4. Subsequently the same techniques are used to probe waveguide integrated detectors to measure their performance and to verify the detection of light from within the waveguide. This chapter contains data measured by the author at the University of Glasgow and measurements of waveguide photo-luminescence (PL) transmission performed by John O'Hara at the University of Sheffield.*

# 4.1 Gallium arsenide quantum photonic integrated circuits

Gallium arsenide and the III-V family of semiconductors provide a promising platform for the realisation of quantum photonic integrated circuits (QPICs). Many of the waveguide circuit elements required for implementation of linear optical quantum computing (LOQC) have been demonstrated in GaAs[200] but the current state of the art involves only small numbers of combined elements [210]. To achieve stable and scalable quantum information processors these elements must be integrated monolithically and be shown to work reliably en masse [48].

The University of Sheffield has a long history of quantum photonics research and houses the Engineering and Physical Sciences Research Council (EPSRC) National Centre for III-V Technologies [296] with molecular beam epitaxy (MBE) facilities for growth of GaAs substrates with embedded quantum dot (QD) single photon sources. As part of an EPSRC Programme Grant [297] QPICs are being developed to include waveguide components with integrated SNSPDs and QD single photon emitters. Thin superconducting films are grown atop GaAs substrates with embedded InAs QDs in the USA by Star Cryoelectronics Inc [298]. Initially tasked with delivering films of 6 nm to 10 nm thickness and a transition temperature of $T_C = 10$ K a number of films were grown at 450°C achieving the specified thicknesses and exhibiting superconducting transitions of 5 K $< T_C <$ 11 K (see Figure 4.1 and Table 4.1).

| Film thickness | $T_C$ (cool down) | $T_C$ (warm up) |
|:---:|:---:|:---:|
| $6 - 8$ nm* | 6.6 K | - |
| $6 - 8$ nm* | 8.8 K | 10.6 K |
| $8 - 10$ nm* | 9.9 K | 10.6 K |
| 6 nm | 4.8 K | 4.9 K |

Table 4.1 Measured $T_C$ of NbTiN samples grown by Star Cryoelectronics Inc. *Thickness of the first grown samples was estimated by deposition time. Later samples received precise thickness measurements by Rutherford backscattering spectroscopy performed by Star Cryoelectronics Inc.

(a)

(b)
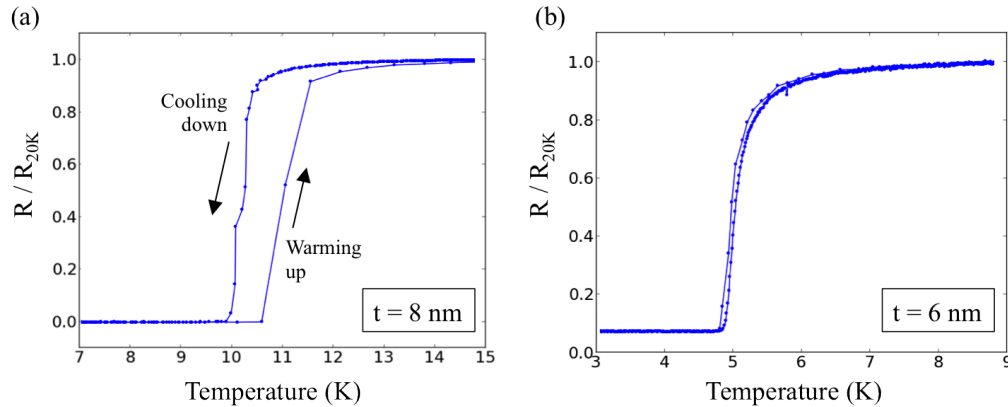


Fig. 4.1 Resistance as a function of temperature for several NbTiN thin films. Physical separation between the thermometers and the superconducting sample at the cold-head results in hysteretic behaviour between warming up and cooling down. **(a)** Films close to 10 nm thick achieved the highest $T_C \simeq 10\ K$. **(b)** Films with a thickness measured more accurately as 6 nm showed transitions close to 5 K.

## 4.2 Integration of detectors with waveguides

The waveguide cross-section is dictated by the GaAs epitaxial layer thickness and the requirement that the width supports only a single mode at quantum dot emission wavelengths ($\lambda = 900 - 1000$ nm). The dimensions used for single mode suspended nanobeam waveguides are height 140 nm and width $< 400$ nm (see Figure 4.3). The ideal width and depth for the nanowire detector are dictated by material choice (NbTiN) and intention to achieve high sensitivity to single photons ($E = \frac{hc}{\lambda} = 1.24 - 1.34$eV) with high uniformity of the nanowire cross-section along its whole length.



| | | |
|---|---|---|
| 7 nm | NbTiN |
| 140 nm | GaAs (embedded InAs QDs) |
| 1 μm | AlGaAs |
| 370 μm | GaAs |
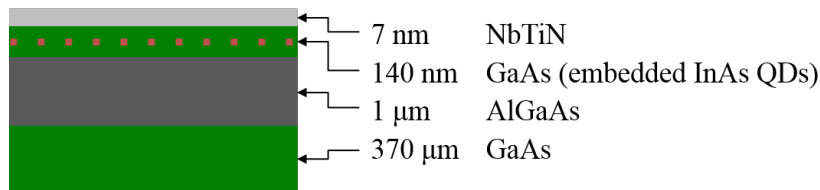
Fig. 4.2 The heterostructure of wafers used to create GaAs waveguide circuits with embedded InAs quantum dots and integrated NbTiN single photon detectors. All III-V semiconductor layers are grown by MBE and the NbTiN superconducting film is subsequently deposited on top by DC magnetron sputtering.
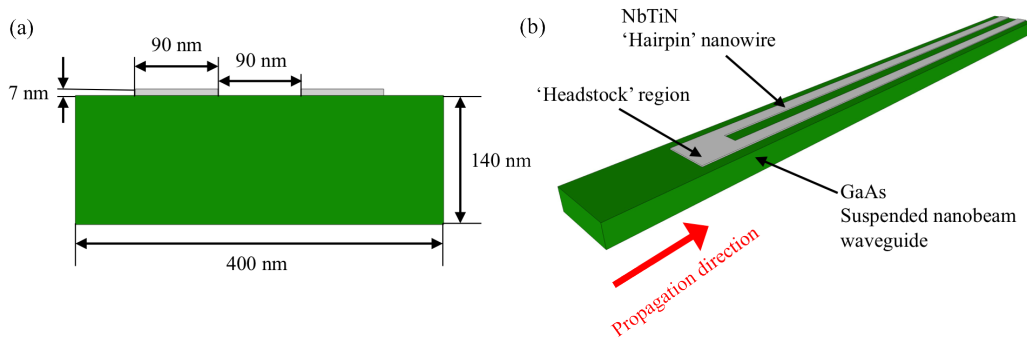
Fig. 4.3 **(a)** Vertical cross-section of waveguide-integrated nanowire detector. GaAs is shown in green with dimensions labelled. The suspended nanobeam waveguide is surrounded on all sides with air/vacuum for maximum index contrast and mode symmetry. The small cross-sectional area supports only a single propagating mode for wavelengths $\lambda = 900 - 1000$ nm. The two sections of nanowire are shown atop the waveguide defined in a thin film of superconducting NbTiN. **(b)** Drawing showing section of waveguide with hairpin shaped nanowire aligned parallel to the waveguide propagation axis.

## 4.2.1   Modelling of waveguide detectors

Refractive index ($n$ and $\kappa$) data were determined using spectroscopic ellipsometry over the wavelength range from $270 - 2400$ nm on 5 nm thick NbTiN films grown by Archan Banerjee at the University of Glasgow by reactive DC magnetron sputtering. Ellipsometry was performed by LOT-QuantumDesign GmbH [299] and the data used to conduct simulations of waveguide integrated detectors as detailed in Section 3.2.5. Photon absorption probability above 99% is expected within $< 20$ μm length of nanowire. An increase in the cross-sectional area of the nanowire would increase absorption efficiency however the inverse is true for the energy sensitivity of the detector, with wider and thicker wires decreasing the likelihood of registering a count after absorption of a single infrared photon. Maintaining consistent thickness of the superconducting film over a large enough area to pattern a uniform detector is a pivotal challenge in SNSPD fabrication. Patterning a hairpin shaped nanowire that retains uniformity over 10 μm or 20 μm is not beyond the state-of-the-art for NbTiN thin film growth nor electron beam lithography. The total nanowire cross-section is designed to increase in the 'head-stock' region to avoid bunching of the super-current as it rounds the 180° turn. The NbTiN at the outside edge of this curve sees a lower current density than the inside, with the detection efficiency being effectively lowered in that localised region. Being the first region into which waveguide light will propagate there is a finite chance that a

waveguide photon is absorbed at the very tip of the detector. The likelihood of this photon registering a count at the readout electronics is lower than if the photon is absorbed anywhere else along the nanowire (see Section 2.2.3). For the detectors simulated in Figure 4.4 the 'head-stock' region is 400 nm in length with a $\sim 20\%$ chance that a waveguide photon will be absorbed into a less sensitive region of NbTiN.
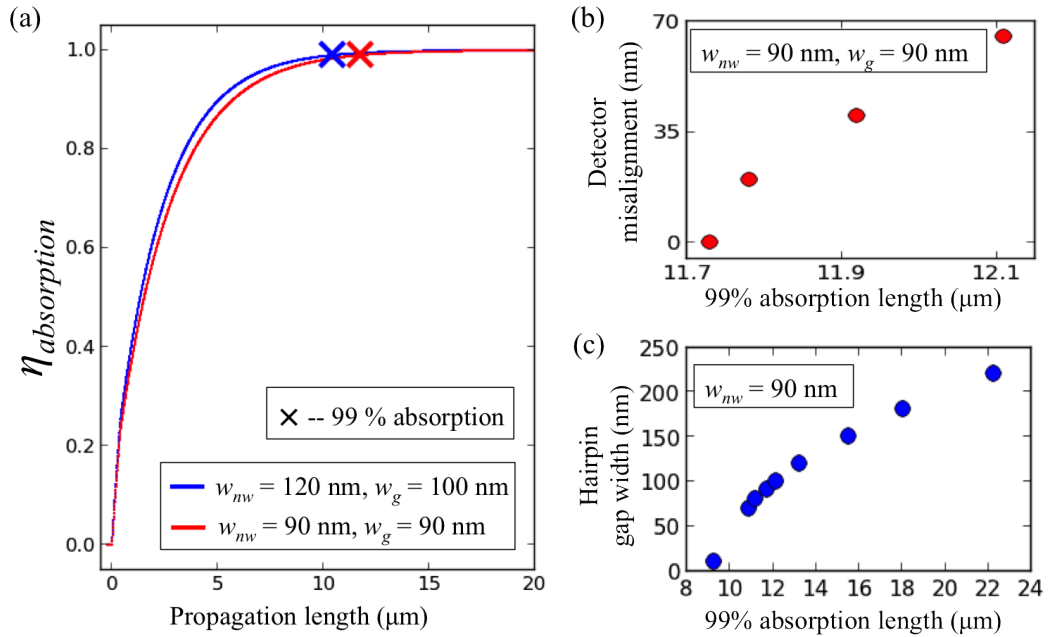


Fig. 4.4 Simulated absorption into waveguide-integrated nanowire detectors (method described in Section 3.2.5). All simulations involve 400 nm width GaAs SNB waveguides, 7 nm thick NbTiN and $\lambda = 950$ nm illumination. **(a)** Normalised absorbed optical power as a function of detector length. The red and blue lines represent simulated nanowires of two different sizes, detailed in the legend. **(b)** The effect of lateral misalignment between the nanowire detector and the centre of the waveguide is shown. Each plotted point represents a single simulated detector. **(c)** The width of the central gap of the hairpin nanowire is investigated. Narrower gaps increase overlap between the waveguide mode and the nanowire with resultingly higher absorption, however this increases the challenge of fabrication.

## 4.2.2    Absorption measurements

Absorption of light into NbTiN nanowires was measured at the University of Sheffield. A 2 spot confocal optical set up was used as described in Section 3.2.5. In the absence of calibrated optical losses through the entire system data are normalised against a reference 'blank' waveguide of identical dimensions to

| Hairpin length | $T_{max}$ | $T_{average}$ |
|:---:|:---:|:---:|
| 5 µm | 2.6 % | 3.4 % |
| 10 µm | $2.3 - 2.8$ % | $2.1 - 3.2$ % |

Table 4.2 Waveguide width 600 nm, waveguide length 15 µm, hairpin nanowire made from 7 nm thick NbTiN patterned into 125 nm wires with an 85 nm gap.

the detector-bearing waveguide, fabricated immediately adjacent. The InAs layer within the substrate is excited with a 633 nm wavelength pump laser generating PL which propagates through the waveguides. NbTiN nanowires were found to absorb $\sim 97\%$ of the PL without significant difference between 5 µm and 10 µm nanowire lengths. Table 4.2 contains a summary of the peak values and spatially averaged values of waveguide transmission as shown in Figure 4.5.
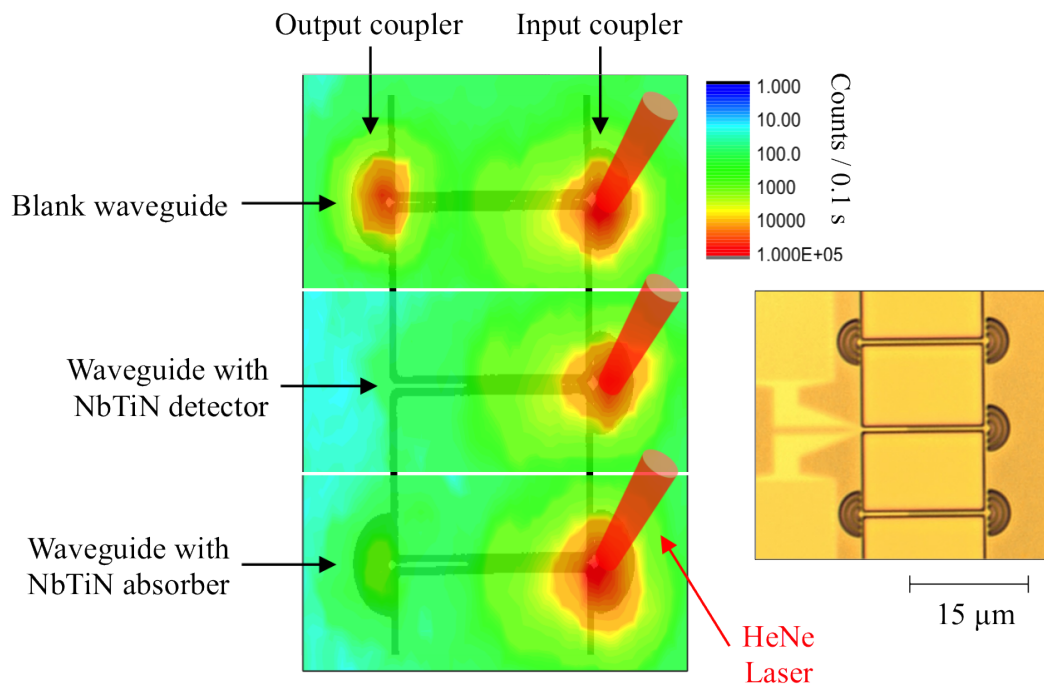


Fig. 4.5 Three parallel waveguides, each measuring 15 µm in length, are mapped in a confocal setup detailed in Figure 3.28. Short wavelength pump light (marked with red light cones) is focussed in a fixed location and the collection spot raster scanned independently over the surrounding area to build up the intensity maps picured. A long-pass filter is used to remove light at the pump wavelength ($\lambda = 632$ nm). A Si-APD records the intensity of collected PL. **Inset** An optical micrograph shows the mapped area. Waveguides and grating couplers are visible. The bottom two waveguides each house an NbTiN nanowire.

## 4.3 Characterisation of detectors

At low temperature the superconducting critical current $I_C$ of detectors is established by measuring the voltage across the detector as a function of bias current $I_B$ as detailed in Section 3.2.3. Biasing a detector close to the critical current $I_B < I_C$ enables the observation of dark count pulses through the readout circuit. Pulse shapes shown in Figure 4.6 (a) were recorded on an Agilent Infiniium DSO80804A (8 GHz, 40 GSamples/second) digital oscilloscope. Inclusion of a 50 Ω shunt resistor in parallel with the device allows current to be diverted from nanowire after it switches to the resistive state reducing Joule heating of the nanowire and preventing the detector from latching. Devices
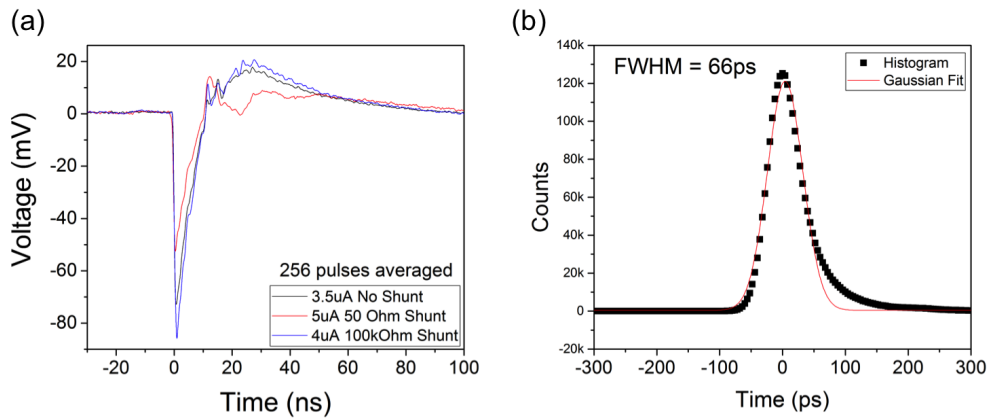


Fig. 4.6 **(a)** Oscilliscope traces of the output pulses from a single detector. **(b)** Timing jitter of a hairpin nanowire detector measured using a $\lambda = 1560$ nm mode-locked laser and a Picoquant time-correlated single photon counting (TCSPC) card. Data is fitted to a Gaussian distribution (red line) with full-width at half-maximum (FWHM) = 66 ps.

mounted in the pulse tube (PT) cooler described in Section 3.2.4 are addressed optically by the miniature microscope. The timing jitter is measured using the fast pulsed $\lambda = 1560$ nm laser and the apparatus detailed in Section 3.2.3. Figure 4.6 (b) shows a histogram of counts recorded by the TCSPC electronics with a Gaussian fit (in red). The FWHM jitter is 66 ps although the measured data is slightly asymmetrical, deviating from the Gaussian fit at higher time values. This behaviour is seen in other waveguide integrated SNSPDs [173, 251]. Nano-optical mapping of detectors is performed with the miniature microscope using a Thorlabs superluminescent diode SLD1050S ($\lambda = 1050$ nm FWHM 50 nm) for illumination. Figure 4.7 shows three SNB waveguides and an integrated detector within a single field of view mapped at 3.7 K. The optical spot diameter is $\sim 2$ μm although when well focussed
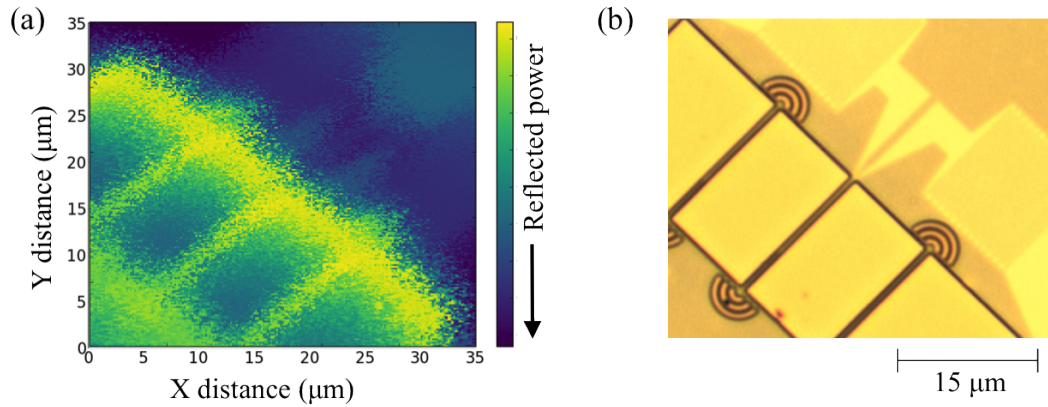
Fig. 4.7 Reflection maps of a sample surface at 3.7 K created with the apparatus in Figure 3.22. The reflected power **(a)** is compared to an optical micrograph **(b)**. This technique enables the nanoscale features of detectors and waveguides to be located and precisely addressed at low temperatures.

it is possible to discern sub-wavelength sized features such as waveguides (width 600 nm) and grating couplers. The single photon response of nanowire detectors was mapped by routing light from the same super luminescent diode through two calibrated variable optical attenuators and a polarisation controller. Rotating the polarisation results in a variation in the count rate at the detector for a constant photon flux. The ratio of count rates from parallel $P_{max}$ and perpendicular $P_{min}$ polarisations was measured as $\frac{P_{min}}{P_{max}} = 0.46$. Figure 4.8 (a) shows a 10 μm long detector mapped at low temperature before the fabrication of an encompassing waveguide. The extension of high count rate along the detector's length suggests good uniformity of the nanowire.

## 4.4    Detecting waveguide-coupled light

Employing the low temperature nano-optical technique described above it is possible to interrogate the nanowire and waveguide grating coupler with single photons mapping the detector response. Figure 4.9 shows 15 μm long straight nanobeam waveguides with a grating coupler at one end and a nanowire detector at the other overlaid onto optical micrographs as a guide to the eye. From both count maps it can be seen that the nanowire is sensitive to direct illumination along its whole length. Moreover the detector registers counts when the grating coupler is illuminated suggesting that the coupler is successfully scattering the light focussed from the microscope into the propagating waveguide mode from which it is absorbed by the NbTiN nanowire triggering an output count.

(a)

(b)
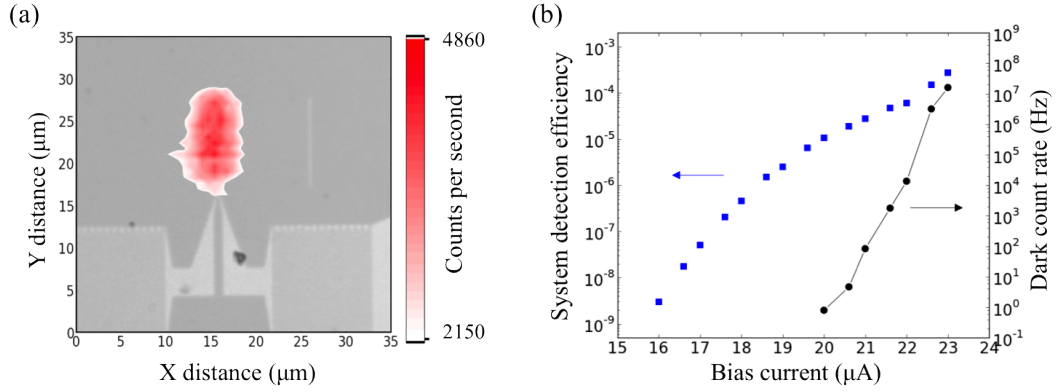


Fig. 4.8 **(a)** A counts map of a hairpin nanowire detector measured at 3.7 K (overlaid onto an optical micrograph of the equivalent area). Figures 3.22 and 3.24 contain a schematic of the equipment used and the measurement process. Single photon response at $\lambda = 1050$ nm is observed over the entire length of the detector ($= 10$ μm) measured with a 2 μm diameter optical spot. There are no waveguides patterned on these samples. **(b)** system detection efficiency (SDE) is measured for a detector as a function of bias current. The detector is made from 7 nm thick NbTiN patterned into 120 nm wide nanowires.

(a)

(b)
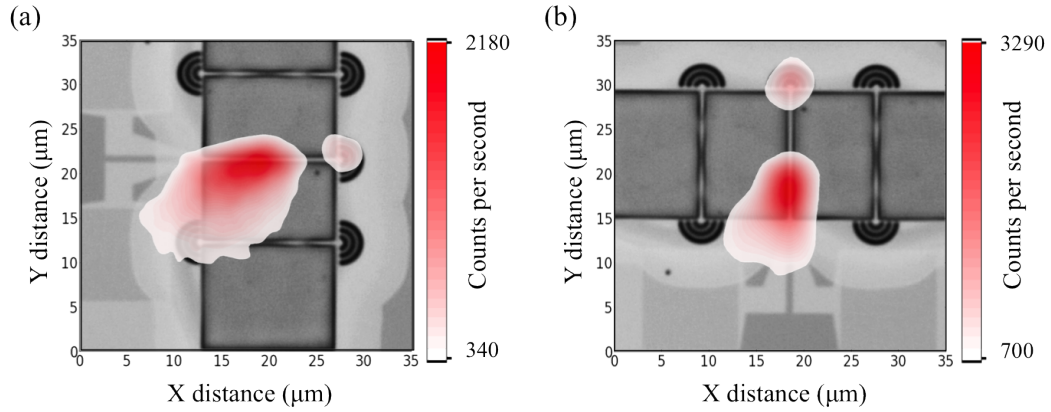


Fig. 4.9 Single photon count maps of 2 detectors were measured at 3.7 K using a super luminescent diode ($\lambda = 1050$ nm) attenuated to the single photon level. Optical micrographs are overlaid as a guide to the eye. Areas of high count rate are shown in red with both images showing counts registered from direct illumination of nanowires as well as light coupled to the waveguides via grating couplers. The nanowire in **(a)** extends 10 μm along the waveguide whereas the detector in **(b)** is 5 μm in length.

In each case the ratio of counts generated by grating coupler illumination $\mathcal{R}_{coupler}$ to counts generated under direct illumination $\mathcal{R}_{direct}$ was $0.27 \leq \mathcal{R}_{coupler}/\mathcal{R}_{direct} \leq 0.59$. This simple ratio however fails to capture the vastly different ways in which the photons are coupled to the detector in each instance. Further comparison of the device efficiency demands that the system losses are considered including coupling of light to the detector as well as the probability

| $l_{wg}$ | $SDE_{direct}$ | $SDE_{coupler}$ | $\eta_{registering}$ | $\eta_{waveguide}$ |
|---|---|---|---|---|
| 5 µm | 0.076 % | 0.045 % | 3.80 % | -19.1 dB |
| 5 µm | 0.194 % | 0.083 % | 9.71 % | -20.6 dB |
| 10 µm | 0.135 % | 0.037 % | 6.77 % | -22.5 dB |
| 10 µm | 0.139 % | 0.047 % | 6.93 % | -21.5 dB |

Table 4.3 System detection efficiency is compared for waveguide integrated detectors under direct perpendicular illumination and for waveguide coupled light. All detectors consist of 120 nm wide nanowires patterned in 7 nm NbTiN on top of 600 nm wide SNB waveguides.

of a photon's absorption into the superconducting nanowire. In the instance of direct illumination the focussed microscope spot has a roughly Gaussian beam profile with FWHM $\simeq 2$ µm. The two side by side wires that make up the detector are only 120 nm each in width thus only around 10% of the spot can overlap the detector, therefore the coupling efficiency $\eta_{coupling} = 0.1$. Perpendicular illumination will also suffer from a low absorption probability $\eta_{absorption}$ due to the extremely thin superconducting film. Simulations of the optical layer structure performed in Essential Macleod suggest that before the nanobeam waveguide is under-etched to remove the AlGaAs $\eta_{absorption} = 14\%$ at $\lambda = 1050$ nm for 7 nm thick NbTiN.

To calculate the effect of under-etching the waveguide the simulation was repeated replacing the AlGaAs layer by vacuum to the same depth (1 µm) which resulted in improved absorption $\eta_{absorption} = 29\%$. For a real device the vacuum gap thickness is not likely to be exactly 1 µm because of the flexibility of the SNB structure. Varying the vacuum gap thickness from 500 nm to 1200 nm in the simulation results in a variation of $\eta_{absorption} = 11 - 65\%$. Following the wet etching process the substrate underneath the SNB can also be rough which would significantly reduce coherent reflection. The combination of SNB flexibility and substrate roughness make it difficult to reliably calculate $\eta_{absorption}$ for a SNB waveguide integrated SNSPD under perpendicular illumination, however a conservative estimate of $\eta_{absorption} = 20\%$ is used in following calculations.

The registering efficiency $\eta_{registering}$ of waveguide integrated SNSPDs is calculated from $SDE_{direct}$ using the equation

$$\eta_{registering} = \frac{SDE_{direct}}{\eta_{absorption} \times \eta_{coupling}} = 3.80\% - 9.71\% \qquad (4.1)$$

where $SDE_{direct}$ is the system detection efficiency calculated by equation 3.3 using the maximum recorded value of $\mathcal{R}$ from the section of the counts map corresponding to direct perpendicular illumination of the nanowire.

When measuring $\mathcal{R}$ whilst illuminating the grating coupler the optical coupling and absorption mechanisms are different to perpendicular illumination and waveguide losses must also be considered. It is assumed that $\eta_{registering}$ remains constant. The system detection efficiency in the waveguide coupled regime $SDE_{coupler}$ can be expressed as

$$SDE_{coupler} = \eta_{registering} \times \eta_{absorption}^{wg} \times \eta_{waveguide} \tag{4.2}$$

in which $\eta_{waveguide}$ comprises all losses between the microscope and the detector. The primary causes of such losses are likely to be inefficient coupling between the focussed optical spot and the propagating waveguide mode followed by inefficient waveguide transmission (see Figure 5.7). The absorption efficiency of waveguide photons into the detector $\eta_{absorption}^{wg} = 0.97$ is taken from measured data in Section 4.2.2.

Table 4.3 shows the calculated efficiency values of four measured devices recorded at a bias level corresponding to $\sim 100$ Hz dark count rate (DCR). The length of SNB waveguide separating the grating coupler from the tip of the detector for each device is denoted by $l_{wg}$. Devices with $l_{wg} = 10$ μm exhibit only fractionally larger waveguide losses than those with $l_{wg} = 5$ μm. This suggests that the transmission loss in the nanobeam waveguide is 0.44 dB.μm$^{-1}$ whereas the magnitude of insertion loss at the grating coupler could be as large as 17.6 dB.

## 4.5 Conclusions

A fabrication process was developed to integrate NbTiN SNSPDs with GaAs SNB waveguides which are narrow enough to support only a single propagating optical mode at $\lambda = 950$ nm. The best devices fabricated achieved uniform nanowire widths of 90 nm with 90 nm spacing on top of 380 nm wide waveguides with $< 50$ nm layer to layer alignment accuracy over 3-stages of electron beam lithography (EBL). The low temperature electrical and optical properties of detectors were measured at the University of Glasgow confirming nanowire uniformity and the detection of waveguide coupled light. At the University of Sheffield high absorption into waveguide-integrated superconducting nanowires

was confirmed by waveguide transmission measurements. Waveguides with NbTiN nanowires of 5 µm and 10 µm lengths were observed to transmit $< 2\%$ of the light transmitted through blank waveguides of identical dimensions. Measured SDE was low despite apparent uniformity. Calculations of the detector registering efficiency $\eta_{registering}$ were between $3.8 - 9.7\%$ at 100 Hz DCR. The registering efficiency of detectors under direct perpendicular illumination was used to estimate optical losses from the waveguide and grating couplers when probed with the miniature microscope at the University of Glasgow.

# Chapter 5

# Quantum photonic integrated circuits

*This Chapter contains measurements and analysis of waveguides and detectors performed at the University of Glasgow by the author. Fabrication of integrated devices was carried out in the JWNC by the author with the exception of the critical point drying (CPD) process which was performed by Dr. Ben Royall at the University of Sheffield. Figure 5.2 contains data measured by John O'Hara at the University of Sheffield on devices fabricated by Dr. Ben Royall. The RSFQ circuit in Section 5.2 was designed and fabricated at National Institute of Information and Communication Technology, Japan (NICT) and measurements performed by the author and Dr. Shigehito Miki.*

## 5.1 Designing a device for on-chip quantum measurement

The increased integration of waveguide components is a necessary step towards realization of a stable and scalable quantum information processor. Quantum photonic integrated circuits (QPICs) as described in Section 2.3.2 must bring together a series of components working together with low enough loss to perform a sensitive quantum measurement such as the Hanbury-Brown Twiss (HBT) measurement [55–58] or two photon interference [59, 300]. By isolating the emission from a single photon source (SPS) and recording coincidence events with a beam splitter and two single photon detectors (SPDs) a measurement of the second order correlation function $g^{(2)}(\tau = 0) < 0.5$ would confirm the

observation of quantum light from the SPS, in the form of a sub-Poissonian (or anti-bunched) stream of photons.

A device was designed and fabricated at the University of Glasgow with the intention of performing an HBT measurement entirely on chip, shown in Figure 5.1. The wafer heterostructure used is shown in Figure 4.2 on page 105. The waveguide circuit is patterned in the top GaAs layer with InAs quantum dots (QDs) embedded in suspended nanobeam (SNB) waveguides designed to act as an SPS. A directional coupler is designed to act as a 50:50 beam-splitter with two identical superconducting nanowire single photon detectors (SNSPDs) integrated with the output SNB waveguides as described in Chapter 4. An integrated filter is also included in the SNB waveguide design as the broad wavelength sensitivity of SNSPDs makes it difficult to natively distinguish between photons of different wavelengths. Optically pumping the embedded QDs is likely to result in photons from multiple QDs, the wetting layer, and the pump laser being present simultaneously in the waveguide. So in addition to integrating the SPS with a beam splitter and SPDs it is necessary to filter the photo-luminescence (PL) before measurement to isolate the PL signal from a single QD.

Information feed-forward is another essential element of linear optical quantum computing (LOQC) which requires events from SPDs to be registered, processed and quickly routed to relevant areas of the processor. At the NICT in Kobe rapid single flux quantum (RSFQ) logic circuits are designed for low temperature readout and processing of signals from SNSPDs. An RSFQ chip was designed by Dr. Hirotaka Terai and Dr. Shigehito Miki to receive inputs from two SNSPDs and compare them with high timing precision as would be necessary to perform a correlation measurement. Measurements were performed by the author and Dr. Miki to demonstrate the operation of these devices mounted in a GM cooler alongside 2 fibre-coupled SNSPDs.

## 5.1.1   Device specification

The integration of SNSPDs with SNBs is described in detail in Chapter 4. GaAs samples grown by molecular beam epitaxy (MBE) at the University of Sheffield contain embedded InAs QDs designed as single photon emitters at $900 \text{ nm} < \lambda < 1000 \text{ nm}$. For an ideal SPS the second order correlation function $g^{(2)}(\tau = 0) = 0$ and for a non-ideal source $g^{(2)}(\tau = 0) < 0.5$ confirms the generation of quantum light (see Section 2.1.3). The observation of a reduction

in $g^{(2)}(\tau)$ at $\tau = 0$ is dependent on the dark count rate and timing jitter of the SPDs used for the measurement. The instrument response function of the detectors creates an uncertainty in the elapsed time between photon absorption at the detector and registration of the event in the counting electronics. Due to this uncertainty it is possible for two photons absorbed with a time delay of $\tau > 0$ between them to be registered at $\tau = 0$ contributing false coincidence events and reducing the visibility of the true $g^{(2)}$ function. Additionally dark counts at either detector could coincide with detection of a PL photon at the other detector generating spurious coincidence events. By pulsing the pump light it is possible to separate PL into pulses at a well defined frequency separating events by more than the QD lifetime and the SPDs timing jitter.
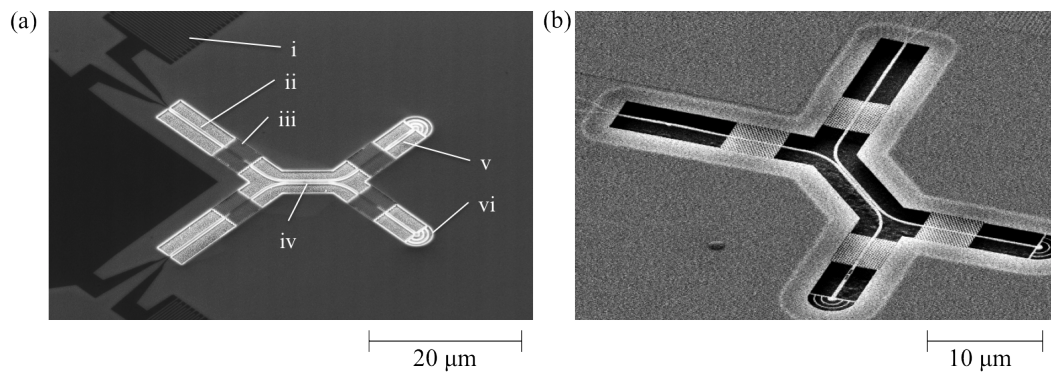


Fig. 5.1 **(a)** A device was designed at the University of Glasgow to be capable of performing quantum measurements entirely on-chip. A beam-splitter (directional coupler, iv) with two detectors (ii) at the outputs is designed to perform an HBT measurement of PL photons emitted from a single QD embedded in the SNB waveguide. Kinetic inductors (i) are included in the detector design to prevent latching. The device includes additional sections of 2D photonic crystal (PhC) waveguide (iii) around the directional coupler intended to act as structural supports whilst enabling broad-band transmission and minimal reflection. A 1D PhC (v) is included on the input arm of the directional coupler and grating couplers (vi) are added to both inputs to aid in device characterisation. **(b)** A completed device after HF wet etching is performed at the University of Sheffield to release the suspended waveguide sections from the susbstrate.

Devices are designed to confine photons within single mode waveguides which enable the the observation of interference effects between indistinguishable photons. InAs QDs, a directional coupler, and SNSPDs are housed in SNB waveguides with grating couplers included to allow the devices to be probed and characterised using light from off-chip. One dimensional PhC cavities have been designed to be incorporated with SNB waveguides and filter PL signal

allowing a narrow wavelength band to pass through the SNB rejecting pump
light and PL from the wetting layer and nearby QDs.

Sections of 2 dimensional PhC are also included in the device design. It
is intended that light will pass between 2-D PhC and SNB waveguides with
minimal loss or reflection. The 2-D PhC sections are also intended to act as
supports for the suspended structures, preventing collapse during fabrication
and holding both parts of the directional coupler at the optimal separation.

## 5.1.2   Device characterisation

### Characterising isolated components

Development of the design and fabrication methods for waveguide components
has been carried out at the University of Sheffield. Figure 5.2 shows verification
of the transmission spectra for PL routed separately through single mode waveg-
uides and narrow wavelength filters and analysed off-chip. SNB waveguides,
2-D PhC waveguides and 1-D PhC filters were individually fabricated by Dr.
Ben Royall and tested by John O'Hara as described in Section 3.2.5. The
rejection ratio of the filter is yet to be confirmed, theoretically or experimentally.
It is possible that the pump wavelengths must be attenuated by $\sim 80$ dB to
make the PL visible at waveguide integrated detectors.
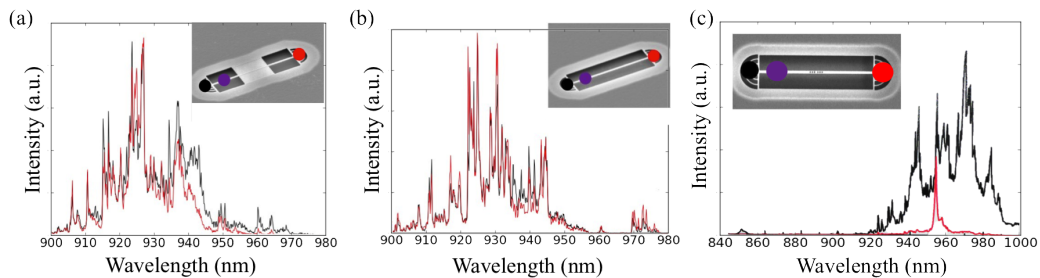


Fig. 5.2 Suspended GaAs waveguide components fabricated at tested at the University
of Sheffield. PL from embedded InAs QDs is generated by a pump laser (purple
spot) focused on the SNB close to a grating coupler. Light is collected from the
nearby grating coupler (black line graph) and the far end (red line) giving a quali-
tative assessment of transmission through the waveguide. **(a)** Straight suspended
nanobeams of single mode dimensions and **(b)** nanobeams with a central section of
2D PhC exhibit good transmission of all PL wavelengths. **(c)** Cavities have a narrow
wavelength pass-band of around 3 nm FWHM which could be selective enough to
isolate 1 emission line from a single QD. The best measured transmission was 78%.
Data courtesy of Zofia Bishop, Dr. Ben Royall, and John O'Hara.

**Characterising the integrated devices**

Incorporating design parameters adapted from components in Figure 5.2 larger integrated devices were fabricated at the University of Glasgow by the author (Figure 5.1). The system detection efficiency (SDE) is measured and the overall yield from fabrication considered.

To develop the technology of GaAs QPICs further it is necessary for many high efficiency detectors to be fabricated simultaneously across the surface of a chip and for low-loss waveguide components to be reliably aligned. Figure 5.3 shows scanning electron micrographs of several successfully fabricated HBT devices. Multi-stage e-beam and dry etching processes were carried out in the JWNC and the final wet etch and CPD to release waveguide structures was performed at the University of Sheffield. Devices yielded well with good alignment of critical features and adherence to dimensions of the original design. All sections of nanobeam waveguide also remained suspended after release. As with previous devices there are residues left that are thought to come from the e-beam resist. These residues are particularly persistent in the holes of PhCs and on top of the nanowires. In the PhCs it is most likely that these will cause a divergence of the transmission properties away from the designed values. Resist residue can be partially removed by $O_2$ plasma ashing and use of hot chemical stripping however these processes must be applied sparingly to avoid destroying the superconducting properties of the detector.
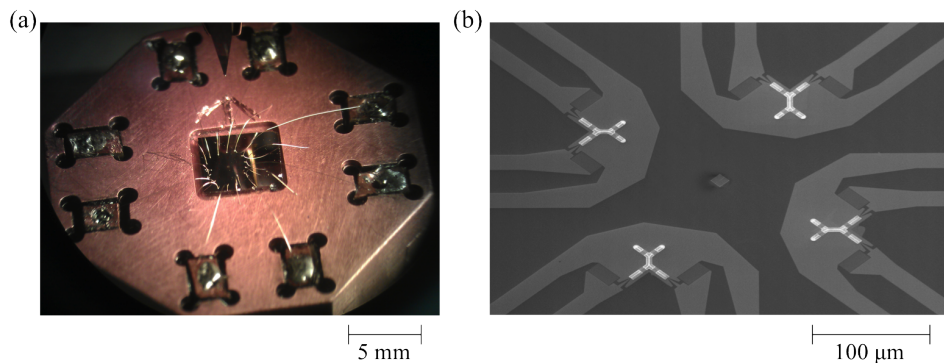


Fig. 5.3 Devices designed for on-chip HBT measurements. **(a)** Chips are mounted on a custom built sample mount at the University of Glasgow and the detectors characterised before transportation under vacuum to the University of Sheffield where they are mounted in the cryostat described in Section 3.2.5 for QD PL experiments. **(b)** A single chip houses 4 devices each with a different length directional coupler designed to achieve different beam-splitting ratios.

Low temperature electrical properties of the devices were confirmed in a Gifford-McMahon (GM) cooler at the University of Glasgow described in Section 3.2.3. Figure 5.4 (a) shows the measured $I_C$ of eight devices on the same chip. The similarity in all but one detector suggests that the fabrication process yields nanowires with good uniformity.
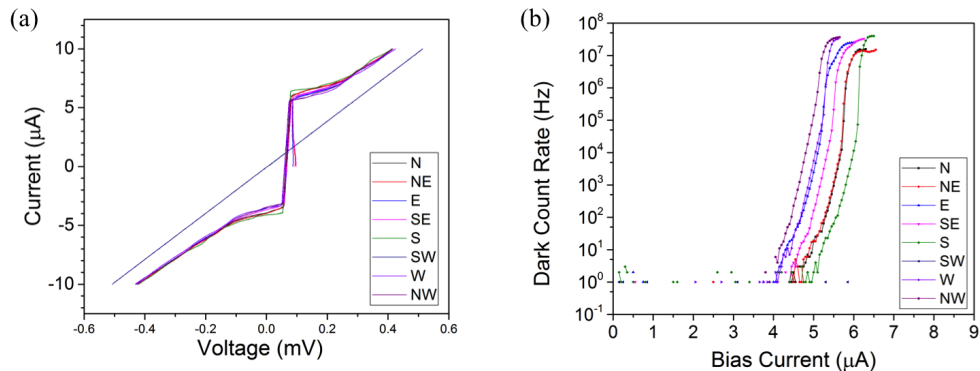
Fig. 5.4 **(a)** Voltage across nanowire devices is measured as a function of applied bias current at 2.2 K. All devices tested simultaneously are on a single chip and display a high degree of uniformity (with the exception of a single wire which does not superconduct). Detectors are biased by a DC voltage source in series with a 100 kΩ resistor and a 50 Ω shunt resistor is placed in parallel with the device. **(b)** The measured dark count rates for the same detectors. The bias circuit is connected to a bias tee with the AC arm leading to 2 low noise amplifiers (55 dB total gain) and a digital counter. The observed dark count rate increases exponentially as the bias current approaches critical level.

Low temperature nano-optical measurements were performed using the set-up detailed in Section 3.2.4 to verify the optical properties of detectors and waveguides. Two separate maps are needed to cover the whole device area with the microscope's $35 \times 35$ μm$^2$ field of view. Figure 5.5 (a) shows a count map recorded over the two detectors, each with an independent bias and readout circuit fed separately to a 2 channel digital counter. There is no evidence of electrical cross-talk between detectors or any significant optical scattering from the vicinity of one detector to the other. Figure 5.5 (b) is a count map recorded over the far end of the device at a higher photon flux. Although the top left of the map shows strong scattering of the bright light towards the detectors there is no evidence of any photon counting signal above the dark count rate (DCR) from either of the input grating couplers .

The apparatus in Figure 3.27 were optimised for testing of GaAs waveguide circuits with integrated SNSPDs. Efforts were taken to align the sample in the optical path and bring the necessary features into focus. This included

(a)



| Detector 1 (blue) | | Detector 2 (red) | | Photon flux |
|---|---|---|---|---|
| $I_B$ | DCR | $I_B$ | DCR | |
| 6.8 μA | 60 Hz | 3.2 μA | 10 Hz | 2.7x10$^8$ s$^{-1}$ |

(b)

| Detector 1 (blue) | | Detector 2 (red) | | Photon flux |
|---|---|---|---|---|
| $I_B$ | DCR | $I_B$ | DCR | |
| 6.8 μA | 120 Hz | 3.2 μA | 60 Hz | 5.4x10$^8$ s$^{-1}$ |
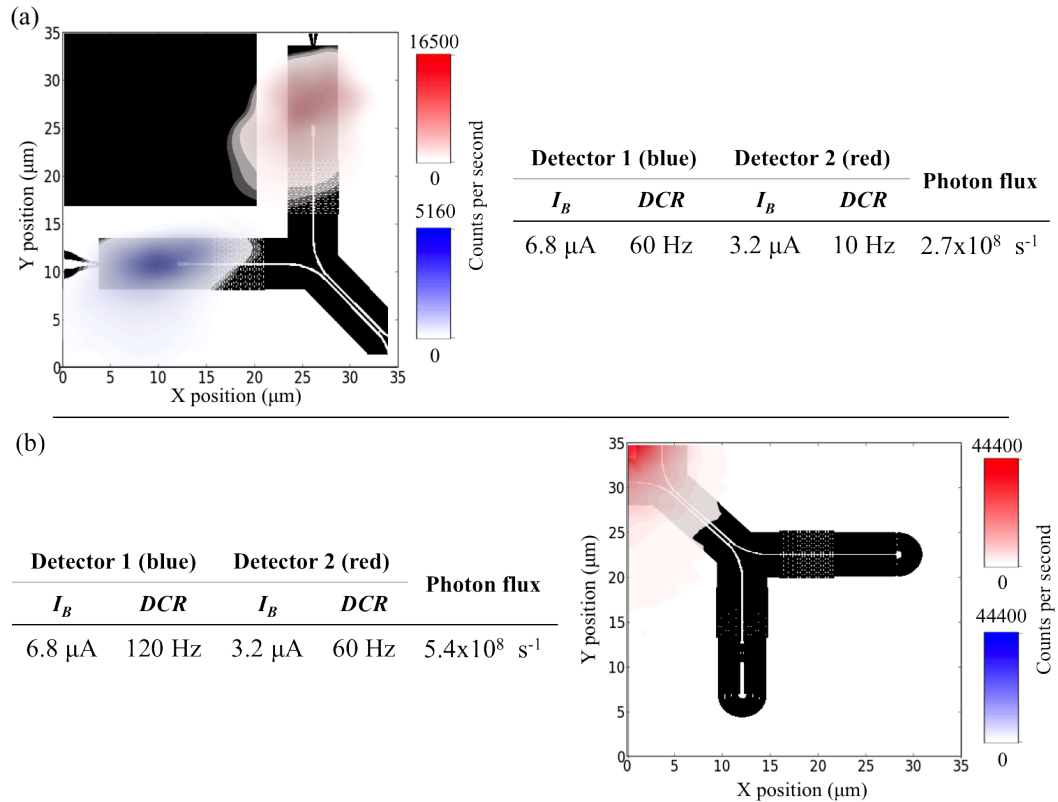


Fig. 5.5 The response of detectors to $\lambda = 1050$ nm photons in a QPIC is mapped using the apparatus described in Section 3.2.4. **(a)** Both detectors show response to direct perpendicular illumination. The variation in peak count rate of approximately 50% between detectors is consistent with their polarisation sensitivity and respective orientations. **(b)** Illumination of the waveguide grating couplers with higher intensity light generates no detector counts above the DCR. The higher photon flux used for this map is enough to cause significant scattering in the top left of the map.

removing polymer sheaths from the brass coaxial cables connected to the sample mount as their rigidity at low temperature hindered the free movement of the piezoelectric motors. Detectors were confirmed to operate inside the cryostat by observation of dark count pulses however the measured critical current dropped to zero over a few minutes or hours following insertion of the vacuum tube into the L-He dewar. It is likely that black-body radiation entering through the optical window is heating the substrate by $\sim 1$ K which surpasses the $T_C = 5$ K of the film (Figure 4.1 (b)). Increased filtering with indium tin oxide (ITO) cold filters should be able to mitigate this effect.

### 5.1.3   Examination of system losses and limitations

Nano-optical mapping confirmed that waveguide integrated SNSPDs were sensitive to single photons at NIR wavelengths under direct perpendicular illumination. However when grating couplers were illuminated at the inputs to the same waveguide circuits no enhancement of the detector count rate was observed above the background DCR. Similar results were obtained by mapping the devices with $\lambda = 840$, 940, and 1050 nm light. Test structures were also fabricated to verify the performance of waveguide components comprising different combinations of components (similar to those in Figure 5.2) with waveguide integrated SNSPDs.

Figure 5.6 shows one such test structure and its single photon response map. The test structure consists of a waveguide integrated SNSPD with multiple SNB and 2-D PhC waveguide sections addressable via a grating coupler. Illuminating the grating coupler with a photon flux of $\Phi = 6.7 \times 10^8$ s$^{-1}$ again leads to no enhancement of the detector count rate above the background DCR of approximately 2000 counts per second (cps).

Using equation 4.1 measured data of $SDE_{direct}$ from waveguide integrated detector can be used to calculate the nanowire registering efficiency $\eta_{registering}$. For the same detector in the waveguide coupled regime equation 5.1 is then used to calculate the pre-detector losses $\eta_{waveguide}$ occurring in the waveguide circuit using the count rate $\mathcal{R}_{coupler}$ measured whilst illuminating the grating coupler.

$$\eta_{waveguide} = \frac{\mathcal{R}_{coupler}}{\Phi \times \eta_{registering} \times \eta_{absorption}^{wg}}. \tag{5.1}$$

Estimates of the waveguide losses can be used to calculate the expected photon flux reaching a waveguide integrated detector when the input grating coupler is illuminated by the miniature microscope. We consider the detector shown in Figure 5.5 (a) at the top (red counts) as it has been characterised via direct illumination and it sits on the waveguide track without a 1-D PhC filter. The components in the path from the input coupler to the detector are listed in Table 5.1 along with estimates of the insertion and transmission loss for each.

A finite element simulation was performed using the estimated component losses from Table 5.1 and the dimensions of fabricated devices, the results of which can be seen in Figure 5.7. The accuracy of estimated losses is confirmed by comparing measured data for straight SNB waveguides from Chapter 4 and the measured data in Figure 5.6. The simulation results suggests that the loss

(a)



10 µm

(b)



10700

Counts per second

1400
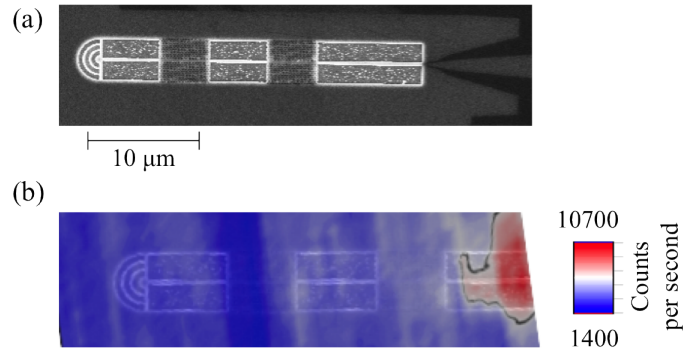
Fig. 5.6 **(a)** SEM image of an SNSPD integrated with a chain of waveguide components. From left to right the components pictured are: input grating coupler, SNB, 2D PhC, SNB, 2D PhC, SNB, waveguide integrated SNSPD. Scale bar is 10 µm. **(b)** A count map taken over the same device after underetching of the structure. A high count rate is visible when the detector is under direct perpendicular illumination ($\lambda = 1050$ nm). Vibration of optics creates some vertical spreading of the high counts region over the detector. This map was built up by stacking successive vertical scans. During data collection the electrical ground fluctuates over time effecting the DCR creating the horizontal variations visible across the map.

| Waveguide component | Estimated insertion loss | Estimated transmission loss | Calculated from |
|---|---|---|---|
| Grating coupler | 18 dB | – | Section 4.4 |
| Suspended nanobeam | 1 dB | 0.4 dB.µm$^{-1}$ | Section 4.4 |
| Directional coupler | 1 dB + 3 dB* | 0.4 dB.µm$^{-1}$ | Figure 5.5(b) |
| 2-D PhC | 3 dB | 1.5 dB.µm$^{-1}$ | Figure 5.6(b) |

Table 5.1 Estimated losses for various waveguide components. * The directional coupler includes 3 dB loss as per the intended 50:50 coupling ratio at the design wavelength of 950 nm.

between the input coupler and detector is 34.05 dB. Considering the calculated $\eta_{registering} = 0.3\%$ and $\eta_{absorption}^{wg} = 97$ % then addressing the input grating coupler with $10^{-10}$ W ($\Phi = 5.4 \times 10^8$ s$^{-1}$) will only translate to a count rate of $< 10$ cps at the detector. Increasing the illuminating photon flux is likely to contribute only slightly to the detection of waveguide photons and more so to detection of light scattered from the substrate back surface. Decreasing $I_B$ to remove dark count signal is also counter-productive as $\eta_{registering}$ will dramatically decrease at lower bias.
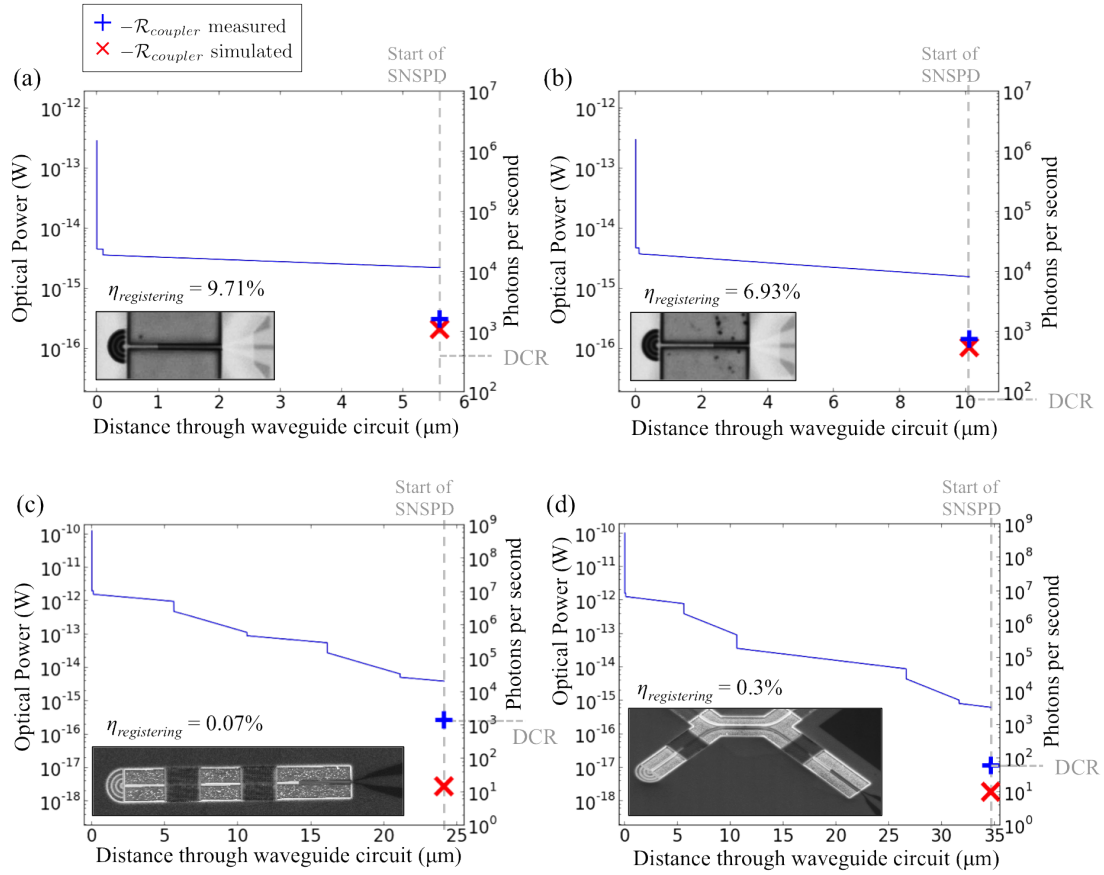
Fig. 5.7 Visualisation of the optical power in a waveguide circuit as a function of distance travelled by light between an input grating coupler and a waveguide integrated detector. Inset images show the layout of different combinations of waveguide components. Losses and reflections from the waveguide cause attenuation of the optical power (blue line) as light propagates through the circuit. The magnitude of the optical power at a certain position in the waveguide circuit is calculated by a discrete propagation simulation and expressed in Watts (left axis) and photon flux (right axis). Due to the very low registering efficiency of detectors the count rate will be only a small fraction of the photon flux arriving at the detector. For waveguide structures **(a)** and **(b)** the count rate $\mathcal{R}_{coupler}$ generated by illuminating the grating coupler (shown with a blue $+$) and $\eta_{registering}$ were used to calculate the losses of SNB waveguides and grating couplers. Table 5.1 contains a summary of the values for waveguide losses used in the simulations. For devices shown in **(c)** and **(d)** calculated waveguide losses were combined with estimates of the loss from 2-D PhC waveguides and directional couplers. For these detectors $\eta_{registering}$ is calculated from measurements under direct illumination and used in simulations to predict $\mathcal{R}_{coupler}$ (red $\times$). The combination of high waveguide losses and low detector efficiency leaves the expected value of $\mathcal{R}_{coupler}$ far below the background DCR.

## 5.2 Rapid single flux quantum read-out circuits

An RSFQ circuit was designed at NICT in Kobe, Japan and fabricated at the National Institute of Advanced Industrial Science and Technology (AIST) foundry in Tsukuba. The custom purpose circuit uses a flip-flop logic mechanism to compare inputs from two SNSPDs generating an output voltage pulse when the detector signals coincide within a 500 ps time window. Figure 5.8 illustrates this concept by showing the positions of voltage pulses on the input and output signal lines as a function of time. The device is armed by the receipt of a voltage pulse (shown in red) from the SNSPD on input channel 1. If a pulse is received on input channel 2 within 500 ps then an output pulse is triggered (shown in blue) on the output signal line. If 500 ps passes after the device is armed without any pulse arriving at input channel 2 then the device is reset to the initial state.

By introducing a variable delay to one of the input channels it is possible to use this device to perform correlation measurements (see Sections 2.1.3 and 3.2.5) and to characterise the timing jitter of SNSPDs without the use of room temperature time-correlated single photon counting (TCSPC) electronics. The second order correlation function $g^{(2)}(\tau) = 1$ for coherent laser light meaning that the laser beam consists of photons spread randomly in time with a Poissonian distribution (see Section 2.1.3). Splitting a laser beam and routing it to two similar SNSPDs should therefore yield a consistent count rate $\mathcal{R}$ from both, regardless of any time difference $\tau$ between the optical paths. For narrow pulsed laser light $\mathcal{R}$ should peak sharply in synchronisation with the laser repetition rate as shown in Figure 2.4 but without the disappearance of the peak at $\tau = 0$. Measuring the output signal from the RSFQ circuit as a function of $\tau$ allows for the timing jitter of both detectors to be probed as the uncertainty in pulse arrival time at the RSFQ chip inputs will translate to a blurring of the output response function around $\tau = 500$ ps as shown in Figure 5.9. Plotting the probability $\mathbb{P}_{out}$ of output pulses being generated as a function of $\tau$ allows the timing jitter $\triangle t_{1,2}$ of SNSPDs on input channels 1 and 2 respectively to be calculated from the derivative $d\mathbb{P}_{out}/d\tau$ which should take the form of a Gaussian with FWHM $\propto \sqrt{\triangle t_1^2 + \triangle t_2^2}$.

Section 2.3.3 describes the basic building blocks of RSFQ logic circuits. The input channels on this RSFQ chip are connected to single mode fibre-coupled SNSPDs. The connections of SNSPDs and the room temperature bias circuitry

Scenario 1 - Coincidence

Input channel 1:
Arming

Input channel 2:
Triggering

Output channel

0                        500 ps        Time

Scenario 2 – No coincidence

Input channel 1:
Arming

Input channel 2:
Triggering

Output channel

0                        500 ps        Time
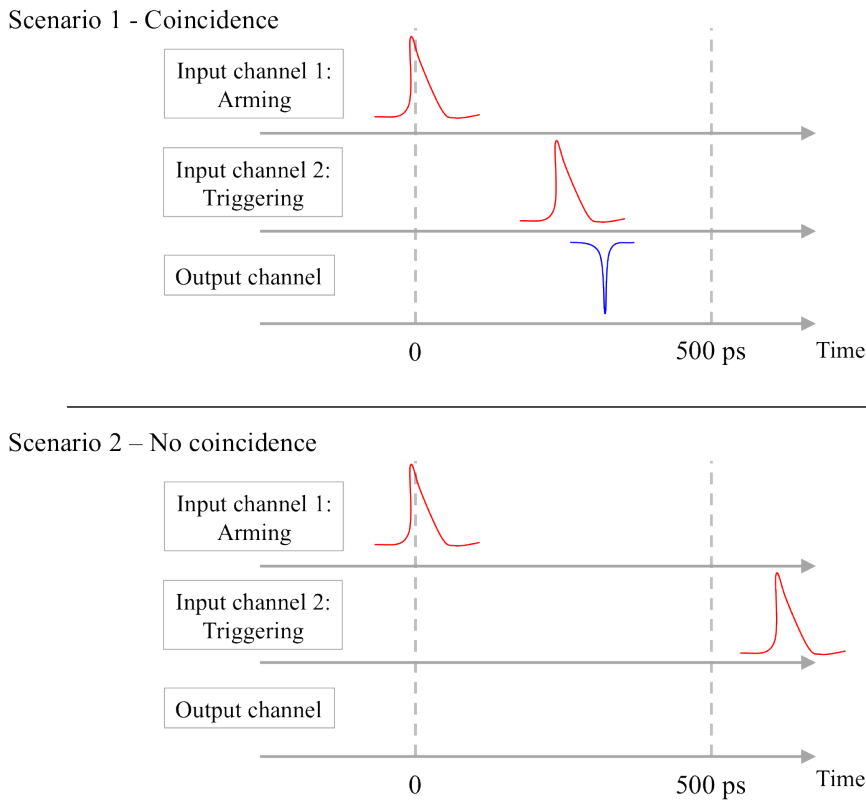
Fig. 5.8 An RSFQ digital flip-flop logic circuit is designed to compare pulses from SNSPDs (pictured in red) on two input channels. The arrival of a pulse on channel 1 arms the circuit. **(a)** If a pulse is received on channel 2 within 500 ps then an RSFQ output pulse (pictured in blue) is triggered. **(b)** If 500 ps elapses without the triggering pulse being recieved then the device resets and awaits the next arming event.

are shown schematically in Figure 5.10. A DC voltage source and bias resistor at room temperature are connected to the RSFQ chip as labelled. A bias tee on chip directs DC bias to SNSPDs via the input signal lines. Voltage pulses from SNSPDs 1 and 2 enter the RSFQ chip at the ports labelled in the diagram. RF pulses are 1 mV amplitude with $1/e$ decay time approx 10 ns. An MC-DC/SFQ converter on each channel translates detector pulses into the short voltage pulses that will be passed around the RSFQ logic circuit. At the output of the RSFQ circuit a superconducting quantum interference device (SQUID) amplifier amplifies the RSFQ pulse from the circuit to a suitable level for registration on the room temperature electronics. Outside the cryostat low noise amplifiers further increase the signal, the same as with SNSPDs in Section 3.2.4.

The RSFQ chip is fixed and wire bonded into a Cu chip carrier which includes printed circuit board (PCB) strip lines for RF signal transmission
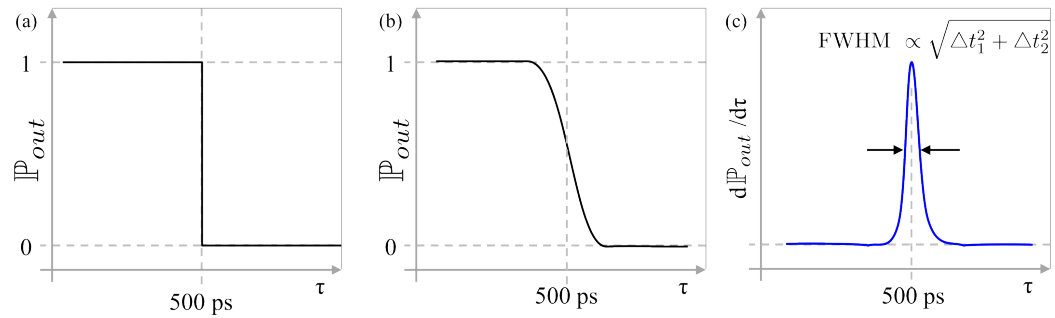
Fig. 5.9 By controlling the arrival time of SNSPD pulses to the inputs of the RSFQ logic circuit the detector timing jitter can be calculated from the observed probability $\mathbb{P}_{out}$ of RSFQ pulse generation. **(a)** Ideal detectors with zero timing jitter would immediately cease triggering RSFQ output pulses when the time delay between inputs exceeds 500 ps. **(b)** The uncertainty in pulse generation time from real detectors causes a variable probability of SNSPD pulses arriving within the 500 ps timing window. **(c)** The rate at which $P_{output}$ drops to zero i.e. $d\mathbb{P}_{out}/d\tau$ is proportional to the FWHM jitter of the detectors.

and a Cu lid which is screwed in place. The packaged chip is placed inside a $\mu$–metal magnetic shield with access holes for miniature coaxial cables and mounted on the 2 K stage of a GM cryocooler. The operation of the RSFQ chip was first verified by connecting a voltage pulse pattern generator to the input channels. The voltage source was attenuated at room temperature to create pulses of similar amplitude to an SNSPD biased close to 25 μA. In this configuration the correct operating levels for the RSFQ circuit bias, the MC-DC/SFQ converters, the SQUID amplifier and an on-chip JTL can be calibrated. The JTL is a variable delay placed on input channel 1 between the SNSPD signal line and the input of the flip-flop circuit. Applying a current $I_{delay} = 0 - 3.5$ mA will off-set the arrival of SFQ pulses on channel 1 by a time proportional to the applied current up to 400 ps.

Two packaged SNSPDs are aligned with SMF-28 single mode optical fibre, thermally anchored to the same cold-head and connected to the RSFQ chip via semi-rigid coaxial cables as shown in Figure 5.11. A pulsed laser (Calmer Inc. pulse width $< 0.1$ ps 10 MHz repetition rate) is connected via optical fibre to variable attenuators, a polarisation controller, and a 50:50 beam-splitter in series. The two beam-splitter outputs are fed through two optical delay lines (0–400 ps) before being routed to the SNSPDs inside the cryostat. Figure 5.12 (a) shows the measured output counts from the RSFQ chip as function of $\tau$ controlled by the optical delay lines. Measured data are fitted to a Gaussian error function the derivative of which is plotted in 5.12 (b). The mean timing
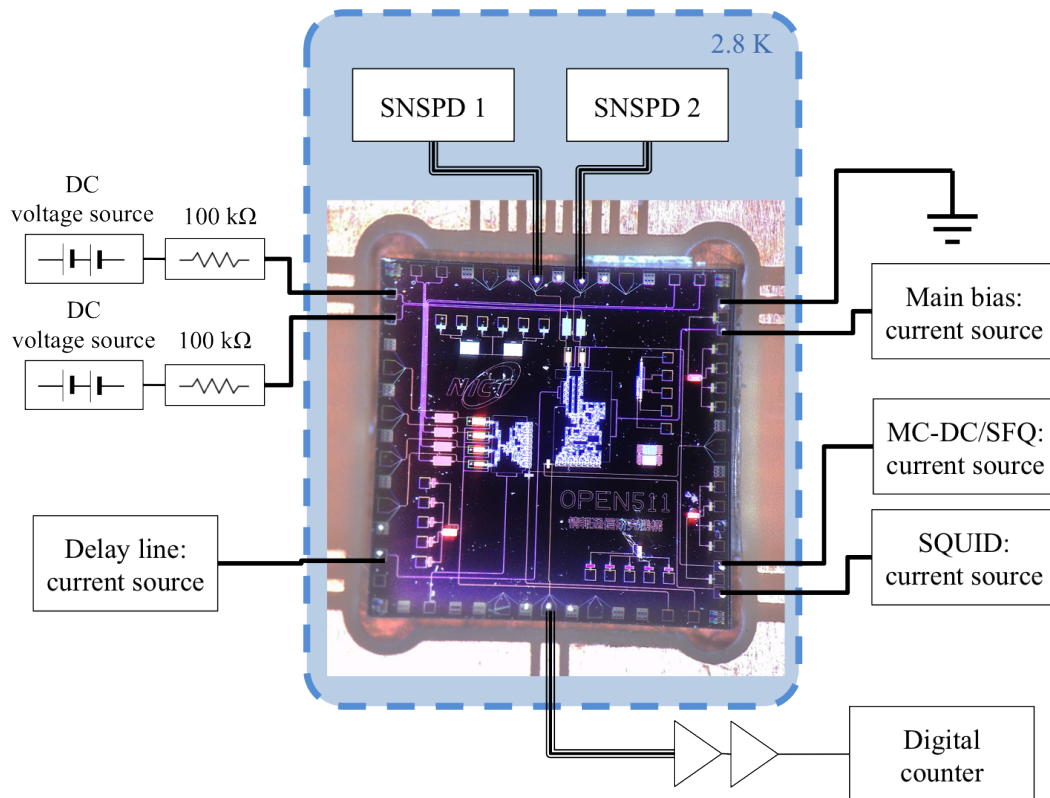
Fig. 5.10 An RSFQ logic chip is operated at low temperature in a GM cryocooler. The chip is connected to SNSPDs inside the cryostat via semi-rigid coaxial cables with DC bias for the SNSPDs routed through the RSFQ chip. Current sources at room temperature provide biasing and tuning for various elements of the RSFQ circuit including the main RSFQ bias, the SQUID amplifier, MC-DC/SFQ converters and a Josephson transmission line (JTL) delay line. The output from the RSFQ chip is routed through low noise amplifiers at room temperature to a digital pulse counter.

jitter $\overline{\triangle t}$ of the SNSPDs is calculated from the derivative using the equation:

$$\overline{\triangle t} = \frac{1}{\sqrt{2}}\text{FWHM} = 69.3 \text{ ps} \tag{5.2}$$

## 5.3   Conclusions

Following the successful demonstration of SNSPDs integrated with SNB waveguides QPICs were fabricated with the aim of generating waveguide coupled PL at the single photon level and routing it via a 50:50 beam-splitter to a pair of waveguide integrated detectors which could be used to perform a correlation measurement of QD single photon emission. The waveguide circuit requires
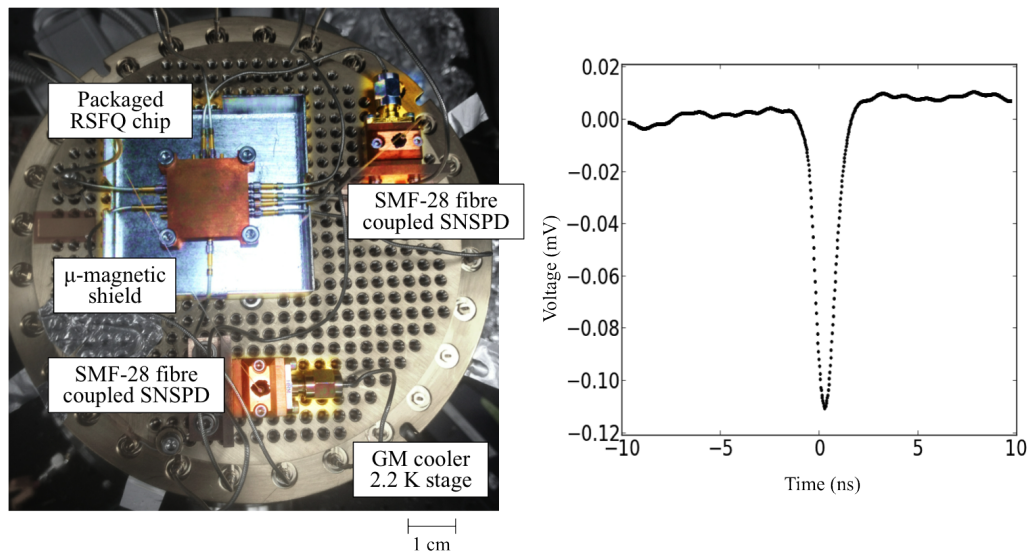
Fig. 5.11 An RSFQ chip is mounted in a Cu chip carrier and $\mu$-magnetic shielding at the 2 K stage of a GM cooler. SNSPDs coupled with SMF-28 optical fibre are anchored to the same cold-head and connected to the RSFQ circuit as shown in Figure 5.10. An oscilloscope trace of the RSFQ output pulse is shown.
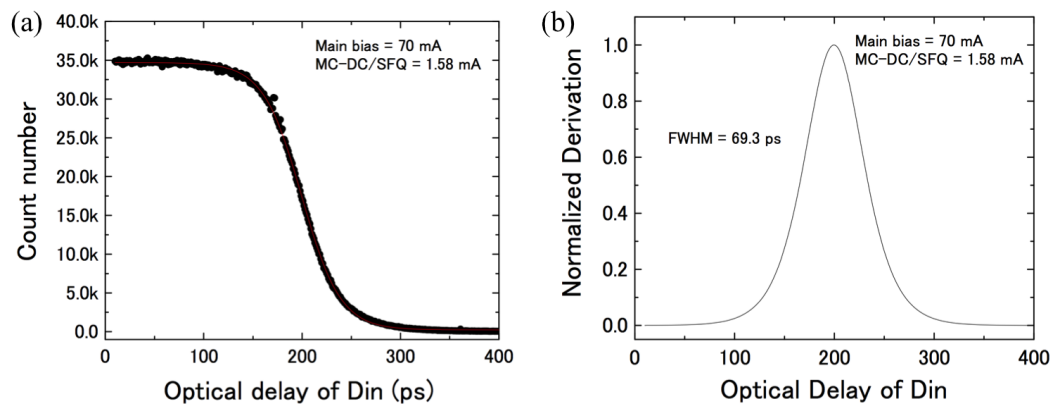


Fig. 5.12 **(a)** Two SNSPDs connected to the inputs of an RSFQ circuit are illuminated with light pulsed laser light routed through a 50:50 beam-splitter. Coincidence counts between the two electrical input channels are recorded as a function of time delay between the two optical path lenghts. **(b)** The derivative of the measured data gives a calculated average timing jitter of the SNSPDs. Data measured by Dr. Shigehito Miki at NICT Kobe.

filtering for the dual purposes of removing pump light and removing unwanted PL from the quantum dot ensemble, both of which would reduce visibility of a $g^{(2)}(0)$ correlation measurement if they are picked up at the detector. A 1D PhC cavity was included in the SNB design in order to perform the necessary filtering. The inclusion of 2D PhCs was necessary as supporting structures for the other suspended sections of the waveguide circuit. 2D PhCs perform the

dual functions of preventing collapse of the SNBs after wet etching and also holding the two arms of the directional coupler at correct separation.

Waveguide circuits and detectors were fabricated to the initial design specification and detectors were again confirmed to be sensitive to single photons at $\lambda = 1050$ nm under direct perpendicular illumination. However it was observed that light coupled into the input grating couplers of the waveguide circuit was unable to be detected at any rate above the background DCR even by adjusting the input photon flux $\Phi$ or the SNSPD bias current $I_B$. Simulations using calculated values of nanowire detection efficiency and estimates of the waveguide transmission efficiency $\eta_{waveguide}$ confirm that the combination of low $\eta_{registering}$ and low $\eta_{waveguide}$ render existing devices likely incapable of performing an on-chip HBT measurement.

Optimising the growth of superconducting thin films is already leading to improvements in waveguide integrated SNSPDs[173]. Waveguide losses can be mitigated with two possible strategies. Firstly the careful optimisation of design parameters will help to ensure low insertion loss between different segments and high transmission through 2D PhCs. Secondly exploration of different fabrication techniques may help to reduce the residues left from the multi-stage processing of superconducting films and GaAs/AlGaAs waveguides. The use of $SiO_2$ and SiN masks for protecting SNSPDs and PhCs during fabrication is a potential avenue for exploration[255]. Strategies to reduce the level of backscattered light (such as the inclusion of anti-reflection coating on the substrate back side) could also be included in future fabrication efforts [257].

RSFQ logic circuits were designed and fabricated at NICT in Japan with the capability of comparing voltage pulses generated by SNSPDs with high efficiency and low timing jitter. The performance of the RSFQ circuit was characterised by measuring the jitter of two SNSPDs illuminated with coherent laser light. The same device is suitable for performing correlation measurements on SPSs using SNSPDs and a variable delay between input channels. In a correlation experiment for a sub-Poissonian stream of single photons the coincidence count rate is expected to disappear at zero time delay whereas a correlated pair source is expected to exhibit a sharp increase in coincidence counts at zero time delay. The prospect of processing detector signals at low temperature with low timing jitter and fast feed-forward of information is highly promising for future development of QPICs for quantum information processing.

# Chapter 6

# Detectors enhanced by multi-layer optical cavities

*This Chapter presents results of the fabrication and characterisation of superconducting nanowire single photon detectors (SNSPDs) fabricated on multi-layered optical cavities designed to enhance absorption of light at the detector and provide high efficiency detectors tailored to specific applications. A carefully designed cavity will promote near unity absorption of photons into the active element of an SNSPD. GaAs/AlGaAs distributed Bragg reflector (DBR) substrates were grown at the University of Sheffield by Dr. Ed Clarke which were used by the author to fabricate and characterise SNSPDs. At National Institute of Information and Communication Technology, Japan (NICT) Kobe SNSPDs were fabricated on dielectric multi-layer substrates by Dr. Shigehito Miki and characterised by Dr. Taro Yamashita and the author.*

## 6.1 Detectors fabricated on GaAs Bragg mirrors

SNSPDs are strong candidates for detectors of single infrared photons with several applications having an immediate need for practical high efficiency detector systems. Single photon detectors are integral to the characterisation of single photon sources (SPSs), an essential technology for creating optical devices that harness the quantum properties of light. Semiconductor quantum dots (QDs) are highly promising as sources of single photons on demand. The second order correlation function $g^{(2)}(\tau)$ of photons from an SPS is of particular interest in quantum information processing as described in Sections 2.1.3 and

2.3. The dark count rate and timing jitter of the detectors have a direct influence over the resolution and visibility of coincidences in an Hanbury-Brown Twiss (HBT) measurement. It is also beneficial for both detectors to be of high and comparable efficiency so that coincidences can be registered at a high rate. InAs QDs grown by molecular beam epitaxy (MBE) at the EPSRC National Centre for III-V Technologies emit photons in the range $900 \text{ nm} \leq \lambda \leq 1000 \text{ nm}$. QD experiments at the University of Sheffield currently rely on silicon single photon avalanche diodes (SPADs) for single photon detection however the Si band-gap curtails detection efficiency at longer wavelengths ($\lambda > 900 \text{ nm}$) [58, 300].

At telecoms wavelengths there is also much demand for high efficiency single photon detectors. It is possible to implement secure communications using quantum key distribution (QKD) over optical fibres but to maximise the distance between communicating parties single photon detectors must have very low dark counts and low timing jitter in addition to high efficiency at the peak transmission band $\lambda = 1550 \text{ nm}$ [301]. With a band-gap of 1.7 µm InGaAs SPADs are a commercially available option for single photon detection however the high dark count and after-pulsing rates require the use of bias gating or forced dead-times to achieve any practical signal to noise ratio. These factors have significant impact on the maximum count rate of a QKD receiver and therefore SNSPDs are well placed to enable faster detection of successive photons and ultimately a faster data transfer rate.

To optimise detection efficiency the substrate of an SNSPD can be modified to create an optical cavity which enhances absorption of photons into the nanowire at target wavelengths. DBR are dielectric mirrors with high reflectivity in a specific range around a central wavelength $\lambda_0$ achieving very high reflectivity due to constructive interference. DBR structures were designed at the University of Sheffield to be grown on GaAs wafers using alternating bi-layers of GaAs and $Al_{0.8}Ga_{0.2}As$. Two variations of the design were optimised for reflection at $\lambda_0 = 1550 \text{ nm}$ and $\lambda_0 = 950 \text{ nm}$.

### 6.1.1 Device fabrication

Substrates were prepared with 600 µm thickness GaAs underlying a DBR stack of 29 $\lambda_0/4$ pairs of GaAs and AlGaAs layers topped by an additional $\lambda_0/4$ AlGaAs layer and a final $\lambda_0/2$ GaAs layer. The quarter wavelength thicknesses were 67.0 nm (114.9 nm) of GaAs and 76.9 nm (128.4 nm) of AlGaAs for the

$\lambda_0 = 950$ nm (1550 nm) mirrors. Figure 6.1 shows the simulated reflectivity of these substrates. The same graphs includes a simulation of the reflectivity from design parameters as well as measurements of the normal incidence reflectivity taken at multiple location over the wafer surface. In both cases the centre of the reflectivity band is slightly red-shifted towards the centre of the wafer with circular symmetry. For both designs the width $w$ of the reflectivity band is $> 100$ nm and the deviation in the centre wavelength of the stop-band across the wafer does not exceed $w/2$. Superconducting films of 8 nm thick NbTiN were grown on DBR substrates by Star Cryoelectronics Inc. [298] before sending to the University of Glasgow for fabrication of SNSPDs using the methods described in Chapter 3.
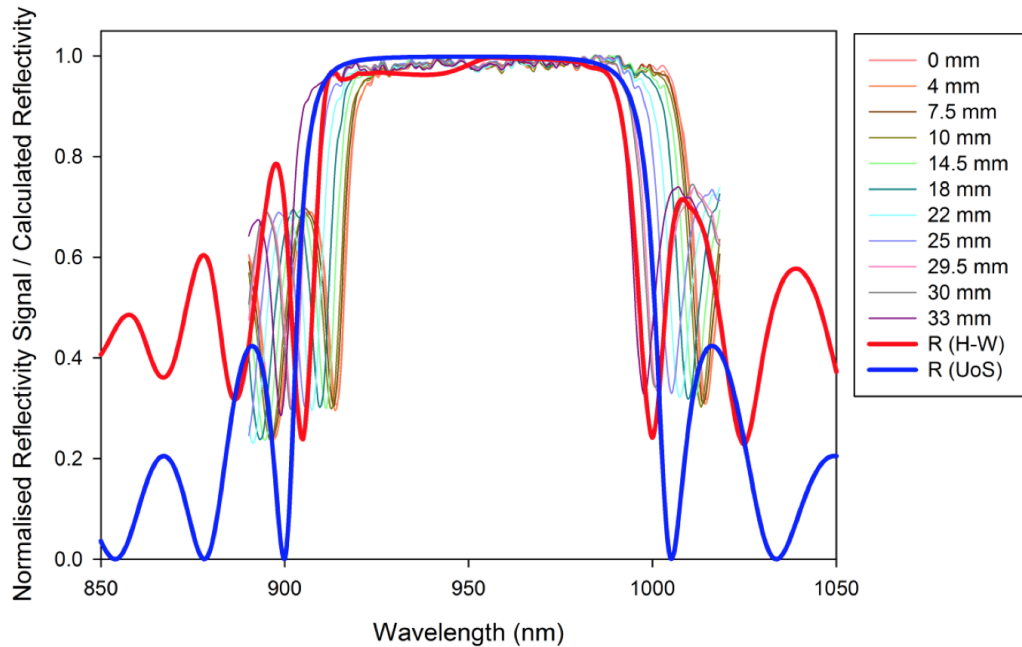


Fig. 6.1 The reflectivity of DBR mirrors was simulated by calculating the electric field immediately above the dielectric stack where the nanowire detector is located under normal incidence illumination. Essential Macleod (Thin films Inc.) was used to perform simulations (thick red and blue lines). Following DBR deposition wafers were characterised by normal incidence reflectivity at varying distances from the centre (thin coloured lines). The same data were compiled for 950 nm (pictured) and 1550 nm (see Figure 6.6) DBRs.

During MBE growth so called oval defects are formed within the material of the DBR. Although significant in height they are spread relatively far apart. The surface density of these features on the 1550 nm DBR mirror was calculated to be $6.34 \times 10^4$ cm$^{-2}$ from optical microscopy images. Fabrication of highly efficient SNSPDs is totally reliant on the deposition of superconducting thin

films of high quality and uniformity. Thin films of NbTiN were deposited by DC magnetron sputtering onto both wafers by Star Cryoelectronics Inc. The wafers were diced into 1 cm square pieces and films of 6 nm and 8 nm thickness deposited. The superconducting critical temperature of the films were measured at the University of Glasgow with 7 K $\leq T_C \leq$ 10 K. Surface roughness was measured with AFM following DBR growth. RMS roughness of 0.5 nm (0.6 nm) was recorded for 950 nm (1550 nm) DBR substrates. Surface roughness after NbTiN thin film deposition was measured by AFM at the University of Glasgow. The new RMS roughness of the 950 nm DBR samples was > 2 nm. Figure 6.2 shows oval defects measured by AFM with prominence of 200 nm. Although most defects are > 5 μm in width occurrences of defects overlapping sensitive features of the detectors were very infrequent.
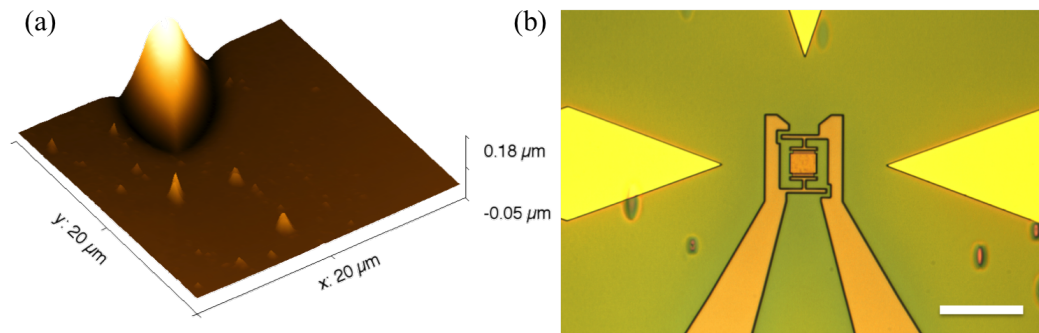


Fig. 6.2 **(a)** AFM micrograph of a region of DBR substrate containing an oval defect. **(b)** An optical micrograph of the surface after detector fabrication shows the distribution of oval defects and confirms that none overlap the detector's smallest features. Scale bar is 20 μm.

### 6.1.2   Device characterisation

Low temperature electrical and optical characterisations of devices were first performed in the pulse-tube cooler as described in Section 3.2.4. Table 6.1 contains room temperature resistance measurements and critical currents measured at 3.7 K.

Measuring a device's kinetic inductance $L_K$ as a function of bias current $I_B$ provides a closer look at the uniformity of the nanowire (see Section 3.2.3). Figure 6.3 shows measured data for 3 nanowire meanders patterned on GaAs/AlGaAs DBR mirrors. The data are fitted to a curve with fitting parameter $C$. The curve for $C = 1$ is shown in black and represents a perfectly uniform nanowire. The device with highest measured uniformity has $C = 0.75$.

| DBR $\lambda_0$ | Nanowire dimensions | | | | $R_{300K}$ | $I_C$ |
|---|---|---|---|---|---|---|
| | Depth | Width | Spacing | Active area | | |
| 950 nm | 8 nm | 130 nm | 75 nm | $5 \times 5$ μm² | 60–160 kΩ | 5–7 μA |
| 950 nm | 8 nm | 90 nm | 90 nm | $10 \times 10$ μm² | 1200–1800 kΩ | 12–20 μA |
| 1550 nm | 8 nm | 65 nm | 105 nm | $10 \times 10$ μm² | 180–660 kΩ | 2–12 μA |

Table 6.1 Electrical properties of SNSPDs fabricated on GaAs/AlGaAs DBR substrates
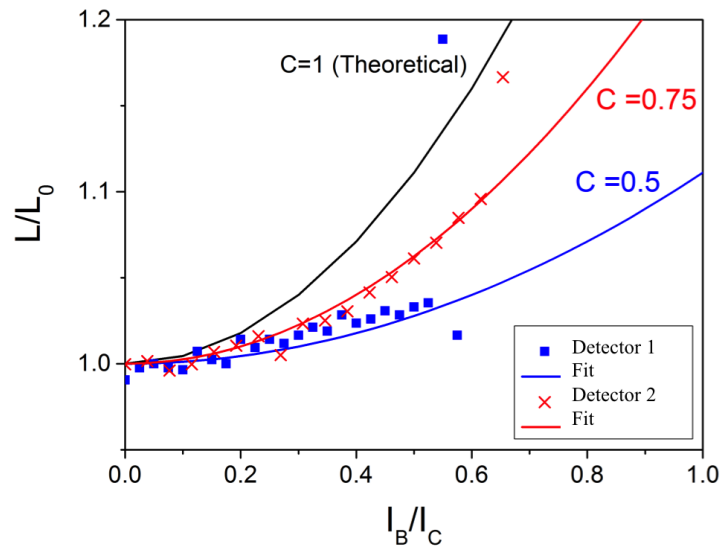


Fig. 6.3 Nanowire inductance is measured as a function of bias current at low temperature for two SNSPDs both with 90 nm wire width covering a 10 μm × 10 μm square area. The data is fitted to a curve with fitting parameter $C$ (equation 3.2). For an ideal uniform nanowire $C = 1$ (black line). The fitted $C$ values for two detectors are $C = 0.75$ (red line) and $C = 0.5$ give an indication of the presence of constrictions along the nanowire. The total circuit inductance is dominated by the kinetic inductance $L_K$ of the superconducting nanowire. Since $L_K \propto l/A$, where $l$ is the wire length and $A$ the nanowire cross-section, distinct segments of the nanowire will contribute differently to the total $L_K$ as they exceed $J_C$ at different times.

Nanowire uniformity ultimately affects the performance of an SNSPD. Photons absorbed at constricted sections will have the highest registering probability $\eta_{registering}$ with wider sections of wire suffering from lower $\eta_{registering}$ (see Section 2.2.3). The nano-optical testing capability at the University of Glasgow described in Section 3.2.4 allows SNSPDs to be characterised on a sub-pixel scale[293]. Mapping the spatial variation in a device's system detection efficiency (SDE) over its active area provides the ultimate test of nanowire uniformity.

(a)

(b)



5 µm
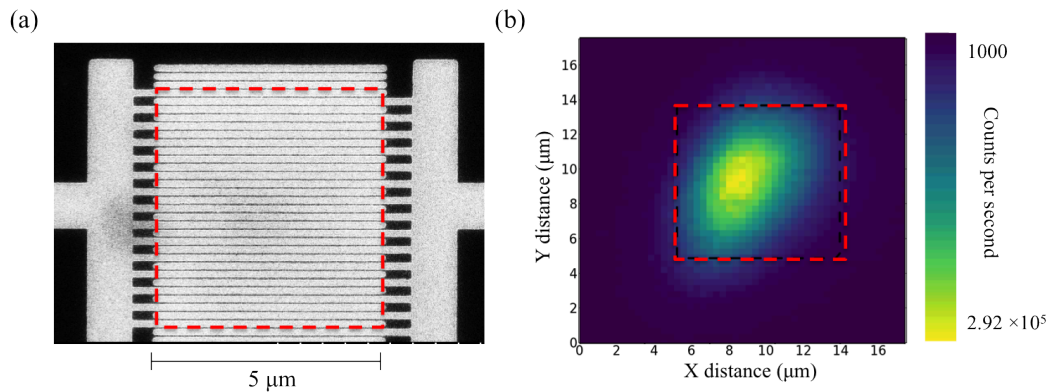
Fig. 6.4 **(a)** Scanning electron micrograph (SEM) of an SNSPD fabricated on a GaAs/AlGaAs DBR mirror $\lambda_0 = 1550$ nm. **(b)** A $\lambda = 1550$ nm laser diode is attenuated to the few photon level and scanned over the biased device to build up a count map. Areas of higher and lower photon sensitivity are easily visible across the active area of the device (red dashed box).

Figure 6.4 (c) shows a map of single photon response for a detector fabricated on a DBR with high reflectivity at $\lambda = 1550$ nm. With an optical spot size of 1.5 µm and the piezo scanner step size $\sim 100$ nm the count maps are able to resolve variations in the single photon sensitivity across the 5 µm × 5 µm active area of the device. The non-uniformity of the nanowire could be introduced during lithography or may have been present in the unpatterned film as a result of the deposition process or inhomogeneity in the DBR structure itself.

Packaging of detectors is important for the ease of applying the technology in photon counting experiments. A detector system was built at the University of Glasgow by Dr. Chandra Mouli Natarajan and shipped to the University of Sheffield for use in conjunction with quantum dot SPSs, both in characterising sources and performing quantum optical measurements. Devices were fabricated in the JWNC on $\lambda = 950$ nm DBR mirrors and fibre coupled with single mode HP1080 optical fibre. Following fabrication samples were protected by spin coating the top surface with resist and then glued to a metal chuck. Material is removed from the backside by pressing and rubbing the upended chuck onto fine grade abrasive diamond lapping film. Successively finer grades of film are used until the substrate backside is made optically smooth and the detector can be aligned to the 5 µm fibre core using the apparatus shown in Section 3.2.1. Figure 6.5 shows results from fibre coupled detectors characterised for SDE at the University of Glasgow (data measured by Dr. Chandra Mouli Natarajan).
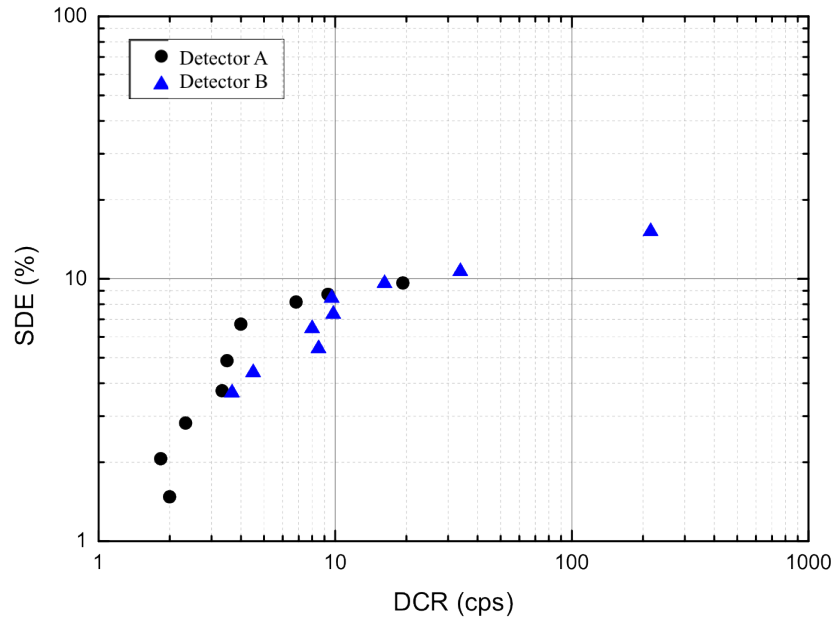
Fig. 6.5 Measured system detection efficiency (SDE) of two SNSPDs on GaAs/AlGaAs DBR substrates ($\lambda_0 = 950$ nm). At fixed current bias data is collected for detector count rate as a function of input photon flux and the efficiency calculated by fitting a curve to this data. Each data point in this figure represents the calculated efficiency parameter measured at a differnet bias level. The experiments were performed with fibre-coupled detectors in a 2.7 K Gifford-McMahon (GM) cryocooler illuminated with a $\lambda = 940$ nm laser diode. Black circles and blue triangles represent two detectors referred to as A and B respectively.

### 6.1.3 Wavelength dependence measurements

A system of 3 tunable lasers with overlapping spectral ranges were used to smoothly and precisely map the wavelength dependence of SDE for SNSPDs patterned on GaAs/AlGaAs DBR substrates in the range 1350 nm $\leq \lambda \leq$ 1650 nm. Whilst sweeping across wavelengths the output power and polarisation from the lasers varies. Both of these factors have a direct impact on SDE and must therefore be controlled for before the SDE spectrum is analysed. Variable optical power is controlled for by simply connecting a power meter to the laser output (all three are fed through one mixer/switch) and recording how the power varies during a full sweep. The measurement is repeated before and after testing the devices to check the stability and reproducibility of the power vs. wavelength curve. The SDE can then easily calculated on a point-by-point basis using the known optical power for each wavelength. At each wavelength the SDE measurement is repeated 256 times over a programmed range of polarisations (see Section 3.2.3).

Figure 6.6 shows the measured SDE for an SNSPD across a range of wavelengths covering the stop band of the DBR mirror on top of which it is fabricated. The upper (solid black line) and lower (solid red line) limits of SDE for each wavelength represent the alignment of photon polarisation either parallel or perpendicular to the nanowire respectively. For all wavelengths the ratio of $\frac{P_{min}}{P_{max}} \simeq 0.5$.
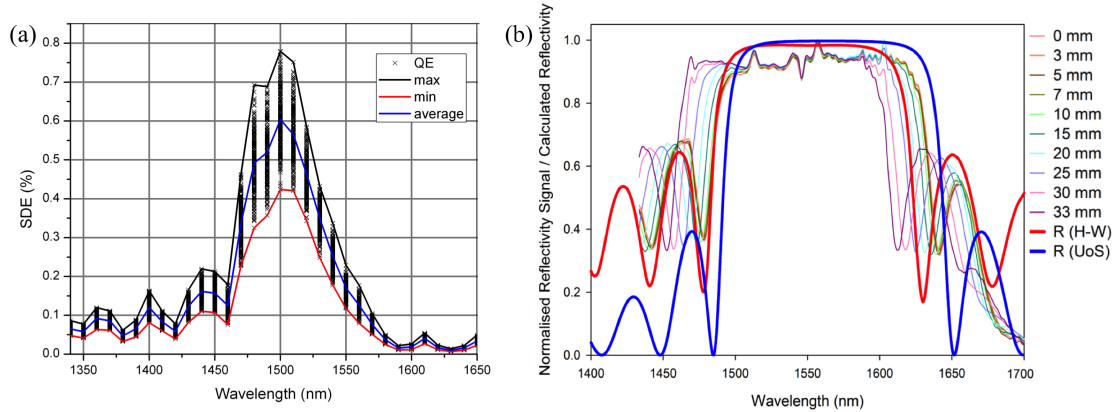


Fig. 6.6 **(a)** Wavelength dependence of system detection efficiency for SNSPDs on a GaAs/AlGaAs $\lambda_0$= 1550 nm DBR mirror. The detector is illuminated by focussed light from a minature confocal mounted at the 3.7 K stage of a pulse-tube cryocooler. A combination of 3 tuneable lasers is used to measure SDE at a range of wavelengths. Calculation of SDE includes a correction for the laser output power at each wavelength. Due to the random variations in polarisation across the lasers' range at each fixed wavelength the SDE measurement is repeated 256 times with a different randomly selected state of a variable polarisation controller (marked with black ×). **(b)** Simulated reflectivity spectra for the detector substrate. Simulation and measurement of a similar substrate with different $\lambda_0$ are detailed in Figure 6.1.

**Inclusion of DBR detectors in a tunable optical cavity**

A tunable cavity was created to maximise the absorption of light from an optical fibre into a thin film SNSPD which can often be the limiting factor in achieving high efficiency single photon detection. A microlens with a DBR coating is glued to the facet of a single mode optical fibre mounted on piezoelectric motors which are used to adjust the cavity length with high precision creating a stable resonant mode that can be tuned over a wavelength range of 100 nm. The operation of the tunable cavity was first verified with an SNSPD patterned in 4 nm NbN on an MgO substrate [294]. The top side of the detector is covered with a 100 nm thick Au mirror separated from the superconducting nanowire by a 250 nm SiO$_2$ layer. Light is coupled through a 250 nm anti-reflection coating

on the back side of the substrate completing the cavity between the Au mirror and the lensed fibre. The total cavity length includes the 45 µm substrate thickness, two 250 nm thick dielectric coatings and the gap to the fibre which is tuned over a range of $45 - 51$ µm. Simulations with Essential Macleod suggest that the cavity length can be adjusted to achieve near unity absorption efficiency into the nanowire detector. The detection efficiency was measured in a pulse tube (PT) cooler at 3.7 K confirming that with the cavity length tuned to maximise absorption the SDE is improved by 40% in comparison to illuminating the same detector with a bare fibre.

An SNSPD fabricated on a GaAs/AlGaAs DBR substrate ($\lambda_0 = 1550$ nm) was then mounted in the tunable cavity. The SDE was measured at a range of wavelengths (1400 nm $< \lambda <$ 1600 nm) and compared to data measured with a bare optical fibre over the same range in $\lambda$. Figure 6.7 shows the measured detection efficiencies from both set-ups as well as simulation of absorption into the nanowire performed with the Essential Macleod matrix transfer software package (from Thin Films Centre). The peak SDE was measured close to $\lambda = 1500$ nm as opposed to the design wavelength of 1550 nm. By using the tunable cavity it is possible to enhance the SDE at $\lambda = 1550$ nm by broadening the stop-band width in that wavelength region.

## 6.2 Non-periodic cavities for tailored absorption bandwidths

By using an optimisation algorithm in multi-layer cavity design it is possible to create a wide range of reflection spectra. Aperiodic multi-layers can achieve stop-band shapes beyond the capability of conventional DBR mirrors[141]. The potential applications of such tailored optical cavities are broad, ranging from fluorescence life-time measurements in the life sciences[302, 94, 95], to remote sensing in atmospheric[303, 304] and fibre based technologies[305]. A cavity with long wavelength cut-off will also act to suppress dark counts caused by black body radiation reaching the detector. For SNSPDs operated at $2 - 4$ K the central wavelengths of the black body radiation spectrum will be strongly suppressed, bringing dark count rates down closer to the intrinsic limits of the material[26, 77].

Whereas a DBR mirror utilises a stack of repeating pairs (of $\lambda_0/4$ dielectric layers) to create an optical stop-band, it is possible to sum the contribution
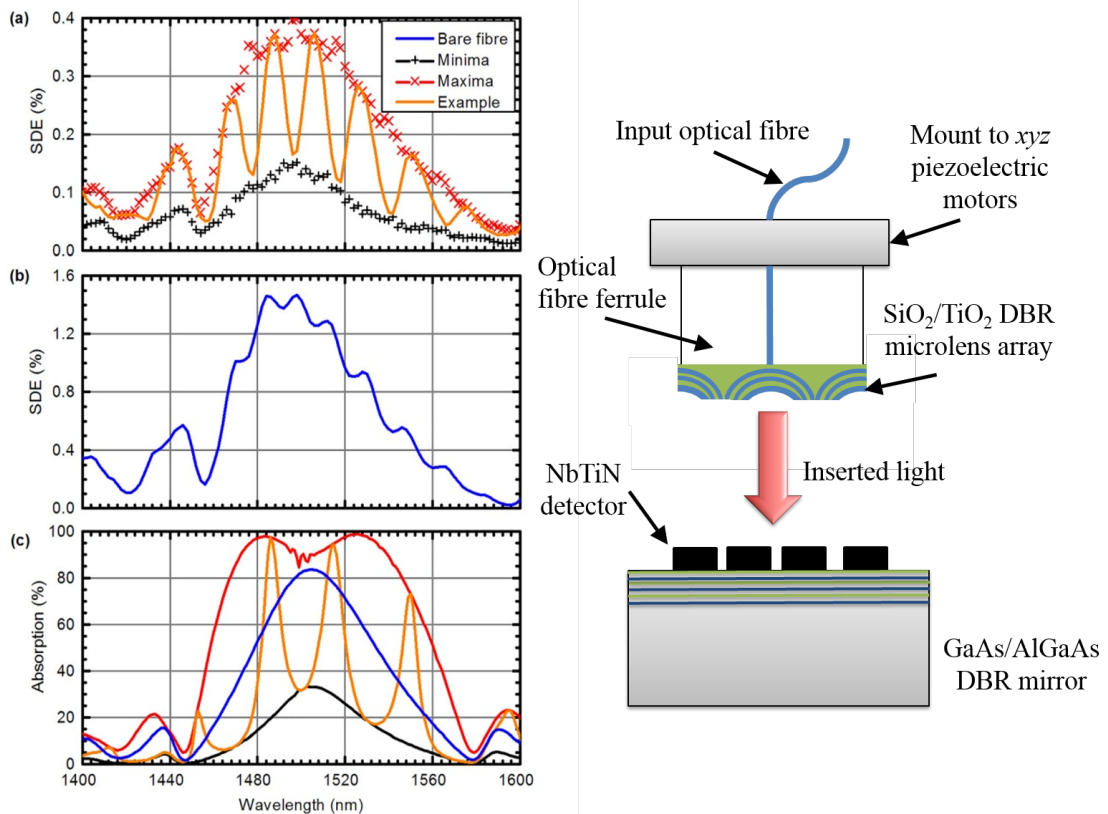
Fig. 6.7 An SNSPD on a $\lambda_0 = 1550$ nm DBR mirror comparison of system detection efficiency for a half-cavity **(a)** versus full tunable cavity **(b)** (as seen in schematic), figure adapted from reference 294. Experiemental restrictions resulted in the optimal cavity length not being established therefore **(a)** contains higher system losses. **(c)** Simulated absorption efficiencies are shown for full-cavity (red/orange/black lines) and bare fibre (blue line) illumination of the same detector. Note that the peak absorption occurs at $\lambda = 1500$ nm, not the designed $\lambda_0 = 1550$ nm. Inclusion of the tunable cavity enables enhanced aborption at $\lambda = 1550$ nm, beneficial for telecoms applications.

of any arbitrary set of interfaces to calculate a reflectivity function with a spectral shape not possible with the symmetry constraints of a DBR (see Figure 6.8). A method for computer aided design of non-periodic dielectric stacks was developed at NICT in Kobe, Japan. A computer program iterates through simulations of an optical stack by systematically varying the thickness of every layer (each one independent from all others). A single iteration of the simulation uses the matrix transfer method to simulate a set configuration of the optical stack calculating the absorption into a 10 nm top layer of NbN over a specified spectral range. To design a device the user specifies some properties of the stop-band shape and the program iterates through possible layer thickness combinations until the design parameters are met. After the layer thicknesses are optimised a second simulation utilises finite element analysis to confirm absorption into the nanowire for different polarisations of incoming photons. This process requires a 2 dimensional finite element simulation which is too demanding on computational resources to complete for every possible combination of layer thicknesses however it is efficient to use as a check on the outcome of 1D Macleod simulations, and to illustrate polarisation dependence of the patterned nanowires.

This method was used to design 3 absorption profiles that are of interest for applications in fluorescence imaging, Raman spectroscopy, remote sensing and quantum cryptography. The individual spectra exhibit features not available to ordinary DBR design, such as wider spectral width or sharp long-wavelength cut-off. The non-periodic dielectric stack designs were realised using $SiO_2$ an $TiO_2$ dielectric layers with NbN nanowire detectors patterned on top using electron beam lithography and reactive ion etching. The performance of detectors was measured at a range of relevant wavelengths and confirmed to show absorption enhancement and suppression in agreement with the design specifications. These detectors achieve high efficiency ($> 80\%$) at the desired wavelengths and strong suppression of detection for light of unwanted wavelengths.

Figure 6.9 shows simulated absorption spectra for two designed optical stop bands that were fabricated. Design 1 uses $\lambda_0 \simeq 500$ nm and for design 2 $\lambda_0 \simeq 800$ nm. Dielectric multi-layers (DMLs) were deposited on Si substrates with a $SiO_2$ buffer layer. Alternating layers of $TiO_2$ and $SiO_2$ were deposited by ion beam evaporation to the thicknesses specified in the individual designs. The refractive indices of these dielectric layers are 3.5 and 4.2 respectively. The dielectric stack terminates with a $\lambda/2$ layer of $SiO_2$ on top of which NbN is deposited by DC magnetron sputtering to a thickness of 10 nm. Nanowires and
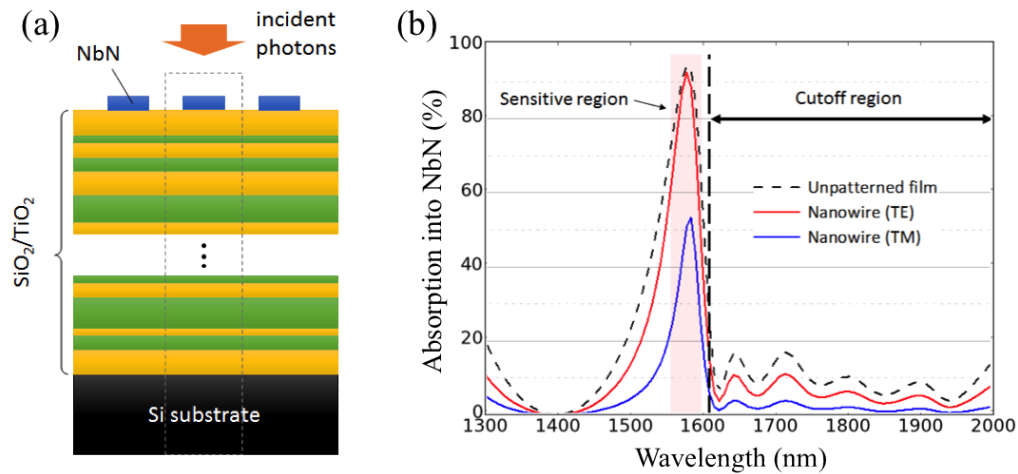
Fig. 6.8 Adapted from reference 141. **(a)** An aperiodic stack of alternating $SiO_2$ and $TiO_2$ layers is deposited on top of an Si substrate with a NbN superconducting nanowire single photon detector patterned on top. **(b)** By tailoring the individual dielectric layer thicknesses optical stop bands of numerous shapes can be created. One simulated example is a detector with high absorption at $\lambda= 1550$ nm and a sharp long wavelength cut-off.

electrical contacts were patterned by electron beam lithography and reactive ion etching. Devices were tested in a GM cryocooler operating at 2 K, optically addressed with single mode or multi-mode fibre aligned to the detector's active area. Device 1 contains 4 pixels in a square formation, each of which is biased separately. Multi-mode fibre is used to couple the detector array to a 60 µm wide optical spot. All detectors are current biased with a resistor and DC voltage source at room temperature. A bias tee outside the refrigerator connects 2 stages of amplification with a total gain of 50 dB to a digital counter. A pair of calibrated optical attenuators are used to reduce the output from a diode laser to the single photon level. The detector's efficiency is probed by comparing input photon number to the number of registered counts, over a range of different bias currents and photon fluxes. A selection of diode lasers of fixed wavelength were used to test the spectral response of detectors at a number of discrete points. A fibre polarisation controller is used to maximise the counts from the detector for a given photon flux and bias current. Without making a direct measurement of the polarisation of photons exiting the optical fibre it is assumed that the maximised count rate occurs when the light is polarised parallel to the nanowires.

The measured SDE of device 1 was 64% when operated as a 4 pixel array. Figure 6.10 shows the results of low temperature characterisation of device
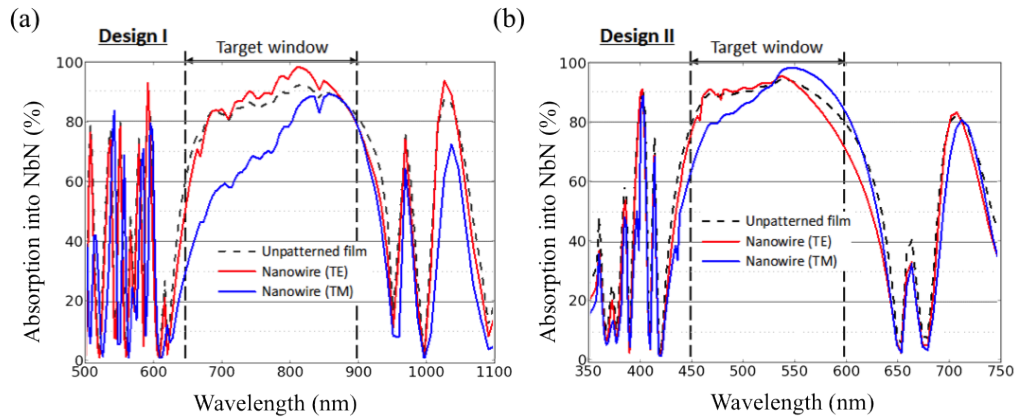
Fig. 6.9 Adapted from reference 141. Simulated absorption spectra for two fabricated SNSPDs on dielectric multilayers. The COMSOL software package was used to perform a finite element simulation of unpatterned 10 nm NbN films as well as patterned nanowires under parallel and perpendicular polarised illumination. **(a)** A broad stop band is designed to cover visible and near infrared wavelengths. **(b)** A narrower stop-band is designed for shorter wavelengths in the visible spectrum. Both detectors are designed to meet demand for high efficiency detectors with excellent timing properties in spectroscopy applications as well as multi-spectral light detection and ranging (LiDAR).

2. The dependence of SDE on bias current is seen to saturate at around $0.8I_C$. Saturation in the efficiency suggests that the nanowires are uniform and that the detector can be biased at a low dark count rate without an exponential reduction in registering efficiency. Tests at different wavelengths confirm that peak efficiency is reached within the designed band for maximum absorption. Wavelengths outside of the DBR stop-band have significantly suppressed efficiency, both for high and lower energy photons.

## 6.3 Conclusions

SNSPDs were fabricated on substrates with periodic and aperiodic multi-layer cavities designed to enhance absorption at specific wavelengths and create high-performance detectors tailored for specific applications. DBR mirrors can achieve near unity absorption efficiency of infrared photons into thin superconducting films also enabling greater ease of aligning and packaging detectors since the devices are transparent at wavelengths outside of the DBR stop-band in contrast to opaque metallic mirrors.

GaAs/AlGaAs DBRs were provided by the University of Sheffield and NbTiN thin superconducting films deposited by Star Cryoelectronics in the

(a)

(b)
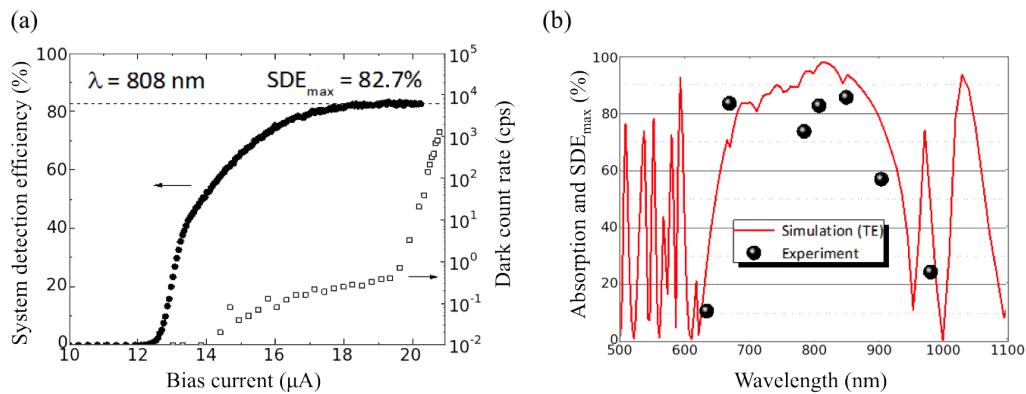
Fig. 6.10 Adapted from reference 141. Low temperature characterisation of an SNSPD fabricated on a dielectric multilayer with high reflectivity in the near infrared. **(a)** System detection efficiency was measured as a function of bias current at a fixed input photon flux. The detection efficiency is seen to saturate at bias currents below $I_C$ reaching a maximum value of 82.7%. With the light path blocked the detector dark count rate is recorded as a function of bias current. **(b)** Seven diode lasers covering a range of wavelengths were used to characterise the stop-band of dielectric multilayers and its effect on detection efficiency as a direct result of wavelength dependent absorption. The measured wavelength dependence (black circles) is in good agreement with the simulated stop-band (red line).

USA. At the University of Glasgow SNSPDs were fabricated on these substrates and characterised optically and electrically at low temperature. The detection of single infrared photons was confirmed and the spectral dependence of SDE on wavelength measured. The yield of uniform nanowires was low as evidenced by the inconsistency of $I_C$ and SDE across measured devices. The ultimate cause for this is likely to be constrictions in the nanowires however it is unclear whether these are mostly introduced during fabrication, film growth, or DBR growth.

Several other dielectric compounds have been used to realise cavities and DBRs for the enhancement of SNSPD performance. Notably $SiO_2/TaO_5$ bilayers have been deposited on Si wafers to create incredibly smooth surfaces. The same technology was developed for the extremely demanding application of mirrors in gravitational wave detectors. Very high quality detectors on $SiO_2/TaO_5$ DBRs with enhanced SDE at $\lambda = 1550$ nm (900 nm) peaking at 90% (85%) were recently demonstrated[140]. To achieve such outstanding results the fabrication procedure must be meticulously optimised. Firstly Si substrates must begin with absolutely minimal surface roughness. Chemical mechanical polishing, acid etching, and plasma ashing can be used to bring the surface roughness down below 1 nm RMS, approaching atomic smoothness.

The dielectric bilayer process adds $< 1$ nm to the substrate roughness. This is helped in part by applying identical DBR structures to both top and bottom sides of the wafer thus reducing strain and deformation at the surfaces. DC magnetron sputtering of Nb-based films can be carefully optimised over a number of parameters including stoichiometry and substrate temperature during deposition. Switching from NbN to amorphous WSi or MoSi in future may help with film uniformity as well as relaxing the requirements for the fabrication of ultra-narrow nanowires. With amorphous superconducting films it is possible to slightly increase nanowire width to achieve higher uniformity whilst maintaining high sensitivity to infrared photons.

At NICT a different type of mirror was used to create highly efficient reflectors for tailored wavelength bands. SNSPDs were fabricated in thin NbN superconducting films on aperiodic DMLs. The yield and uniformity of detectors was good and several high efficiency detectors were used to demonstrate 2 different mirror designs. The peak measured SDE was $> 80\%$ at $\lambda = 808$ nm. There are several factors that could contribute to the SDE being less than perfect. Firstly the temperature of operation could be decreased to increase the device's registering efficiency. This would come at a high cost however and the loss of convenience that comes with performing experiments in a commercially available GM cooler. The fact that the SDE appears to saturate at bias currents below $I_C$ (see Figure 6.10 (a)) is an indication of high quality superconducting films and nanowires without any major constrictions. Its is unknown though if the DML matches the design specification with a high degree of uniformity which leads to an uncertainty in the true probability of absorption of photons into the detector. The use of lasers tunable over a wide range would allow for a more full characterisation of both the system insertion losses as well as finding the true position of the absorption maximum. For similar reasons a tunable polarisation controller could be used to carefully select the optimum polarisation for input light. The novel method of using aperiodic DMLs for tailoring the wavelength dependence of SNSPDs can be applied to long wavelength cut-off filtering of dark counts as well as a host of future detector applications.

# Chapter 7

# Conclusions

## 7.1 Summary of results

Fabrication and experiments have been detailed in this thesis which relate to the application of superconducting nanowire single photon detectors to quantum information processing. The observation of quantum effects with photons is extremely demanding with low tolerance of losses and noise introduced at any stage of an experiment, from the source through to the detector. Superconducting nanowires were introduced as a photon counting technology in 2001 and over 15 years have undergone considerable technical development. Today they are a preferred choice of single photon detector particularly in applications demanding of low timing jitter, low dark counts and high efficiency at infrared wavelengths.

Optical quantum computing can be achieved with a combination of single photon sources, beam-splitters, phase shifters, single photon detectors and electrical information feed-forward. Integrated waveguide circuits present the best platform for such a quantum information processor that is both stable and scalable. The III-V semiconductor platform is suitable for both waveguide circuits and single photon sources in the form of InAs quantum dots. With photon emission occurring at $\lambda > 900$ nm the low efficiency of Si avalanche photodiodes at long wavelengths limits their use in III-V quantum photonics. Perhaps more critically the monolithic integration with waveguide circuits is clearly preferable for the single-layer constituents of SNSPDs as opposed to complex doped semiconductor junctions. This thesis presents novel demonstrations of detectors integrated with single mode suspended nanobeam waveguides as well as integrated waveguide circuits designed to perform quantum

photonic measurements entirely on-chip. These represent a step forward for optical quantum information processing.

### 7.1.1 Fabrication of waveguide circuits and integrated superconducting detectors

Fabrication processes were developed at the University of Glasgow based on methods developed elsewhere and optimised for the precise alignment of hairpin nanowires with single mode suspended nanobeam waveguides. Although working prototypes have been made, and the wires show uniform yield over each chip, there is substantial ground to be made up in terms of detector efficiency and waveguide losses. Superconducting nanowire detectors integrated with waveguide circuits were characterised at 3.7 K however the lower than expected superconducting transition temperature of NbTiN films precluded their use in photo-luminescence (PL) experiments conducted at 4.2 K. Detector efficiency can be hugely improved by the optimisation of film growth and with the use of alternative superconducting materials such as MoSi [173]. Waveguide losses can be mitigated by improving the final edge roughness following fabrication. Although the edge roughness of etch masks used is of good quality the total process including multiple etches and stripping leaves a significant amount of unwanted material distributed over device surfaces. One possible route to pursue is the use of HSQ resist and SiN masks for waveguide etching. These place a hard dielectric mask over the wires and might enable smooth waveguide etching without resist getting stuck in the holes of photonic crystals (PhC). Wires will also be protected from stronger cleaning processes, such as $O_2$ ashing, which might allow for a cleaner final device. The optical effect of a dielectric layer above the nanowire is likely to be worth the trade off for improved waveguide losses. Simulations could confirm this.

### 7.1.2 Testing integrated detectors with GaAs single mode waveguide circuits

Through the EPSRC Semiconductor Integrated Quantum Optical Circuits Programme Grant NbTiN films were grown on GaAs substrates with embedded InAs quantum dots and a buried AlGaAs sacrificial layer. Substrates were grown by molecular beam epitaxy (MBE) in Sheffield and films by DC magnetron sputtering in USA. The initial specification was for films to be $6 - 10$ nm

thick with superconducting critical temperature $T_C > 10$ K. Films delivered were of specified thickness however $5$ K $\leq T_C \leq 10$ K. Low $T_C$ is a possible indicator of inhomogeneity across the film material and defects are a likely cause of constrictions within nanowire detectors which restrict detection efficiency. Detectors were fabricated in successful integration with suspended nanobeam (SNB) waveguides of single mode dimensions for $\lambda \geq 950$ nm. Waveguide integrated detectors were shown to be responsive to light at the single photon level showing detection of direct perpendicular illumination as well as light from a waveguide mode coupled in via a diffraction grating. The registering efficiency of waveguide integrated detectors was calculated from the measured system detection efficiency (SDE) and estimates of the coupling and absorption losses. Out of several detectors tested the best recorded efficiency was 9.71 %. Waveguide circuits with integrated SNSPDs were designed and fabricated for the purpose of carrying out an on-chip correlation measurement of single photons emitted from an InAs quantum dot embedded within the waveguide circuit. A 50:50 beam-splitter, a 1-D PhC filter, and 2-D PhC waveguides were added to the circuit. The first fabricated devices were shown to have operational detectors but to be unable to verify the detection of waveguide coupled light nor the correct operation of the newly introduced waveguide components. The combination of low efficiency detectors and waveguide losses likely leaves the count rate of waveguide coupled photons lower than the background noise caused by detector dark counts and photons back-scattered through the substrate. Although all components were separately confirmed to function within acceptable parameters it would be highly beneficial to systematically optimise the waveguide circuit. Simulations of individual components can be used to maximise transmission and multi-component simulations can be used to minimise insertion losses and back reflections from mode mismatch between successive components. Systematic testing of waveguide circuits with iterative feedback to fabrication parameters could be used to create waveguide circuits with high transmission from source to detector and also achieve accurate 50:50 beam-splitters as well as filters with high rejection of light at pump-wavelength and unwanted exciton wavelengths.

### 7.1.3 Superconducting logic circuits for SNSPD read-out

Rapid single flux quantum (RSFQ) logic is a promising supporting technology for SNSPDs. Digital circuits can be built from Josephson junctions into custom

designed processors that process signals from SNSPD very quickly with low timing jitter and low power consumption. RSFQ circuits are well suited to multiplexing arrays of SNSPDs and potentially providing fast readout and feed-forward of information in an optical quantum computer. At NICT, Japan RSFQ circuits are designed and fabricated specifically for use with SNSPDs. An RSFQ circuit was tested by the author as a demonstrator of the low timing jitter of RSFQ circuits. The circuit was designed to combine the signal from two SNSPDs in a flip-flop circuit with a variable time delay between the two inputs. This enables a measurement of the intrinsic timing jitter from superconducting detectors without including the limiting performance of room temperature amplification and TCSPC electronics.

### 7.1.4 Detectors enhanced by multi-layer cavities

Multi-layer cavities were investigated as a means of enhancing detector performance as wavelengths of specific interest. Distributed Bragg reflectors (DBRs) were grown in GaAs/AlGaAs at the University of Sheffield by MBE with thin films of superconducting NbTiN deposited on top by DC magnetron sputtering. At the University of Glasgow SNSPDs were patterned on these substrates, coupled with single mode optical fibre, and tested at low temperature. At 2.7 K detectors optimised for absorption at $\lambda = 950$ nm were shown to have 20 % SDE at that wavelength. Devices designed for high efficiency at $\lambda = 1550$ nm were tested at 3.7 K under a miniature confocal microscope. The spatial uniformity of detectors was mapped and the SDE measured over a broad range of wavelengths and polarisations. At NICT, Japan detectors were fabricated on aperiodic dielectric multi-layers made from $SiO_2/TiO_2$. Detectors were fabricated on theses substrates from NbN superconducting thin films and tested at 2.2 K in a GM cryocooler with single mode optical fibre coupling. Rather than use the repeating layer system of a Bragg reflector a computer program optimises the cavity design by varying layer thicknesses independently from each other. In this way, stop band shapes impossible to realize with periodic DBRs can be acheived. Two optical windows were designed and fabricated, one with very wide bandwidth and one in the visible range. SNSPDs were tested at a range of wavelengths around the designed stop-band and confirmed to have very high efficiency in correspondence to the designed absorption maxima and minima. For devices of the first design the highest measured system detection efficiency (SDE) was 80% at $\lambda = 800$ nm. Devices fabricated to the second design achieved an SDE of 64% at $\lambda = 640$ nm.

## 7.2 Outlook

Work continues in Glasgow on the development of waveguide integrated superconducting single photon detectors. With in-house superconducting film deposition capability NbN, NbTiN and MoSi films are being grown on a range of substrates including silicon-on-insulator. Through Professor Marc Sorel there is considerable expertise in Glasgow with Si waveguide circuits which can be leveraged in the future to create quantum enhanced devices with integrated single photon detectors.

Apparatus is being assembled for the screening of optical circuits with integrated detectors. Utilising RF probes, a fibre array, and piezoelectric motors multiple devices can be tested across a single sample in one cool-down which will be a huge boost to the development process of quantum photonic integrated circuits (QPICs). Thorough optimisation of waveguide structures and integrated detectors will be necessary to achieve low loss transmission of single photons as well as efficient detection. Precise calibration of waveguide integrated detectors remains challenging as it can be difficult to accurately predict photon flux inside a waveguide circuit making accurate calibration difficult. Incorporating a beam splitter leading to an output grating coupler can act as a reference port for monitoring the photon flux within a waveguide circuit however an unknown splitting ratio, waveguide bend losses and coupler losses can all contribute significantly to the uncertainty of such a measurement.

The development of robust sources of pure single photon states that can be reliably fabricated *en masse* are vital to the progress of QPICs. State of the art semiconductor quantum dots (QDs) are progressing towards emission at telecom wavelengths and fabrication with deterministic placement. The quality and efficiency of individual QDs remains somewhat unpredictable although techniques for tuning and enhancing PL emission are currently being developed. Several alternative single photon sources have been proposed as waveguide integrable devices. Doped carbon nanotubes (CNTs) can be manufactured in large quantities and single one deposited onto electrical contacts in close proximity to an optical waveguide with electrical pumping resulting in single photon emission. Photon pair sources in Si waveguide spirals and ring resonators are both attractive candidates for inclusion in silicon QPICs and potential integration with CMOS control electronics.

Recent review articles provide great detail on the variety of current research into quantum integrated photonics [210, 306]. A number of different

material platforms are considered all of which have seen increased development and integration of components suitable for quantum information processing. Promising routes towards large scale integration of quantum photonic circuits are presented by a number of possibilities including GaAs and III–V materials, widely compatible Si photonics, and through hybrid devices [307, 308].

# References

[1] http://folk.uio.no/sigurdkn/pingmap/. World maps of ping time as a function of location.

[2] Francis Galton. On the Construction of Isochronic Passage Charts. *Proceedings of the Royal Geographical Society*, 1881.

[3] http://www.nisenet.org/catalog/scientific-image-human-red-blood-cells-sem. Scientific Image - Human Red Blood Cells (SEM). Janice Carr, CDC.

[4] Christiaan Huygens. *Traité de la lumière: où sont expliquées les causes de ce qui luy arrive dans la reflexion, & dans la refraction, et particulierement dans l'etrange refraction du cistal d'Islande.* Chez Pierre Van der Aa, 1690.

[5] Isaac Newton. *Opticks: or a treatise of the reflexions, refractions, inflexions and colours of light.* 1704.

[6] James Clerk Maxwell. *A treatise on electricity and magnetism*, volume 1. Clarendon press, 1881.

[7] Albert Michelson and Edward Morley. On the relative motion of the earth and the luminiferous ether. *Am. J. Science*, 34:333, 1887.

[8] Albert Einstein. Zur elektrodynamik bewegter körper. *Annalen der physik*, 322(10):891–921, 1905.

[9] David J Griffiths. *Introduction to electrodynamics.* American Association of Physics Teachers, 2005.

[10] Open Courseware, Physics, Massachusetts Institute of Technology: MIT. https://ocw.mit.edu/courses/physics/.

[11] HyperPhysics website hosted by the Department of Physics and Astronomy, Georgia State University. http://hyperphysics.phy-astr.gsu.edu/hbase/emcon.html.

[12] Max Planck. Über eine Verbesserung der Wien'schen Spectralgleichung. *Verhandlungen der Deutschen Physikalischen Gesellschaft*, 2:202–204, 1900.

[13] Max Planck. Zur Theorie des Gesetzes der Energieverteilung im Normalspectrum. *Verhandlungen der Deutschen Physikalischen Gesellschaft*, 2:237–245, 1900.

[14] Albert Einstein. On a heuristic point of view concerning the generation and transformation of light. *Annals of Physics*, 322(6):132–148, 1905.

[15] Gilbert N Lewis. The conservation of photons. *Nature*, 118:874–875, 1926.

[16] Paul AM Dirac. The quantum theory of the emission and absorption of radiation. In *Proceedings of the Royal Society of London A: Mathematical, Physical and Engineering Sciences*, volume 114, pages 243–265. The Royal Society, 1927.

[17] Willis E Lamb Jr. Theory of an optical maser. *Physical Review*, 134(6A):A1429, 1964.

[18] Roy J Glauber. The quantum theory of optical coherence. *Physical Review*, 130(6):2529, 1963.

[19] Roy J Glauber. Nobel lecture: One hundred years of light quanta. *Reviews of modern physics*, 78(4):1267, 2006.

[20] A Einstein, B Podolsky, and N Rosen. Can Quantum-Mechanical Description of Physical Reality Be Considered Complete? *Physical Review*, 47(10):777–780, 1935.

[21] Marissa Giustina, Alexandra Mech, Sven Ramelow, Bernhard Wittmann, Johannes Kofler, Jörn Beyer, Adriana Lita, Brice Calkins, Thomas Gerrits, Sae Woo Nam, et al. Bell violation using entangled photons without the fair-sampling assumption. *Nature*, 497(7448):227–230, 2013.

[22] Nigel Sim, Mei Fun Cheng, Dmitri Bessarab, C Michael Jones, and Leonid A Krivitsky. Measurement of photon statistics with live photoreceptor cells. *Physical Review Letters*, 109(11):113601, 2012.

[23] Foster Rieke and Denis A Baylor. Single-photon detection by rod cells of the retina. *Reviews of Modern Physics*, 70(3):1027, 1998.

[24] Silvano Donati. *Photodetectors: devices, circuits, and applications.* Prentice Hall PTR, 1999.

[25] Robert H Hadfield. Single-photon detectors for optical quantum information applications. *Nature Photonics*, 3(12):696–705, 2009.

[26] Hiroyuki Shibata, Kaoru Shimizu, Hiroki Takesue, and Yasuhiro Tokura. Ultimate low system dark-count rate for superconducting nanowire single-photon detector. *Optics Letters*, 40(14):3428–31, 2015.

[27] R Clark Jones. Proposal of the detectivity d** for detectors limited by radiation noise. *JOSA*, 50(11):1058–1059, 1960.

[28] S Cova, M Ghioni, A Lotito, I Rech, and F Zappa. Evolution and prospects for single-photon avalanche diodes and quenching circuits. *Journal of Modern Optics*, 51(9-10):1267–1288, 2004.

[29] C. Kittel. *Introduction to Solid State Physics*. John Wiley, New York, 6th edition, 1986.

[30] Rostislav V Roussev, Carsten Langrock, Jonathan R Kurz, and M M Fejer. Periodically poled lithium niobate waveguide sum-frequency generator for efficient single-photon detection at communication wavelengths. *Optics Letters*, 29(13):1518–20, 2004.

[31] Carsten Langrock, Eleni Diamanti, Rostislav V Roussev, Yoshihisa Yamamoto, Martin M Fejer, and Hiroki Takesue. Highly efficient single-photon detection at communication wavelengths by use of upconversion in reverse-proton-exchanged periodically poled LiNbO$_3$ waveguides. *Optics Letters*, 30(13):1725–1727, 2005.

[32] A Lacaita, F Zappa, S Cova, and P Lovati. Single-photon detection beyond 1 $\mu$m: performance of commercially available InGaAs/InP detectors. *Applied Optics*, 35(16):2986–2996, 1996.

[33] F Zappa, P Webb, A Lacaita, and S Cova. Nanosecond single-photon timing with InGaAs/InP photodiodes. *Optics Letters*, 19(11):846–848, 1994.

[34] Philip A Hiskett, Gerald S Buller, Alison Y Loudon, Jason M Smith, Ivair Gontijo, Andrew C Walker, Paul D Townsend, and Michael J Robertson. Performance and design of InGaAs/InP photodiodes for single-photon counting at 1.55 $\mu$m. *Applied Optics*, 39(36):6818–6829, 2000.

[35] Jun Zhang, Patrick Eraerds, Nino Walenta, Claudio Barreiro, Rob Thew, and Hugo Zbinden. 2.23 GHz gating InGaAs/InP single-photon avalanche diode for quantum key distribution. In *SPIE Defense, Security, and Sensing*, page 76810Z. International Society for Optics and Photonics, 2010.

[36] Jun Zhang, Rob Thew, Claudio Barreiro, and Hugo Zbinden. Practical fast gate rate InGaAs/InP single-photon avalanche photodiodes. *Applied Physics Letters*, 95(9):091103, 2009.

[37] Robert Thomas Thew, Damien Stucki, J-D Gautier, Hugo Zbinden, and A Rochas. Free-running InGaAs/InP avalanche photodiode with active quenching for single photon counting at telecom wavelengths. *Applied Physics Letters*, 91(20):201114, 2007.

[38] Photomultiplier tube manufacturers: Hamamatsu Photonics. http://www.hamamatsu.com/eu/en/index.html.

[39] Simone Tisa, Franco Zappa, and Sergio Cova. Monolithic quad-cells for single-photon timing and tracking. In *International Congress on Optics and Optoelectronics*, pages 658305–658305. International Society for Optics and Photonics, 2007.

[40] Adriana E Lita, Aaron J Miller, and Sae Woo Nam. Counting near-infrared single-photons with 95% efficiency. *Optics Express*, 16(5):3032–3040, 2008.

[41] Chandra M Natarajan, Michael G Tanner, and Robert H Hadfield. Superconducting nanowire single-photon detectors: physics and applications. *Superconductor Science and Technology*, 25(6):063001, 2012.

[42] A Verevkin, J Zhang, Roman Sobolewski, A Lipatov, O Okunev, G Chulkova, A Korneev, K Smirnov, GN Gol'tsman, and A Semenov. Detection efficiency of large-active-area NbN single-photon superconducting detectors in the ultraviolet to near-infrared range. *Applied Physics Letters*, 80(25):4687–4689, 2002.

[43] A Korneev, Yu Korneeva, I Florya, B Voronov, and G Gol'tsman. NbN nanowire superconducting single-photon detector for mid-infrared. *Physics Procedia*, 36:72–76, 2012.

[44] Andrew J Kerman, Eric A Dauler, Bryan S Robinson, Richard Barron, David O Caplan, Mark L Stevens, John J Carney, Scott A Hamilton, William E Keicher, Joel KW Yang, et al. Superconducting nanowire photon-counting detectors for optical communications. *Lincoln Laboratory Journal*, 16(1):217, 2006.

[45] G. W. Fraser, J. S. Heslop-Harrison, T. Schwarzacher, a. D. Holland, P. Verhoeve, and a. Peacock. Detection of multiple fluorescent labels using superconducting tunnel junction detectors. *Review of Scientific Instruments*, 74(9):4140, 2003.

[46] Robert H Hadfield and Göran Johansson. *Superconducting Devices in Quantum Optics.* Springer Quantum Science and Technology Series, 2016.

[47] Kunihiro Inomata, Zhirong Lin, Kazuki Koshino, William D. Oliver, Jaw-Shen Tsai, Tsuyoshi Yamamoto, and Yasunobu Nakamura. Single microwave-photon detector using an artificial $\lambda$-type three-level system. *Nature Communications*, 7:12303, 2016.

[48] Emanuel Knill, Raymond Laflamme, and Gerald J Milburn. A scheme for efficient quantum computation with linear optics. *Nature*, 409(6816):46–52, 2001.

[49] Werner Heisenberg. Über den anschaulichen inhalt der quantentheoretischen kinematik und mechanik. *Zeitschrift für Physik*, 43(3-4):172–198, 1927.

[50] William K Wootters and Wojciech H Zurek. A single quantum cannot be cloned. *Nature*, 299(5886):802–803, 1982.

[51] Michael A Nielsen and Isaac Chuang. *Quantum computation and quantum information.* Cambridge University Press, 2002.

[52] Gilles Brassard, Norbert Lütkenhaus, Tal Mor, and Barry C Sanders. Limitations on practical quantum cryptography. *Physical Review Letters*, 85(6):1330, 2000.

[53] AL Migdall, D Branning, and S Castelletto. Tailoring single-photon and multiphoton probabilities of a single-photon on-demand source. *Physical Review A*, 66(5):053805, 2002.

[54] Mark Fox. *Quantum optics: an introduction*, volume 15. OUP Oxford, 2006.

[55] R Hanbury Brown and Richard Q Twiss. Correlation between photons in two coherent beams of light. *Nature*, 177(4497):27–29, 1956.

[56] R Hanbury Brown and Richard Q Twiss. Interferometry of the intensity fluctuations in light. I. Basic theory: the correlation between photons in coherent beams of radiation. In *Proceedings of the Royal Society of London A: Mathematical, Physical and Engineering Sciences*, number 1230, pages 300–324. The Royal Society, 1957.

[57] R Hanbury Brown and RQ Twiss. Interferometry of the intensity fluctuations in light II. An experimental test of the theory for partially coherent light. In *Proceedings of the Royal Society of London A: Mathematical, Physical and Engineering Sciences*, number 1234, pages 291–319. The Royal Society, 1958.

[58] N. Prtljaga, R. J. Coles, J. O'Hara, B. Royall, E. Clarke, a. M. Fox, and M. S. Skolnick. Monolithic integration of a quantum emitter with a compact on-chip beam-splitter. *Applied Physics Letters*, 104(23):231107, 2014.

[59] CK Hong, ZY Ou, and Leonard Mandel. Measurement of subpicosecond time intervals between two photons by interference. *Physical Review Letters*, 59(18):2044, 1987.

[60] Alex D Semenov, Gregory N Gol'tsman, and Alexander A Korneev. Quantum detection by current carrying superconducting film. *Physica C: Superconductivity*, 351(4):349–356, 2001.

[61] G. N. Gol'tsman, O. Okunev, G. Chulkova, a. Lipatov, a. Semenov, K. Smirnov, B. Voronov, a. Dzardanov, C. Williams, and Roman Sobolewski. Picosecond superconducting single-photon optical detector. *Applied Physics Letters*, 79(6):705, 2001.

[62] R Leoni, F Mattioli, MG Castellano, S Cibella, P Carelli, S Pagano, D Perez de Lara, M Ejrnaes, MP Lisitskyi, E Esposito, et al. Fabrication and test of superconducting single photon detectors. *Nuclear Instruments and Methods in Physics Research Section A: Accelerators, Spectrometers, Detectors and Associated Equipment*, 559(2):564–566, 2006.

[63] Jeffrey A Stern and William H Farr. Fabrication and characterization of superconducting NbN nanowire single photon detectors. *IEEE Transactions on Applied Superconductivity*, 17(2):306–309, 2007.

[64] H Kamerlingh Onnes. The superconductivity of mercury. *Comm. Phys. Lab. Univ. Leiden*, 122:124, 1911.

[65] John Bardeen, Leon N Cooper, and John Robert Schrieffer. Theory of superconductivity. *Physical Review*, 108(5):1175, 1957.

[66] V. L. Ginzburg and L. D. Landau. *Translation. Zh. Eksperim. i. Teor. Fiz.*, 20:1064, 1950.

[67] Michael Tinkham. *Introduction to superconductivity*. Courier Corporation, 1996.

[68] Walther Meissner and Robert Ochsenfeld. A new effect at the occurrence of superconductivity. *Natural Sciences*, 21(44):787–788, 1933.

[69] Fritz London and Heinz London. The electromagnetic equations of the supraconductor. In *Proceedings of the Royal Society of London A: Mathematical, Physical and Engineering Sciences*, number 866, pages 71–88. The Royal Society, 1935.

[70] AA Abrikosov. Soviet Phys. JETP (English Transl.) 5, 1174 (1957); AL Ginzburg and LD Landau, Zh. Eksperim. i Teor. Fiz. 20, 1064 (1950); VL Ginzburg. *Nuovo cimento*, 2:1234, 1955.

[71] Yachin Ivry, Chung Soo Kim, Andrew E. Dane, Domenico De Fazio, Adam N. McCaughan, Kristen A. Sunter, Qingyuan Zhao, and Karl K. Berggren. Universal scaling of the critical temperature for thin films near the superconducting-to-insulating transition. *Physical Review B - Condensed Matter and Materials Physics*, 90(21):1–8, 2014.

[72] A Casaburi, RM Heath, Michael George Tanner, R Cristiano, M Ejrnaes, C Nappi, and RH Hadfield. Current distribution in a parallel configuration superconducting strip-line detector. *Applied Physics Letters*, 103(1):013503, 2013.

[73] Andrew J Kerman, Joel KW Yang, Richard J Molnar, Eric A Dauler, and Karl K Berggren. Electrothermal feedback in superconducting nanowire single-photon detectors. *Physical Review B*, 79(10):100509, 2009.

[74] Viacheslav Burenkov, He Xu, Bing Qi, Robert H. Hadfield, and Hoi-Kwong Lo. Investigations of afterpulsing and detection efficiency recovery in superconducting nanowire single-photon detectors. *Journal of Applied Physics*, 113(21):213102, 2013.

[75] JJ Renema, Giulia Frucci, Zili Zhou, Francesco Mattioli, Allesandro Gaggero, Roberto Leoni, Michiel JA de Dood, Andrea Fiore, and Martin P van Exter. Universal response curve for nanowire superconducting single-photon detectors. *Physical Review B*, 87(17):174526, 2013.

[76] Tao Jia, Chao Wan, Limin Zhao, Yu Zhou, Qingyuan Zhao, Min Gu, Xiaoqing Jia, Labao Zhang, Biaobing Jin, Jian Chen, et al. Temperature dependence of niobium superconducting nanowire single-photon detectors in He-3 cryocooler. *Chinese Science Bulletin*, 59(28):3549–3553, 2014.

[77] Taro Yamashita, Shigehito Miki, Wei Qiu, Mikio Fujiwara, Masahide Sasaki, and Zhen Wang. Temperature dependent performances of superconducting nanowire single-photon detectors in an ultralow-temperature region. *Applied Physics Express*, 3(10):102502, 2010.

[78] Andreas Engel, Kevin Inderbitzin, Andreas Schilling, Robert Lusche, Alexei Semenov, Heinz-Wilhelm Hübers, Dagmar Henrich, Matthias Hofherr, Konstantin Ilin, and Michael Siegel. Temperature-dependence of detection efficiency in NbN and TaN SNSPD. *IEEE Transactions on Applied Superconductivity*, 23(3):2300505–2300505, 2013.

[79] Dagmar Henrich, P Reichensperger, M Hofherr, JM Meckbach, Konstantin Ilin, Michael Siegel, A Semenov, Anna Zotova, and D Yu Vodolazov. Geometry-induced reduction of the critical current in superconducting nanowires. *Physical Review B*, 86(14):144504, 2012.

[80] Andreas Engel, JJ Renema, Konstantin Ilin, and A Semenov. Detection mechanism of superconducting nanowire single-photon detectors. *Superconductor Science and Technology*, 28(11):114003, 2015.

[81] John R. Clem and Karl K. Berggren. Geometry-dependent critical currents in superconducting nanocircuits. *Physical Review B - Condensed Matter and Materials Physics*, 84(17):1–27, 2011.

[82] Mohsen K Akhlaghi, Haig Atikian, Amin Eftekharian, Marko Loncar, and A Hamed Majedi. Reduced dark counts in optimized geometries for superconducting nanowire single photon detectors. *Optics Express*, 20(21):23610–23616, 2012.

[83] R Radebaugh. Refrigeration for superconductors. *Proceedings of the IEEE*, 92(10):1719–1734, 2004.

[84] Eric A Dauler, Matthew E Grein, Andrew J Kerman, Francesco Marsili, Shigehito Miki, Sae Woo Nam, Matthew D Shaw, Hirotaka Terai, Varun B Verma, and Taro Yamashita. Review of superconducting nanowire single-photon detector system design options and demonstrated performance. *Optical Engineering*, 53(8):081907–081907, 2014.

[85] Julia Toussaint, Roman Grüner, Marco Schubert, Torsten May, Hans-Georg Meyer, Benjamin Dietzek, Jürgen Popp, Matthias Hofherr, Matthias Arndt, Dagmar Henrich, et al. Superconducting single-photon counting system for optical experiments requiring time-resolution in the picosecond range. *Review of Scientific Instruments*, 83(12):123103, 2012.

[86] Shigehito Miki, Mikio Fujiwara, Masahide Sasaki, and Zhen Wang. Development of SNSPD system with Gifford-McMahon cryocooler. *IEEE Transactions on Applied Superconductivity*, 19(3):332–335, 2009.

[87] Peter J Lowell, Galen C O'Neil, Jason M Underwood, and Joel N Ullom. Macroscale refrigeration by nanoscale electron transport. *Applied Physics Letters*, 102(8):082601, 2013.

[88] Yun-Pil Shim and Charles Tahan. Superconducting-semiconductor quantum devices: from qubits to particle detectors. *IEEE Journal of Selected Topics in Quantum Electronics*, 21(2):1–9, 2015.

[89] Alan Migdall and Jonathan Dowling. Introduction to Journal of Modern Optics Special Issue on Single-photon: detectors, applications, and measurement methods. *Journal of Modern Optics*, 51(9-10):1265–1266, 2004.

[90] Trung D Vo, Jiakun He, Eric Magi, Matthew J Collins, Alex S Clark, Brian G Ferguson, Chunle Xiong, and Benjamin J Eggleton. Chalcogenide fiber-based distributed temperature sensor with sub-centimeter spatial resolution and enhanced accuracy. *Optics Express*, 22(2):1560–1568, 2014.

[91] Ryan E Warburton, Aongus McCarthy, Andrew M Wallace, Sergio Hernandez-Marin, Robert H Hadfield, Sae Woo Nam, and Gerald S Buller. Subcentimeter depth resolution using a single-photon counting time-of-flight laser ranging system at 1550 nm wavelength. *Optics Letters*, 32(15):2266–2268, 2007.

[92] Gerald S Buller, Aongus McCarthy, Ximing Ren, Nathan R Gemmell, Robert J Collins, Nils J Krichel, Michael G Tanner, Andrew M Wallace, Sandor Dorenbos, Val Zwiller, et al. Depth imaging at kilometer range using time-correlated single-photon counting at wavelengths of 850 nm and 1560 nm. In *SPIE NanoScience+ Engineering*, pages 84601I–84601I. International Society for Optics and Photonics, 2012.

[93] Valentin Atanassov, Georgi Jelev, and Lubomira Kraleva. Major Remote Sensing Development Tendencies in the Coming Decade. In *Space, Ecology, Safety Conference*, pages 289–296, 2010.

[94] X Michalet, RA Colyer, G Scalia, A Ingargiola, R Lin, JE Millaud, S Weiss, Oswald HW Siegmund, Anton S Tremsin, John V Vallerga, et al. Development of new photon-counting detectors for single-molecule fluorescence microscopy. *Philosophical Transactions of the Royal Society of London B: Biological Sciences*, 368(1611):20120035, 2013.

[95] Nathan R Gemmell, Aongus McCarthy, Baochang Liu, Michael G Tanner, Sander D Dorenbos, Valery Zwiller, Michael S Patterson, Gerald S Buller, Brian C Wilson, and Robert H Hadfield. Singlet oxygen luminescence detection with a fiber-coupled superconducting nanowire single-photon detector. *Optics Express*, 21(4):5005–5013, 2013.

[96] Robert H R.H. Hadfield, Martin J M.J. Stevens, Steven S.S. Gruber, a.J. Aaron J Miller, R.E. Robert E Schwall, Richard P R.P. Mirin, and S.W. Sae Woo Nam. Single photon source characterization with a superconducting single photon detector. *Optics Express*, 13(26):10846, 2005.

[97] Martin J. Stevens, Robert H. Hadfield, Robert E. Schwall, Sae Woo Nam, Richard P. Mirin, and James A. Gupta. Fast lifetime measurements of infrared emitters using a low-jitter superconducting single-photon detector. *Applied Physics Letters*, 89(3):031109, 2006.

[98] Robert H. Hadfield, Martin J. Stevens, Richard P. Mirin, and Sae Woo Nam. Single-photon source characterization with twin infrared-sensitive superconducting single-photon detectors. *Journal of Applied Physics*, 101(10):103104, 2007.

[99] C Zinoni, B Alloing, LH Li, F Marsili, A Fiore, L Lunghi, A Gerardino, Yu B Vakhtomin, KV Smirnov, and GN Gol'tsman. Single-photon experiments at telecommunication wavelengths using nanowire superconducting detectors. *Applied Physics Letters*, 91(3):031106, 2007.

[100] Toshiki Kobayashi, Rikizo Ikuta, Shuto Yasui, Shigehito Miki, Taro Yamashita, Hirotaka Terai, Takashi Yamamoto, Masato Koashi, and Nobuyuki Imoto. Frequency-domain hong–ou–mandel interference. *Nature Photonics*, 10(7):441–444, 2016.

[101] Kristiaan De Greve, Leo Yu, Peter L McMahon, Jason S Pelc, Chandra M Natarajan, Na Young Kim, Eisuke Abe, Sebastian Maier, Christian Schneider, Martin Kamp, Sven Höfling, Robert H Hadfield, Alfred Forchel, M M Fejer, and Yoshihisa Yamamoto. Quantum-dot spin-photon entanglement via frequency downconversion to telecom wavelength. *Nature*, 491(7424):421–5, 2012.

[102] Chandra M Natarajan, Lijian Zhang, Hendrik Coldenstrodt-Ronge, Gaia Donati, Sander N Dorenbos, Val Zwiller, Ian A Walmsley, and Robert H Hadfield. Quantum detector tomography of a time-multiplexed superconducting nanowire single-photon detector at telecom wavelengths. *Optics Express*, 21(1):893–902, 2013.

[103] Deny R. Hamel, Lynden K. Shalm, Hannes Hübel, Aaron J. Miller, Francesco Marsili, Varun B. Verma, Richard P. Mirin, Sae Woo Nam, Kevin J. Resch, and Thomas Jennewein. Direct generation of three-photon polarization entanglement. *Nature Photonics*, 8(10):801–807, 2014.

[104] Félix Bussières, Christoph Clausen, Alexey Tiranov, Boris Korzh, Varun B. Verma, Sae Woo Nam, Francesco Marsili, Alban Ferrier, Philippe Goldner, Harald Herrmann, Christine Silberhorn, Wolfgang Sohler, Mikael Afzelius, and Nicolas Gisin. Quantum teleportation from a telecom-wavelength photon to a solid-state quantum memory. *Nature Photonics*, 8(10):775–778, 2014.

[105] Jelmer J Renema, Giulia Frucci, Michiel JA de Dood, Richard Gill, Andrea Fiore, and Martin P van Exter. Tomography and state reconstruction with superconducting single-photon detectors. *Physical Review A*, 86(6):062113, 2012.

[106] Leo Yu, Chandra M. Natarajan, Tomoyuki Horikiri, Carsten Langrock, Jason S. Pelc, Michael G. Tanner, Eisuke Abe, Sebastian Maier, Christian Schneider, Sven Höfling, Martin Kamp, Robert H. Hadfield, Martin M. Fejer, and Yoshihisa Yamamoto. Two-photon interference at telecom wavelengths for time-bin-encoded single photons from quantum-dot spin qubits. *Nature Communications*, 6(May):8955, 2015.

[107] Hiroki Takesue, Shellee D Dyer, Martin J Stevens, Varun Verma, Richard P Mirin, and Sae Woo Nam. Quantum Teleportation over 100 km of Fiber using MoSi Superconducting Nanowire Single-Photon Detectors. In *CLEO: QELS_Fundamental Science*, pages FF1A–4. Optical Society of America, 2015.

[108] Reuben S Aspden, Nathan R. Gemmell, Peter a Morris, Daniel S. Tasca, Lena Mertens, Michael G Tanner, Robert A. Kirkwood, Alessandro Ruggeri, Alberto Tosi, Robert W. Boyd, Gerald S. Buller, Robert H. Hadfield, and Miles J. Padgett. Photon-sparse microscopy : Visible light imaging using infrared illumination. *Optica*, 2(12):1049–1052, 2015.

[109] Hiroki Takesue, Sae Woo Nam, Qiang Zhang, Robert H Hadfield, Toshimori Honjo, Kiyoshi Tamaki, and Yoshihisa Yamamoto. Quantum key distribution over a 40-dB channel loss using superconducting single-photon detectors. *Nature Photonics*, 1(6):343–348, 2007.

[110] Hiroyuki Shibata, Toshimori Honjo, and Kaoru Shimizu. Quantum key distribution over a 72 dB channel loss using ultralow dark count superconducting single-photon detectors. *Optics Letters*, 39(17):5078–5081, 2014.

[111] Michael G Tanner, Vadim Makarov, and Robert H Hadfield. Optimised quantum hacking of superconducting nanowire single-photon detectors. *Optics Express*, 22(6):6734–6748, 2014.

[112] Koji Azuma, Kiyoshi Tamaki, and William J. Munro. All-photonic intercity quantum key distribution. *Nature Communications*, 6:10171, 2015.

[113] Shigehito Miki, Taro Yamashita, Zhen Wang, and Hirotaka Terai. A 64-pixel NbTiN superconducting nanowire single-photon detector array for spatially resolved photon detection. *Optics Express*, 22(7):7811–7820, 2014.

[114] Varun B Verma, R Horansky, Francesco Marsili, JA Stern, MD Shaw, Adriana E Lita, Richard P Mirin, and Sae Woo Nam. A four-pixel single-photon pulse-position array fabricated from wsi superconducting nanowire single-photon detectors. *Applied Physics Letters*, 104(5):051115, 2014.

[115] M. S. Allman, V. B. Verma, M. Stevens, T. Gerrits, R. D. Horansky, A. E. Lita, F. Marsili, A. Beyer, M. D. Shaw, D. Kumor, R. Mirin, and S. W. Nam. A near-infrared 64-pixel superconducting nanowire single photon detector array with integrated multiplexed readout. *Applied Physics Letters*, 106(19):1–5, 2015.

[116] O Kahl, S Ferrari, V Kovalyuk, A Vetter, G Lewes-Malandrakis, C Nebel, A Korneev, G Gol'tsman, and W Pernice. Spectrally resolved single-photon imaging with hybrid superconducting-nanophotonic circuits. *arXiv preprint arXiv:1609.07857*, 2016.

[117] Robert Hadfield. AFRL-AFOSR-UK-TR-2012-0052. *EOARD/AFSOR Final Report*, 2012.

[118] Matthew Shaw, Jeffrey A. Stern, Kevin Birnbaum, Meera Srinivasan, Michael Cheng, Kevin Quirk, Abhijit Biswas, Francesco Marsili, Varun Verma, Richard P. Mirin, Sae Woo Nam, and William Farr. Tungsten silicide superconducting nanowire arrays for the lunar laser OCTL terminal. In *CLEO Proceedings*, page QM4L.7, 2013.

[119] S. Jahanmirinejad, G. Frucci, F. Mattioli, D. Sahin, a. Gaggero, R. Leoni, and a. Fiore. Photon-number resolving detector based on a series array of superconducting nanowires. *Applied Physics Letters*, 101(7):072602, 2012.

[120] Eric A Dauler, Bryan S Robinson, Andrew J Kerman, Joel KW Yang, Kristine M Rosfjord, Vikas Anant, Boris Voronov, Gregory Gol'tsman, and Karl K Berggren. Multi-element superconducting nanowire single-photon detector. *IEEE Transactions on Applied Superconductivity*, 17(2):279–284, 2007.

[121] D Rosenberg, AJ Kerman, RJ Molnar, and EA Dauler. High-speed and high-efficiency superconducting nanowire single photon detector array. *Optics Express*, 21(2):1440–1447, 2013.

[122] Joel K W Yang, Eric Dauler, Antonin Ferri, Aaron Pearlman, Aleksandr Verevkin, Gregory Gol'tsman, Boris Voronov, Roman Sobolewski, William E Keicher, and Karl K Berggren. Fabrication Development for Nanowire GHz-Counting-Rate Single-Photon Detectors. *IEEE Transactions on Applied Supercondcutivity*, 15(2):626–630, 2005.

[123] Shigehito Miki, Mikio Fujiwara, Masahide Sasaki, Wang Zhen, Burm Baek, Sae Woo Nam, Aaron J Miller, and Robert H Hadfield. Large sensitive-area NbN nanowire superconducting single-photon detectors fabricated on single-crystal MgO substrates. *Applied Physics Letters*, 92(6), 2008.

[124] Xiaolong Hu, Tian Zhong, James E White, Eric A Dauler, Faraz Najafi, Charles H Herder, Franco NC Wong, and Karl K Berggren. Fiber-coupled nanowire photon counter at 1550 nm with 24% system detection efficiency. *Optics Letters*, 34(23):3607–3609, 2009.

[125] Aaron J Miller, Adriana E Lita, Brice Calkins, Igor Vayshenker, Steven M Gruber, and Sae Woo Nam. Compact cryogenic self-aligning fiber-to-detector coupling with losses below one percent. *Optics Express*, 19(10):9102–9110, 2011.

[126] Risheng Cheng, Xiang Guo, Xiaosong Ma, Linran Fan, King Y Fong, Menno Poot, and Hong X Tang. Self-aligned multi-channel superconducting nanowire avalanche photodetector. *arXiv preprint arXiv:1601.01719*, 2016.

[127] Labao Zhang, Ming Gu, Tao Jia, Ruiyin Xu, Chao Wan, Lin Kang, Jian Chen, and Peiheng Wu. Multimode fiber coupled superconductor nanowire single-photon detector. *IEEE Photonics Journal*, 6(5):1–8, 2014.

[128] VB Verma, Francesco Marsili, S Harrington, Adriana E Lita, Richard P Mirin, and Sae Woo Nam. A three-dimensional, polarization-insensitive superconducting nanowire avalanche photodetector. *Applied Physics Letters*, 101(25):251114, 2012.

[129] S. N. Dorenbos, E. M. Reiger, N. Akopian, U. Perinetti, V. Zwiller, T. Zijlstra, and T. M. Klapwijk. Superconducting single photon detectors with minimized polarization dependence. *Applied Physics Letters*, 93(16):161102, 2008.

[130] Fan Zheng, Xudong Tao, Mengmeng Yang, Guanghao Zhu, Biaobing Jin, Lin Kang, Weiwei Xu, Jian Chen, and Peiheng Wu. Design of efficient superconducting nanowire single photon detectors with high polarization sensitivity for polarimetric imaging. *JOSA B*, 33(11):2256–2264, 2016.

[131] Fan Zheng, Ruiying Xu, Guanghao Zhu, Biaobing Jin, Lin Kang, Weiwei Xu, Jian Chen, and Peiheng Wu. Design of a polarization-insensitive superconducting nanowire single photon detector with high detection efficiency. *Scientific Reports*, 6, 2016.

[132] Liang Tang, Sukru Ekin Kocabas, Salman Latif, Ali K Okyay, Dany-Sebastien Ly-Gagnon, Krishna C Saraswat, and David AB Miller. Nanometre-scale germanium photodetector enhanced by a near-infrared dipole antenna. *Nature Photonics*, 2(4):226–229, 2008.

[133] Robert M Heath, Michael G Tanner, Timothy D Drysdale, Shigehito Miki, Vincenzo Giannini, Stefan A Maier, and Robert H Hadfield. Nanoantenna enhancement for telecom-wavelength superconducting single photon detectors. *Nano Letters*, 15(2):819–822, 2015.

[134] Kristine M Rosfjord, Joel KW Yang, Eric A Dauler, Andrew J Kerman, Vikas Anant, Boris M Voronov, Gregory N Gol'tsman, and Karl K Berggren. Nanowire single-photon detector with an integrated optical cavity and anti-reflection coating. *Optics Express*, 14(2):527–534, 2006.

[135] Shigehito Miki, Masanori Takeda, Mikio Fujiwara, Masahide Sasaki, and Zhen Wang. Compactly packaged superconducting nanowire single-photon detector with an optical cavity for multichannel system. *Optics Express*, 17(26):23557–23564, 2009.

[136] Shigehito Miki, Taro Yamashita, Hirotaka Terai, and Zhen Wang. High performance fiber-coupled NbTiN superconducting nanowire single photon detectors with gifford-mcmahon cryocooler. *Optics Express*, 21(8):10208–10214, 2013.

[137] Taro Yamashita, Shigehito Miki, Hirotaka Terai, and Zhen Wang. Low-filling-factor superconducting single photon detector with high system detection efficiency. *Optics Express*, 21(22):27177–84, 2013.

[138] Michael G Tanner, CM Natarajan, VK Pottapenjara, JA O'Connor, RJ Warburton, RH Hadfield, B Baek, S Nam, SN Dorenbos, E Bermúdez Ureña, et al. Enhanced telecom wavelength single-photon detection with NbTiN superconducting nanowires on oxidized silicon. *Applied Physics Letters*, 96(22):221109, 2010.

[139] Marsili F., Verma V. B., Stern J. A., Harrington S., Lita A. E., Gerrits T., Vayshenker I., Baek B., Shaw M. D., Mirin R. P., and Nam S. W. Detecting single infrared photons with 93% system efficiency. *Nature Photonics*, 7(3):210–214, 2013.

[140] W. J. Zhang, L. X. You, H. Li, J. Huang, C. L. Lv, L. Zhang, X. Y. Liu, J. J. Wu, Z. Wang, and X. M. Xie. NbN superconducting nanowire single photon detector with efficiency over 90% at 1550 nm wavelength operational at compact cryocooler temperature. *arXiv preprint arXiv:1609.00429*, 2016.

[141] Taro Yamashita, Kentaro Waki, Shigehito Miki, Robert A. Kirkwood, Robert H. Hadfield, and Hirotaka Terai. Superconducting nanowire single-photon detectors with non-periodic dielectric multilayers. *Scientific Reports*, 6:35240, 2016.

[142] H Angus Macleod. Turning value monitoring of narrow-band all-dielectric thin-film optical filters. *Journal of Modern Optics*, 19(1):1–28, 1972.

[143] Dubravko I Babic and Scott W Corzine. Analytic expressions for the reflection delay, penetration depth, and absorptance of quarter-wave dielectric mirrors. *IEEE Journal of Quantum Electronics*, 28(2):514–524, 1992.

[144] Robert M. Heath. *Nano-Optical Studies of Superconducting Nanowire Devices for Single Photon Detection*. University of Glasgow, 2014.

[145] Mária Csete, Gábor Szekeres, András Szenes, Balázs Bánhelyi, Tibor Csendes, and Gábor Szabó. Optimized superconducting nanowire single photon detectors to maximize absorptance. *arXiv preprint arXiv:1509.06301*, 2015.

[146] V. Kovalyuk, W. Hartmann, O. Kahl, N. Kaurova, A. Korneev, G. Gol'tsman, and W. H. P. Pernice. Absorption engineering of NbN nanowires deposited on silicon nitride nanophotonic circuits. *Optics Express*, 21(19):22683–22692, 2013.

[147] Joel KW Yang, Andrew J Kerman, Eric A Dauler, Vikas Anant, Kristine M Rosfjord, and Karl K Berggren. Modeling the electrical and thermal response of superconducting nanowire single-photon detectors. *IEEE Transactions on Applied Superconductivity*, 17(2):581–585, 2007.

[148] Reinier W. Heeres and Valery Zwiller. Superconducting detector dynamics studied by quantum pump-probe spectroscopy. *Applied Physics Letters*, 101(11):112603, 2012.

[149] Andrew J Kerman, Eric A Dauler, William E Keicher, Joel KW Yang, Karl K Berggren, G Gol'tsman, and B Voronov. Kinetic-inductance-limited reset time of superconducting nanowire photon counters. *Applied Physics Letters*, 88(11):111116, 2006.

[150] Niccolò Calandri, Qing-Yuan Zhao, Di Zhu, Andrew Dane, and Karl K Berggren. Superconducting nanowire detector jitter limited by detector geometry. *Applied Physics Letters*, 109(15):152601, 2016.

[151] Harold S Gamble, Kam O Leong, Syed H Raza, Brian M Armstrong, SJ Neil Mitchell, Suidong Yang, Vince Fusco, and Carson Stewart. Coplanar waveguides on SOI and OPS substrates. In *Microelectronic and MEMS Technologies*, pages 363–371. International Society for Optics and Photonics, 2001.

[152] A Eldek, Atef Z Elsherbeni, and Charles E Smith. Analysis of transmission and reflection from modified coplanar waveguide structures. *Applied Computational Electromagnetics Society Journal*, 17(2):158–165, 2002.

[153] Da-Wei He, Xin-Hong Cheng, Zhong-Jian Wang, Da-Wei Xu, Zhao-Rui Song, and Yue-Hui Yu. An analytical model for coplanar waveguide on silicon-on-insulator substrate with conformal mapping technique. *Chinese Physics B*, 20(1):010210, 2011.

[154] M Ejrnaes, A Casaburi, O Quaranta, S Marchetti, A Gaggero, F Mattioli, R Leoni, S Pagano, and R Cristiano. Characterization of parallel superconducting nanowire single photon detectors. *Superconductor Science and Technology*, 22(5):055006, 2009.

[155] Anthony J Annunziata, Orlando Quaranta, Daniel F Santavicca, Alessandro Casaburi, Luigi Frunzio, Mikkel Ejrnaes, Michael J Rooks, Roberto Cristiano, Sergio Pagano, Aviad Frydman, et al. Reset dynamics and latching in niobium superconducting nanowire single-photon detectors. *Journal of Applied Physics*, 108(8):084507, 2010.

[156] RH Hadfield, AJ Miller, SW Nam, RL Kautz, and RE Schwall. Low-frequency phase locking in high-inductance superconducting nanowires. *Applied Physics Letters*, 87(20):203505, 2005.

[157] JJ Renema, R Gaudio, Q Wang, Z Zhou, A Gaggero, F Mattioli, R Leoni, D Sahin, MJA De Dood, A Fiore, et al. Experimental test of theories of the detection mechanism in a nanowire superconducting single photon detector. *Physical Review Letters*, 112(11):117604, 2014.

[158] Vikas Anant, Andrew J Kerman, Eric A Dauler, Joel KW Yang, Kristine M Rosfjord, and Karl K Berggren. Optical properties of superconducting nanowire single-photon detectors. *Optics Express*, 16(14):10750–10761, 2008.

[159] Andrew J Kerman, Eric A Dauler, Joel KW Yang, Kristine M Rosfjord, Vikas Anant, Karl K Berggren, Gregory N Gol'tsman, and Boris M Voronov. Constriction-limited detection efficiency of superconducting nanowire single-photon detectors. *Applied Physics Letters*, 90(10):101110, 2007.

[160] Francesco Marsili, Faraz Najafi, Eric Dauler, Francesco Bellei, Xiaolong Hu, Maria Csete, Richard J Molnar, and Karl K Berggren. Single-photon detectors based on ultranarrow superconducting nanowires. *Nano Letters*, 11(5):2048–2053, 2011.

[161] M Ejrnaes, A Casaburi, R Cristiano, O Quaranta, S Marchetti, N Martucciello, S Pagano, A Gaggero, F Mattioli, and R Leoni. Properties

of cascade switch superconducting nanowire single photon detectors. In *International Conference on Quantum Comunication and Quantum Networking*, pages 150–157. Springer, 2009.

[162] F. Najafi, F. Marsili, E. Dauler, R. J. Molnar, and K. K. Berggren. Timing performance of 30-nm-wide superconducting nanowire avalanche photodetectors. *Applied Physics Letters*, 100(15):152602, 2012.

[163] Hiroyuki Shibata, Kaoru Shimizu, Hiroki Takesue, and Yasuhiro Tokura. Superconducting nanowire single-photon detector with ultralow dark count rate using cold optical filters. *Applied Physics Express*, 6(7):072801, 2013.

[164] Konstantin Smirnov, Yury Vachtomin, Alexander Divochiy, Andrey Antipov, and Gregory Gol'tsman. Dependence of dark count rates in superconducting single photon detectors on the filtering effect of standard single mode optical fibers. *Applied Physics Express*, 8(2):022501, 2015.

[165] U. Nasti, L. Parlato, M. Ejrnaes, R. Cristiano, T. Taino, H. Myoren, Roman Sobolewski, and G. Pepe. Thermal fluctuations in superconductor/ferromagnet nanostripes. *Physical Review B*, 92(1):014501, 2015.

[166] M Ejrnaes, A Casaburi, R Cristiano, O Quaranta, S Marchetti, N Martucciello, S Pagano, A Gaggero, F Mattioli, R Leoni, et al. Timing jitter of cascade switch superconducting nanowire single photon detectors. *Applied Physics Letters*, 95(13):132503, 2009.

[167] JA O'Connor, MG Tanner, CM Natarajan, GS Buller, RJ Warburton, S Miki, Z Wang, SW Nam, and RH Hadfield. Spatial dependence of output pulse delay in a niobium nitride nanowire superconducting single-photon detector. *Applied Physics Letters*, 98(20):201116, 2011.

[168] Haig A Atikian, Amin Eftekharian, A Jafari Salim, Michael J Burek, Jennifer T Choy, A Hamed Majedi, and Marko Lončar. Superconducting nanowire single photon detector on diamond. *Applied Physics Letters*, 104(12):122602, 2014.

[169] Labao Zhang, Xiachao Yan, Chengtao Jiang, Sen Zhang, Yajun Chen, Jian Chen, Lin Kang, and Peiheng Wu. SNSPDs on a Magnesium Fluoride Substrate for High System Efficiency and Ultra-Wide Band. *IEEE Photonics Technology Letters*, 28(22):2522–2525, 2016.

[170] SN Dorenbos, EM Reiger, U Perinetti, V Zwiller, T Zijlstra, and TM Klapwijk. Low noise superconducting single photon detectors on silicon. *Applied Physics Letters*, 93(13):131101, 2008.

[171] Yu P Korneeva, M Yu Mikhailov, Yu P Pershin, N N Manova, A V Divochiy, Yu B Vakhtomin, A A Korneev, K V Smirnov, A G Sivakov, A Yu Devizenko, and G N Gol'tsman. Superconducting single-photon detector made of MoSi film. *Superconductor Science and Technology*, 27(9):095012, 2014.

[172] D Bosworth, S-L Sahonta, RH Hadfield, and ZH Barber. Amorphous molybdenum silicon superconducting thin films. *AIP Advances*, 5(8):087106, 2015.

[173] Jian Li, Robert A. Kirkwood, Luke J. Baker, David Bosworth, Kleanthis Erotokritou, Archan Banerjee, Robert M. Heath, Chandra M. Natarajan, Zoe H. Barber, Marc Sorel, and Robert H. Hadfield. Nano-optical single-photon response mapping of waveguide integrated molybdenum silicide (MoSi) superconducting nanowires. *Optics Express*, 24(13):13931–13938, 2016.

[174] V. B. Verma, A. E. Lita, M. R. Vissers, F. Marsili, D. P. Pappas, R. P. Mirin, and S. W. Nam. Superconducting nanowire single photon detectors fabricated from an amorphous $Mo_{0.75}Ge_{0.25}$ thin film. *Applied Physics Letters*, 105(2):022602, 2014.

[175] H Shibata, H Takesue, T Honjo, T Akazaki, and Y Tokura. Single-photon detection using magnesium diboride superconducting nanowires. *Applied Physics Letters*, 97(21):212504, 2010.

[176] Hiroyuki Shibata, Tatsushi Akazaki, and Yasuhiro Tokura. Fabrication of $MgB_2$ nanowire single-photon detector with meander structure. *Applied Physics Express*, 6(2):023101, 2013.

[177] Noe Curtz, Edmond Koller, Hugo Zbinden, Michel Decroux, Louis Antognazza, Øystein Fischer, and Nicolas Gisin. Patterning of ultrathin YBCO nanowires using a new focused-ion-beam process. *Superconductor Science and Technology*, 23(4):045015, 2010.

[178] R Arpaia, M Ejrnaes, L Parlato, F Tafuri, R Cristiano, D Golubev, Roman Sobolewski, T Bauch, F Lombardi, and GP Pepe. High-temperature superconducting nanowires for photon detection. *Physica C: Superconductivity and its Applications*, 509:16–21, 2015.

[179] Aleksander Divochiy, Francesco Marsili, David Bitauld, Alessandro Gaggero, Roberto Leoni, Francesco Mattioli, Alexander Korneev, Vitaliy Seleznev, Nataliya Kaurova, Olga Minaeva, et al. Superconducting nanowire photon-number-resolving detector at telecommunication wavelengths. *Nature Photonics*, 2(5):302–306, 2008.

[180] D. Sahin, A. Gaggero, Z. Zhou, S. Jahanmirinejad, F. Mattioli, R. Leoni, J. Beetz, M. Lermer, M. Kamp, S. Höfling, and A. Fiore. Waveguide photon-number-resolving detectors for quantum photonic integrated circuits. *Applied Physics Letters*, 103(11):111116, 2013.

[181] V. B. Verma, R. Horansky, F. Marsili, J. A. Stern, M. D. Shaw, A. E. Lita, R. P. Mirin, and S. W. Nam. A four-pixel single-photon pulse-position array fabricated from WSi superconducting nanowire single-photon detectors. *Applied Physics Letters*, 104(5):051115, 2014.

[182] Shigehito Miki, Hirotaka Terai, Taro Yamashita, Kazumasa Makise, Mikio Fujiwara, Masahide Sasaki, and Zhen Wang. Superconducting single photon detectors integrated with single flux quantum readout circuits in a cryocooler. *Applied Physics Letters*, 99(11):111108, 2011.

[183] T Ortlepp, M Hofherr, L Fritzsch, S Engert, K Ilin, D Rall, H Toepfer, H-G Meyer, and M Siegel. Demonstration of digital readout circuit for superconducting nanowire single photon detector. *Optics Express*, 19(19):18593–18601, 2011.

[184] CE Shannon. A mathematical theory of communication, Bell System Technical Journal 27: 379-423 and 623–656. *Mathematical Reviews (MathSciNet): MR10, 133e*, 1948.

[185] George Boole. *An investigation of the laws of thought: on which are founded the mathematical theories of logic and probabilities.* Dover Publications, 1854.

[186] Alan Mathison Turing. On computable numbers, with an application to the entscheidungsproblem. *J. of Math*, 58(345-363):5, 1936.

[187] Alan Mathison Turing. On computable numbers, with an application to the entscheidungsproblem: A correction. *Proceedings of the London Mathematical Society*, 2(1):544, 1938.

[188] David Deutsch. Quantum theory, the church-turing principle and the universal quantum computer. In *Proceedings of the Royal Society of London A: Mathematical, Physical and Engineering Sciences*, volume 400, pages 97–117. The Royal Society, 1985.

[189] Peter W Shor. Algorithms for quantum computation: Discrete logarithms and factoring. In *Foundations of Computer Science, 1994 Proceedings., 35th Annual Symposium on*, pages 124–134. IEEE, 1994.

[190] Peter W Shor. Polynomial-time algorithms for prime factorization and discrete logarithms on a quantum computer. *SIAM review*, 41(2):303–332, 1999.

[191] Lov K Grover. Quantum mechanics helps in searching for a needle in a haystack. *Physical review letters*, 79(2):325, 1997.

[192] T D Ladd, F Jelezko, R Laflamme, Y Nakamura, C Monroe, and J L O'Brien. Quantum computers. *Nature*, 464(7285):45–53, 2010.

[193] Nathan K Langford. Encoding , manipulating and measuring quantum information in optics. *University of Queensland*, 2007.

[194] Gilles Brassard. Brief history of quantum cryptography: A personal perspective. In *IEEE Information Theory Workshop on Theory and Practice in Information-Theoretic Security, 2005.*, pages 19–23. IEEE, 2005.

[195] Charles H Bennett and Gilles Brassard. An update on quantum cryptography. In *Workshop on the Theory and Application of Cryptographic Techniques*, pages 475–480. Springer, 1984.

[196] I.D. Quantique 'quantum-safe crypto solutions'. http://www.idquantique.com/.

[197] Lars Lydersen, Carlos Wiechers, Christoffer Wittmann, Dominique Elser, Johannes Skaar, and Vadim Makarov. Hacking commercial quantum cryptography systems by tailored bright illumination. *Nature Photonics*, 4(10):686–689, 2010.

[198] Jeremy L O'Brien. Optical quantum computing. *Science*, 318(5856):1567–1570, 2007.

[199] Peter Bermel, Alejandro Rodriguez, Steven Johnson, John Joannopoulos, and Marin Soljačić. Single-photon all-optical switching using waveguide-cavity quantum electrodynamics. *Physical Review A*, 74(4):043818, 2006.

[200] Pieter Kok, W. J. Munro, Kae Nemoto, T. C. Ralph, Jonathan P. Dowling, and G. J. Milburn. Linear optical quantum computing with photonic qubits. *Reviews of Modern Physics*, 79(1):135–174, 2007.

[201] Jeremy L O'Brien, Akira Furusawa, and Jelena Vučković. Photonic quantum technologies. *Nature Photonics*, 3(12):687–695, 2009.

[202] Stefanie Barz, Elham Kashefi, Anne Broadbent, Joseph F Fitzsimons, Anton Zeilinger, and Philip Walther. Demonstration of blind quantum computing. *Science (New York, N.Y.)*, 335(6066):303–8, 2012.

[203] Tomohisa Nagata, Ryo Okamoto, Jeremy L O'Brien, Keiji Sasaki, and Shigeki Takeuchi. Beating the standard quantum limit with four-entangled photons. *Science (New York, N.Y.)*, 316(5825):726–9, 2007.

[204] Jonathan CF Matthews, Alberto Politi, André Stefanov, and Jeremy L O'Brien. Manipulation of multiphoton entanglement in waveguide quantum circuits. *Nature Photonics*, 3(6):346–350, 2009.

[205] Xiao-Qi Zhou, Pruet Kalasuwan, Timothy C Ralph, and Jeremy L O'Brien. Calculating unknown eigenvalues with a quantum algorithm. *Nature Photonics*, 7(3):223–228, 2013.

[206] Jacob Mower, Nicholas C Harris, Gregory R Steinbrecher, Yoav Lahini, and Dirk Englund. High-fidelity quantum state evolution in imperfect photonic integrated circuits. *Physical Review A*, 92(3):032322, 2015.

[207] Jeremy L O'Brien, GJ Pryde, Alexei Gilchrist, DFV James, NK Langford, TC Ralph, and AG White. Quantum process tomography of a controlled-NOT gate. *Physical Review Letters*, 93(8):080502, 2004.

[208] Benjamin J. Metcalf, Justin B. Spring, Peter C. Humphreys, Nicholas Thomas-Peter, Marco Barbieri, W. Steven Kolthammer, Xian-Min Jin, Nathan K. Langford, Dmytro Kundys, James C. Gates, Brian J. Smith, Peter G. R. Smith, and Ian A. Walmsley. Quantum teleportation on a photonic chip. *Nature Photonics*, 8(10):770–774, 2014.

[209] Jeremy L O'Brien, Geoffrey J Pryde, Andrew G White, Timothy C Ralph, and David Branning. Demonstration of an all-optical quantum controlled-NOT gate. *Nature*, 426(6964):264–267, 2003.

[210] Christof P Dietrich, Andrea Fiore, Mark G Thompson, Martin Kamp, and Sven Höfling. GaAs integrated quantum photonics: Towards compact and multi-functional quantum photonic integrated circuits. *Laser & Photonics Reviews*, 25:1–25, 2016.

[211] N Lusardi, JWN Los, RBM Gourgues, G Bulgarini, and A Geraci. Photon counting with photon number resolution through superconducting nanowires coupled to a multi-channel tdc in fpga. *Review of Scientific Instruments*, 88(3):035003, 2017.

[212] Alberto Politi, Martin J Cryan, John G Rarity, Siyuan Yu, and Jeremy L O'Brien. Silica-on-silicon waveguide quantum circuits. *Science*, 320(5876):646–649, 2008.

[213] Damien Bonneau, Mirko Lobino, Pisu Jiang, Chandra M Natarajan, Michael G Tanner, Robert H Hadfield, Sanders N Dorenbos, Val Zwiller, Mark G Thompson, and Jeremy L O'Brien. Fast path and polarization manipulation of telecom wavelength single photons in lithium niobate waveguide devices. *Physical Review Letters*, 108(5):053601, 2012.

[214] Damien Bonneau, Erman Engin, Kazuya Ohira, Nob Suzuki, Haruhiko Yoshida, Norio Iizuka, Mizunori Ezaki, Chandra M Natarajan, Michael G Tanner, Robert H Hadfield, et al. Quantum interference and manipulation of entanglement in silicon wire waveguide quantum circuits. *New Journal of Physics*, 14(4):045003, 2012.

[215] CM Natarajan, A Peruzzo, S Miki, M Sasaki, Z Wang, B Baek, S Nam, RH Hadfield, and JL O'Brien. Operating quantum waveguide circuits with superconducting single-photon detectors. *Applied Physics Letters*, 96(21):211101, 2010.

[216] JW Silverstone, R Santagati, D Bonneau, MJ Strain, M Sorel, JL O'Brien, and MG Thompson. Qubit entanglement between ring-resonator photon-pair sources on a silicon chip. *Nature Communications*, 6, 2015.

[217] Peyman Sarrafi, Eric Y Zhu, Ksenia Dolgaleva, Barry M Holmes, David C Hutchings, J Stewart Aitchison, and Li Qian. Continuous-wave quasi-phase-matched waveguide correlated photon pair source on a III–V chip. *Applied Physics Letters*, 103(25):251115, 2013.

[218] S. Fattah Poor, T. B. Hoang, L. Midolo, C. P. Dietrich, L. H. Li, E. H. Linfield, J. F P Schouwenberg, T. Xia, F. M. Pagliano, F. W M Van Otten, and a. Fiore. Efficient coupling of single photons to ridge-waveguide photonic integrated circuits. *Applied Physics Letters*, 102, 2013.

[219] VSC Manga Rao and Stephen Hughes. Single quantum dot spontaneous emission in a finite-size photonic crystal waveguide: proposal for an efficient 'on chip' single photon gun. *Physical Review Letters*, 99(19):193901, 2007.

[220] Andrei Faraon, Ilya Fushman, Dirk Englund, Nick Stoltz, Pierre Petroff, and Jelena Vučković. Coherent generation of non-classical light on a chip via photon-induced tunnelling and blockade. *Nature Physics*, 4(11):859–863, 2008.

[221] Raj B Patel, Anthony J Bennett, Ian Farrer, Christine A Nicoll, David A Ritchie, and Andrew J Shields. Two-photon interference of the emission from electrically tunable remote quantum dots. *Nature Photonics*, 4(9):632–635, 2010.

[222] L Midolo, F Pagliano, TB Hoang, T Xia, FWM van Otten, LH Li, EH Linfield, M Lermer, S Höfling, and A Fiore. Spontaneous emission control of single quantum dots by electromechanical tuning of a photonic crystal cavity. *Applied Physics Letters*, 101(9):091106, 2012.

[223] JP Hadden, JP Harrison, AC Stanley-Clarke, L Marseglia, Y-LD Ho, BR Patton, JL O'Brien, and JG Rarity. Strongly enhanced photon collection from diamond defect centers under microfabricated integrated solid immersion lenses. *Applied Physics Letters*, 97(24):241901, 2010.

[224] Xuedan Ma, Nicolai F Hartmann, Jon KS Baldwin, Stephen K Doorn, and Han Htoon. Room-temperature single-photon generation from solitary dopants of carbon nanotubes. *Nature Nanotechnology*, 10(8):671–675, 2015.

[225] M Ravaro, Y Seurin, S Ducci, G Leo, V Berger, A De Rossi, and G Assanto. Nonlinear AlGaAs waveguide for the generation of counterpropagating twin photons in the telecom range. *Journal of Applied Physics*, 98(6):063103, 2005.

[226] Rolf Horn, Payam Abolghasem, Bhavin J Bijlani, Dongpeng Kang, AS Helmy, and Gregor Weihs. Monolithic source of photon pairs. *Physical Review Letters*, 108(15):153605, 2012.

[227] Qiang Zhang, Xiuping Xie, Hiroki Takesue, Sae Woo Nam, Carsten Langrock, MM Fejer, and Yoshihisa Yamamoto. Correlated photon-pair generation in reverse-proton-exchange PPLN waveguides with integrated mode demultiplexer at 10 GHz clock. *Optics express*, 15(16):10288–10293, 2007.

[228] Sébastien Tanzilli, Hugues De Riedmatten, H Tittel, Hugo Zbinden, Pascal Baldi, Marc De Micheli, Daniel Barry Ostrowsky, and Nicolas Gisin. Highly efficient photon-pair source using periodically poled lithium niobate waveguide. *Electronics Letters*, 37(1):26–28, 2001.

[229] Joshua W Silverstone, Damien Bonneau, Kazuya Ohira, Nob Suzuki, Haruhiko Yoshida, Norio Iizuka, Mizunori Ezaki, Chandra M Natarajan, Michael G Tanner, Robert H Hadfield, et al. On-chip quantum interference between silicon photon-pair sources. *Nature Photonics*, 8(2):104–108, 2014.

[230] Christopher Richard Doerr and Katsunari Okamoto. Advances in Silica Planar Lightwave Circuits. *Journal of Lightwave Technology*, 24(12):4763–4789, 2006.

[231] Lorenzo Eds Pavesi and David J Lockwood. *Koji Yamada in, Silicon Photonics II: Components and Integration.* Springer, 2011.

[232] A Talneau, KH Lee, and I Sagnes. Spectral behavior and dispersion-less propagation in indium phosphide suspended photonic wires. *IEEE Photonics Technology Letters*, 21(12):775–777, 2009.

[233] Döndü Sahin, Alessandro Gaggero, Thang Ba Hoang, Giulia Frucci, Francesco Mattioli, Roberto Leoni, Johannes Beetz, Matthias Lermer, Martin Kamp, Sven Höfling, and Andrea Fiore. Integrated autocorrelator based on superconducting nanowires. *Optics Express*, 21(9):11162–11170, 2013.

[234] G. Reithmaier, S. Lichtmannecker, T. Reichert, P. Hasch, K. Müller, M. Bichler, R. Gross, and J. J. Finley. On-chip time resolved detection of quantum dot emission using integrated superconducting single photon detectors. *Scientific Reports*, 1:1901, 2013.

[235] E Yablonovitch. Inhibited spontaneous emission in solid-state physics and electronics. *Physical Review Letters*, 58(20):2059–2062, 1987.

[236] Sajeev John. Strong localization of photons in certain disordered dielectric superlattices. *Physical Review Letters*, 58(23):2486–2489, 1987.

[237] Robert D. Meade, a. Devenyi, J. D. Joannopoulos, O. L. Alerhand, D. a. Smith, and K. Kash. Novel applications of photonic band gap materials: Low-loss bends and high Q cavities. *Journal of Applied Physics*, 75(9):4753–4755, 1994.

[238] Thomas F Krauss, M Richard, and Stuart Brand. Two-dimensional photonic-bandgap structures operating at near-infrared wavelengths. *Nature*, 383(6602):699–702, 1996.

[239] Aliakbar Jafarpour. *Ultra Low-Loss and Wideband Photonic Crystal Waveguides for Dense Photonic Integrated Systems*. Georgia Institute of Technology, 2006.

[240] Liam O'Faolain, Xiaodong Yuan, Douglas McIntyre, Stephen Thoms, Harold Chong, RM De La Rue, and Thomas F Krauss. Low-loss propagation in photonic crystal waveguides. *Electronics Letters*, 42(25):1, 2006.

[241] Attila Mekis, J. Chen, I. Kurland, Shanhui Fan, Pierre Villeneuve, and J. Joannopoulos. High Transmission through Sharp Bends in Photonic Crystal Waveguides. *Physical Review Letters*, 77(18):3787–3790, 1996.

[242] Simone Ferrari, Oliver Kahl, Vadim Kovalyuk, Gregory N Gol'tsman, Alexander Korneev, and Wolfram HP Pernice. Waveguide-integrated single-and multi-photon detection at telecom wavelengths using superconducting nanowires. *Applied Physics Letters*, 106(15):151101, 2015.

[243] Svetlana Khasminskaya, Felix Pyatkov, Karolina Słowik, Simone Ferrari, Oliver Kahl, Vadim Kovalyuk, Patrik Rath, Andreas Vetter, Frank Hennrich, Manfred M Kappes, et al. Fully integrated quantum photonic circuit with an electrically driven light source. *Nature Photonics*, 10(11):727–732, 2016.

[244] C. Schuck, W. H. P. Pernice, and H. X. Tang. NbTiN superconducting nanowire detectors for visible and telecom wavelengths single photon counting on $Si_3N_4$ photonic circuits. *Applied Physics Letters*, 102:051101, 2013.

[245] Carsten Schuck, Wolfram H. P. Pernice, and Hong X. Tang. Waveguide integrated low noise NbTiN nanowire single-photon detectors with milli-Hz dark count rate. *Scientific Reports*, 1:1893, 2013.

[246] W. H. P. Pernice, C. Schuck, O. Minaeva, M. Li, G. N. Gol'tsman, A. V. Sergienko, and H. X. Tang. High-speed and high-efficiency travelling wave single-photon detectors embedded in nanophotonic circuits. *Nature Communications*, 3:1325, 2012.

[247] C. Schuck, W. H. P. Pernice, O. Minaeva, M. Li, G. Gol'tsman, A. V. Sergienko, and H. X. Tang. Matrix of integrated superconducting single-photon detectors with high timing resolution. In *IEEE Transactions on Applied Superconductivity*, volume 3, 2013.

[248] Faraz Najafi, Jacob Mower, Nicholas C Harris, Francesco Bellei, Andrew Dane, Catherine Lee, Xiaolong Hu, Prashanta Kharel, Francesco Marsili, Solomon Assefa, et al. On-chip detection of non-classical light by scalable integration of single-photon detectors. *Nature Communications*, 6, 2015.

[249] Faraz Najafi, Andrew Dane, Francesco Bellei, Qingyuan Zhao, Kristen A Sunter, Adam N McCaughan, and Karl K Berggren. Fabrication process yielding saturated nanowire single-photon detectors with 24-ps jitter. *IEEE Journal of Selected Topics in Quantum Electronics*, 21(2):1–7, 2015.

[250] Andreas Vetter, Simone Ferrari, Patrik Rath, Rasoul Alaee, Oliver Kahl, Vadim Kovalyuk, Silvia Diewald, Gregory N Gol'tsman, Alexander Korneev, Carsten Rockstuhl, et al. Cavity-enhanced and ultrafast superconducting single-photon detectors. *Nano Letters*, 16(11):7085–7092, 2016.

[251] Mohsen K Akhlaghi, Ellen Schelew, and Jeff F Young. Waveguide integrated superconducting single-photon detectors implemented as near-perfect absorbers of coherent radiation. *Nature Communications*, 6, 2015.

[252] Patrik Rath, Oliver Kahl, Simone Ferrari, Fabian Sproll, Georgia Lewes-Malandrakis, Dietmar Brink, Konstantin Ilin, Michael Siegel, Christoph Nebel, and Wolfram Pernice. Superconducting single-photon detectors integrated with diamond nanophotonic circuits. *Light: Science & Applications*, 4(10):e338, 2015.

[253] J. P. Sprengers, A. Gaggero, D. Sahin, S. Jahanmirinejad, G. Frucci, F. Mattioli, R. Leoni, J. Beetz, M. Lermer, M. Kamp, S. Höfling, R. Sanjines, and A. Fiore. Waveguide superconducting single-photon detectors for integrated quantum photonic circuits. *Applied Physics Letters*, 99:181110, 2011.

[254] A. Gaggero, S. Jahanmiri Nejad, F. Marsili, F. Mattioli, R. Leoni, D. Bitauld, D. Sahin, G. J. Hamhuis, R. Nötzel, R. Sanjines, and A. Fiore. Nanowire superconducting single-photon detectors on GaAs for integrated quantum photonic applications. *Applied Physics Letters*, 97:151108, 2010.

[255] Giulia Enrica Digeronimo, Maurangelo Petruzzella, Simone Birindelli, Rosalinda Gaudio, Sartoon Fattah Poor, Frank WM van Otten, and Andrea Fiore. Integration of single-photon sources and detectors on GaAs. *Multidisciplinary Digital Publishing Institute*, 3:55, 2016.

[256] G. Reithmaier, F. Flassig, P. Hasch, S. Lichtmannecker, K. Müller, J. Vučković, R. Gross, M. Kaniber, and J. J. Finley. A carrier relaxation bottleneck probed in single InGaAs quantum dots using integrated superconducting single photon detectors. *Applied Physics Letters*, 105(8):1–5, 2014.

[257] G. Reithmaier, M. Kaniber, F. Flassig, S. Lichtmannecker, K. Müller, A. Andrejew, J. Vučković, R. Gross, and J. J. Finley. On-Chip Generation, Routing, and Detection of Resonance Fluorescence. *Nano Letters*, 15(8):5208–5213, 2015.

[258] Brice Calkins, Paolo L. Mennea, Adriana E. Lita, Benjamin J. Metcalf, W. Steven Kolthammer, Antia Lamas-Linares, Justin B. Spring, Peter C. Humphreys, Richard P. Mirin, James C. Gates, Peter G. R. Smith, Ian A. Walmsley, Thomas Gerrits, and Sae Woo Nam. High quantum-efficiency photon-number-resolving detector for photonic on-chip information processing. *Optics Express*, 21:22657–22670, 2013.

[259] Aleksandra Markina-Khusid. *Design and simulation for the fabrication of integrated semiconductor optical logic gates*. Massachusetts Institute of Technology, 2005.

[260] S Cao, L Sun, J Noad, R James, D Coulas, G Lovell, E Higgins, and K Laliberte. Multimode interference couplers for 2x2 high speed GaAs-GaAlAs electro-optic switches. In *Integrated Optoelectronic Devices 2006*, pages 61160O–61160O. International Society for Optics and Photonics, 2006.

[261] Trung-Thanh Le and Laurence W. Cahill. The design of SOI-MMI couplers with arbitrary power splitting ratios using slotted waveguide structures. *2009 IEEE LEOS Annual Meeting Conference Proceedings*, 2:246–247, 2009.

[262] Isa Kiyat, Atilla Aydinli, and Nadir Dagli. A compact silicon-on-insulator polarization splitter. *IEEE photonics technology letters*, 17(1):100–102, 2005.

[263] Bing Shen, Peng Wang, Randy Polson, and Rajesh Menon. An integrated-nanophotonics polarization beamsplitter with $2.4 \times 2.4 \ \mu m^2$ footprint. *Nature Photonics*, 9(6):378–382, 2015.

[264] Peter C Humphreys, Benjamin J Metcalf, Justin B Spring, Merritt Moore, Patrick S Salter, Martin J Booth, W Steven Kolthammer, and Ian A

Walmsley. Strain-optic active control for quantum integrated photonics. *Optics Express*, 22(18):21719–21726, 2014.

[265] Ed L Wooten, Karl M Kissa, Alfredo Yi-Yan, Edmond J Murphy, Donald A Lafaw, Peter F Hallemeier, David Maack, Daniel V Attanasio, Daniel J Fritz, Gregory J McBrien, et al. A review of lithium niobate modulators for fiber-optic communications systems. *IEEE Journal of selected topics in Quantum Electronics*, 6(1):69–82, 2000.

[266] J. Amet, F.I. Baida, G.W. Burr, and M.-P. Bernal. The superprism effect in lithium niobate photonic crystals for ultra-fast, ultra-compact electro-optical switching. *Photonics and Nanostructures - Fundamentals and Applications*, 6(1):47–59, 2008.

[267] C. Bentham, I. E. Itskevich, R. J. Coles, B. Royall, E. Clarke, J. O'Hara, N. Prtljaga, A. M. Fox, M. S. Skolnick, and L. R. Wilson. On-chip electrically controlled routing of photons from a single quantum dot. *Applied Physics Letters*, 106(22), 2015.

[268] RJ Coles, N Prtljaga, B Royall, Isaac John Luxmoore, AM Fox, and MS Skolnick. Waveguide-coupled photonic crystal cavity for quantum dot spin readout. *Optics Express*, 22(3):2376–2385, 2014.

[269] Günther Roelkens, Dries Van Thourhout, and Roel Baets. High efficiency grating coupler between silicon-on-insulator waveguides and perfectly vertical optical fibers. *Optics Letters*, 32(11):1495–1497, 2007.

[270] G Roelkens, D Vermeulen, D Van Thourhout, R Baets, S Brision, P Lyan, P Gautier, and J Fédéli. High efficiency diffractive grating couplers for interfacing a single mode optical fiber with a nanophotonic silicon-on-insulator waveguide circuit High efficiency diffractive grating couplers for interfacing a single mode optical fiber with a nanophotoni. *Applied Physics Letters*, 92(13):131101, 2008.

[271] Yun Wang, Xu Wang, Jonas Flueckiger, Han Yun, Wei Shi, Richard Bojko, Nicolas a. F. Jaeger, and Lukas Chrostowski. Focusing sub-wavelength grating couplers with low back reflections for rapid prototyping of silicon photonic circuits. *Optics Express*, 22(17):20652, 2014.

[272] Chubing Peng and William Challener. Input-grating couplers for narrow Gaussian beam: influence of groove depth. *Optics Express*, 12(26):6481–6490, 2004.

[273] Dirk Taillaert, Peter Bienstman, and Roel Baets. Compact efficient broadband grating coupler for silicon-on-insulator waveguides. *Optics Letters*, 29(23):2749–51, 2004.

[274] Tong Chen, Hansuek Lee, Jiang Li, Oskar Painter, and Kerry J Vahala. Ultra-low-loss optical delay line on a silicon chip. In *Frontiers in Optics*, page FWS1. Optical Society of America, 2011.

[275] Christoph Clausen, Imam Usmani, Félix Bussières, Nicolas Sangouard, Mikael Afzelius, Hugues de Riedmatten, and Nicolas Gisin. Quantum storage of photonic entanglement in a crystal. *Nature*, 469(7331):508–11, 2011.

[276] I. Luxmoore, N. Wasley, a. Ramsay, a. Thijssen, R. Oulton, M. Hugues, S. Kasture, V. Achanta, A. Fox, and M. Skolnick. Interfacing Spins in an InGaAs Quantum Dot to a Semiconductor Waveguide Circuit Using Emitted Photons. *Physical Review Letters*, 110(3):037402, 2013.

[277] Konstantin K Likharev and Vasilii K Semenov. RSFQ logic/memory family: a new Josephson-junction technology for sub-terahertz-clock-frequency digital systems. *IEEE Transactions on Applied Superconductivity*, 1(1):3–28, 1991.

[278] Hirotaka Terai, Shigetoshi Miki, and Zhen Wang. Readout electronics using single-flux-quantum circuit technology for superconducting single-photon detector array. *IEEE Transactions on Applied Superconductivity*, 19(3):350–353, 2009.

[279] Hirotaka Terai, Shigehito Miki, Taro Yamashita, Kazumasa Makise, and Zhen Wang. Demonstration of single-flux-quantum readout operation for superconducting single-photon detectors. *Applied Physics Letters*, 97(11):112510, 2010.

[280] M Tanaka, T Kawamoto, Yuki Yamanashi, Y Kamiya, A Akimoto, K Fujiwara, A Fujimaki, Nobuyuki Yoshikawa, H Terai, and S Yorozu. Design of a pipelined 8-bit-serial single-flux-quantum microprocessor with multiple ALUs. *Superconductor Science and Technology*, 19(5):S344, 2006.

[281] Yoshiyuki Makiuchi Cen Shawn Wu and ChiiDong Chen. *High-energy Electron Beam Lithography for Nanoscale Fabrication*. InTech, 2010.

[282] Lhadi Merhari. *Hybrid nanocomposites for nanotechnology*. Springer, 2009.

[283] Shigehito Miki, Masanori Takeda, Mikio Fujiwara, Masahide Sasaki, Akira Otomo, and Zhen Wang. Superconducting NbTiN nanowire single photon detectors with low kinetic inductance. *Applied Physics Express*, 2(7):075002, 2009.

[284] Günther Reithmaier, Jörg Senf, Stefan Lichtmannecker, Thorsten Reichert, Fabian Flassig, Andrej Voss, Rudolf Gross, and JJ Finley. Optimisation of NbN thin films on GaAs substrates for in-situ single photon detection in structured photonic devices. *Journal of Applied Physics*, 113(14):143507, 2013.

[285] O. V. Balachova, M. a R Alves, J. W. Swart, E. S. Braga, and L. Cescato. CF4 plasma etching of materials used in microelectronics manufacturing. *Microelectronics Journal*, 31:213–215, 2000.

[286] Kirt R Williams, Kishan Gupta, and Matthew Wasilik. Etch rates for micromachining processing-part II. *Journal of Microelectromechanical Systems*, 12(6):761–778, 2003.

[287] Ki Hyun Kim, Zentaro Akase, Toshiaki Suzuki, and Daisuke Shindo. Charging Effects on SEM/SIM Contrast of Metal/Insulator System in Various Metallic Coating Conditions. *Materials Transactions*, 51(6):1080–1083, 2010.

[288] David a. Czaplewski and Leonidas E. Ocola. Increased pattern transfer fidelity of ZEP 520A during reactive ion etching through chemical modifications by additional dosing of the electron beam resist. *Journal of Vacuum Science & Technology B: Microelectronics and Nanometer Structures*, 29(2):021601, 2011.

[289] Chandra Mouli Natarajan. *Superconducting nanowire single-photon detectors for advanced photon-counting applications*. Heriot-Watt University, 2011.

[290] H Kamerlingh Onnes. The liquefaction of helium. *Koninklijke Nederlandse Akademie von Wetenschappen, Proceedings*, 11:1908–1909, 1908.

[291] H Kamerlingh Onnes. Further experiments with liquid helium. In *Proceedings of the KNAW*, volume 13, pages 1910–1911, 1911.

[292] Alexander Högele, Stefan Seidl, Martin Kroner, Khaled Karrai, Christian Schulhauser, Omar Sqalli, Jan Scrimgeour, and Richard J Warburton. Fiber-based confocal microscope for cryogenic spectroscopy. *Review of Scientific Instruments*, 79(2):023709, 2008.

[293] Robert H Hadfield, Paul A Dalgarno, John A O'Connor, Euan Ramsay, Richard J Warburton, Eric J Gansen, Burm Baek, Martin J Stevens, Richard P Mirin, and Sae Woo Nam. Submicrometer photoresponse mapping of nanowire superconducting single-photon detectors. *Applied Physics Letters*, 91(24):241108–241108, 2007.

[294] Robert M Heath, Michael G Tanner, Robert A Kirkwood, Shigehito Miki, Richard J Warburton, and Robert H Hadfield. A tunable fiber-coupled optical cavity for agile enhancement of detector absorption. *Journal of Applied Physics*, 120(11):113101, 2016.

[295] Waveguide optical simulation software: Lumerical Computational Solutions, Inc. https://www.lumerical.com/tcad-products/.

[296] Engineering and Physical Sciences Research Council (EPSRC) National Centre for III-V Technologies. http://www.epsrciii-vcentre.com/.

[297] EPSRC Programme Grant 'Semiconductor integrated quantum optical circuits' EP/J007544/1 (2012-2017). http://gow.epsrc.ac.uk/NGBOViewGrant.aspx?GrantRef=EP/J007544/1.

[298] Star Cryoelectronics Inc. superconducting thin film growth. http://starcryo.com/.

[299] LOT Quantum Design ellipsometry measurements. http://lot-qd.co.uk/en/.

[300] N. Prtljaga, C. Bentham, J. O'Hara, B. Royall, E. Clarke, L. R. Wilson, M. S. Skolnick, and A. M. Fox. On-chip interference of single photons from an embedded quantum dot and an external laser. *Applied Physics Letters*, 108(25):7–11, 2016.

[301] Iris Choi, Robert J Young, and Paul D Townsend. Quantum key distribution on a 10Gb/s WDM-PON. *Optics Express*, 18(9):9600–9612, 2010.

[302] Haw Yang, Guobin Luo, Pallop Karnchanaphanurach, Tai-Man Louie, Ivan Rech, Sergio Cova, Luying Xun, and X Sunney Xie. Protein conformational dynamics probed by single-molecule electron transfer. *Science*, 302(5643):262–266, 2003.

[303] James B Abshire, Haris Riris, Graham Allan, Xiaoli Sun, Jeffrey Chen, S Randy Kawa, Jian-Ping Mao, Mark Stephen, John F Burris, and MA Krainak. Laser sounder for global measurement the $CO_2$ concentrations in the troposphere from space. *Laser*, 500:550, 2007.

[304] Andrew M Wallace, Aongus McCarthy, Caroline J Nichol, Ximing Ren, Simone Morak, Daniel Martinez-Ramirez, Iain H Woodhouse, and Gerald S Buller. Design and evaluation of multispectral lidar for the recovery of arboreal parameters. *IEEE Transactions on Geoscience and Remote Sensing*, 52(8):4942–4954, 2014.

[305] Shellee D Dyer, Michael G Tanner, Burm Baek, Robert H Hadfield, and Sae Woo Nam. Analysis of a distributed fiber-optic temperature sensor using single-photon detectors. *Optics Express*, 20(4):3456–3466, 2012.

[306] Joshua W Silverstone, Damien Bonneau, Jeremy L O'Brien, and Mark G Thompson. Silicon quantum photonics. *IEEE Journal of Selected Topics in Quantum Electronics*, 22(6):390–402, 2016.

[307] Marcelo Davanco, Jin Liu, Luca Sapienza, Chen-Zhao Zhang, Jose Vinicius De Miranda Cardoso, Varun Verma, Richard Mirin, Sae Woo Nam, Liu Liu, and Kartik Srinivasan. A heterogeneous III-V/silicon integration platform for on-chip quantum photonic circuits with single quantum dot devices. *arXiv preprint arXiv:1611.07654*, 2016.

[308] Simeon Bogdanov, MY Shalaginov, Alexandra Boltasseva, and Vladimir M Shalaev. Material platforms for integrated quantum photonics. *Optical Materials Express*, 7(1):111–132, 2017.

# Appendix A

# List of publications

- <u>R.A. Kirkwood</u>, J. O'Hara, B. Royall, N. Prtljaga, C.M. Natarajan, M.G. Tanner, A. Casaburi, M. Fox, M. Skolnick, and R.H. Hadfield. A scalable fabrication process for superconducting nanowire single photon detectors integrated with GaAs waveguide circuits, *Under preparation*

- T. Yamashita, K. Waki, S. Miki, <u>R.A. Kirkwood</u>, R.H. Hadfield, and H. Terai. Superconducting nanowire single-photon detectors with non-periodic dielectric multilayers, *Scientific Reports* 6, 35240, 2016

- R.M. Heath, M.G. Tanner, <u>R.A. Kirkwood</u>, S. Miki, R.J. Warburton, and R.H. Hadfield. A tunable fibre-coupled optical cavity for agile enhancement of detector absorption, *Journal of Applied Physics* 120, p. 113101, 2016

- J. Li, <u>R.A. Kirkwood</u>, L.J. Baker, D. Bosworth, K. Erotokritou, A. Banerjee, R.M. Heath, C.M. Natarajan, Z.H. Barber, M. Sorel, and R.H. Hadfield. Nano-Optical Single-Photon Photoresponse Mapping of Waveguide Integrated Molybdenum Silicide (MoSi) Superconducting Nanowires, *Optics Express* 24 (13), pp. 13931-13938, 2016

**The following are not directly relevant to this thesis:**

- R.S. Aspden, N.R. Gemmell, P.A. Morris, D.S. Tasca, L. Mertens, M.G. Tanner, <u>R.A. Kirkwood</u>, A. Ruggeri, A. Tosi, R.W. Boyd, G.S. Buller, R.H. Hadfield, and M.J. Padgett. Photon-sparse microscopy: visible light imaging using infrared illumination, *Optica* 2 (12), pp. 1049-1052, 2015

- A. Heuer-Jungemann, <u>R.A. Kirkwood</u>, A.H. El-Sahgeer, T. Brown, and A.G. Kanaras. Copper-free click chemistry as an emerging tool for the programmed ligation of DNA-functionalised gold nanoparticles, *Nanoscale* 5 (16), pp. 7209-7212, 2013

# Appendix B

# List of presentations

- META 2016 Conference on meta-materials, Malaga, Spain. *Oral presentation.* July 2016

  *"Superconducting Nanowire Single Photon Detectors Integrated with GaAs Waveguide Circuits"*

- Oxford University Physics department, Oxford, UK. *Invited seminar.* June 2016

  *"Superconducting single photon detectors integrated with optical waveguides"*

- Superconductors-based sensors and quantum technologies workshop, Moscow, Russia. *"Oral presentation.* April 2016

  *"SSPDs integrated with GaAs waveguide circuits"*

- EPSRC Programme Grant away day, Sheffield, UK. *Oral presentation.* January 2016

  *"Superconducting nanowires for Optical Quantum Information Processing"*

- ISEC 2015 International superconductive electronics conference, Nagoya, Japan. *Invited oral presentation.* July 2015

  *"SNSPDs for Quantum Information Processing"*

- Photon '14 conference, London, UK. *Poster presentation.* September 2014

  *"Superconducting Nanowires For Optical Quantum Information Processing"*

- ASC 2014 Applied superconductivity conference, Charlotte, NC, USA. *Poster presentation.* August 2014

  *"Superconducting Nanowires For Optical Quantum Information Processing"*

- University of Glasgow Optoelectronics group residential, The Burn, Angus, UK. *Oral presentation.* August 2014

  *"SNSPDs for Optical Quantum Information Processing"*

- Nanomaterials and spectroscopy group meeting, Cambridge, UK. *Oral presentation.* April 2014

  *"Waveguide Integrated Superconducting Nanowire Single Photon Detectors"*

- SU2P symposium, University of Strathclyde, Glasgow, UK. *Poster presentation.* March 2014

  *"Superconducting nanowires for Optical Quantum Information Processing"*

- Institute of Physics Superconductivity group meeting, National Physical Laboratory, London, UK. *Poster, winner of 'Best Presentation' prize.* November 2013

  *"Superconducting Nanowires for Optical Quantum Information Processing"*

- ESAS European school on applied superconductivity, Genoa, Italy. *Summer school attendee, poster and oral presentations.* August 2013

  *"SNSPDs for integrated on-chip quantum information processing"*

- EPSRC programme grant review meeting, Sheffield, UK. *Poster presentation.* June 2013

  *"Fabricating Waveguide Integrated Superconducting Nanowires"*

- University of Glasgow Optoelectronics group residential, The Burn, Angus, UK. *Oral presentation.* May 2013

  *"SNSPDs for integrated on-chip quantum information processing"*